

Characterizing the Nonlinear Mechanical Response of Liver to Surgical Manipulation

A thesis presented

by

Amy Elizabeth Kerdok

to

The Division of Engineering and Applied Sciences

in partial fulfillment of the requirements for the degree of

Doctor of Philosophy

in the subject of

Engineering Sciences

Harvard University

Cambridge, MA

May 25, 2006

Robert D. Howe
Thesis Advisor

Amy Elizabeth Kerdok
Author

Characterizing the Nonlinear Mechanical Response of Liver to Surgical Manipulation

Abstract

Computer-aided medical technologies such as simulators for surgical training and planning require accurate representation of soft tissue behavior under large deformations. Limited datasets, and unrealistic models for soft tissues currently hinder the advancement of surgical simulation. This work identifies the nonlinear mechanical response of liver through the development of a physically-based constitutive model.

The effects of perfusion on the viscoelastic response of liver are identified, and a perfusion apparatus is created that approximates the *in vivo* condition. Indentation tests measuring the response of whole, perfused, porcine livers under finite deformations (~30% nominal strain) are conducted. Results indicate a time dependent, nonlinear, viscoelastic, force-displacement behavior. A constitutive model describes the time varying response through the combined contributions of three subsystems: collagenous capsule, parenchyma, and fluid filled vessels. Solving the inverse problem through iterative finite element modeling identifies the seven independent material parameters. The model is capable of capturing the salient features of the data. Modifications to the model and methods for ensuring the uniqueness of the parameters are presented. Additionally, a technique is described for assessing the tradeoff between accuracy and computation time necessary for real-time implementation.

This work presents data and modeling efforts to realize a constitutive model for liver whose parameters have a physical basis. The model can predict the behavior of liver independent of loading modality. Implementing such physically-based constitutive models into simulation systems provide realistic behavior, and ensure that errors made are not from the virtual environment.

Contents

Abstract	iii
Contents	iv
Nomenclature	vii
Acknowledgements	xi
Dedication	xiii
Chapter 1 Introduction	1
1.1 Minimally Invasive Surgery	1
1.2 Surgical Simulation	4
1.2.1 <i>Components of a Simulator</i>	5
1.2.2 <i>Current Simulator Status and Future Challenges</i>	7
1.3 Biological Material Property Identification	8
1.3.1 <i>The Challenge</i>	8
1.3.2 <i>The Liver</i>	9
1.3.3 <i>Biological Tissue Testing</i>	13
1.3.4 <i>Biological Tissue Modeling</i>	14
1.4 Thesis Aims and Outline	20
Chapter 2 Viscoelastic Effects of Perfusion of Liver Mechanics	22
2.1 Introduction	22
2.2 Methods and Materials	24
2.2.1 <i>Ex Vivo Liver Perfusion System</i>	24
2.2.2 <i>Indentation Test Instruments</i>	25
2.2.3 <i>Experimental Protocol and Environmental Conditions</i>	27
2.2.4 <i>In Vivo Whole Organ Testing</i>	28
2.2.5 <i>In Vitro Excised Section Testing</i>	29
2.2.6 <i>Ex Vivo Perfused Whole Organ Testing</i>	29
2.2.7 <i>Ex Vivo Post-Perfused Whole Organ Testing</i>	29
2.2.8 <i>Ex Vivo Post-Perfused Whole Organ Independent Test Over Time</i>	30
2.2.9 <i>Ex Vivo Perfused Independent Mechanical Damage Test</i>	30
2.2.10 <i>Data Analysis – Lumped Element Modeling</i>	30
2.3 Results	32

2.3.1 <i>Frequency Response Indentation tests</i>	32
2.3.2 <i>Large Strain Creep Indentation</i>	34
2.3.3 <i>Histology</i>	39
2.4 Discussion	39
Chapter 3 Mechanical Viscoelastic Testing of Liver	44
3.1 Background: Mechanical Testing of Liver	44
3.2 Uniaxial <i>Ex Vivo</i> Liver Capsule Testing	46
3.2.1 <i>Materials and Methods</i>	46
3.2.2 <i>Results</i>	47
3.3 <i>Ex Vivo</i> Whole Perfused Liver Indentation testing	49
3.3.1 <i>Lessons Learned from Perfusion Study</i>	49
3.3.2 <i>Motorized Indentation Test System</i>	49
3.3.3 <i>Experimental Protocol</i>	51
3.3.4 <i>Sine Wave Testing Over Time</i>	52
3.3.5 <i>Constant Strain-Rate Ramp Testing Across Frequencies</i>	56
3.3.6 <i>Multiple Ramp Indentation Testing</i>	60
3.3.7 <i>Stress Relaxation</i>	65
3.3.8 <i>Creep</i>	67
3.4 Discussion	68
Chapter 4 Nonlinear Physically-Based Constitutive Model and Parameter ID	70
4.1 Physiologically Derived Constitutive Model	71
4.1.1 <i>Motivation</i>	71
4.2 Constitutive Framework	72
4.2.1 <i>Isochoric Network</i>	73
4.2.2 <i>Volumetric Network</i>	78
4.2.3 <i>Hyperelastic 2D Collagenous Capsule</i>	80
4.3 Physical Interpretation of Framework in Relation to Observed Experimental Response	80
4.3.1 <i>Material Parameter Estimation</i>	82
4.4 Parameter Identification via Iterative Inverse Finite Element Modeling	85
4.4.1 <i>Numerical Approximation of Constitutive Model</i>	85

4.4.2 <i>Inverse Finite Element Modeling</i>	86
4.4.2 <i>Optimization Technique</i>	88
4.5 Results	89
4.5.1 <i>Uniaxial Capsule Tests</i>	89
4.5.2 <i>Liver Ramp Indentation Optimization</i>	90
4.5.3 <i>Validation</i>	100
4.6 Discussion	101
Chapter 5 Assessing the Accuracy of Real-Time Surgical Simulation Models	104
5.1 Motivation	104
5.2 Methods	107
5.2.1 <i>Truth Cube</i>	107
5.2.2 <i>Experimental Setup</i>	109
5.2.3 <i>Experimental Protocol</i>	110
5.2.4 <i>Image Processing</i>	111
5.2.5 <i>Finite Element Modeling</i>	111
5.2.6 <i>Biological Tissue Phantom</i>	112
5.3 Results	112
5.4 Discussion	116
Chapter 6 Conclusions and Future Work	119
6.1 Nonlinear Viscoelastic Mechanical Response of perfused Whole Livers Under Finite Indentation	119
6.2 Physically-Based Nonlinear Constitutive Model and Parameter ID	121
6.3 Assessing the Accuracy of Real-Time Surgical Simulation Models	123
6.4 Future Work	123
6.4.1 <i>Constitutive model Parameter Uniqueness</i>	123
6.4.2 <i>Applying Technologies to Other Organs</i>	123
6.4.3 <i>Internal parenchyma Measurements</i>	124
6.5 Final Words	124
Appendix A Characterization of Motorized Indentation System	125
Appendix B Linear Analytical Approximation of the Constitutive Model	133
Appendix C Instrumented Balloon Catheter	138
References	143

Nomenclature

Chapter 1

σ :	Cauchy Stress
λ :	stretch
U:	strain energy
P:	hydrostatic pressure
C, α , μ , β :	material parameters/constants
D:	compressibility factor
I_{1-3} :	1 st -3 rd invariants of the principle stretches
J:	total change in volume
μ_0 :	initial shear modulus
λ_L :	locking stretch
q:	volumetric flow rate
κ :	permeability coefficient
∇P :	pressure gradient

Chapter 2

K:	spring stiffness of first order Voigt model
B:	damping constant of first order Voigt model
f_c :	characteristic break frequency
F_0 :	applied step load for second order lumped element model
x_{0-2} :	displacement of second order lumped element model
K_{0-2} :	spring stiffnesses of second order lumped element model
$B_{1,2}$:	damping constants of second order lumped element model
A_0 :	amplitude of steady state creep displacement
$A_{1,2}$:	amplitude of the first and second time constants (τ_1 , τ_2), respectively

Chapter 4

$\underline{\mathbf{1}}$:	identity tensor
b:	fibril length
\mathbf{B}_c :	left Cauchy-Green stretch tensor for collagen
\mathbf{B}_{cap} :	2D left Cauchy-Green stretch tensor
c_p :	specific heat
$\tilde{\mathbf{D}}_p$:	parenchyma stretch tensor
ε_v :	volumetric strain
E_p :	Hencky strain
ϕ_0 :	solid content of tissue initially
ϕ_s :	solid content of tissue
ϕ_f :	fluid content of tissue
Φ :	objective function (MSE)

Chapter 4 Continued

f_{fibril} :	elastic force from collagen fibril
f_w :	initial volume fraction of water in tissue
\mathbf{F} :	total deformation gradient tensor
$\bar{\mathbf{F}}$:	isochoric deformation gradient tensor
\mathbf{F}_c :	deformation gradient tensor for collagen
\mathbf{F}_p :	deformation gradient tensor for parenchyma
F_{cap} :	force from capsule
F_{model} :	force from capsule model
G_p :	linear elastic shear modulus for parenchyma
$\dot{\gamma}^v$:	viscous shear strain rate
$\dot{\gamma}_0^v$:	initial viscous shear strain rate
h :	thickness of finite element model
H :	confined compression modulus
J :	volumetric Jacobian
J^* :	effective volumetric Jacobian
K_i :	reference stiffness in collagen fibril
K_{cap} :	area expansion modulus for capsule
K_{Lim} :	limiting bulk modulus
K_0 :	small strain bulk modulus
K_s :	constitutive parameter related to K_0
κ :	Darcy's hydraulic permeability
κ_0 :	permeability without a volumetric strain
κ_D :	thermal conductivity
l :	length scale for permeability parameter
L^{-1} :	inverse Langevin
$\tilde{\mathbf{L}}_p$:	viscous velocity gradient
$\lambda_{1,2,3}$:	principal stretches
λ_f :	current fibril stretch
λ_{Lcap} :	locking stretch for capsule
λ_{Linear} :	critical stretch of capsule
λ_L :	locking stretch for collagen fibril
m :	exponent of viscous shear strain rate
M :	exponent for nonlinear permeability
n :	number of data points for objective function
N :	direction of the viscous stress
ρ :	density of fluid
P_{fluid} :	dynamic fluid pressure
q :	volume flow rate
r_{gen} :	heat source term
\mathbf{R}_p :	rotation tensor for the parenchyma
σ_{Heq} :	hydrostatic equilibrium stress
S_p :	shear strength modulus
T :	temperature

Chapter 4 Continued

\mathbf{T}_c :	stress tensor from collagen
\mathbf{T}_{cap} :	membrane stress tensor
\mathbf{T}_e :	elastic back stress tensor from parenchyma
$\tilde{\mathbf{T}}_e$:	elastic stress tensor from parenchyma (in instantaneous-unloaded configuration)
\mathbf{T}_h :	hydrostatic stress tensor
\mathbf{T}_{iso} :	deviatoric stress tensor
\mathbf{T}_{tissue} :	total stress tensor in tissue
\mathbf{T}_v :	viscous stress tensor from parenchyma
$\tilde{\mathbf{T}}_v$:	viscous stress from parenchyma (in instantaneous-unloaded configuration)
\mathbf{T}_v' :	deviator of the viscous stress
τ :	magnitude of the viscous stress
τ_{perf} :	characteristic time constant for changes in perfusion
τ_{vol} :	characteristic time constant for changes in volume
μ_0 :	initial shear modulus for collagen
μ_{cap} :	initial shear modulus for capsule
μ_{Lim} :	limiting shear modulus for collagen
μ_{LimCap} :	limiting shear modulus for capsule
V :	current volume
V_0 :	initial volume
V_{eq} :	equilibrium volume after a step change in perfusion pressure
\mathbf{V}_p :	left stretch tensor for parenchyma
w :	width of liver in finite element model

Appendix A

T_{peak} :	time from 0 to the peak of the first oscillation for the motorized indenter response
T_{ss} :	time from 0 to when the motorized indenter response is within 2% of the steady state value
δ :	log decrement of the motorized indenter's oscillatory response
ω_n :	natural frequency of the motorized indenter's oscillatory response
ξ :	damping ratio of the motorized indenter's oscillatory response
%OS:	amount of overshoot of the first oscillation for the motorized indenter response
A_{cal} :	accelerometer calibration constant
M :	amplitude of commanded sine wave
x :	displacement of commanded sine wave
ω :	frequency of commanded sine wave
A_{signal} :	raw voltage signal from accelerometer
A_{Gain} :	accelerometer voltage gain
A_{amp} :	amplitude of accelerometer voltage signal

Appendix B

R:	radius of indenter
h:	thickness of tissue
G:	shear modulus
G^* :	complex shear modulus
G_S :	storage component of shear modulus
G_D :	loss component of shear modulus
B:	bulk modulus
B^* :	complex bulk modulus
B_S :	storage component of bulk modulus
B_D :	loss component of bulk modulus
E:	overall modulus
E^* :	complex modulus
E_S :	storage modulus
E_D :	loss modulus
$E_{0,1,2}$:	Young's modulus of elastic elements of model
$\eta_{1,2}$:	Damping constants of viscous elements of model
σ :	Cauchy stress
ε :	strain
ω :	frequency of sine wave
δ :	phase shift

Acknowledgements

“Gratitude is happiness doubled by wonder.”
 -G.K. Chesterton

To get the job done, scientists rely on not only their intuition and knowledge, but also their resources. It goes without saying that this thesis, and the many years that went into it, would not have been possible if it weren't for my amazing, and seemingly endless, support network. The number of teachers, academic advisers, and mentors who helped lead me down this path, and the cheerleaders that kept me on it, are too numerous to account for. But there are certainly a few that need mention.

I'd first like to thank my thesis committee. Prof. Vlassak was part of this journey from day one. I admire his responsiveness and timeliness to all matters. He was always the first to respond to an email asking for help, or time, despite his own busy schedule. I tremendously appreciated his accountability. Prof. Stone was a late addition to my committee, but a valuable one. His authentic enthusiasm to all matters of science and engineering brings life to any and all projects he encounters. I greatly appreciated his creativeness, challenges, and time. Prof. Socrate was my savior. Without her modeling efforts, I had no thesis. Her optimism, generosity, down-to-earth style, and overall concern for her students, establishes her as role-model for all who encounter her. And finally, Prof Howe, who took me on without hesitation after my first adviser suddenly passed away. Rob's support and interest in creating top-notch engineers made my graduate school experience a productive one. I thank him for providing me the opportunity to develop my love for teaching, and for the amazing team of lab-mates he put together.

My biorobotics “boys” were my true mentors, as it's not so much what you work on, but who you work with, that matter. Sol, Doug, Aaron, Paul, Petr, Chris, Ryan, Marius, Masa, and Shelten, I can't thank you enough for making this experience the most enjoyable one it could have been. You are all amazing people, I have the utmost respect for you and I will miss you greatly. And the girls, Heather, Anna, and Yuri, I am humbled to have been able to work with you all. Lastly, for my undergraduate students, Diana, Yi, and Cami, your diligence and patience are commendable, and it was an honor to have worked with such bright, young, students.

There were many other academic advisors and mentors that ought to be thanked as well. All the people at CIMIT: Mark, Dr. Dawson, Stephane, Vincent, Xu, Nick, ... it was truly exciting to be a part of your environment, and work under your support. And I certainly can't forget all the people who offered their time, resources, and assistance towards my experimental efforts: Jeff, Rita, Mark, Takashi, Mass Histology services, Enduratech, and the many piggies who willingly gave up their livers for my work. Thanks!

Lastly, I thank my family and friends for rooting me during this time, and always. The Harvard cycling team was the best outlet I could have asked for, and the friendships and memories (not to mention scars and stories) I made there will indeed last a lifetime. Nat, Janet, and Pam in particular, thanks for your endless support and energy. Pam, your patience and optimism were my lifeline – here's to future ‘adventures’ together.

Michelle, I thank you for your hospitality and editing efforts. Mom, dad, gram, Say, Pat, Deb, Bill, Faith, Nancy... and the rest of the family clan, you never were quite sure what I was up to, but you believed in me, and that mattered more than you'll ever know. You all kept me real and focused on life's subtleties and joys, and for that I am most grateful.

Finally, I want to thank the Division of Engineering and Applied Sciences, the Whitaker Foundation, the Harvard-MIT division of Health Sciences and Technology (HST), and the US Army for funding this work over the years. HST in particular, was a truly unique opportunity. I am humbled by the confidence they had in admitting me to their program, and for the inspirational people and opportunities I encountered along the way.

“The Journey of a thousand miles begins with one step.”

- *Lau Tzu*

So here we go...

Dedication

"Anyone who stops learning is old, whether at 20 or 80. Anyone who keeps learning stays young."

-Henry Ford

For Madeline – my grandmother, mentor, friend, and inspiration. Her youthful curiosity and life-long thirst for learning and teaching kept her 100 years young, while affecting the lives of countless others. Only life's experiences can bring someone wisdom; it's what we chose to do with that wisdom that matters. Madeline could be counted on to listen, to direct, and to offer her collection of wisdoms to you if you opened your heart to her. Her endless generosity and pure joy in both getting the most from life, and seeing other people live life to their fullest potential, was an admirable quality that I can only hope to live up to. So this thesis is for you Grammy J – my first step towards realizing all that life can bring.

Chapter 1

Introduction

The rapid expansion and unprecedented acceptance of computer-aided technologies is changing the face of procedural-based medicine. Although alternatives to open surgical procedures were performed with such devices as the Lichtleiter in 1806, and the automatic insufflator in 1960, it was the miniaturization of the video camera in 1982 that led to the utility and wide-spread acceptance of image-guided minimally invasive surgical procedures (Gandsas 2005). Further advances in imaging and visualization modalities, combined with the integration of robotics and new surgical tools, have altered the way in which procedural-based medicine will be conducted for years to come. However, such a change in the “status quo” comes with inherent challenges.

One of the largest hindrances in advancing training and planning minimally invasive medical technologies is a lack of understanding of the mechanical response of soft tissues to surgical manipulations. This work focuses on accurately characterizing the mechanical behavior of solid abdominal organs to large deformation. In particular, the biomechanical response of whole liver is acquired using a novel perfusion system and viscoelastic testing methods. A nonlinear, physically based constitutive model is developed. The material properties of the model are identified and validated from the mechanical testing data using iterative inverse finite element techniques. Lastly, a method is developed for assessing the trade-off between accurate tissue models and real-time implementation.

This chapter motivates the need for such information by first describing the benefits and drawbacks of minimally invasive surgery, followed by a description of surgical simulation including the necessary components and challenges of simulators. This leads to a discussion on the challenges of identifying soft tissue material properties including a detailed account of the structure and function of the liver, other researcher’s test methods, and their constitutive models.

1.1. Minimally Invasive Surgery

Current abdominal minimally invasive surgical (MIS) procedures typically require several small incisions to be made in the body. These establish 3-10 mm diameter ports for the insertion of a high magnification video camera (endoscope or laparoscope) and long surgical instruments (graspers, scissors, needle drivers, staplers, electro-surgical devices) (Figure 1.1) (Tendick, et al. 2000). A large internal working space is created by introducing gas into the region of interest, and images captured from the scope are

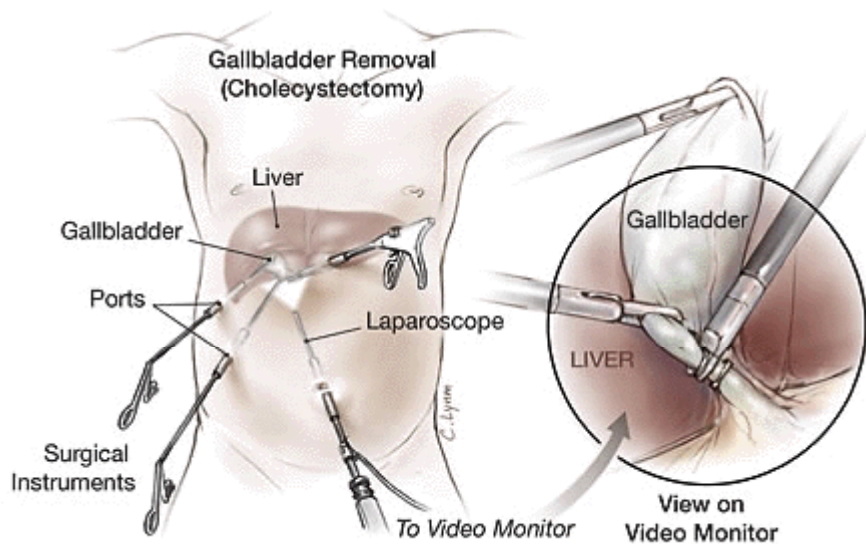


Figure 1.1 An illustration of laparoscopic surgery performed on the liver showing three instruments and a scope. The inset is an enlargement of the view from the monitor showing the gallbladder being removed from the liver at the cystic duct (permission granted from The Budapest University of Technology and Economics: www.dsy.hu/ion/laparoscopia.htm on May 10, 2006 from Mr. Robert Gyurcsanyi).

displayed on an external monitor (Medina 2003). Abdominal MIS is called laparoscopic surgery and is performed on most internal organs including the liver, spleen, kidney, pancreas, stomach, female reproductive organs, bladder, prostate, and intestines. Currently, 90% of all cholecystectomies (gallbladder removal) are now being done laparoscopically. Robots, such as the da Vinci Surgical System (Intuitive Surgical, Sunnyvale, CA), have been utilized as surgical assistants, holding the scope and manipulating the tools as commanded by a surgeon sitting at a remote console (Howe and Matsuoka 1999). Together, MIS and robotics enable procedures that used to require large incisions to be executed with minimal trauma to the patient (Rosen, et al. 2002). Reduced tissue damage lessens pain, scarring, and recovery time, and less exposure to air decreases infection rates (Meadows 2005; Rosen, et al. 2002; Tendick, et al. 2000).

Despite the positive patient outcome, MIS is far from perfect. The Institute of Medicine (IOM) clearly illustrated this in a 1999 report that stated over 98,000 people die each year in US hospitals due to medical errors (Medicine 2000). Thus, being cared for by a physician is the 7th leading cause of death in the United States (Dawson 2002). The IOM defines a medical error as “the failure of a planned action to be completed as intended or the use of a wrong plan to achieve an aim” (Medicine 2000). Although medical errors occur across the entire healthcare spectrum from drug prescriptions to surgical mishaps, Gallagher and Cates (2004) argue that many of these medical errors are caused by human factors associated with MIS image-guided techniques (arthroscopy, laparoscopy, flexible endoscopy, catheter-based techniques). This unfortunate result is not surprising since MIS procedures use specially designed instruments with limited ranges of motion, have a fulcrum effect that is both disorienting and reduces dexterity, offer a two-dimensional display to represent three-dimensional anatomy, lack haptic feedback and tactile sensation, and require difficult hand-eye coordination that produces a proprioceptive-visual conflict requiring increased cognitive effort (Szekely, et al. 2000a; Szekely, et al. 2000b;

Tendick, et al. 2000). In summary, surgeons using MIS not only lose the third dimension but also are hampered by reduced tactile feedback since their ten fingers are separated from the surgical anatomy by long instruments (Picinbono, et al. 2002).

Part of the challenge is that these new medical technologies require new skill sets. The way in which we educate our physicians has not yet fully incorporated these new techniques. For hundred's of years, medical training has consisted of a time-based apprenticeships system: "see one, do one, teach one." Procedural techniques are learned through practicing on mechanical models, animals, cadavers, volunteers, and patients. The drawbacks of these modes of training include the lack of realism of mechanical models, animals' limited pathology and dissimilar anatomy, the lack of physiological response and altered tissue properties of cadavers, and the obvious ethical and safety concerns associated with the use of live humans (Liu, et al. 2003; Tendick, et al. 2000). Furthermore, there is the expense of consuming medical devices for non therapeutic uses and the strain on already limited senior physician time (Gallagher and Cates 2004). The current time-based system depends on the chance availability of instructive patient encounters rather than on consistent designed exposure to fundamental medical problems (Gallagher and Cates 2004; Gordan and Pawlowski 2002). Residents are only trained on whatever cases happen to walk in the door. With the recent reduction in a resident's hours and a reduction in the number of patients (due to increasing healthcare costs and an increase in the emphasis on outpatient services and reduction of duration of inpatient care), only 5-18 patients are available to a resident over a period of 39-53 days (Dubois, et al. 1998; Liu, et al. 2003). Under the current system, surgeons of all levels are poorly equipped both to learn and practice the unique skills required for applying new medical technologies.

The apprenticeship model survives, however, due to the limitations of training media outside the operating room, and because traditional open surgery techniques rely on repetition to acquire the necessary hand-eye coordination (Tendick, et al. 2000). MIS presents an opportunity to evolve from time-and number of procedures-based training to a competency-based system in which such factors as limited patient contact and the need for subjective mentor feedback will be eliminated. One possible solution would be to use virtual environments similar to those used in training pilots (Rolfe and Staples 1986). The first medical simulators were used to train anesthesiologists at Stanford in 1994 (Gaba, et al. 1994). Since then, high-fidelity physical mannequin simulators have greatly improved the retention rate of acquiring surgical skills and thus the quality of medical education (Gordan 2002; Gordan and Pawlowski 2002). The Human Patient Simulator™ (Medical Education Technologies Inc., Sarasota, FL) is one such example featuring, an audible voice, reactive eyes, life-like chest movements, breath sounds, heart tones, and palpable pulses. These mannequins are a very useful teaching tool for advanced cardiac and/or trauma life support, anesthesia, general physiology, pathophysiology, pharmacology, and patient/doctor courses (Dawson 2002; Gordan and Pawlowski 2002; Gordan, et al. 2001). However, although these mannequins are excellent for team training, crisis management, and they allow for the practice of some minimally invasive procedures such as intubations and chest tube insertion, they do not enable surgical-procedure training, planning, and assessment (Dawson 2002).

1.2. Surgical Simulation

Surgical tasks require an optimal application of forces and torques to produce the proper motions of surgical instruments (Rosen, et al. 2002). Due to the unique perceptual-motor relationships required to conduct these tasks in a minimally invasive environment, mastering and assessing these skills is difficult. Virtual environments that can teach these skills and plan these procedures are now becoming available (Figure 1.2) (Liu, et al. 2003; Tendick, et al. 2000). The goal of surgical simulation is generation of realistic human anatomical and physiological responses to surgical manipulations for the purposes of training, planning, and assessing patient outcomes in a risk-free environment (Liu, et al. 2003). A simulator provides a platform for experiential learning for new surgeons as well as those returning to practice after an extended absence. It also can provide a medium to train in a field where procedures and tools rapidly change. In addition to permitting surgeons to safely prototype new procedures, simulation also may allow biomedical engineers a safe environment to design new medical devices.

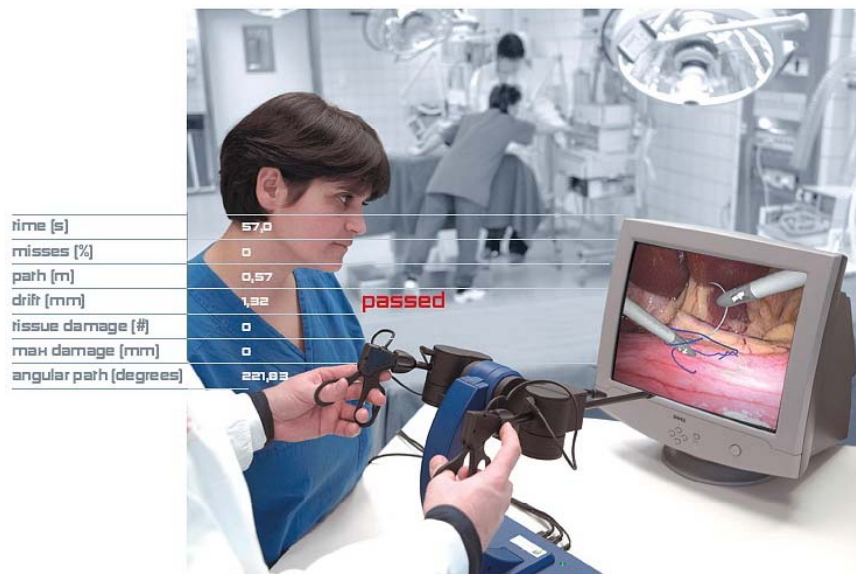


Figure 1.2 Example of a commercially available surgical simulator, LapSim® by Surgical Science (Science 2004). Shown is the console with mounted surgical tools, video screen, and training measures (permission granted to use image from <http://www.laparoscopy.ru/edu/lapsim.html> by Mr. Thomas Ragnarsson on May 8, 2006).

Creating realistic virtual surgical environments requires the acquisition of accurate biomechanical information, development of efficient computation strategies, and integration of acceptable validation protocols (Delingette 1998). To engage surgeons through multiple sensory channels, simulators must properly portray soft tissue deformation under interactions typical of actual surgical manipulations. To create a realistic visual and haptic interface, the tissues must be physically well defined and their interactions with tools and each other updated in real-time. Due to the complexity of biological tissue models and limited computational resources, there exists a trade-off

between computational speed and biomechanical accuracy. The question remains as to how accurate a simulator must be for it to be useful. Feedback from surgeons suggests that a bad simulator is worse than no simulator, and that simulators must be realistic enough so that any errors are made by the surgeon and not as a result of the virtual environment.

1.2.1. Components of a Simulator

Surgical simulation systems comprise of instrument devices, optics devices, a mechanical computation engine, a graphics computation engine, and a communications link (Szekely, et al. 2000a). Incorporated into the system are graphical anatomic models, deformable tissue models, collision-detection algorithms, visual and haptic display, and real-time integration strategies (Figure 1.3).

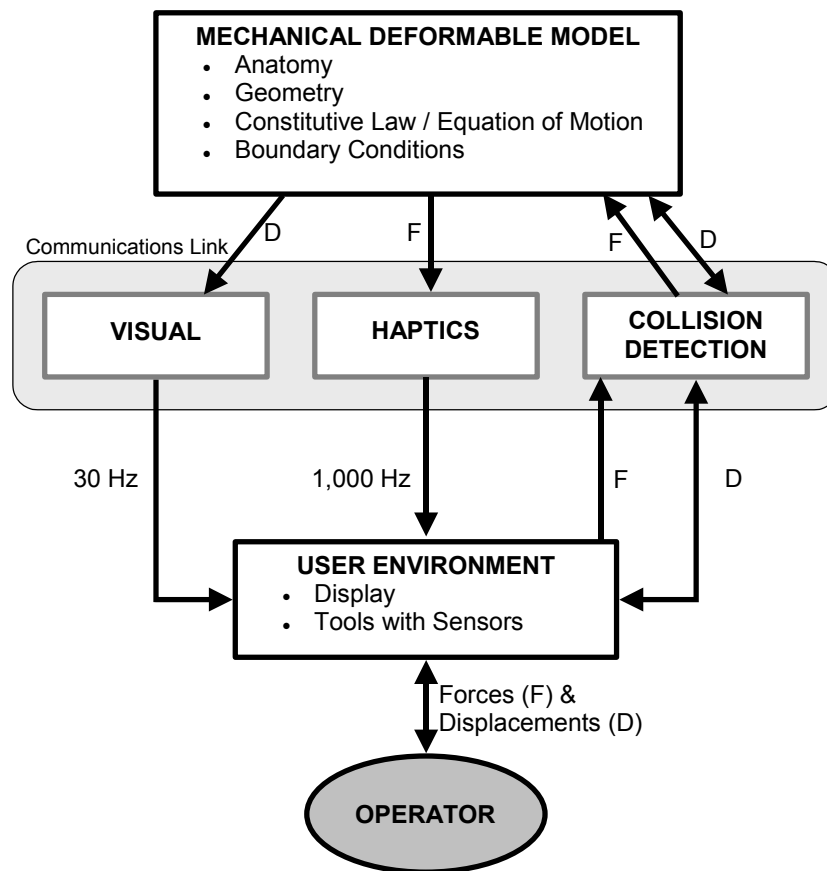


Figure 1.3 Components of a surgical simulator.

First, the anatomical region of interest is graphically represented using viable human data. This is accomplished, for example, using image segmentation techniques on the visible human database (United States National Library of Medicine, National Institute of Health Bethesda, MD) to accurately portray organs and their corresponding morphological structures (tendons, ligaments, etc.) (Szekely, et al. 2000a). Organ-specific

texture and illumination provided by the surgical scope create appropriate spatial perception.

Two types of deformable models are commonly used to represent organ behavior. Kinematically based models represent the first generation of biological tissue models (Delingette 1998). These are geometrically driven models that propagate displacements of volumes to represent deformation using splines, free-form deformations, or chain-mail algorithms (Delingette 1998; Szekely, et al. 2000a). Physically based models incorporate organ-specific material properties and thus are potentially more realistic. There are two common approaches to physically based models: discrete and continuous. Mass-spring discrete models use a network of point masses to describe the region of interest. These masses are connected by spring-dampers, and fuzzy logic plus neural networks, or fast finite-element models (FEM) can be used to determine the spring's parameters (Kuhnappel, et al. 1997). Discrete models are fast and computationally efficient and therefore useful in representing cutting and suturing tasks (Delingette 1998). However, their inability to capture complex and realistic biological material behavior as well as their numerical instability have led most researchers to use continuous models (Bro-Nielsen and Cotin 1996; Cotin, et al. 1999; Delingette 1998; Picinbono, et al. 2004; Szekely, et al. 2000a; Szekely, et al. 2000b).

These models permit a continuous formulation, relating deformation to energy (Cotin, et al. 1996). Since no closed-form solution is available for such models, a discrete approximation is achieved by using FEM or similar methods to break the region of interest into volumetric elements connected via nodes. Nodal displacements are then interpolated to obtain the element deformations. This approach is considered the method of choice for mathematically modeling complex mechanical systems, such as human organs, that exhibit irregular geometry, heterogeneous components, and nonlinear constitutive behavior (Hutter, et al. 2000). Continuous models accurately represent the mechanical behavior of soft tissues by directly relating absolute stress and strain and by capturing non-reversible behavior. However, this result is done in a computationally inefficient manner. Computing the internal forces and inverting the mass and damping matrices consume very large amounts of memory, thus making real-time simulation difficult (Wu, et al. 2001).

Recognizing the need to reduce the inner complexity of FEM, researchers are looking for ways to decrease the computational costs of using continuous deformable models (Meseure, et al. 2003). An explicit scheme (versus the more commonly used implicit scheme) is faster because it avoids the need to compute iterative solutions. However, explicit schemes accumulate errors, are only conditionally stable, and thus are generally not favored (Szekely, et al. 2000b; Wu, et al. 2001). Hutter tried using reduced-volume integration based on absolute strain (2000). Others have tried to separate the surface from the volume, and use offline precomputation with adaptive mesh refinements to decrease the overall number of elements (Bro-Nielsen and Cotin 1996; Cotin, et al. 1996; Wu, et al. 2001). Some have tried to integrate both deformable modeling schemes to combine the relative efficiency of the mass-spring systems with the fidelity of the continuous models (Meseure, et al. 2003). Since both models have the same differential equation of motion, researchers have combined them using Finite Difference Methods (Debunne, et al. 2001) or Mass/Tensor systems (Cotin, et al. 2000; Picinbono, et al. 2002).

Besides the inherent difficulty in solving the complex, deformable biomechanical models, real-time computation is further compromised by the necessity of detecting

collisions. The types of collisions to be detected include tool-tissue interactions, self-collisions, and 2D collisions. The challenges include determining the region of interest of the collision and the effects the collision will have on the tissue. For instance, suturing and cutting changes the tissue's topology, boundary conditions, and overall interactions (Delingette 1998; Picinbono, et al. 2002). Meseure et al. (2003) have used penalty-based methods where spheres represent the volume of the body, and forces are applied between colliding spheres to prevent interpenetration and to measure an intersection zone.

Part of the collision-detection problem resides in the disparity between haptic and visual update rates. Haptic update rates are on the order of 300-10,000 Hz (depending on the stiffness of the material) and thus easily satisfy the required visual update rates of 30 Hz (Delingette 1998; Picinbono, et al. 2002). This discrepancy causes a synchronization disconnect when a surgeon moves a device and anticipates both force-feedback and visual-deformation information. The model must detect the collision, compute the contact force, properly display the deformation (~30 Hz) and provide force feedback to the surgeon (~1000 Hz) (Cotin, et al. 1999). Szekely has attempted to solve this simultaneous communication problem by using 64-node parallel computers, whereas Picinbono uses a force-extrapolation technique (Picinbono, et al. 2002; Szekely, et al. 2000a; Szekely, et al. 2000b).

1.2.2. Current Simulator Status and Future Challenges

Most commercially available computer-based surgical simulators are procedure specific. The CathSim® Accutouch® simulator (Immersion Medical, Gaithersburg, MD) trains nursing students how to properly gain vascular access using a single degree of freedom-haptic interface and three degrees of freedom-needle and catheter-orientation data. LapSim® (Surgical Science, Göteborg, Sweden) teaches basic skills for laparoscopic procedures such as instrument navigation, suturing, coordination, grasping, lifting, and dissection (Figure 1.2). Immersion Medical has taken the same simulator and incorporated specific surgical procedures from cholecystectomy to Nissen fundoplication. The ProCedicus VIST™ and MIST™ simulators (Mentice AB, Göthenburg, Sweden) are currently the only clinically validated systems used in training for vascular interventions and laparoscopic procedures respectively.

Two studies using the ProCedicus MIST™ system have shown that virtual reality simulators improve the performance of laparoscopic cholecystectomy by decreasing overall surgical time, tissue trauma, and errors (Grantcharov, et al. 2004; Seymour and Gallagher 2002). Despite the evidence of these studies, several challenges remain before computer-based simulators can be used as the new standard for surgical training, planning, and assessment. For instance, most current commercial simulators do not include force feedback, have unrealistic representations of physiological effects (i.e. bleeding, blood pooling, tissue tearing), do not deform tissues in real-time, and focus on single applications (Liu, et al. 2003; Tendick, et al. 2000).

There are several major research simulators and groups that provide accurate data and methods for these projects. As mentioned above, Szekely uses parallel computing for real-time deformation and haptic rendering of his LASSO (laparoscopic surgery simulator) project (Szekely, et al. 2000a; Szekely, et al. 2000b). Karlsruhe has developed an endoscopic surgical trainer called VEST® (virtual endoscopic surgery training) System One (VSOOne™), that includes three haptic force feedback devices and one endoscopic

camera (Kuhnappel, et al. 1997). This system uses KISMET: Kinematic Simulation, Monitoring and Off-line Program Environment for Telerobotics (Bremen, Germany). INRIA has a hepatic surgical simulator platform that features real-time haptic updates to two force-feedback devices (Picinbono, et al. 2004; Picinbono, et al. 2002). Lastly, the University of California Berkley has developed a surgical simulation test bed using a PHANTOM haptic interface (Sensable Technologies, Woburn, MA) and MIS tools called VESTA (virtual environments for surgical training and augmentation) (Tendick, et al. 2000).

Although progress has been made developing realistic computer-based surgical simulators, many obstacles remain before the simulators can achieve their full potential. Liu et al (2003) have identified four key areas: understanding and realistic modeling of tissue and organ properties; achieving visual and haptic realism; obtaining realistic interactions between physical objects; and understanding and measuring the learning process in surgical skills acquisition. Of these, the accurate mechanical characterization of soft tissues to large deformations is the most severely lacking. The biomechanical representation of soft tissues is so critical to the advancement of surgical simulation that they have been called “the black-hole of simulation” (Satava 2005). Szekely has stated that, “realistic simulation of tissue behavior during interventions is one of the most challenging research areas in surgical simulation” (2000a). Accurate tissue models are not only needed to increase the realism of surgical simulators, but also to validate their results. Currently these systems rely on subjective surgical feedback to determine the realism of a simulator; the challenge is to be able to compare the output to quantified physical data and robust biomechanical models.

1.3. Biological Material Property Identification

1.3.1. The challenge

The goal of mechanically characterizing a material is to predict the deformation and/or motion of that material when subjected to external loads (forces and/or displacements). To accomplish this end, carefully controlled experiments are conducted on specified geometries of the material of interest. Loads are applied either statically or as a function of time, and the resulting displacements and forces are recorded. These specific forces and displacements are converted to stresses and strains for a more general interpretation via a constitutive law specific to the material. The constants of this law are known as the material’s parameters. If the constitutive law is correct and robust, the parameters are all that is needed to predict various deformation scenarios that cannot be easily tested – like surgical manipulations. However, biological materials are dissimilar from engineering materials and thus the same test methods, assumptions and constitutive models cannot be applied.

Their assumed simplicity and controllable, well defined testing conditions allow for most engineering materials to be characterized using first order constitutive models that can be solved analytically. Soft, nonload-bearing biological tissues are difficult to characterize due to their inherent complexity, variability, and the much larger strains to which they are often subjected. Many soft tissues are heterogeneous (material parameters vary throughout the tissue); nearly incompressible; porous; innervated; responsive to their environment (pH, temperature, health status); have a nonzero reference stress state; are capable of remodeling; and often have poorly known boundary conditions (Fung 1993;

Hayashi 2001; Humphrey 2002). Soft biological tissues can also be characterized by the following common physical features of their material response under finite strains: a nonlinear stress-strain relationship (due to contact, geometric, and material nonlinearities); viscoelasticity (exhibit hysteresis loops in cyclic loading and unloading, exhibit creep under a constant stress, and stress relaxation under a constant strain); preconditioning with repeated cycles; and time and rate dependency (although hysteresis is rate independent) (Fung 1993; Rubin and Bodner 2002). To further complicate the situation, biological behavior varies from point to point, time to time, and from individual to individual (Humphrey 2002). Due to this range of “normal” behavior, the “normal” response of tissue cannot be uniquely defined (Gallagher, et al. 1982). Both testing and modeling biological tissues in a meaningful manner is a formidable challenge. It requires special techniques and complex constitutive models that cannot be solved analytically. Numerical approximation methods are required to solve the inverse problem to determine the values of the multiple material parameters. Even if these challenges are met, questions of validity and uniqueness remain.

Tissues are exposed to different stresses based on their structure and function. The amount a tissue can distend is often what makes one tissue different from another. For instance, mechanically load-bearing, hard tissues such as bone and teeth undergo infinitesimal strains and can be tested and modeled similarly to engineering materials. Other tissues like skin, which can distend to well over 100% of its rest length, need more complex testing modalities and models. Until recently, only soft tissues with mechanical functioning such as muscles, tendons, ligaments, and cartilage have been extensively studied under finite deformations. Nonload-bearing soft tissues such as most abdominal organs have just recently begun to be mechanically characterized for purposes of surgical simulation.

How does one characterize an entire organ? At what level are its constituents considered? As discussed below, the liver comprises vessels, fluid, cells, nerves, and ligaments (including the external capsule). These can be further broken down into specific cells having internal organelles and extracellular matrices, and specific vessels with their endothelium and either blood, bile, or lymph content. Since the response of a material to applied loads depends on its internal composition, modeling the intricate nature of each micro structural component may produce the most accurate description of an organ's behavior, but this would be excessively complex. Surgeons interact mechanically with an entire organ, thus one should both measure the intact organ and determine the simplest subset of components that, when combined, mathematically describe the complete behavior. What follows is a detailed description of the liver followed by a summary of how soft tissues have been tested and modeled.

1.3.2. The Liver

The liver is the largest internal organ in the human body (Gray 1977). Although its vascular, metabolic, and secretory/excretory functions are necessary to sustain life, the liver is a nonload-bearing organ and has limited mechanical function. It has been described as a friable soft solid that is easily lacerated (Gray 1977). Due to its complex behavior and non-mechanical function, very little data has been collected to understand its mechanical properties. Yet, as a large abdominal organ located anteriorly beneath the diaphragm, it covers many abdominal structures including the stomach, duodenum,

colon, right kidney, and the right adrenal gland (Thomas 1997). To surgically access these various structures, one has to manipulate this soft organ under large deformations. As an organ that will inevitably be included directly (i.e. the common cholecystectomy procedure [~600,000 cases per year in US]) or indirectly in many surgical simulations, the liver's mechanical response when subjected to large manipulations is perhaps best investigated by first reviewing its structure and function.

The liver occupies the right hypochondrium, situated behind and below the right lower rib cage and beneath the diaphragm (Figure 1.4) (Davide Brunelli 2001; Holmes 2003; Thomas 1997). In humans, it is a wedge and measures 20-23 cm, 15-17.5 cm, and 10-12.5 cm in the transverse, vertical, and anterior/posterior dimensions, respectively (Gray 1977). A typical human liver weighs between 1.1-1.7 kg. There are two interconnected lobes (right and left) externally separated on the anterior side by the falciform ligament with the larger right lobe further subdivided into the right, caudate, and quadrate lobes. The liver is often segmented for transplant purposes based on eight vascular regions, defined by the major branches of the portal triad and hepatic veins. Five ligaments tether the liver to the diaphragm (its superior boundary condition), surround and support its vasculature, and provide a two-layered fibrous capsule (peritoneum) that encases the liver except for a bare area where it directly adheres to the diaphragm. Finally, there are five external vessels: portal vein, hepatic artery, hepatic vein (leading into the inferior vena cava), lymphatic duct, and hepatic duct. The portal vein, hepatic artery, and hepatic duct each enter the liver posteriorly and inferiorly via the porta hepatis, enclosed by a loose

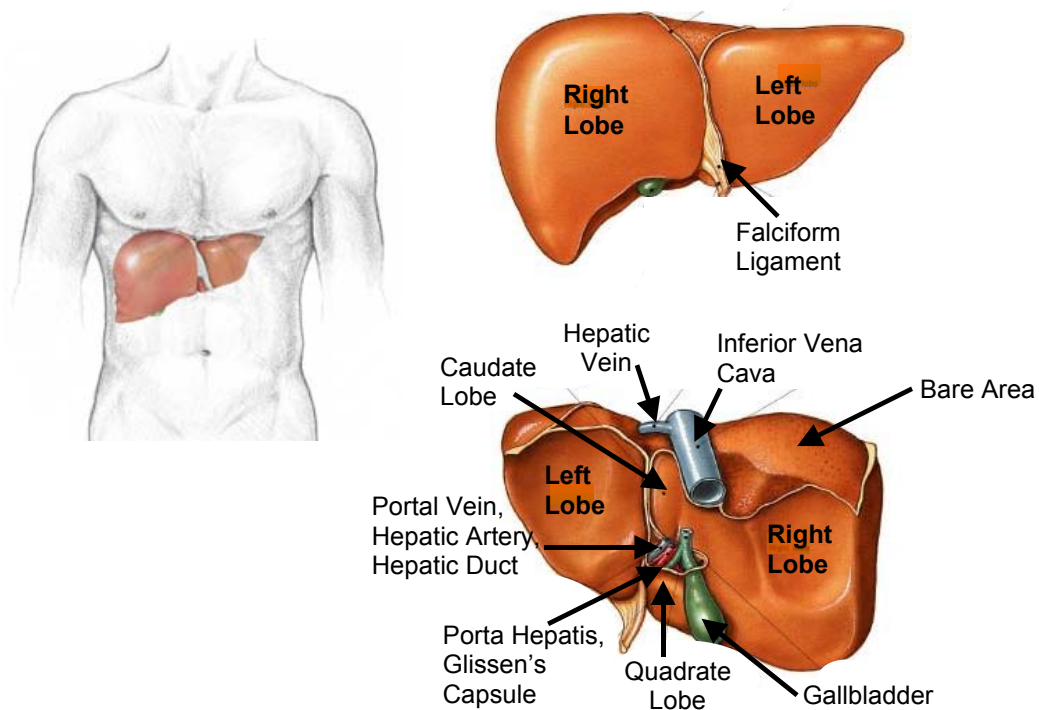


Figure 1.4 (Top Left) Anatomical location of the human liver in situ. (Top) Anterior view of the liver showing the falciform ligament and right and left lobes. (Bottom) Inferior view of the liver showing the vessels, capsule, gallbladder, porta hepatis, and caudate and quadrate lobes (Holmes 2003; Rao 2002).

areolar tissue called Glisson's capsule. These three vessels are called the portal triad and run in parallel throughout the liver in a predominantly longitudinal orientation. The capsule containing the portal triad is invested into the tissue throughout the liver and thus serves as a supporting network for the parenchyma as well as a means of separating the lobules which are the functional units of the liver (Thomas 1997).

The liver lobule is a hexagonal cylindrical structure 0.8-2.0 mm in diameter and several millimeters long (Figure 1.5) (Guyton and Hall 1996). There are between 100,000 and 1,000,000 individual lobules in an adult human liver, resulting in a nearly homogenous parenchymal internal structure on a macroscopic scale (Melvin, et al. 1973). The lobules are considered the functional units of the liver and are constructed of a sea of hepatocytes between the septae walls, with the portal triads at each corner and a central vein at the center. Since there is a 1:1 ratio of portal triad vessels to central veins, the internal structure and functional unit of the liver can also be described with the central veins at the corner of the hexagon. This is called the acinus.

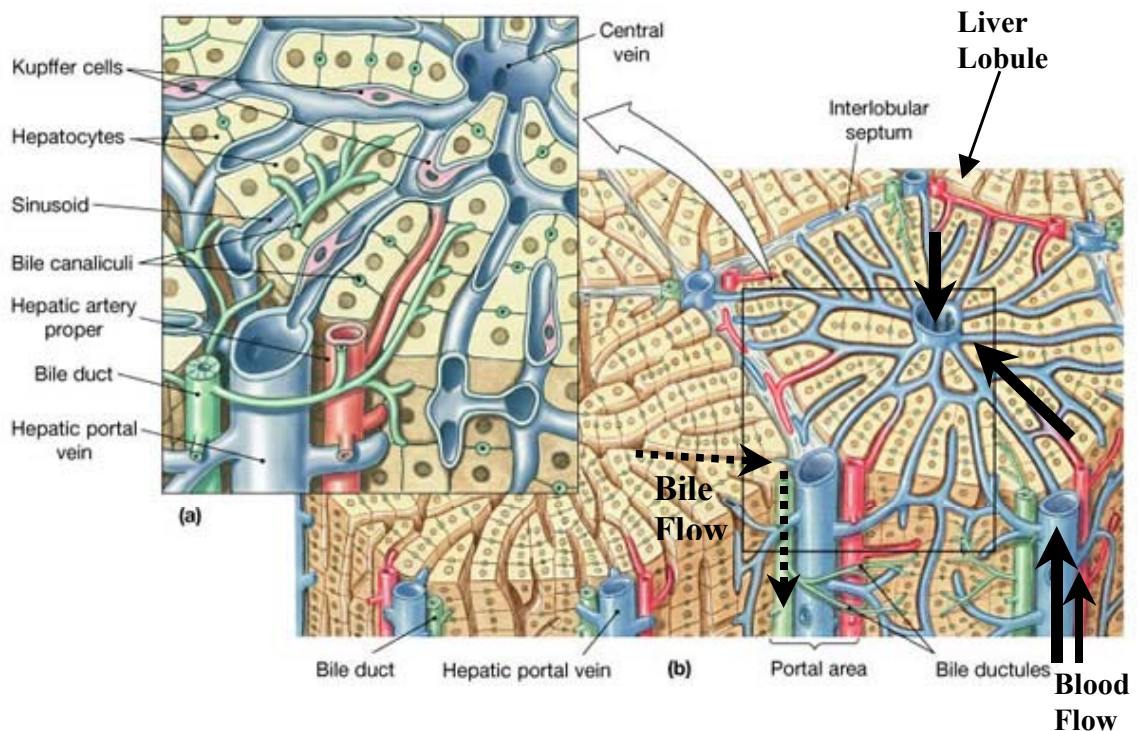


Figure 1.5 Detail of liver lobule and portal triad showing hexagonal structure, vasculature, blood and bile flow pattern, and the plate arrangement of hepatocytes (Cummings 2004).

The liver is a highly vascular and dynamic organ. One of its main vascular functions is to act as a blood reservoir. It normally contains 450 mL (10% of the body's blood volume), but can expand to retain up to 1 L (Guyton and Hall 1996). It receives 29% of the total resting cardiac output, or 1.4 L/min of blood. The liver receives 75% of the blood supply from the mesenteric vein, which carries unoxygenated blood from the stomach, spleen and small intestine. The portal vein is a large (35 μm average diameter

throughout, 15 mm at entrance), elastically distensible, low-pressure (9 mmHg) vessel that transports 1.05 L/min of blood into the liver's capillaries. The remaining 25% of the liver's blood supply comes from the hepatic artery, at a rate of 350 mL/min. The hepatic artery carries oxygenated blood from the celiac branch of the aorta and is a small (12 μm average diameter throughout, 2 mm at entrance), non-distensible, high-pressure (97 mmHg) vessel. The oxygenated blood disperses to feed the walls of the other vessels and ducts, the gallbladder, and finally the hepatocytes (Gray 1977; Mitzner 1974). Blood from the terminal branches of the portal veins and hepatic arteries enter into a vast sea of special capillaries called sinusoids. These sinusoids are fenestrated, distensible vascular structures that pass throughout the liver between plates of hepatocytes. The sinusoids branch and anastomose into a large network of over a billion parallel vessels per lobule to slowly bring blood from the portal vein and hepatic artery past the hepatocytes, and to clear away the cell's waste products to the central vein. The central veins group into larger hepatic veins before ultimately leaving the liver and draining into the inferior vena cava at the superior surface. Hepatic veins are unique in that they are devoid of valves. They have very little cellular content and thus bind to the walls of the canals through which they run and remain patent when the liver is sectioned (Gray 1977).

The liver's unique vascular structure serves as a blood filter. Normally, capillaries exchange blood with the interstitial fluid via diffusion through thin-walled, permeable capillaries. The blood pressure within the capillaries serves to drive the fluid out at the arterial end, and the negative interstitial pressure forces it in at the venous end. Similarly, an osmotic pressure gradient pulls fluid out of the capillaries into the interstitium and pushes it back in again (Guyton and Hall 1996). The liver capillaries filter the blood in a different way. Sinusoids are devoid of a diaphragm and basal lamina and contain large pores that are 150-175 nm in diameter (Braet and Wisse 2002). Groups of these fenestrae are arranged in sieve plates throughout the vessel. The vessels are lined with endothelial cells and special macrophages called Kupfer cells. The Kupfer cells filter the blood by digesting various waste products. Other molecules are allowed to pass through the fenestrae into the perisinusoidal spaces where they are processed by plates of hepatocytes. Since fluids, solutes, and various sized particles and plasma proteins pass into the interstitium freely, there is a limited osmotic gradient (Braet and Wisse 2002; Mitzner 1974; Nakata, et al. 1960). Instead, the number and size of the pores in the sinusoids control plasma filtration by altering the pressure inside the vessel. In other words, the sinusoids act like a dynamic filter, varying their porosity in response to hormones, drugs, and toxins (Braet and Wisse 2002).

The hepatocytes constitute 80% of the liver's cellular mass and perform the various metabolic and secretory and excretory functions of the liver. Metabolically the liver is responsible for controlling the synthesis, utilization, and storage of carbohydrates, proteins, fats, and vitamins and for detoxifying metabolic waste products and toxins that enter the body (Burkitt, et al. 1997). The liver is also responsible for the production and secretion of bile to aid in digestion (bile is a salt that emulsifies fats so that they are easier to digest). The hepatocytes produce 800-1,000 mL of bile per day that is collected within canaliculi between the cells and carried away by the hepatic bile ducts (12.6 μm diameter) into the gallbladder for storage. The liver is also responsible for producing half of the body's lymph (Guyton and Hall 1996). Lymph is collected from the perisinusoidal spaces into vessels that travel with the portal triad throughout the liver.

Perhaps most interesting is that the liver has the unique capability of regeneration. Whether injured or a small piece removed, the liver seems capable of unlimited proliferation to meet the demands of its body (Brown 1997).

In summary, the liver is extremely interesting and complex, and is composed of vascular, structural, and cellular elements (blood, bile, lymph, collagen, hepatocytes, endothelial cells) making it difficult to characterize. Due to limited availability of human livers, this work focuses on mechanically characterizing porcine liver. Although porcine liver has been shown to be a suitable test surrogate in many respects to a human liver (Snedeker, et al. 2005a; Snedeker, et al. 2005b), some differences ought to be noted. A porcine liver is segmented into five lobes (although they are congruent where they join), is thinner, and has more pronounced septae. Therefore pig liver is expected to be stiffer than human liver.

1.3.3. Biological Tissue Testing

Many testing modalities have been used to characterize soft tissue behavior. The type of organ being tested dictates what test will be performed. For instance, one needs to consider the organ's cellularity, fluid content, boundary conditions, whether it is hollow or solid, and how or if the organ is typically loaded. Either indirect noninvasive imaging methods or direct mechanical testing have been used to capture the common physical features associated with soft tissue mechanics; namely, their nonlinear stress-strain relationship, viscoelasticity, repeat-loading variability, and strain-rate dependency.

Ultrasound has been used in combination with indentation to accurately assess the distance between the skin and bone to measure the thickness of the underlying tissue on external limbs (Tonuk and Silver-Thorn 2003; Zhang, et al. 1997). Elastography, also known as elasticity imaging, combines biomechanics and radiology (Gao, et al. 1996). The objective is to create an image of the distribution of the internal strain which is related to the mechanical properties of the tissue (Krouskop, et al. 1998). Ultrasound (US) or magnetic resonance imaging (MRI) is used to capture an image before and after a load is applied to visualize the internal strain field. However, this process assumes that the acoustic properties of tissues are a function of chemical composition and temperature. Analysis is therefore difficult since tissues are at the same temperature and have very similar chemical make-ups. Elastography currently can only obtain relative stiffness differences. It is adequate at finding a stiff lesion within a soft tissue, and can discern obvious tissues like fat and bone. Also, the frequency range used to obtain elastograms involve vibrations on the order of 20-1,000 Hz, which is much larger than what is used in surgical gestures (Gao, et al. 1996). Despite these limitations, some people have tried to obtain linear material properties of bovine muscle and liver (Chen, et al. 1996; Maaß and Kuhnappel 1999).

Mechanically, researchers have tested tissues by adapting instruments similar to those used on engineering materials, namely traditional uniaxial tension and compression, indentation, and shear devices. More novel devices include an aspiration device that acts on the tissues surface tension by applying a vacuum pressure (Vuskovic, et al. 1999), or modified surgical graspers that collect force and displacement information (Brown, et al. 2002; Rosen, et al. 1999).

In spite of the fact that the mechanical behavior of living tissues is drastically altered post mortem (loss of innervation, perfusion, temperature, etc.) or when their boundary conditions are disrupted (i.e. when the organ is no longer intact), the majority

of soft tissues to date have been tested *ex vivo* (Fung 1993; Krouskop, et al. 1998; Liu, et al. 2003; Park and Lakes 1992). Yamada (1970) and Duck (1990) provide references to many of these results which have been conducted on cadaveric human and various *ex vivo* animal tissues (Duck 1990; Yamada 1970). *Ex vivo* tests are attractive because control of test conditions is much easier than for *in vivo* tests; the material is cut into small sample sizes of known geometries and often tested using traditional material testing devices. In doing so, the force displacement response can be more simply transformed into material properties since the geometry and loading conditions are precisely known. For example, uniaxial tension tests on caterpillar cuticles (Alexander, et al. 1999) and pig brains (Miller 2001) have been conducted using automated extensometers. Several groups have conducted similar uniaxial compression experiments on human cervix (both confined and unconfined) (Febvay, et al. 2003), as well as pig liver, kidney and brain (confined) (Miller, et al. 2000b). Some groups use *ex vivo* testing to obtain multi-modality information. For instance, Hu and Desai performed large nominal strain (30%) tests on pig liver using both indentation and uniaxial compression tests (Hu and Desai 2003; Hu and Desai 2004). Liu and Bilston used strain and stress-controlled rheometers in a parallel plate configuration to test bovine liver, under both strain and shear-controlled torsion across frequencies, and in shear-stress relaxation (Liu and Bilston 2000; Liu and Bilston 2002).

Ex vivo tests are particularly useful when only a small sample of the tissue is available, as when Yeh et al. (2002) tested various pathological human liver samples in uniaxial compression. They are also practical when a complicated multiaxial result is sought like the triaxial shear device used to test anisotropic myocardium (Dokos, et al. 2000b). Lastly, *ex vivo* testing is preferred when the animal's safety is at risk, such as during high-impact testing, and initial testing and validation of devices prior to *in vivo* testing (Arbogast, et al. 1997; Nava, et al. 2003; Tholey, et al. 2004), and for human data. For impact testing, perfused pig kidneys have been tested at high rates (up to 25 m/s) in uniaxial compression, shear, tension, and creep (Farshad, et al. 1999; Snedeker, et al. 2005a; Snedeker, et al. 2005b). Saraf et al. conducted impact-loading tests in confined compression and shear to obtain the instantaneous bulk moduli of post-mortem human hearts, liver, lung, and stomach (Saraf, et al. 2005). Carter et al. collected *ex vivo* indentation data on pig spleen and kidney prior to testing human livers *in vivo* (Carter, et al. 2001). Vuskovic's aspiration device was used by Kauer et al. to collect *ex vivo* data on human uteri, while Nava et al. used it to collect data on *ex vivo* human liver and compare it to *ex vivo* bovine liver (Kauer, et al. 2001; Nava, et al. 2004; Nava, et al. 2003; Vuskovic, et al. 1999).

Despite the benefits of testing soft tissues *ex vivo*, the results are not representative of the tissue's natural response. Changes in boundary conditions greatly alter the biomechanical properties: temperature affects viscosity, hydration affects both elasticity and viscosity, the breakdown of proteins affect stiffness, and the loss of blood supply alters resting stress and viscosity (Kim, et al. 2003; Tay, et al. 2002). Furthermore, the results are not repeatable (Liu, et al. 2003; Seki and Iwamoto 1998b). Therefore, several groups have attempted to test *in vivo* to capture the organ's natural mechanical response to controlled stimuli while the inherent boundary conditions are intact. Researchers have used simple indentation devices to capture the response of human liver (Carter, et al. 2001), and of pig stomach (Brouwer, et al. 2001), spleen (Brouwer, et al. 2001), liver (Brouwer, et al. 2001; Kim, et al. 2003; Ottensmeyer and Salisbury 2001a; Ottensmeyer 2002; Tay, et al. 2002), and brain (Miller, et al. 2000b). Although some of these tests attempted to capture the viscoelastic

response by sampling across frequencies (Ottensmeyer and Salisbury 2001a; Ottensmeyer 2002) and including stress relaxation tests (Tay, et al. 2002), nearly all fail to capture the physical characteristics required for complete soft tissue identification. Most involve only small indentations, did not measure sample thickness, and suffered from cardiac and respiratory noise, of which all contributed to difficulty in interpreting the data. Others have either built new devices or adapted existing devices to collect *in vivo* data, primarily relying on a grasping modality to test the organs. Brower et al. have an extensometer device for testing hollow pig organs in tension (stomach, intestine, gallbladder) (Brouwer, et al. 2001). Brown et al. use a modified Babcock grasper to study pig spleen, liver, lung, stomach, colon, and small bowel under haversinusoidal and stress relaxation compressive grasps (Brown, et al. 2003; Brown, et al. 2002; Rosen, et al. 1999). Grasping generates some of the same problems as those experienced with indentation. In addition, it is limited to distal parts of the organ and induces a non-uniform load to the tissue, thus creating large, undefined stress concentrations. Melvin et al. conducted unconfined compression-impact tests on monkey livers and spleens removed from, but still being perfused by the animal (Melvin, et al. 1973).

This last study, in particular, raises questions as to the ethics of performing mechanical tests *in vivo*. Limited accessibility, inherent physiological noise, rigid body motion, and unknown boundary conditions make analyzing *in vivo* data difficult. To minimize errors in position measurements due to pulmonary motion, Ottensmeyer (2002) suspended artificial ventilation of the animals, but could only do so for periods of approximately 30 seconds, limiting the data collection time severely.

The need to collect realistic mechanical responses of organs to surgical manipulation persists. Although studies comparing various devices and tissue conditions have been conducted to understand the differences between (easily controlled) *ex vivo* and (realistic) *in vivo* measurements, neither an interpretable *in vivo* device nor an *ex vivo* system to mimic the *in vivo* response have been developed (Brouwer, et al. 2001; Brown, et al. 2003; Davies 2002; Gefen and Margulies 2004a; Kalanovic, et al. 2003; Kauer, et al. 2001; Kerdok, et al. 2005). Brown compared the difference in the mechanical response of grasping pig liver, spleen, and small bowel in both *in vivo* and *ex vivo* conditions (Brown 2003), but only collected data on the first squeeze; therefore, he did not compare the same location across conditions and did not capture the known variability of repeated loads. He was also unable to record thickness, and thus his results serve only as a qualitative comparison of the structural differences but not the material property differences. Davies collected indentation data on pig spleen in both unperfused and perfused *ex vivo* states (Davies 2002). Results showed differences between the two conditions, with large variability depending on the type of perfusate used, but did not have *in vivo* data for comparison. Gefen and Margulies did compare the mechanical response to indenting a pig brain in both the *in vivo* and *ex vivo* cases at the same location (2004a), and their results show no significant difference between the two conditions, suggesting that the brain's mechanical response is independent from perfusion. It is important to note that the volume fraction and pressure of blood in the brain is significantly less than that of abdominal organs such as the liver and spleen.

The work presented here demonstrates a novel *ex vivo* test system that nearly replicates the *in vivo* response and in doing so, reveals the effects of perfusion on the mechanical response of liver to large indentations (Kerdok, et al. 2005). This *ex vivo* system allows for large strain-indentation data to be collected at various loading rates for

multiple indentations and under long-term constant load (creep) and force (stress relaxation) conditions. This carefully collected data is readily interpretable and thus can be modeled by solving the inverse problem.

1.3.4. Biological Tissue Modeling

Mechanics is the study of describing the motion and deformation of a material in response to a given load. If the material is assumed to be continuously distributed throughout its volume, completely filling the space that it occupies so that it can be considered a macroscopic body, it can be treated as a material continuum rather than one that must be modeled at the level of its molecular structure (Fung 1994; Maaß and Kuhnappel 1999). The properties defining the continuum include those of its constituents, such as density, elasticity, viscosity, conductivity, etc., as well as how those constituents move in terms of local displacements and velocities (kinematics) and their response to volume and surface forces (dynamics) (Fung 1994).

The “forward problem” consists of a continuum body of known geometry, material parameters, and applied loads for which displacements, strains, and stresses are unknown. The deformation (displacement and reaction forces) of the body is found by using the equation of motion to solve for the unknown displacements. Taking the gradient of the displacement field and then applying the constitutive relations, obtain the strains and stresses. Substituting these back into the equation of motion results in the reaction forces. The reader is referred to a textbook on continuum mechanics for further details (Fung 1994).

In the case of biological tissues, the material parameters are not known a priori, thus making the forward problem impossible to solve. Even if the parameters were known, the complexity of biological tissues and the finite-loading conditions imposed during surgery result in a set of partial differential equations that cannot be solved analytically. This latter problem is addressed with numerical approximation schemes such as the finite element method (FEM). FEM allows for an approximate solution on a subset of the continuum: the body is divided into elements with nodes. The nodal displacements become the unknowns and a shape function is used to interpolate the nodal displacements into a continuous deformation. The principle of virtual work is used to transform the differential equation of motion into a set of algebraic equations that can be solved at each node. The “inverse problem” then, is the estimation of the material parameters (the forward problem’s inputs) from displacement and force data from carefully controlled experiments (the forward problem’s outputs) using an assumed constitutive relation. An iterative process adjusts the material parameters from an initial assumed set of values until the force-displacement output of trial solutions from the model matches the force-displacement results of the experiment.

One important challenge is determining which constitutive relation to use. A constitutive relation describes the relationship between stress and strain within the body. For biological tissues, these relations must be simple enough to solve for a broad range of problems, but complete enough to realistically describe the behavior under a variety of loading conditions (Krouskop, et al. 1998). A good constitutive relation should represent the full three-dimensional nature of the stress-strain response while using a minimal number of parameters to physically represent the deformation process (Arruda and Boyce 1993).

There are two fundamental approaches for identifying the functional forms of the constitutive equations for soft tissues: the phenomenological approach where models are fit to experimental data directly, and a physics-based approach where strain energy functions are derived based on physical laws. The phenomenological models may result in better agreement with the data, but have little-to-no physical relevance and are often not applicable outside the range of stretches tested (Anand 1996). The physics-based models capture the effects of the various constituents on the mechanical response (elasticity, viscosity, plasticity, etc.) and thus lead to more meaningful understanding of the parameters.

Despite the fact that phenomenological models do not address the histological basis for the observed biological behavior, they are frequently used due to their simplicity. The parameters of these equations account for mathematical features of the data, such as the nonlinear force-displacement response, its initial slope, amount of dissipation, rate of stress relaxation etc., rather than the actual properties of the material (Rubin and Bodner 2002). This often results in an equation with several non-unique parameters. Equations can take the form of polynomials like Zheng and Mak's quadratic fit to indentation tests on lower limbs, and Maaß and Kuhnappel's third-order polynomial fit to tensile and compressive tests on various bovine tissues, or exponentials like Rubin and Bodner's 14-parameter model for facial tissue (Maaß and Kuhnappel 1999; Rubin and Bodner 2002; Zheng and Mak 1999).

Various elasticity, viscoelasticity, and mixture theories have been applied to modeling biological tissues. Linear elastic theories are generally not well suited to soft tissues, but their simplicity has led many to use them approximate the behavior of tissue under small strains (<10%) (Chen, et al. 1996; Kalanovic, et al. 2003; Ottensmeyer 2002). Some groups have also used linear elasticity theory to break up the nonlinear elastic response into piecewise linear regions (Bischoff, et al. 2000; Hu and Desai 2003; Hu and Desai 2004; Kim, et al. 2003).

A viscoelastic material exhibits both elastic solid-like, and viscous fluid-like behaviors, which are modeled by a spring and dashpot, respectively. These materials will continue to deform when under a constant force (creep), continue to relax under a constant displacement (stress relaxation), and exhibit hysteresis under cyclic loading where the loading response is different from the unloading. The basic building blocks of viscoelastic theories include the Voigt (spring and dashpot in series), Maxwell (spring and dashpot in parallel), and standard linear solid (spring in parallel with a Voigt model or spring in series with a Maxwell) models. Some biological tissues have been modeled via viscoelastic models utilizing a linear elastic spring. These include the Maxwell models used by Liu and Bilston (2000, 2002) for *ex vivo* bovine liver, and the standard linear solid models used by Farshad et al. (1999) for *ex vivo* kidney, and by Kim et al. on *in vivo* porcine liver (2003).

Introduced by Fung (1993), quasilinear viscoelasticity (QLV) models combine finite nonlinear elasticity with linear viscoelasticity. On the viscous side, QLV is limited to low strain-rates (0.06-0.75% strain/sec) and is not sufficiently generalized to describe many of the complicated behaviors of soft tissue such as different short-term and long-term viscous responses (Humphrey 2002). It is also unable to capture the effects of preconditioning unless a history-dependent state variable is added (Nava, et al. 2004).

Despite these limitations, QLV is still the most popular form of constitutive model found in the literature for biological tissues.

There are two frameworks from which to define the strain energy functions that give rise to the finite elasticity part of QLV. Strain energy is defined as the potential energy stored in a body by virtue of an elastic deformation (Gallagher, et al. 1982). A material is said to be hyperelastic if it possesses a strain energy function (Equation 1.1):

$$\sigma(\lambda) = \frac{\partial U}{\partial \lambda} \lambda + P \quad (1.1)$$

where σ is the stress, U is the strain energy, λ is the stretch, and P is the hydrostatic pressure (Maaß and Kuhnappel 1999).

Strain energy expressions are either derived from a continuum mechanics approach, where the stress arises from an increase in specific internal energy with respect to strain (invariant-based approach), or a statistical mechanics approach where the stress arises from a decrease of the specific entropy with respect to strain (Arruda and Boyce 1993; Fung 1993).

In the former case, researchers have primarily used either polynomial or exponential forms of the strain energy function. For polynomials, the Reduced Polynomial (Equation 1.2) formulation or the Ogden formulation (Equation 1.3) and their lower-order Mooney-Rivlin (Equation 1.7) and Neo-Hookean forms have been most commonly used:

$$U = \sum_{i+j=1}^N C_{ij} (I_1 - 3)^i (I_2 - 3)^j + \sum_{i=1}^N \frac{1}{D_i} (J - 1)^{2i} \quad (1.2)$$

$$U = \sum_{i=1}^N \frac{2\mu_i}{\alpha_i^2} (\overline{\lambda_1^{\alpha_i}} + \overline{\lambda_2^{\alpha_i}} + \overline{\lambda_3^{\alpha_i}} - 3) + \sum_{i=1}^N \frac{1}{D_i} (J - 1)^{2i} \quad (1.3)$$

where C , α , and $\mu=2(C_1+C_2)$ are material parameters, D is a compressibility factor (Bulk modulus = $2/D$), and I_1 and I_2 are the first and second invariants of the principle stretches $\lambda_1, \lambda_2, \lambda_3$ defined as

$$\begin{aligned} I_1 &= \lambda_1^2 + \lambda_2^2 + \lambda_3^2 \\ I_2 &= \lambda_1^2 \lambda_2^2 + \lambda_1^2 \lambda_3^2 + \lambda_2^2 \lambda_3^2 \\ I_3 &= J^2 = \lambda_1^2 \lambda_2^2 \lambda_3^2 \end{aligned} \quad (1.4-1.6)$$

where J is the total change in volume and thus I_3 is zero if incompressibility is assumed. If $N=1$ in the reduced polynomial form, or if $N=2$, $\alpha_1=2$, and $\alpha_2=-2$ in the Ogden formulation and incompressibility is assumed, Equations 1.2 and 1.3 reduce to the Mooney-Rivlin strain energy function

$$U = \frac{\mu_1}{2} (I_1 - 3) + \frac{\mu_2}{2} (I_2 - 3) \quad (1.7)$$

The Fung Exponential (Equation 1.8) or the Blatz Exponential (Equation 1.9) models are the exponential models most typically used

$$U = \frac{\alpha}{2\beta} e^{\beta(I_1-3)} - 1 \quad (1.8)$$

$$U = \frac{\beta}{\alpha(\alpha+1)} \left(e^{-\alpha+\frac{\alpha}{\lambda}} + \frac{e^{-\alpha+\alpha\lambda^2}}{2} \right) \quad (1.9)$$

where α and β are the material parameters.

Nava et al report a 13-parameter reduced polynomial model with one additional relaxation term for indentation tests on bovine livers (Nava, et al. 2004). The most commonly used model is the two-parameter Mooney-Rivlin model which has been used to model pig brain (Miller 2000a, 2001), pig liver (Miller 2000a; Miller, et al. 2000b; Nava, et al. 2003), pig kidney (Miller 2000a; Miller, et al. 2000b), pig spleen (Davies 2002), and human uterus (Kauer, et al. 2001). Despite reasonable fits to the experimental data, the Mooney-Rivlin model is not good for slower strain-rates (Miller 2000b), and can result in unrealistic values for the parameters suggesting an unbounded deformation energy (Davies 2002).

The Fung Exponential model has been used to model various pig organs from liver and spleen to small intestines and bladder (Brouwer, et al. 2001; Brown, et al. 2003; Carter, et al. 2001; Davies 2002; Rosen, et al. 1999). The kidney and liver have also been modeled using the Blatz Exponential model (Farshad, et al. 1999; Kim, et al. 2003). Again, although the fits to the experimental data are reasonable, these models are not capable of approximating different types of testing modalities well (Davies 2002).

In the statistical mechanics approach, the constitutive relation is based on the change in entropy that occurs when long molecules are stretched, thus the model parameters are more physically relevant. Some of these models build upon the 8-chain network models originally used in rubber mechanics (Arruda and Boyce 1993; Boyce and Arruda 2000) and can be simplified to a 5th order polynomial function represented as (ABAQUS 1997)

$$U = \mu_0 \sum_{i=1}^5 \frac{C_i}{\lambda_L^{2i-2}} (I_1^i - 3^i) + \frac{1}{D} \left(\frac{J-1}{2} - \ln J \right) \quad (1.10)$$

where μ_0 is the initial shear modulus and λ_L is the locking stretch of the collagen network.

The motivation to apply these models to biological tissues came in 1995 when Marko and Siggia used a modified version of the Arruda-Boyce long-chain, polymer-mechanics model to describe the stretching of DNA (Marko and Siggia 1995). Since then others have suggested that the mechanical response of soft tissue at large stretches is dominated by the macromolecular collagen network found in all tissues. Cartilage, skin, cervix, chorioamnion (fetal membrane), and breast have been modeled in this manner (Bischoff, et al. 2000; Bischoff, et al. 1999; Febvay 2003; Febvay, et al. 2003; Jordan, et al. 2005a; Liu, et al. 2004; Prevost 2006; Socrate and Boyce 2001). These models are more useful because they have better predictive capabilities with fewer material parameters than their invariant-based counterparts (Bischoff, et al. 2000; Boyce and Arruda 2000).

Another theoretical formulation commonly used to develop constitutive relations for biological tissues arises from the biphasic or mixture theories initially created to study water-infiltrated soils (Suh and Spilker 1994; Zhu and Wang 1998). These models account for

viscoelastic effects through momentum exchanges between solid and fluid constituents, allowing for the fluid viscosity itself to be neglected (Humphrey 2002). This framework uses Darcy's law, developed to describe the flow of water through a porous medium, and thereby defines a permeability (flow rate of fluid-to-solid per unit area of tissue)

$$\mathbf{q} = \kappa \nabla P \quad (1.11)$$

where q is the volumetric flow rate, κ is the permeability, and ∇P is the pressure gradient.

The challenge for modeling biological tissues is to define the scale level of the various solid and fluid constituents. Initially, researchers used a linear biphasic one in which cartilage tissue was modeled as an elastic isotropic solid and an inviscid flow (Mow, et al. 1980). Researchers have since treated the solid phase as a nonlinear hyperelastic material and the fluid phase with nonlinear strain dependant permeability functions to describe the behavior of cartilage, meniscus, growth plates, and intervertebral discs (Zhu and Wang 1998). This framework assumes that the two phases are immiscible and incompressible, and that there are no chemical reactions, mass transfers, temperature changes, heat supply, inertial effects, body forces, angular momentum, or energy dissipation between them. Some or all of these assumptions are generally violated in biological environments.

Although many of the theories above come close to capturing the typical response of externally loaded biological tissues, none are applicable across all tissues, and none capture the experimental data from all possible, finite deformation testing modalities. This work attempts to define a model drawn from the strengths of many of these theories, while also minimizing complexity. The goal is to establish one model whose parameters can be directly linked to a histological basis of the tissue being studied under rates and loading conditions consistent with surgical manipulations. Such a model could then be used to describe the behavior of multiple soft tissues independent from loading modality, where only the parameters of the model would differ between and across tissue type.

1.4. Thesis Aims and Outline

- I. *To obtain a qualitative, mechanical understanding of the liver as a whole organ, and determine the effects of its unique anatomy on the observed behavior.* In Chapter 2, the effects of perfusion in porcine livers are compared using both large strain creep and small strain indentations. A novel *ex vivo* testing configuration is developed that allows a whole organ to be perfused to physiologic pressures and temperature. Two independent testing devices are then used at consistent locations on several livers, across four different testing environments (*in vivo*, whole organ *ex vivo* perfused, whole organ *ex vivo* post-perfused, and an excised section) and their results are then qualitatively compared.
- II. *To measure the viscoelastic response of liver under surgically relevant deformations.* In Chapter 3, an *ex vivo* testing system is developed incorporating the perfusion system described in Chapter 2. The *ex vivo* response of liver across indentation rate and number is explored to determine a testing protocol to capture

the desired response. The perfused liver's force and displacement response to multiple, large-strain indentations at loading rates from 0.2 to 40 mm/s (roughly 0.1 to 2 Hz) are collected. For validation purposes both stress relaxation and creep tests are also conducted for dwell times between 30-60 minutes respectively. The liver's capsule is also independently tested in uniaxial tension

- III. To develop a constitutive model whose parameters represent the liver's unique physical composition and capture its mechanical response.* In Chapter 4, the constitutive model developed to represent the mechanical behavior of liver under finite deformations is described. A finite element model is created replicating the experimental boundary conditions and results of Chapter 3. A nonlinear optimization method is used to iteratively identify the material parameters of the model to solve the inverse problem. Start values for the parameterization are chosen by manually fitting the data to the ramp indentation and stress relaxation tests, from the literature, and from independent tests conducted to capture the sensitivity of select parameters. Ramps from each rate of the multiple (repeated) indentation data in parallel with the stress relaxation data are used to define the material parameters. The full block of ramp indentations and the creep data are used to validate the model.
- IV. To create a physical standard that can be used to assess the accuracy versus real-time performance tradeoff of the computer algorithms developed for real-time surgical simulation.* The previous chapters focused on developing a realistic constitutive model for liver tissue. Such a "ground truth" model is initially required since real-time models sacrifice accuracy for speed. In chapter 5, a method is described that assesses this trade-off and begins to quantitatively address the question of how accurate the deformable models used in surgical simulation need to be.

Chapter 2

Viscoelastic Effects of Perfusion on Liver Mechanics

2.1. Introduction

Due to the complexity of their internal composition and anatomical setting, characterizing the nonlinear viscoelastic behavior of soft, nonload-bearing tissues like the liver is a difficult challenge. A standard method for testing soft tissues is needed to produce repeatable, reliable results that can be mathematically modeled to capture the natural behavior of the tissue. The goals of this chapter are to understand the effects of the *in vivo* environment on the mechanical response of liver, develop an *ex vivo* system to replicate the mechanically relevant *in vivo* conditions, and begin to understand the mechanical response of liver to finite deformations so that better test strategies may be developed.

Material characterization via constitutive modeling requires data acquisition on a known geometry, with known loading conditions and known external constraints. Realistic constitutive modeling for biological soft tissues also requires concurrent control of both geometric and physiologic boundary conditions such as perfusate, perfusion pressure, temperature, and surface hydration. Typically, force-displacement responses of soft tissues are collected under two conditions: *ex vivo* and *in vivo*. As mentioned previously, *ex vivo* experiments allow for precise control of the boundary conditions leading to a better mathematical representation of the observed behavior. In addition, these types of experiments are good for device and protocol development, allow for multi-modality testing, are the only option for testing small tissue samples of limited availability (such as human pathologic tissue), and are a more ethical option regarding animal safety. However, there are also many documented observations on how disturbances to the *ex vivo* tested-tissue affect its constituents. Fung has described the effect of increased temperature on proteins, noting that collagen shrinks to 1/3 its original length at 65 °C as compared with the 35 °C *in vivo* environment (1993). Park and Lakes have commented on the importance of “unbound” water on the mechanical properties of tissues (1992). As an example, they observed water being squeezed out of an aortic specimen in an open laboratory setting as compared with what likely happens in the

closed, controlled, *in vivo* environment. Thus, despite the potential benefits of *ex vivo* testing, constitutive laws derived from excised tissues to validate and predict the behavior of intact organs must be questioned.

In vivo testing methods maintain the natural state of the tissue and thus provide a more realistic test-bed for constitutive law development. However, performing the necessary tests for accurate material property characterization *in vivo* is obviously difficult. There are accessibility issues, ill-defined boundary conditions, and ethical considerations related to the use of animal and human subjects. In addition, data from *in vivo* tests are difficult to interpret due to the limited datasets, small deformations atypical of surgical manipulations, difficulty in obtaining proper instrument alignment on sizable specimens, complications from physiological noise, and the inability to account for and control the internal condition of the organ.

These considerations highlight the importance of understanding the differences in the tissue's mechanical response between the *in vivo* and *ex vivo* conditions (Brown, et al. 2003; Gefen and Margulies 2004b), as well as the need to develop a new test method to incorporate the strengths of both conditions (Table 2.1). Brown has postulated (2003), "... [It] is possible that one day a transformation can be derived that estimates "pseudo-in-vivo" properties from *ex-corporis* testing. The ease of testing *ex-corporis* relative to *in vivo* would certainly make this a worthwhile pursuit."

Table 2.1 Benefits and drawbacks of *in vivo* and *ex vivo* testing and an attempt at what a combination of the two would be like.

ATTRIBUTE	TESTING ENVIRONMENT		
	<i>IN VIVO</i>	Nearly <i>In Vivo</i>	<i>EX VIVO</i>
Mechanical Behavior	Accurate	Good enough?	Poor
Viability	Many hours	~5 hours	<1 hour
Accessibility	Difficult	Easy	Easy
Boundary Conditions	Uncontrolled	Controlled	Controlled
Noise & Variability	Great	Minimal	Minimal
Ethical Concerns	Live animal, more sacrifices	Fewer animals, more experiments	Fewer animals, more experiments

In this chapter, an attempt at answering this call is made by introducing an *ex vivo* perfusion system that permits carefully controlled mechanical measurements on porcine liver in a nearly *in vivo* state. It is hypothesized that maintaining temperature, hydration, and vascular pressure to physiologic levels can closely approximate the organ's natural *in*

vivo condition. This system was derived from information found in organ transplant literature. Employing the perfusion system, the mechanical properties of freshly harvested whole porcine livers are assessed using two indentation devices. One measures small strains across a range of frequencies and the other measures large-strain creep responses over time. Tests at the same locations of the same livers allowed comparisons of the results across four different conditions: *in vivo*, *ex vivo* perfused, *ex vivo* post-perfused, and *in vitro* on an excised section. Fitting the data to empirical models provided a quantitative comparison and time-scale estimation of the viscoelastic response of liver across conditions. Two independent tests were done to further understand the effects and limitations of the *ex vivo* conditions: an *ex vivo* post-perfused liver was tested with both instruments over time, and a mechanical damage test was done using the creep device on an *ex vivo* perfused organ. Lastly, to assess differences across condition and time, histological comparisons were made from biopsies taken during testing.

2.2. Methods and Materials

2.2.1. *Ex Vivo Liver Perfusion System*

It has been shown that both cold and warm ischemic time severely affect the structure and function of the liver: hepatocellular injury occurs within 60 min of warm ischemia, endothelial cell injury occurs within 4 hours of warm ischemia (Platz, et al. 1997; Schon, et al. 2001). The current standard for preserving a liver's structure and function for transplantation for up to 12-18 hours requires that the organ be perfused with a preservation solution and be cold stored (Rossi 2003; Wahlberg, et al. 1986). Cold storing alone the metabolic rate of the liver 12-13 times so that it does not biodegrade, and cellular viability and organ function are retained (Schon, et al. 2001). However, the material properties of the liver obviously cannot be measured while the organ is frozen, and it has been shown that cold, static storage causes hepatocyte apoptosis and also affects the endothelial cell lining upon reperfusion, leading to cellular swelling and permanent ischemic injury (Butler, et al. 2002). Also, the most common preservation solution (the University of Wisconsin solution) has been shown to leave crystals in the organs that would interfere with material property testing (Tullius, et al. 2002).

Another approach for maintaining extracorporeal liver viability is to use warm perfusion systems. Such normothermic extracorporeal liver perfusion (NELP) systems maintain liver function without inflicting hepatocellular or endothelial cell injury (Schon, et al. 2001). Applications include: organ preservation, organ bypass (as bridge to transplant or for time to allow a native organ to repair), organ resuscitation, and experimental applications on isolated liver physiology studies (Butler, et al. 2002).

To preserve a liver's mechanical viability during *ex vivo* mechanical testing, a freshly harvested liver is flushed with cold veterinary lactated ringer's solution (Henry Schein, Melville, NY) for transport to the mechanical testing laboratory. There, a NELP system attempts to maintain the mechanical integrity of the whole organ while mimicking physiologic conditions in an *ex vivo* setting. This perfusion system (Figure 2.1) maintains temperature, hydration, and pressure for a whole porcine liver *ex vivo* during indentation testing. Six liters of the lactated ringer's solution were pumped to two elevated reservoirs in order to hydrostatically maintain physiologic pressures of 97 ± 5 mmHg to the hepatic artery and 18 ± 2 mmHg to the portal vein. PVC tubing from each reservoir was fitted

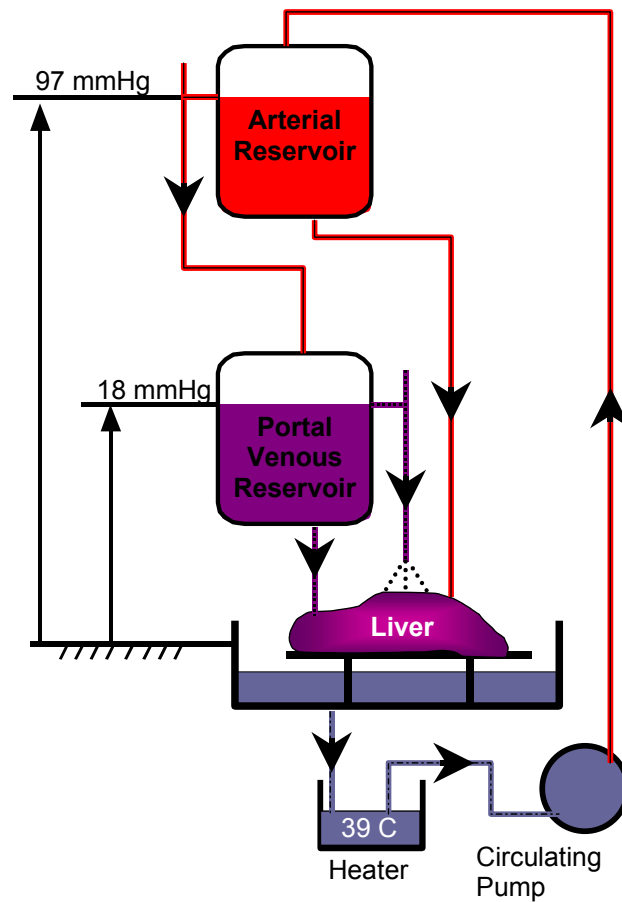


Figure 2.1 The *ex vivo* liver perfusion system.

with an appropriately sized connector and sutured to the proper artery. The perfusate was allowed to drain via the intrahepatic vena cava into a bath where it was heated to 39 °C (porcine core temperature) and pumped to the arterial reservoir. The arterial reservoir overflow fed the portal venous reservoir, whose overflow in turn provided hydration to the organ's surface without submerging the organ. To ensure consistent measurements, the organ was stabilized on a sturdy plate covered with fine grit sandpaper. The perfusion pressure was held constant rather than mimicking physiologic pulsatile pressure, to enable accurate force-displacement measurements.

2.2.2. Indentation Test Instruments

Although the results are more difficult to interpret than uniaxial testing, indentation instruments were used in this study because they allow force and displacement measurements to be made anywhere on the surface of the organ while maintaining the organizational and structural integrity of the tissue. Two indentation instruments were used to acquire viscoelastic mechanical measurements on the surface of intact livers across conditions. The Tissue Material Property Sampling Tool (TeMPeST¹)

¹ The TeMPeST was built by Dr. Mark Ottensmeyer to measure the small-strain compliance of solid organ tissues (Figure 2.2A). The TeMPeST has previously been used to measure the properties of

is a device designed by a collaborating laboratory that examines the small strain (0-5%) frequency response (0.1-200 Hz) (Ottensmeyer and Salisbury 2001b), while a creep indentation device captures the large strain (10-50%) time domain response (over 300 seconds). The diameters of these devices were selected based on the observations from Zhang et al (1997), who suggested that the radius of the indenter be ten times less than the thickness of the tissue sample, to ensure a homogenous material assumption and to minimize the effects from the bottom surface. The diameters were made as large as possible to minimize stress concentrations (particularly for the large-strain creep device), to obtain a uniform loading over a larger local volume of tissue, and to improve the signal-to-noise ratio. Given that the tissue thickness ranged from 20 to 39 mm across all testing conditions, the diameters were selected to be 5 mm and 6 mm for the TeMPeST and creep devices, respectively.

The TeMPeST applied a sinusoidal indentation force with monotonically increasing or decreasing frequency (chirp) to the tissue between 0.1 and 200 Hz, under either a 45 N or 90 N nominal preload force (actual mean loads varied between 10 and 70 N, due to tissue relaxation), and a nominal amplitude of 30 N (between 4 and 10 N below instrument resonance [80 Hz] and up to 30 N at resonance) to avoid loss of tissue contact. In these tests, only relative displacement from the (unmeasured) preloaded depth could be measured. A minimum of five tests was done for each condition at each location, with roughly 11 indentations per test. One data set was collected every 2-3 minutes, with the actual test taking 16.4 seconds *in vivo* and 32.8 seconds *ex vivo*.

The creep indenter performed normal indentation tests with large strains typical of surgical manipulations (Figure 2.2B). The device was rigidly mounted to the same platen on which the liver rests to avoid relative motion artifacts. A 6 mm-diameter flat cylindrical punch rests on the tissue surface, with a 3 g counter weighted load. A standard laboratory brass weight was placed at near-zero velocity onto a platform mounted co-axially with the indenter tip. An 11.5 cm lever arm with 4 cm of vertical travel connected the indenter to the base, allowing measurements nearly any where on the organ surface. Applied loads of 20 g and 100 g generated nominal surface stresses of 6.9 kPa and 34.7 kPa, respectively. The angular position of the measurement arm was sampled over five minutes at 1 kHz using a miniature contact-less rotary position sensor (Midori America Corporation, Fullerton, CA) (resolution 11 μm , RMS 20 μm). The maximum depth of indentation was on the order of 12 mm, so a small angle approximation was assumed and the voltage from the rotary sensor was converted directly to indentation depth using a linear factor. Organ thickness measurements were taken prior to every

porcine liver and spleen *in vivo*, rodent (rat) liver and kidney *ex vivo* (Bruyns and Ottensmeyer 2002; Ottensmeyer 2002), and has been used in initial investigations of bovine, ovine and human vocal tissue samples *ex vivo*. A 5 mm circular punch vibrates the tissue while recording applied load (LPM 562 force sensor, Cooper Instruments, Warrenton, VA) and relative displacement (099 XS-B LVDT position sensor, Schaevitz, Hampton, VA). A voice coil motor is controlled in open-loop mode, using commanded current as a proxy for applied force. In free space, the device behaves as a mass-spring-damper system, with a natural frequency of 66 Hz, a static stiffness of 275 N/m and a damping ratio of 0.14. When in contact with soft tissue, the combined stiffness rises, increasing the natural frequency (approximately 80 Hz in the case of porcine liver). The sampling frequency of 2 kHz, enables measurements to approximately 200 Hz. The range of motion is 1 mm (RMS 0.18 μm) and forces up to 300 mN (RMS 0.15 mN) may be exerted. For a complete description, the reader is referred to Dr. Ottensmeyer's thesis (2001).

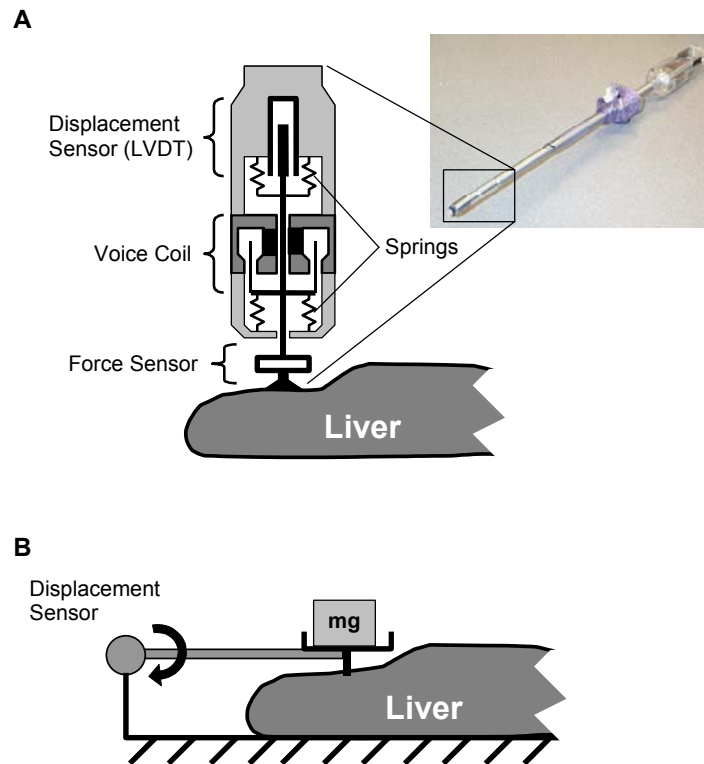


Figure 2.2 (A) Small strain frequency response device. Detail shows the voice coil driven indenter with flexures and sensors. (B) Large strain creep indentation device.

indentation measurement, with a dial indicator for purposes of reporting nominal strain (displacement/preindented thickness).

2.2.3. Experimental Protocol and Environmental Conditions

Livers from four pigs, 27 to 37 kg (mean 32.5 kg), were used in this study. Each were tested *in vivo*, *ex vivo* perfused, and *ex vivo* post-perfused, while three had sections removed that were tested *in vitro* (Figure 2.3). The total duration of testing varied based on the number of locations tested and indentations performed, but on average the total test time was between 5-8 hours. The experimental protocol was approved by the Harvard Medical School Center for Animal Resources & Comparative Medicine Institutional Review Board. Two additional pig livers were used for independent studies on the *ex vivo* unperfused and perfused conditions.

Samples for histological analysis were taken from three of the environmental condition livers using a 15-gauge core biopsy needle (Mediatech Boston Scientific, Watertown, MA) on a lobe of the liver that was not tested using the indentation devices. A control sample was taken immediately post sacrifice, and again post harvest after flushing with the lactated ringer's solution. Samples were then taken every hour across all conditions tested, including one upon test completion (24 samples in total). They were then stored in 10% buffered formalin for 36 hours then transferred to 70% alcohol for transport to a histology laboratory (Mass Histology Service, Worcester, MA). For the independent mechanical damage test on the *ex vivo* perfused liver, 6 mm core samples

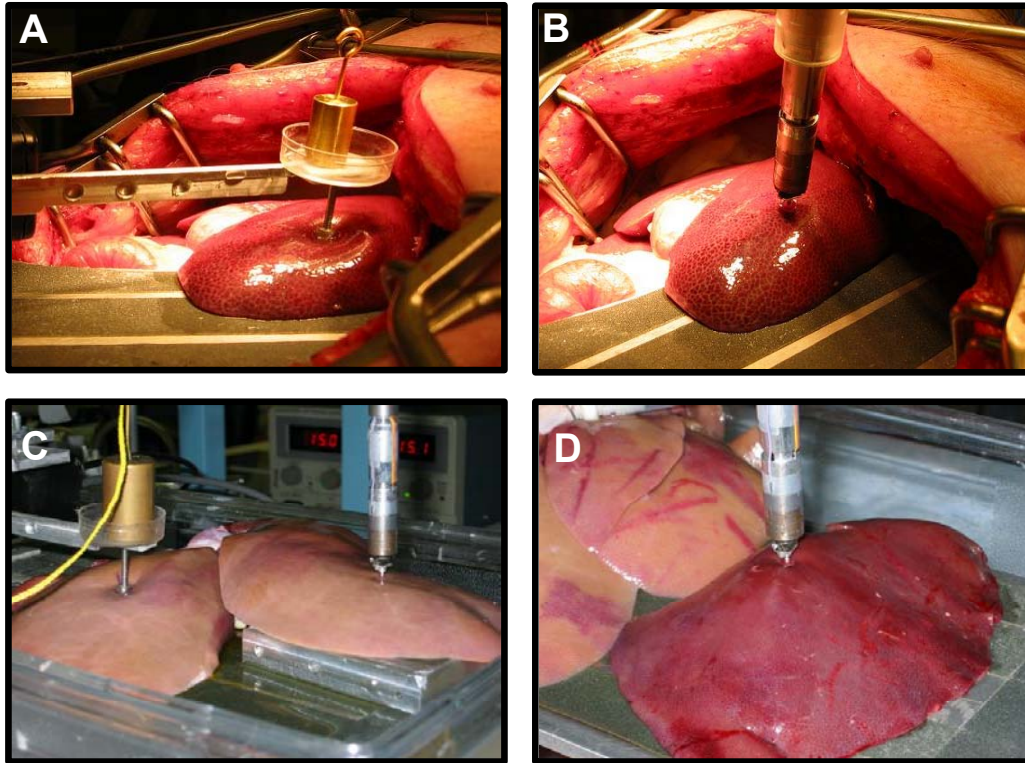


Figure 2.3 Examples of the two indentation test instruments and the various environmental conditions tested. (A) Large strain creep device *in vivo*. (B) TeMPeST *in vivo*. (C) Both instruments *ex vivo* perfused. (D) TeMPeST *ex vivo* excised section.

were taken at each location following the completion of the test, and prepared in a similar manner to those above. A grid report of the hematoxylin and eosin (H&E) stains was obtained from a pathologist to determine cellular damage and structural integrity across conditions for all biopsies.

2.2.4. *In Vivo Whole Organ Testing*

In vivo tests were performed on the four deeply anesthetized animals on assisted ventilation with 100% oxygen. The abdomen of the pig was exposed and a lobe of the liver was situated on the 3 mm thick platen of the creep device. Locations where the thickness was between 20 to 37 mm (mean 24.8 mm) were chosen and marked with a tissue-marking pen. The TeMPeST acquired compliance data on the liver for periods of 20 seconds. Ventilation was suspended during data collection to prevent pulmonary motions from saturating the position-sensor measurements. Indentations using the creep device were made at the same locations, but without the necessity for suspending ventilation due to the rigid mounting of the device to the platform where the organ rests. Two to four indentations using both the 20 g and 100 g loads were made at each location. Initial position-sensor values were noted and the load was applied in pseudo-random order for 300 sec, with repetition of the first load at the end. Once the load was removed, the organ was allowed to recover to within 1 mm of its preindented state (typically

200 sec) before applying the next load. The total time for *in vivo* testing was between 1.5-3 hours depending upon the number of locations and indentations performed.

2.2.5. *In Vitro* Excised Section Testing

Following *in vivo* testing, heparin was injected systemically to minimize clotting (1 mL/10kg of 1,000 units/mL), and the animal was sacrificed with an injection of KCl. The liver was harvested by carefully dissecting the connecting ligaments and by severing the inferior vena cava and the portahepatis as far away from the liver as possible. A lobe was removed and immediately tested with the TeMPeST (*in vitro* excised section testing). The cut surface of the remainder of the organ was cauterized to prevent leakage and the organ was flushed with one liter of heparinized (5,000 units) cold lactated ringer's solution (~10 °C). Both the excised lobe and the remaining flushed organ were packed on ice and transported to the laboratory. Once at the laboratory, the same locations of the excised section were then tested again at room temperature approximately every 20 minutes with the TeMPeST. This condition most closely represents many previous *ex vivo* tests: blood-filled cut sections tested at room temperature, several hours post mortem (Dokos, et al. 2000a; Hu and Desai 2004; Liu and Bilston 2002; Miller 2001; Miller, et al. 2000a; Nava, et al. 2003; Valtorta and Mazza 2004). Long data collection periods for the creep device precluded timely collection of both *ex vivo* perfused and *in vitro* excised measurements. The number of *in vitro* indentations was therefore limited in favor of gathering more complete *ex vivo* perfused data. One of the excised lobes was tested with both instruments post mortem and again at the laboratory using the 20 g load for the creep device.

2.2.6. *Ex Vivo* Perfused Whole Organ Testing

Upon arrival at the laboratory (114 ± 22 minutes of cold ischemic time post mortem), the hepatic artery and portal veins of the liver were sutured to the arterial and portal venous perfusate reservoir tubing connectors. Perfusion was begun and the organ was allowed to come to physiological temperature before testing was resumed within 20 minutes. A cannula was sutured to the hepatic inferior vena cava to ensure that the outflow remained patent. TeMPeST and creep indentation tests were performed in the same manner and at the same locations as the *in vivo* tests, to adequately compare across conditions as well as to minimize variation in the measurements due to the unknown locations of large vessels or connective tissues within the organ. The total time for *ex vivo* perfused testing was 183 ± 47 minutes, depending upon the number of locations tested.

2.2.7. *Ex Vivo* Post-Perfused Whole Organ Testing

Following the completion of testing on the perfused organ, the inlet tubes were clamped to stop the flow, while the outlet remained patent. The organ was tested again with both instruments in the same locations over time to observe any further changes in the response, typically 30-60 minutes. The creep device applied three to four sequential indentations, one every 10-20 minutes. Since initial trials had revealed that the tissue's response changed with indentation in the unperfused states, and because only the large strain response was desired, only the 100 g load was used.

2.2.8. *Ex Vivo Post-Perfused Whole Organ Independent Test Over Time*

To ensure that the differences in the responses observed between the *ex vivo* whole organ perfused test and the *ex vivo* whole organ post-perfused test were not due to the latter occurring hours after animal sacrifice and the perfusion test, an independent *ex vivo* post-perfused test was conducted. A 30 kg pig was systemically heparinized, sacrificed, and the liver was harvested and flushed as above. It was brought to the laboratory, flushed again with perfusate at 39 °C, and the inlets were clamped as in the post-perfused condition. Creep measurements using 100 g were made on the same location (22.8 mm thick) beginning 100 minutes post sacrifice. Measurements were taken every 20 minutes for 100 minutes.

2.2.9. *Ex Vivo Perfused Independent Mechanical Damage Test*

To systematically explore the effects of large strain on the creep response and to make certain that no irreversible damage was being done to the liver's structural integrity, a mechanical damage test was performed on an independent whole perfused liver. An 80 kg pig was sacrificed and the liver harvested as above. Perfusion was established 140 minutes post sacrifice. Ten evenly spaced locations with similar thicknesses on a single lobe were marked out (roughly 15 mm between locations). At each location the creep device was loaded with 10, 20, 50, 70, 100, 125, 150, 200, 250, or 300 g laboratory masses and displacement measurements were recorded over 300 seconds. Since each indentation was in a new location, there was no need to wait between indentations. After all indentations were completed, a 6 mm diameter core biopsy was taken at each location and in four control regions, and the histology was evaluated for structural integrity and cellular damage. Despite the larger animal, the thickness of the liver was 30.36 ± 3.5 mm, consistent with the perfused thickness measurements taken on the smaller pigs (30.79 ± 8.61 mm for the 100 g case).

2.2.10. *Data Analysis – Lumped Element Modeling*

To compare the effects of environmental condition on the viscoelastic properties of porcine livers, the collected data were fit to empirical first order (TeMPeST) and second order (creep device) lumped element models of the tissue (Figure 2.4). These models are not constitutive laws for the material, but rather a means of quantifying the differences seen across conditions and to determine the time scales of the viscoelastic nature of the tissue.

The simplest model that captures small deformation viscoelastic behavior is the first order parallel spring-dashpot (Voigt) model (Figure 2.4A). Fitting this model to the TeMPeST data involved calculating the frequency-dependent complex compliance of the tissue by taking the ratio of the Fast Fourier Transforms of the position and force signals over the frequency range of interest. A characteristic Voigt model curve was fit to each of the unfiltered compliance versus frequency data sets by minimizing the sum of squared errors. This yielded the static compliance (inverse stiffness $1/K$, m/N) and the characteristic (break) frequency (f_c Hz). The damping constant of the Voigt model was then calculated as $B=K/(2\pi f_c)$.

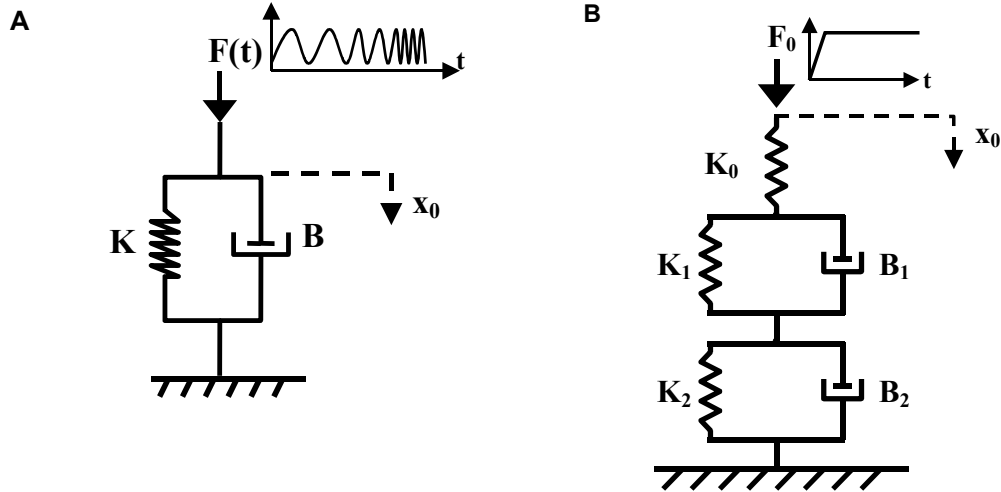


Figure 2.4 Lumped element models used to quantitatively describe the tissue response. (A) First order Voigt model for small strain response to a force input of a sinusoidal frequency chirp $F(t)$. (B) Second order model for large strain response to a step load F_0 .

A first order model showed poor agreement for the creep results and thus a second order model was used (Figure 2.4B). The response for each segment of the model was found assuming initial conditions of zero displacement for x_1 and x_2 and the applied step function $x_0(0) = F_0/K_0$

$$x_0(t) = F_0 \left[\left(\frac{1}{K_0} + \frac{1}{K_1} + \frac{1}{K_2} \right) - \frac{1}{K_1} e^{-\left(\frac{K_1}{B_1}\right)t} - \frac{1}{K_2} e^{-\left(\frac{K_2}{B_2}\right)t} \right] \quad (2.1)$$

$$x_1(t) = F_0 \left[\left(\frac{1}{K_1} + \frac{1}{K_2} \right) - \frac{1}{K_1} e^{-\left(\frac{K_1}{B_1}\right)t} - \frac{1}{K_2} e^{-\left(\frac{K_2}{B_2}\right)t} \right] \quad (2.2)$$

$$x_2(t) = F_0 \left[\frac{1}{K_2} - \frac{1}{K_2} e^{-\left(\frac{K_2}{B_2}\right)t} \right] \quad (2.3)$$

where F_0 is the applied load (N), x_0 is the overall displacement response (mm), x_1 is the displacement due to the two spring and dashpot series (mm), x_2 is the displacement response due to the second spring and dashpot (mm), K_0 , K_1 , K_2 are the elastic spring constants (N/mm), and B_1 and B_2 are the viscous dashpot constants (Ns/mm).

The position and time data from the creep indentation device were zeroed at the start of each indentation, filtered forward and backward using a second order low-pass Butterworth filter with a cutoff frequency of 50 Hz, and truncated at 290 seconds to ensure that all sets were of the same length. Since instantaneous load application was not possible, the creep tests were divided into loading (ramp) and response phases. An independent test measured the time of load application using a force sensor: the duration of the ramp phase was $t=0$ to 0.163 sec and $t=0$ to 0.236 sec for the 20 g and 100 g loads, respectively. The total response

$$x_0(t) = A_0 - A_1 e^{-t/\tau_1} - A_2 e^{-t/\tau_2} \quad (2.4)$$

was fit from the end of the ramp phase to 290 seconds where A_0 is the amplitude of the steady-state displacement defined by $A_0 = F_0(1/K_0 + 1/K_1 + 1/K_2)$, and $A_1 = F_0/K_1$ and $A_2 = F_0/K_2$ are the amplitude contributions due to the creep time constants $\tau_1 = B_1/K_1$ and $\tau_2 = B_2/K_2$. A_0 is obtained from taking the mean of the last 10 seconds of displacement data (assuming that a steady-state nominal strain had been achieved). Initial values are given to the two time constants and their weights and a gradient descent search was performed to minimize the normalized mean square error (MSE) of the model response and data.

2.3. Results

2.3.1. Frequency Response Indentation Tests

Typical compliance and phase versus frequency plots, with the model fit for the *ex vivo* perfused condition under a low preload (mean = 24.7 mN) are shown in Figure 2.5. The first order Voigt model captures the nearly in-phase variation between force and displacement at low frequencies and the 90° phase shift at the upper end of the measured frequency range. Below ~ 40 Hz, the tissue behaves like a linear elastic spring with compliance ~ 0.02 m/N, while above 40 Hz the viscous behavior is evident. The observed low frequency noise is a result of the tissue's inherent nonlinearity; the nonlinear stiffness results in a distorted sinusoidal response, leading to oscillations in the Fourier transform of the measured position and force signals. When testing linearly elastic materials such as silicone gels, this oscillation is greatly reduced.

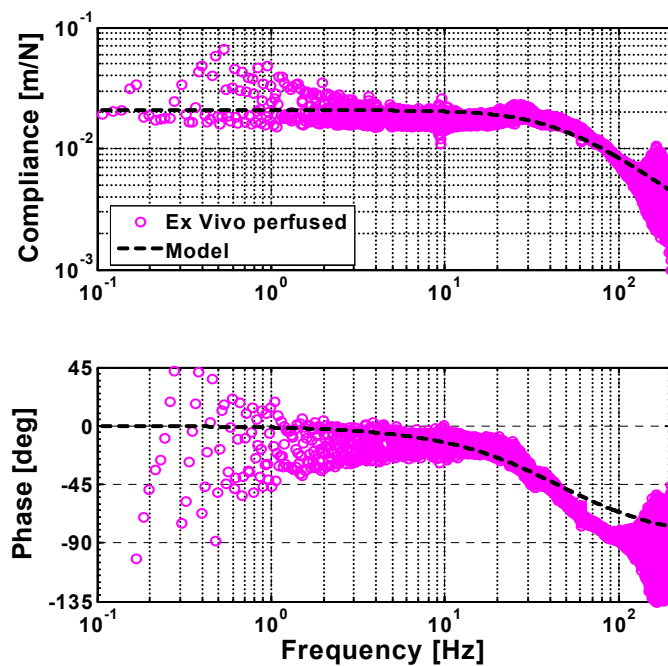


Figure 2.5 Typical Bode plot of compliance (Top) and phase (Bottom) versus frequency. The circles are data from an *ex vivo* perfused test under a low preload (24.7 mN) and the dashed line is the Voigt model fit.

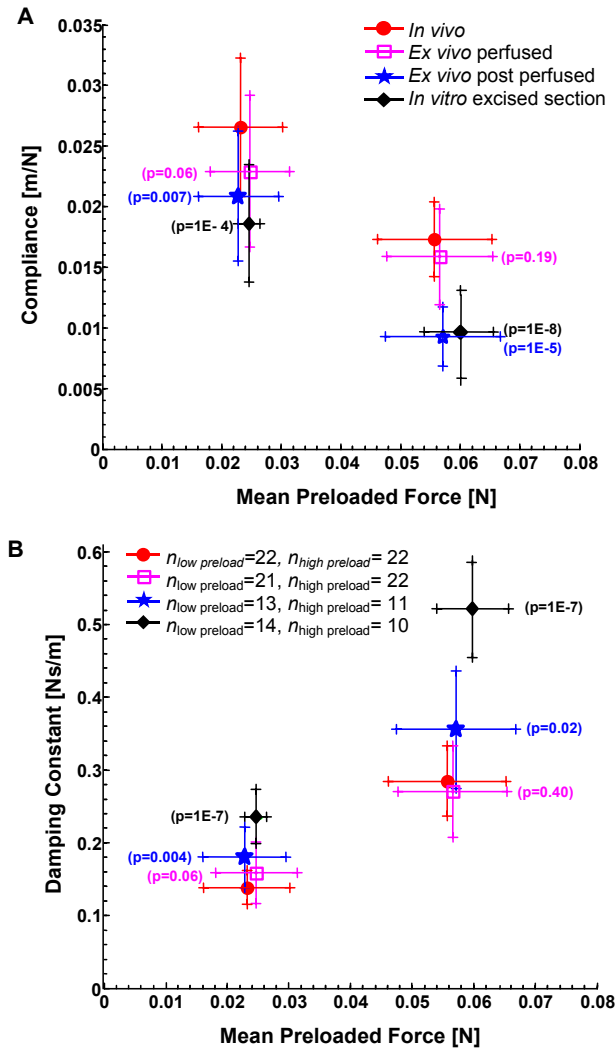


Figure 2.6 Model parameters from the small strain frequency response. (A) Mean compliance versus preloaded force \pm standard deviation (SD). (B) Mean damping constant versus preloaded force \pm SD for each condition. P-values for all cases compared with the *in vivo* case are shown next to their corresponding mean value.

The mean and standard deviation of compliance and damping constant versus mean preloaded force for all conditions are shown in Figure 2.6. The variation in preload force is due to stress relaxation. These results illustrate that in all cases tissue compliance falls (stiffness increases) as applied load increases. Conversely, as applied load increased, the damping coefficient also increased in all cases.

A two-sample, two-tailed Student *t*-test assuming unequal variances was conducted on the means of both parameters for each preload and compared with the *in vivo* condition with a 5% significance level. The compliance and damping coefficient for the *ex vivo* perfused condition was statistically the same as those for the *in vivo* condition under the same preload. Conversely, the other two conditions' parameters were significantly different from the *in vivo* condition for both preloads. The high preload

results indicate that the *ex vivo* post-perfused and excised section conditions are both stiffer (47% both cases) and more viscous (23% and 87%, respectively) than the *in vivo* condition, and that the *ex vivo* perfused condition is similar to the *in vivo* condition.

2.3.2. Large Strain Creep Indentation

Typical creep response and model fits for three indentations across all conditions on one representative liver are shown in Figure 2.7. The *in vivo* and *ex vivo* perfused conditions show a consistent response for repeated indentations. Conversely, both unperfused conditions exhibit permanent deformation, as well as stiffening and decreased viscosity with repeated indentations. Table 2.2 reports the mean and standard deviations of changes in indentation characteristics between pairs of successive indentations within

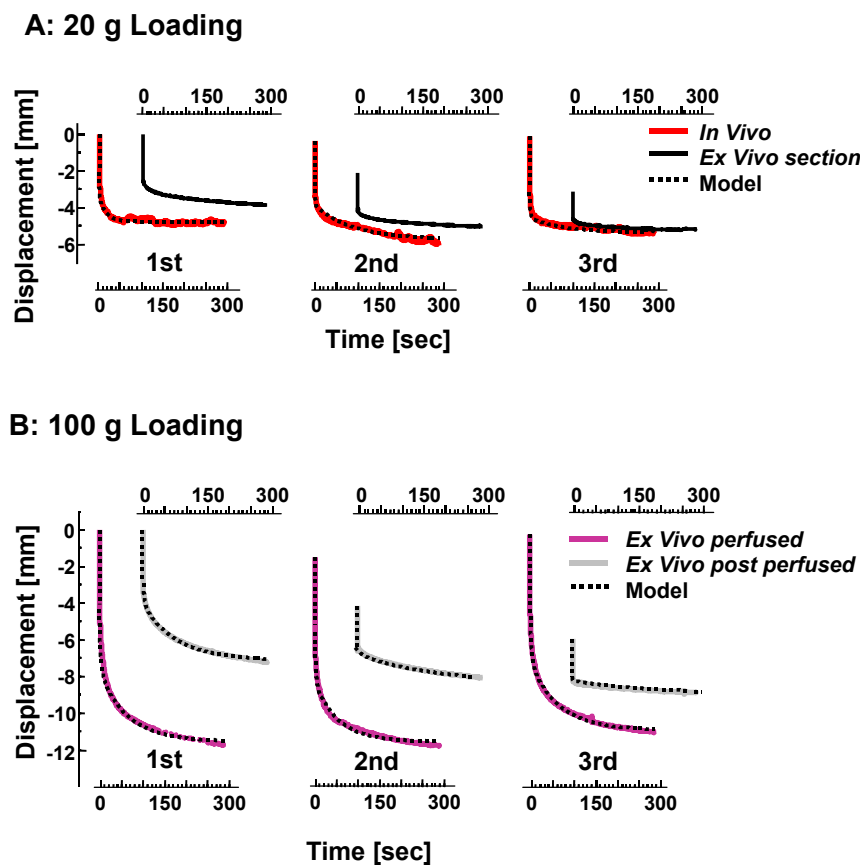


Figure 2.7 Typical creep data for 3 indentations from one porcine liver for all four conditions. The top plot compares indentations between the *in vivo* response (90 minutes between first and last indentation) and the *in vitro* response (30 minutes between the first and last indentation) under a 20 g load. The bottom plot compares indentations between the *ex vivo* perfused (78 minutes between first and last indentation) and *ex vivo* post perfused (30 minutes between the first and last indentation) responses under a 100g load. The initial ramp and second order model fitted to the *in vivo*, *ex vivo* perfused, and *ex vivo* post perfused indentations are plotted as dotted lines.

18 minutes of each other and across three conditions, including results from the independent unperfused test (Figure 2.8). These characteristics are represented in terms of differences in permanent deformation (denoted by the difference in the indenter's initial contact with the surface as compared with the first indentation), depth of indentation, and nominal steady-state strain. The results show that the *in vivo* and *ex vivo* perfused conditions produce consistent responses with repeated indentations. The strain differences in the indentation characteristics for these two conditions were less than 2% and 4% for the 20 g and 100 g cases respectively and were also statistically indistinguishable from each other (each $p > 0.05$) with the exception of steady-state strain ($p = 0.04$). In contrast, the post-perfused condition showed an inconsistent response with repeated indentations, including 11.9% permanent strain deformation, 7.2% difference in indentation strain, and 4.6% difference in steady-state nominal strain. The results from the independent unperfused test are similar to the post-perfused results with a 15% permanent strain deformation, 5% difference in indentation strain, and 10% difference in steady-state nominal strain. Thus the behaviors observed when testing post perfusion several hours after animal sacrifice were nearly identical to those tested immediately after sacrifice under the same condition: a stiffening of the steady-state response (revealed by a 5.3 mm permanent deformation and a decreased overall displacement under the same load), and a decrease in viscosity (a flattening of the initial curve) with both repeated indentation and time.

To compare variability in the liver time scales and amplitudes between indentations and across conditions, the means and standard deviations of the model parameters (τ_1 , τ_2 , A_0 , A_1 , A_2) for pairs of sequential indentations were calculated and are shown in Figure 2.9. The parameters for the *in vivo* and *ex vivo* perfused conditions were similar to each other and consistent with repeated indentations under both loads ($p > 0.05$).

The mean values for τ_1 and τ_2 are 1.86 ± 1.03 sec and 51.3 ± 18.0 sec with similar weights on the order of 0.08 for the 20 g load and 0.026 for the 100 g load. The value of A_0 was 0.239 ± 0.078 and 0.466 ± 0.083 for the 20 g and 100 g loads, respectively. The *ex vivo* post-perfused condition had a consistent value for τ_1 between indentations ($p = 0.283$) that was also statistically indistinguishable from the *in vivo* case ($p = 0.603$).

The rest of the parameters suggest that the post-perfused condition is neither consistent with repeated indentations nor comparable to the *in vivo* case ($p < 0.05$), with the exception of A_2 ($p = 0.30$).

The overall shape of the large-strain creep response across conditions was compared by zeroing the displacements of all trials at the start of the indentation, and comparing the means of each condition at each point in time. Figure 2.10 shows means and standard deviations of the responses for the three conditions tested. The results show that the *ex vivo* perfused condition closely approximated the *in vivo* condition, with $p > 0.05$ at all times in the 20 g loading condition. Similarly, $p > 0.05$ for times greater than 27 seconds in the 100 g loading condition. The *ex vivo* post-perfused response is significantly different from the *in vivo* case with $p \ll 0.05$ for times greater than 22 ms. In addition, increasing the load under the perfused conditions by a factor of five doubled the mean steady-state response in the perfused conditions, which suggests strain hardening.

Table 2.2 Means (\pm SD) of the differences observed in the indentation characteristics for pairs of successive large strain creep indentations across three conditions including the independent unperfused test.

	Condition	# of pairs	Δ_i , Mean Initial Contact Strain (\pm SD)	$\Delta_D = D_1 - D_2$, Mean Indentation Strain (\pm SD)	Δ_{ss} , Mean Steady-State Strain (\pm SD)
20 g	<i>In Vivo</i>	4	0.008 (0.008)	0.016 (0.009)	-0.021 (0.013)
	<i>Ex Vivo</i> Perfused	4	-0.001 (0.023)	0.015 (0.016)	0.015 (0.032)
100 g	<i>In Vivo</i>	4	0.042 (0.035)	0.036 (0.020)	-0.043 (0.021)
	<i>Ex Vivo</i> Perfused	5	0.043 (0.081)	0.014 (0.015)	-0.039 (0.088)
	<i>Ex Vivo</i> Post Perfused	4	0.119 (0.031)	0.072 (0.031)	-0.046 (0.031)
	Independent <i>Ex Vivo</i> Unperfused	1	0.150	0.050	-0.100

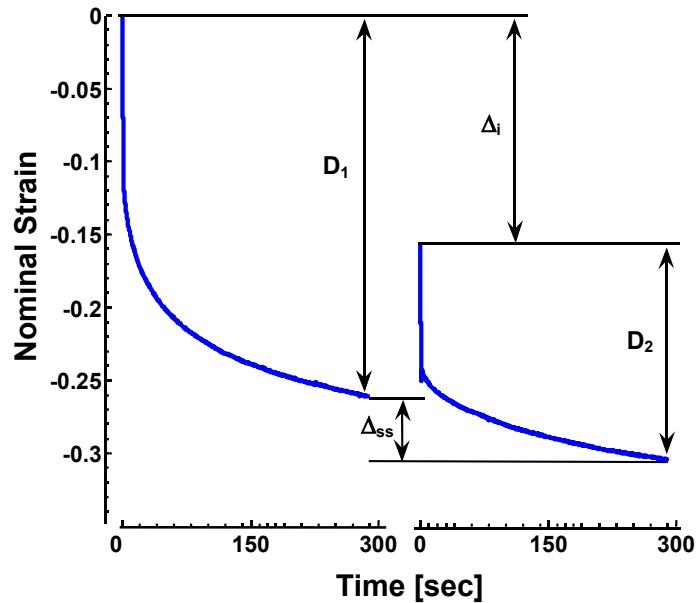


Figure 2.8 Definitions of measures for characterizing differences observed between successive large strain creep indentations, shown on a representative plot of data from a pair of *ex vivo* post perfused indentations. Δ_i is the change in the initial point of contact with the surface (permanent deformation), Δ_D is the difference in depth of indentation ($D_1 - D_2$), and Δ_{ss} is the difference in nominal steady state strain.

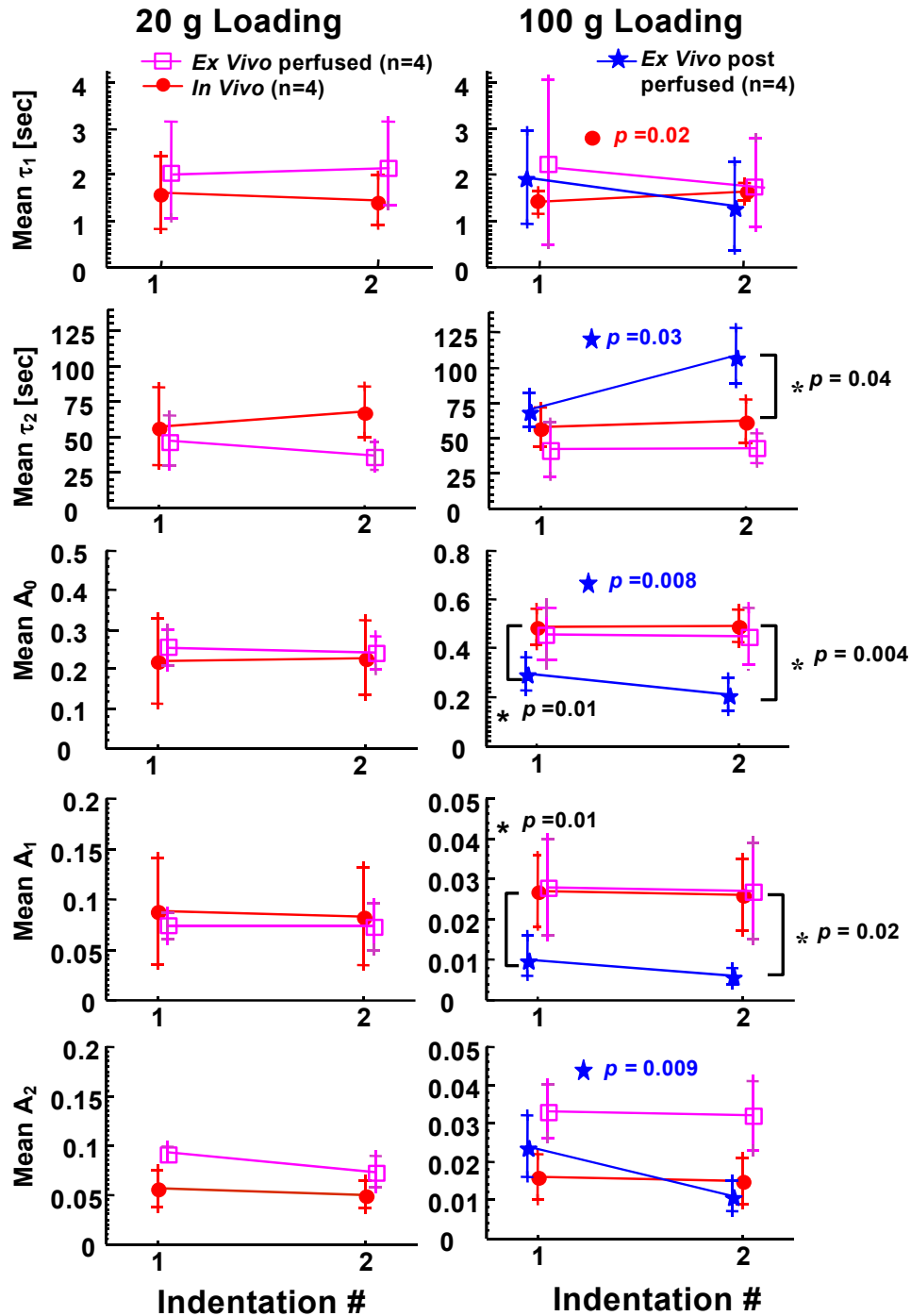


Figure 2.9 The mean and SD of the creep model parameters (τ_1 , τ_2 , A_0 , A_1 , A_2) for sequential indentations under both loads across the *in vivo*, *ex vivo* perfused, and *ex vivo* post perfused conditions. P-values with a symbol denotes a significant difference between indentations for that condition and an asterisk (*) denotes a significant difference compared with the *in vivo* case for a particular indentation.

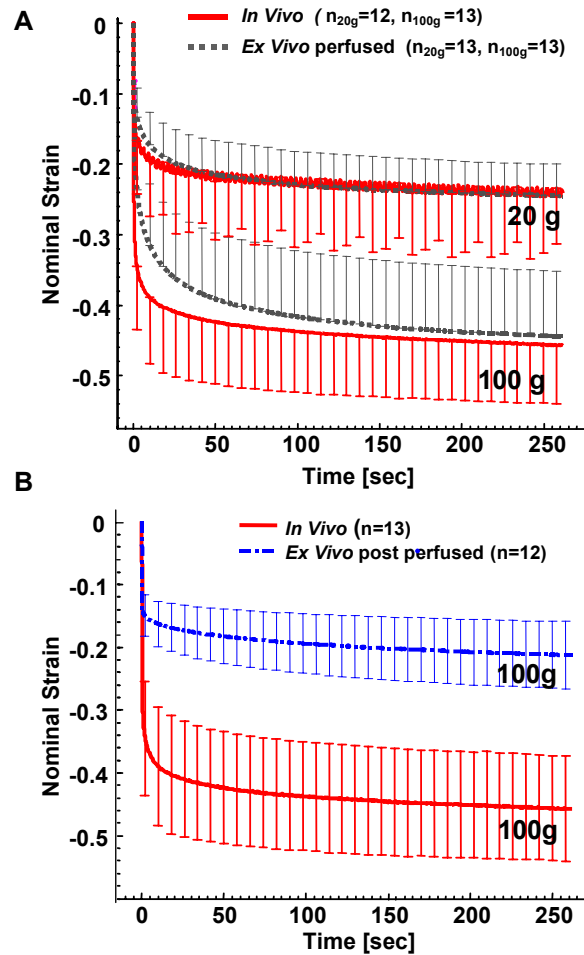


Figure 2.10 (A) Mean nominal strain (\pm SD) of the means versus time for the *in vivo* and *ex vivo* perfused creep datasets. The upper SD is shown for the *ex vivo* perfused and the lower SD for the *in vivo*. (B) Mean nominal strain (\pm SD) of the means versus time for the *in vivo* and *ex vivo* post-perfused creep data with 100 g load.

For the independent mechanical damage test, each indentation was taken on a different location, thus only a qualitative comparison between measurements may be made. The results suggest an increase in steady-state nominal strain with an increase in load from 20 g to 125 g (Figure 2.11). Beyond 125 g there was little to no change in steady-state nominal strain with increased load. In fact, a 58% increase in load resulted in only 12% variations in steady-state strain. The initial curvature, however, did consistently change and revealed a slower creep response with increasing load, a more viscous response. However, this could also be due to it taking longer to load the larger weights; thus for a real mechanical response evaluation a motorized indenter ought to be used. No permanent deformations were observed.

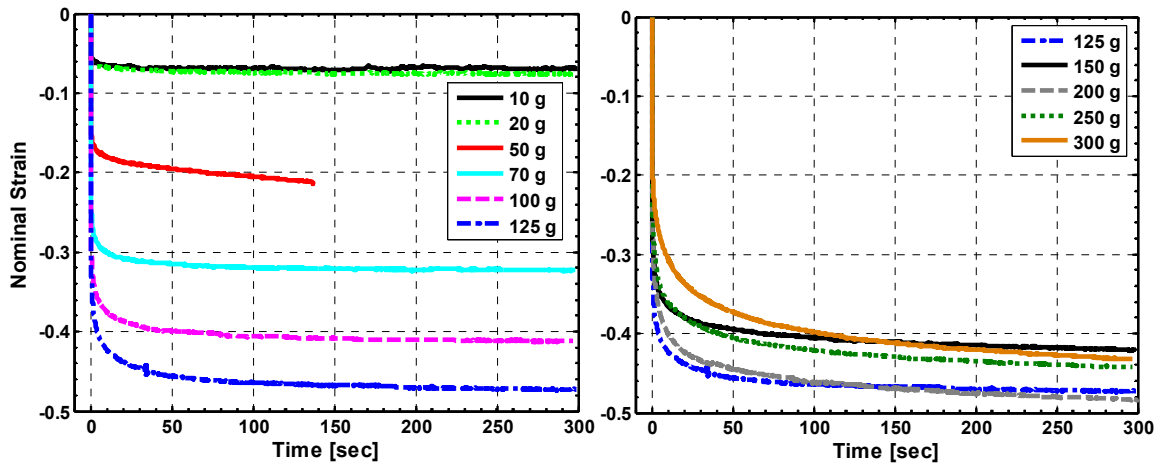


Figure 2.11 Results from the large strain independent *ex vivo* perfused mechanical damage test over time. (Top) Results from the 10 to 125 g loadings. Note that the 50 g loading was truncated to 140 seconds as there was an observed blockage in the perfusion line. (Bottom) Results from the 125 g to 300 g loadings showing strain hardening.

2.3.3. Histology

The analysis of the histology specimen from the three livers across conditions indicated that the structural integrity of the tissue was maintained over time in the experimental states compared with the control state. The categories studied were: cellular swelling and pyknotic nuclei as indicators for degeneration, rupture as a trauma indicator, and cytoplasmic changes and necrotic cells to indicate stages of cell death. On a scale of 0-4, where 0 indicates no observed changes and 4 indicates severe changes, the mean score was between 0 and 1.7 across all conditions and time, and included a comparison between controls taken immediately post mortem and upon completion of the *ex vivo* tests five hours later. Some minimal changes were noted in the cytoplasm (dissociation of cells from the normal chord structure) beyond two hours into the perfused case and in the nonperfused conditions. It was also noted that the *ex vivo* perfused samples experienced some cellular contraction, contrasted with the noteworthy cellular swelling observed over time in the *in vitro* excised sections. Minimal cell death was observed.

The histology from the mechanical damage test also did not reveal any differences between the various loadings. In fact, any changes noted were consistent with those seen in the previous tests. The maximum applied load induces a nominal stress of 104 kPa, which was well below the 232 ± 64 kPa *in vivo* injury threshold (Melvin, et al. 1973) and the 451 kPa *ex vivo* breaking stress reported by Seki and Iwamoto (1998b). The results of this test support the results from the 20g and 100g loads used for the previous tests, and also set limits for future indentation testing.

2.4. Discussion

This study presents a standard method for testing soft tissues to produce repeatable and reliable results that can be mathematically modeled to capture the natural

behavior of the tissue. To control the physiologic conditions that have the greatest effect on the mechanical response of the organ, an *ex vivo* normothermic perfusion system that regulates the perfusate, perfusion pressure, temperature, and surface hydration for the liver was built. The results of this study suggest that both geometric and physiologic boundary conditions must be considered and controlled when characterizing well-vascularized, solid, whole organs. Specifically, the elastic and viscous properties of liver are affected by perfusion as measured by both small-strain frequency response and large-strain creep indentation tests. The small-strain frequency tests show that both unperfused conditions were stiffer and more viscous than the *in vivo* condition under high preloads. The large-strain creep device showed permanent strain deformation for successive indentations for the post-perfused *ex vivo* tissues. The new perfusion system allowed for nearly *in vivo* results using both instruments in a controlled *ex vivo* set-up. The *ex vivo* perfused tissues exhibited similar viscoelastic behavior to the *in vivo* tissues and showed consistency (less than 4% strain differences) between successive indentations. In particular, the *ex vivo* perfused livers showed a small strain frequency response with mean compliances of 0.026 m/N and 0.017 m/N, and mean damping constants of 0.138 Ns/m and 0.285 Ns/m for the low and high preloads, respectively. The large strain creep response on these same livers showed mean time constants of 1.86 and 51.3 seconds with amplitudes of 0.08 and 0.026, and steady-state nominal strain amplitudes of 0.24 and 0.47 for the 20 g and 100 g loads, respectively.

For over 25 years, researchers have identified the need to maintain the turgor of the liver at a level comparable to normal hemodynamic pressures (Melvin, et al. 1973), yet no one has properly studied the effects of perfusion pressure on the mechanical response of the organ, nor tested it in a perfused state *ex vivo*. While Snedeker et al. perfused a whole kidney for impact testing, it is unclear if their perfusion pressure was maintained or simply used to fill the organ prior to testing (Snedeker, et al. 2005a). Davies attempted mechanical testing on perfused pig spleens, but emphasis was placed primarily on what perfusate was used rather than on the mechanical response (Davies 2002).

The results obtained here both address the need to test whole perfused livers, and enlarge upon previous work on *in vivo* and *ex vivo* soft tissue material properties. While direct comparisons are not straightforward, the results of others qualitatively support my observation that the liver is stiffer *ex vivo* than *in vivo* (Brown, et al. 2003; Brown, et al. 2002; Farshad, et al. 1999; Maaß and Kuhnappel 1999). Brown et al. also note that the *in vivo* condition had more recovery between indentations than did the *ex vivo*, with the latter stiffening with successive loadings and time post mortem. Gefan and Margulies (2004) made indentation measurements (strain < 20%) in the same three locations in porcine brains in both the *in vivo* and *ex vivo* states in order to compare the effects of perfusion. They reported that perfusion did not make a significant difference in material property identification. Brain tissue is nearly homogenous, however, and does not hold the same volume fraction of blood as the liver. Thus the effects of perfusion on the viscoelastic properties of tissue are likely organ dependant.

Some researchers have made invasive independent measurements on the liver parenchyma (homogeneous internal tissue) and on the external capsule (Seki and Iwamoto 1998a; Valtorta and Mazza 2004). Their results suggest that the capsule is stiffer than the parenchyma and acts as a stiffening membrane for the organ. The results from the small-strain frequency response support this observation, showing an increase in both the

elastic and viscous responses with increased preload across all conditions. In the low preload case, the small displacement of the elastic capsule should lead to lower increases in stiffness and viscosity. The near statistical distinction ($p=0.06$) observed between the *in vivo* and *ex vivo* perfused cases is likely due to a slight mismatch in perfusion pressure, making the organ artificially stiffer than the *in vivo* case.

Melvin tested *in vivo* Rhesus monkey livers to failure at impact rates of 5 cm/s to 500 cm/sec (Melvin, et al. 1973). He found that liver fails at a maximum nominal stress of 232 ± 64 kPa, at 54% nominal strain for the lowest impact velocity. The mechanical damage test of this study statically applied nominal stresses from 3.1-93 kPa, achieving nominal strains of ~45%. Therefore, it should be no surprise that the results this study showed little to no histological damage. The similarity in response between the 10 and 20 g loading (steady-state nominal strains of 6.9% and 7.5% respectively) could be an effect of these small loads not generating enough stress to overcome the stiff elastic capsule. Since the other tests in this study using a 20g load showed differences in creep response across perfused condition, perhaps the 10g load was too light. Future tests will use loads greater than 20 g to ensure involvement of the full parenchyma. The strain hardening observed at loads greater than 125 g is likely due to a critical limit being obtained where the majority of fluid in the local volume under the indenter is removed and an elastic response from the parenchyma remains.

Many researchers “precondition” their *ex vivo* tissue samples with cyclic loading to obtain a steady-state response (Brouwer, et al. 2001; Dokos, et al. 2000a; Liu and Bilston 2002). Although this may make sense to simulate the *in vivo* state for tissues that undergo cyclic deformations such as the heart and tendons, my results suggest that preconditioning soft nonload-bearing, unperfused tissues drives fluid from the tissue, thus changing its viscous characteristics and internal boundary conditions. Because blood is more viscous than Ringer’s solution and its viscosity increases with time post mortem, the excised section should exhibit the highest viscosity among all cases compared with the *in vivo* case. These results show both an increase in the stiffness and viscosity of the organ, and a permanent deformation with repeated indentation for the blood-filled excised section, and also for the *ex vivo* post-perfused condition. Conversely, the stiffness and viscosity remained consistent with repeated indentations for both the *in vivo* and perfused *ex vivo* conditions, demonstrating the need for preserving the physiological boundary conditions when making mechanical measurements.

To maintain the internal boundary conditions and mechanical viability of the liver post mortem for the time course of these tests, a perfusion system for *ex vivo* organs based on normothermic perfusion systems used in organ transplant systems was designed (Butler, et al. 2002; Platz, et al. 1997; Schon, et al. 2001). Butler demonstrated that the hepatocytes consume very little oxygen and suggested that this is due to the lack of innervation inhibiting hormonal stimuli that would normally activate these cells (Butler, et al. 2002). His system maintained a liver for 72 hours. He also reported that decreasing the metabolic activities, removing toxins and acids, and regulating pH and electrolytes were keys to his success. This study was not concerned with maintaining liver function, but rather its structural integrity. The focus was on preventing unnecessary swelling (via osmotic pressure differences) and clotting using Lactated Ringer’s solution as the initial perfusate post-systemic heparinization, and ignoring cellular metabolism. The consistency seen in this study with repeated indentations, the similarities to the *in vivo* condition, and the

histology results showing minimal changes in cellular integrity, suggest that the cold ischemic time caused no cellular damage, and that the perfusion system preserved the mechanical viability of the liver for the five-hour duration of the *ex vivo* testing.

Despite the similarities in the viscoelastic response of the liver in the *in vivo* and *ex vivo* perfused conditions, small differences were seen that motivate improvements to the system for future measurements. The *ex vivo* perfused condition was slightly stiffer, thicker, less viscous, and experienced cellular dissociation as compared with the *in vivo* condition. This suggests that there was a mismatch in perfusion pressures and perfusate concentration. More recent examination of the literature on porcine physiology has shown that the perfusion pressure for the hepatic portal venous branch of the system is smaller than the value used in this study, which was based on human values (Rasmussen, et al. 1999). Optimally, the perfusate pressures would be determined with presacrificial arterial and venous measurements. It may also be useful to include perfusates with plasma proteins or other blood-mimicking products to better match the oncotic and viscous properties, as well as metabolic inhibitors such as Histidine Tryptophan Ketoglutarate (effective in warm-state organ preservation) to increase the mechanically viable time post mortem (Butler, et al. 2002; Schon, et al. 2001).

Quantitative analysis of the perfused creep data under large deformations typical of surgical manipulation suggests that two time scales (1.86 and 51.3 seconds for the 300 second creep test reported here) are needed to describe the viscous parenchymal response of the liver. The manual control of the creep device limits the value of the lower time constant and thus future measurements ought to use a motorized indentation system that can apply large-strain indentations to the liver's surface at varied rates and with nearly instantaneous step loads. Nevertheless, results from this study suggest that at least two time constants are present in the liver. Physical reasoning suggests that the two time constants are from movement of fluid in two distinct pathways: one is from the inherent viscosity of the cells and the free exchange of interstitial fluid in the liver parenchyma, and another is due to blood flow in the liver's vasculature. In fact, using the empirical model presented here and Poiseuille's formulation to simplify the flow through the liver, it is possible that the redistribution of fluid from large-strain indentation is initially accounted for by an elastic response and is then absorbed by flowing through the vasculature until equilibrium is achieved. It is quite possible that multiple time constants exist to account for flow through the various-sized vessels and dense microvasculature of the liver, but this work suggests that at least two are needed to describe the behavior as a whole. In future studies, it may be possible to use the perfusion system to vary the perfusate pressure to tease out the viscoelastic effects from those due to interstitial fluid and extracellular matrix, and from those due to blood and vasculature.

To address the needs of surgical simulation, the goal is to develop a constitutive model of the whole liver. Successful modeling requires data from a known geometry, with known loading conditions and external constraints. This study shows that both geometric and physiologic boundary conditions must be controlled, and that these can be done concurrently. In addition to controlling these boundary conditions, it would be ideal to model the individual contributions of the various tissue constituents (capsule, parenchyma, vessels) in the context of the whole organ. However, the intimate connections of the vasculature and capsule throughout the parenchyma make this a nearly impossible task. It may be possible to take measurements that emphasize one of the

constituents over the others. For example, internal testing devices could make measurements that do not directly involve the external capsule (Kerdok and Howe 2003). Uniaxial tension testing of a carefully dissected segment of the liver's capsule could also produce meaningful data. Lastly, although this study used noninvasive surface indentations to allow for quantitative comparisons of mechanical response across conditions, complete mechanical characterization would involve stress and strain-rates that will bring the organ to failure and induce impact injuries. The need for boundary condition control and the potential invasiveness of future tests mandates the use of *ex vivo* testing that can nearly approximate the *in vivo* condition.

Chapter 3

Mechanical Viscoelastic Testing of Liver

Advancements in realistic surgical simulation require the appropriate collection and analysis of the behavior of biological tissue undergoing finite deformations typical of surgical manipulations. The previous chapter revealed that both geometric and physiologic boundary conditions must be concurrently maintained to capture the complete viscoelastic response of a solid perfused organ such as the liver. In order to develop a constitutive model capable of predicting complex surgical scenarios, multiple testing modalities should be simultaneously obtained so that the fundamental nature of the tissue's behavior under such conditions is not missed.

Studying how others have mechanically tested the liver helped determine the range of deformations necessary for surgical applications while still adhering to the confines of the liver's intrinsic mechanical limitations. Test methods and equipment have been developed to maximize the viscoelastic and mechanical information that can be gathered from whole, intact, perfused livers as well as their external capsules. The results of this chapter will aid in the development of a constitutive model for the liver whose parameters can directly correspond with the physical constituents of the tissue.

3.1. Background: Mechanical Testing of Liver

To obtain a mechanical understanding of a composite material like an organ, it would make sense to independently test each component and then sum their responses. However, due to the complex interconnections and intrinsic relationships of these constituents to each other in a biological setting (biochemically, neurologically, mechanically, etc.), it is nearly impossible to independently tease out the mechanics of each constituent. Since each component of the organ does contribute to the overall mechanical response, there are ways to determine a subset of significant constituents. For instance, the previous chapter detailed how perfusion affects the viscoelastic response of liver. It also suggested that the external capsule might have a unique mechanical response that could be tested independently. The parenchyma of the organ, however, ought to remain intact and be treated as a homogenous medium. The liver is thus assumed to be the sum of its fluid content (perfused vessels), its tough external membrane (capsule), and its homogenous viscoelastic parenchyma. To establish which tests will capture the

complete viscoelastic response of these parts (and therefore the whole organ under surgical manipulation) the literature was consulted on soft tissue testing methods, mechanical limitations of the liver, and MIS gestures.

Several groups have tried to capture the nonlinear viscoelastic response of liver. Melvin et al. explored the strain-rate effects of *in vivo* monkey liver by performing uniaxial compression impact tests to 35% nominal strain (Melvin, et al. 1973). Their rates varied from 0.2 to 38 Hz. On a more surgically relevant scale, Brown et al. tested *in vivo* porcine livers to 30% nominal strain using indentations at constant strain-rates of 0.1-2 Hz (2-40 mm/s) (Brown, et al. 2003), and using motorized graspers at cyclic loadings of 0.25-3 Hz (8.2-65.4 mm/s) (Brown 2003). Kim et al. (2003) and Tay et al. (2002) performed *in vivo* sinusoidal indentation tests on porcine livers from 0.5 to 3 Hz with 1.5 mm amplitude and a 4 mm preload. The necessity for having such a large preload was likely due to the known effects of stress relaxation under a constant displacement, and creep under a constant load. Liu and Bliston (2000) found that *ex vivo* shear tests on bovine livers had a linear limit of 0.2% strain and that the tissue experienced stress relaxation for over 3,000 seconds. This is further evidenced by the results of Nava et al. (2004) who used an aspiration device on *ex vivo* bovine liver to perform eight loading cycles of 1.5 mm amplitude displacements over 200 seconds. The effects of preconditioning were evident in this study, as successive stiffening was noted for each cycle.

Melvin's impact tests also suggest that the injury threshold for *in vivo* perfused liver is 310 kPa, and the maximum stress is 622 kPa (1973). Others have reported similar values and compare the effects of the capsule. Seki and Iwamoto (1988b) found that the breaking stress of *ex vivo* liver was 451 kPa with the capsule intact, and 353 kPa with the capsule removed. Similarly, Brown found that *ex vivo* liver with the capsule intact fails between 30-43% nominal strains at stresses of 220-420 kPa, and that the parenchyma alone fails between 35-60% nominal strains at stresses of 160-280 kPa (2003).

These tests highlight the importance of the capsule in the liver's mechanical response to deformation. Davies showed that without a capsule, the spleen was less resistant to loads (2002). Similarly, Picibono et al. found that the stiff, elastic capsule plays an important role in liver deformation (2002). They and others suggest that the imbalance of stiffness between the capsule and the underlying parenchyma can be used in medical simulations to include anisotropy as well as to penalize the stretch of the organ surface (Casson and Laugier 1999; Picinbono, et al. 2002).

Designing experiments to capture the realistic behavior of liver under surgical manipulation involves understanding what types of gestures surgeons use in addition to the types of tests that will bring out the viscoelastic behavior. For instance, most people find that to obtain a repeatable state of tissue response they must precondition their samples 10-20 cycles (Brown, et al. 2003; Fung 1993). However, surgeons do not precondition the organ before performing a surgical task. Initial tissue responses are thus critical for realistic simulation. The bandwidth of normal human motor responses suggest that assessing tissue behavior beyond 10 Hz is irrelevant for simulating normal gestures (Ottensmeyer 2001). Several groups have outfitted MIS instruments with force sensors and motion trackers so that real-time surgical gestures could be quantified. One instrumented MIS tool found that surgeons typically penetrate the abdominal wall at speeds of 10-15 mm/s generating forces of ~10 N (Dubois, et al. 2002). Brown and Rosen's BLUE-

Dragon revealed that surgeons grasp with less than 10 N of force (mean was 7.35 N) and for less than 10 seconds (2.3 sec mean, 66.3 sec maximum) at frequencies typically less than 2 Hz (5 Hz maximum) (Brown, et al. 2004; Rosen, et al. 2002).

In summary, characterizing the complex mechanical behavior of the liver under surgical manipulation involves capturing the nonlinear force-displacement response to finite deformations (up to 40% nominal strain), the strain-rate sensitivity (up to 2 Hz), the repeat loading variability (with special attention to the first indentation), and the viscoelastic response (hysteresis, stress relaxation, and creep). This chapter describes the methods and results of various *ex vivo* tests conducted on the liver capsule and on the whole perfused liver. These include uniaxial tension tests on liver capsule and several different indentation tests on whole perfused livers. The indentation tests imposed finite displacements between 30-40% nominal strain (displacement / thickness) and included: multiple sinusoidal indentations at 1Hz over time, single load/unload ramp indentations at constant rates from 0.14 to 200 mm/s (0.25 to 20Hz), blocks of 9-12 load/unload ramp indentations from 0.2 to 40 mm/s (0.01 to 2Hz), stress relaxation indentations from 1,200 to 1,800 seconds, and creep indentations to 3,600 seconds.

3.2. Uniaxial *Ex Vivo* Liver Capsule Testing

3.2.1. Materials and Methods

When handling the liver, the tough outer membrane covering nearly the entire surface of the liver is not initially noticeable. This is because the capsule is integrated into the liver's architecture and is not merely an additional layer of tough membrane, as it is on other organs. The intricate relationship between the capsule and the parenchyma is evidenced by their simultaneous rupture during impact testing (Snedeker, et al. 2005a; Snedeker, et al. 2005b). If the liver is sliced open such that a section of the soft and friable parenchyma is exposed, the significance of the capsule in maintaining the structural integrity of the organ is evident.

To independently determine the nonlinear elastic properties of the liver's capsule, uniaxial tension tests were conducted to failure on nine samples from two different porcine livers (70 kg pig mass). These tests were conducted on livers independent from the indentation tests due to the destructive nature of the tests. The livers were harvested from the freshly sacrificed animals and flushed with one liter of cold Lactated Ringer's Solution (Henry Schein, Melville, NY). The livers were kept on ice and their surfaces hydrated with the Ringer's solution until testing (3-6 hours post sacrifice). Samples were prepared by removing a piece of the liver and carefully dissecting away the parenchyma with a scalpel blade until about 1 mm of tissue remained. The residual parenchyma was then removed with fine tweezers and additional scraping as needed. Careful attention was given to maintain the integrity of the capsule while removing all visible tissue. To address any potential anisotropy of the material, the location and orientation of the specimen from the liver were noted when possible. The three specimen from the first liver were cut to 6 mm wide by >15 mm long using a disc cutter on a ruled cutting board. The six specimen from the second liver were cut to 10 mm wide by >15 mm long using a similar approach. All samples were kept hydrated with Ringer's solution. The thickness of the capsule was determined by placing a 10 x 10 mm specimen between two glass

cover slips of known thickness. A micrometer was used to record the thickness in multiple locations across the specimen. The mean thickness was measured to be 83 μm .

Each sample was placed in a jig with aluminum clamps covered in fine grit sandpaper to minimize slippage. The clamps were spaced 10 mm apart using a spacer. The sample was carefully laid across the spacer and the ends were screwed together in the clamps before placing the jig into the tensile testing machine (Figure 3.1). The jig was secured into the testing machine, leaving slack between the clamps to avoid a pretension on the sample. Once in the machine (Zwick/Roell Z2.5/TSIS, Ulm, Germany), the upper grip was displaced vertically until a zero force was recorded on the 20 N load cell (1 mN resolution). Samples were then tested to failure at a velocity of 0.25 mm/s while recording displacement (1 μm resolution), time, and load at a sample rate between 3-10 Hz.

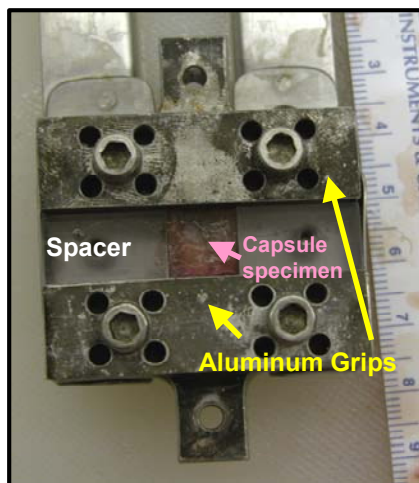


Figure 3.1 Example of a 10 mm by 10 mm capsule specimen clamped into the aluminum uniaxial tension testing jig.

3.2.2 Results

The force displacement results show a nonlinear response typical of collagenous biomaterials (Figure 3.2). There is a low stiffness initial “toe” region followed by a stiffer linear region until failure. The smaller samples show maximum forces of 1.25 N at axial displacements of 3.5 mm (corresponding to a 35% nominal axial strain), and a mean stiffness of 789 N/m (± 157) in the linear region. The larger samples show the expected relative increase in maximum force (~ 3.75 N) for the same level of axial strain, and mean stiffness of 1,777 N/m (± 566) in the linear region. Consistencies in the results suggest independence on orientation and location (Figure 3.3). Therefore, the capsule could be described as a hyperelastic, isotropic, thin membrane, and will be modeled as such in the next chapter.

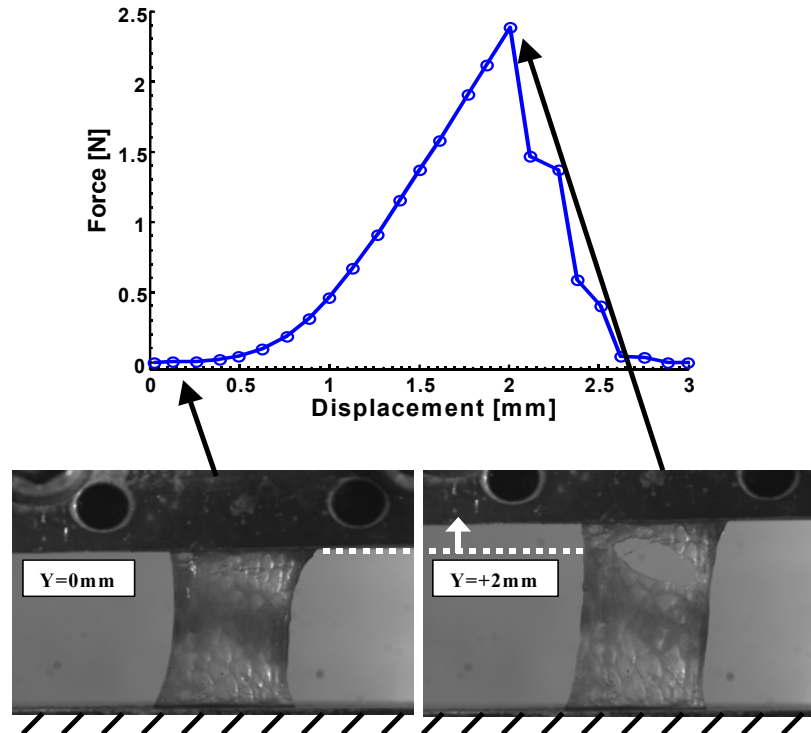


Figure 3.2: Representative force versus displacement data from a 10 mm wide liver capsule tested to failure in uniaxial tension at a rate of 0.25 mm/s.

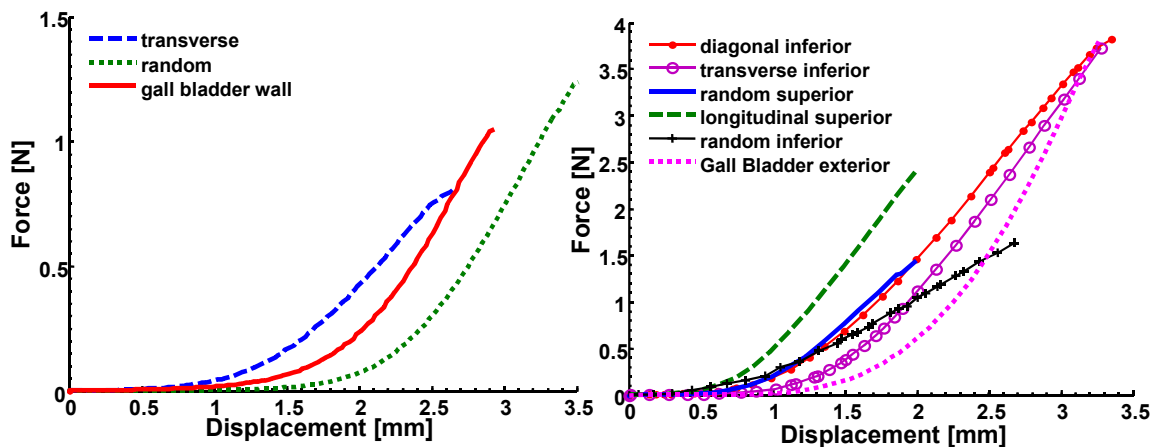


Figure 3.3 Results of the uniaxial tension tests of the liver capsule. (Left) The first liver with specimen from 3 different locations and orientations having an initial test area of $6 \times 10 \text{ mm}^2$. (Right) The second liver with specimen from either the inferior or superior side of the liver oriented in either the diagonal, transverse, or longitudinal directions. Initial test area for these specimen were all $10 \times 10 \text{ mm}^2$. All tests were performed at 0.25 mm/s.

3.3. *Ex Vivo* Whole Perfused Liver Indentation Testing

3.3.1. *Lessons Learned from Perfusion Study*

The previous chapter described an *ex vivo* testing system that successfully acts as an *in vivo* surrogate for perfused organs like the liver. Although the histology report suggested that structural integrity of the parenchyma was maintained using the perfusion system, there were some alterations noted that could be attested to cellular degradation and endothelial damage as well as an increased perfusion pressure (Schon, et al. 2001). Tests conducted in this chapter will use the same system but will better match the animal's physiologic pressure, and will use a new perfusate. Rather than metabolically inhibiting the cells, the transplant literature was consulted to find a means of actively sustaining their viability for up to 6 hours. Several perfusate recipes were found that suggested common necessary ingredients: glucose (5% Dextrose), oxygen (hematocrit of ~20% to drive cellular activity and remove waste products), and water with appropriately sized particles for osmotic pressure balances (Lactated Ringers Solution with Hetastarch in a 4:1 ratio) (Peter, et al. 2002; Schon, et al. 2001; Umehara, et al. 2004). The whole organ tests conducted in this chapter used a perfusate that consisted of five liters of Dextrose 5% Lactated Ringers Solution (D5RL) and one liter of 6% Hetastarch (Henry Schein, Melville, NY). The set-up was the same as in Figure 2.1, except that the area of the collecting bin was increased and the closed reservoir tanks volume were reduced to maximize surface area exposure to room air oxygen. The liver was tested in its anatomical position, with the portal vein and hepatic artery inlets entering from beneath the organ and the inferior vena cava (IVC) open to air above. In this way, the organ hydrated itself as the perfusion flowed from the IVC over the surface of the liver, into the holding pan, and out the drainage holes to the collecting bin below. The heating system was modified into a double boiler set-up to prevent over-heating.

In addition to the changes in perfusion, observations from the large deformation creep results from Chapter 2 influenced the test protocol used here. The mechanical damage tests suggested that nominal stresses applied to the surface of the liver should be between 2.2-108 kPa (i.e. 25-125 g using a 6 mm indenter). A motorized indenter would ensure constant strain-rate loadings and perhaps reveal a time constant <1.88 sec due to the ability to apply step loads faster than could be done manually. Lastly, differences seen between loadings and the non steady-state creep value after 300 sec of loading, suggest that time between indentations and the duration of the test should be increased.

3.3.2. *Motorized Indentation Test System*

The TestBench™ Series system with a high fidelity linear actuator was used for the indentation testing experiments (Bose Corporation EnduraTEC Systems Group, Minnetonka, MN). The system's LM1 motor was implemented using their PID control system (WinTest™ Digital Controller and PCI Control software version 2.58, build 359) into a custom support for the indentation testing experiments (Figure 3.4). The system measures displacement using a LVDT (Schaevitz MHR-250 from Measurement Specialties, Hampton, VA) with ± 6.3 mm travel (0.559 μm RMS alone, 3.9 μm RMS with controller), force using a 22 N submersible load cell (0.49 mN RMS alone, 13 mN RMS with controller) (Honeywell Sensotec Sensors Model 31, Columbus Ohio), and

acceleration using a ± 50 g accelerometer (0.024 V RMS alone, 0.204V RMS with controller) (Kistler, Amherst NY). A full characterization of the system including the calibration protocol for the sensors can be found in Appendix A.

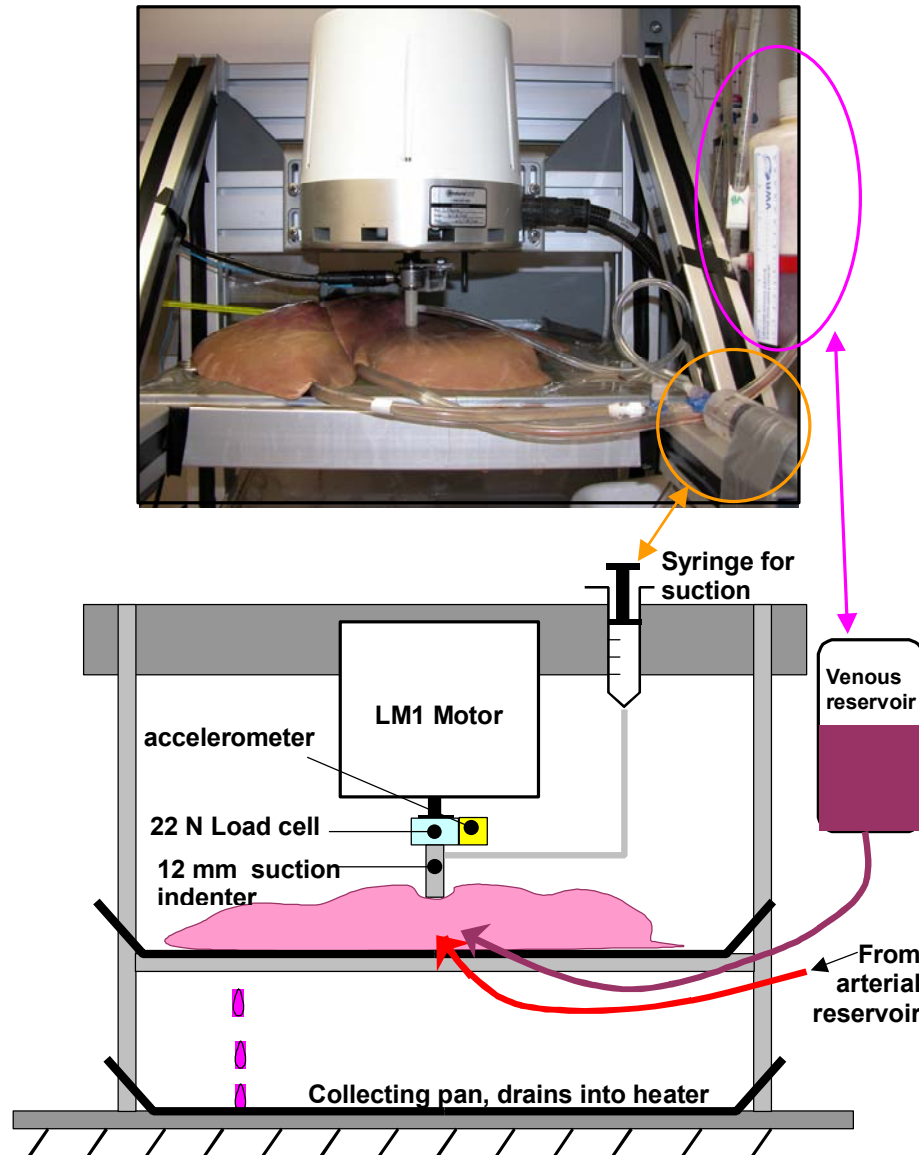


Figure 3.4 Photo and schematic of the experimental set-up.

As was described in Chapter 2, indentation was selected as the deformation modality because it allows for force and displacement data to be collected over time or frequency, anywhere on intact organs, while still maintaining the structural organization of the tissue. A 12 mm diameter flat, cylindrical indenter was used in these studies to both maximize the signal-to-noise ratio, and to mimic either a surgical tool tip or a

surgeon's finger. To ensure known boundary conditions (i.e. impose a no-slip condition) the indenter was designed to allow for suction at the tip. A hollow PEEK (Polyetheretherketone) indenter included a 6.5 mm diameter x 3 mm thick porous polyethylene filter plug with a 70 μm pore-size embedded at the indentation surface (Figure 3.5). This filter was chosen because its larger pore size offered maximum filtration (thus suction of air) while still maintaining good rigidity. A 60 cc syringe was connected to the indenter via PVC tubing and used to provide the necessary suction.

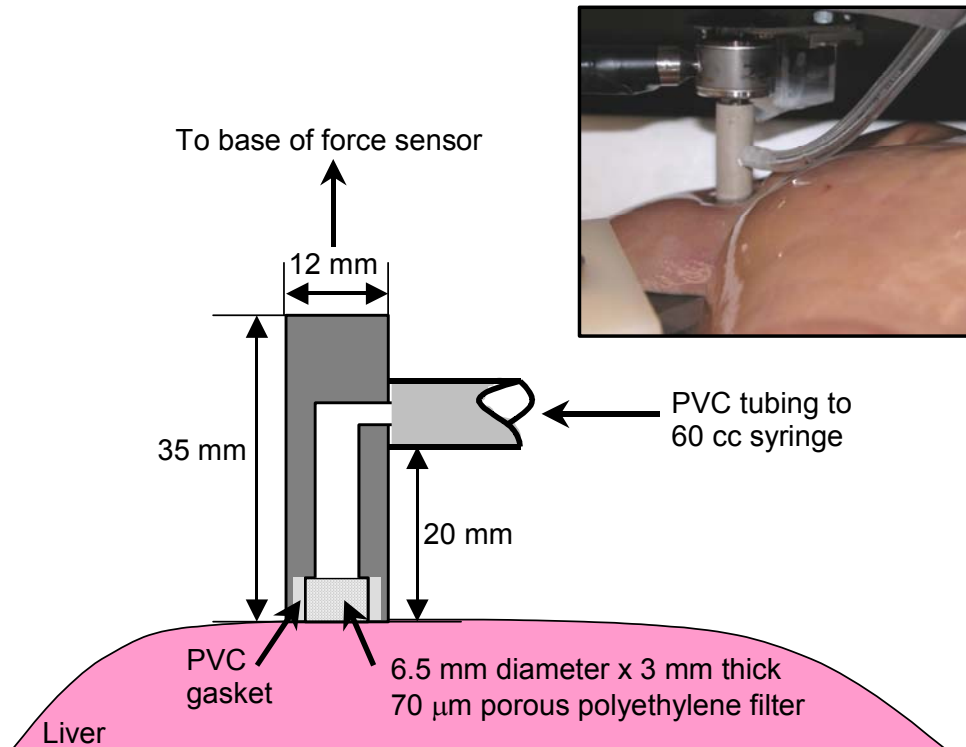


Figure 3.5 Schematic of the suction indenter tip on the liver's surface. Inset is photo of indenter during an experiment on a porcine liver.

3.3.3. Experimental Protocol

As was mentioned above, several types of indentation tests were conducted to characterize the nonlinear mechanical response of six porcine livers. In all cases, the livers from freshly sacrificed 30-100 kg pigs (60 kg mean mass) were harvested as illustrated in Chapter 2 and perfused with the new perfusate described above. The perfusate was fed continuously into the liver with a mean portal venous pressure of 7.98 mmHg (± 1.44), a mean hepatic arterial pressure of 94.77 mmHg (± 1.75), and at a mean temperature of 33 $^{\circ}\text{C}$ (± 4.34). The mean cold ischemic time was 96 minutes (± 16) and there was on average 80 minutes (± 36) of perfusion before testing began during which time the PID controller gains were set on a lobe of the liver not used for testing (see Appendix A). Total test time ranged from 185 to 288 minutes depending on the type of test; all tests were concluded within 6.5 hours post sacrifice. Temperature and pressure

were continuously monitored throughout the tests to ensure proper perfusion of the liver. Thickness was measured by first recording the distance from the bottom of the indenter at the neutral (0 mm) position to the plate on which the liver rests (y_p). For each location of the tested liver, contact was considered established when a compressive force less than -0.01 N was recorded (mean $F_0 = -0.0584$ N). The LVDT position was noted at that slightly preloaded contact (y_0), and suction was applied. The thickness of the liver (mean 30.9 ± 6.3 mm) was equal to the sum of y_p and y_0 .

What follows are detailed descriptions of the indentation tests and their results. The first two tests (sine wave testing over time, and constant rate load/unload ramp tests across frequency) were conducted to understand the material in a general sense. The results of these tests were then used for the development of the protocol of the second set of experiments as well as for initial estimates for the parameters of the constitutive model in the next chapter. The second set of viscoelastic tests consisted of blocks of multiple indentation ramp tests across surgically relevant rates, stress relaxation tests, and creep indentation tests. The results of these last three tests were used to identify and validate the parameters of the constitutive law in Chapter 4, providing an accurate response for surgically relevant manipulation of the liver.

3.3.4. Sine Wave Testing over Time

3.3.4.1. Methods

The goals of performing continuous sine wave deformation tests were to determine the effects of repeat indentation and recovery time on the mechanical response, and to verify the viability of the new perfusate. A sine wave displacement loading condition was imposed with peak-to-peak amplitudes equal to 30% nominal strain, at 1 Hz. The force response was monitored to determine the repeatability and consistency of the behavior. To assess whether changes seen were from total number of indentations, amount of recovery time, time of test, or cellular changes, two different tests were conducted.

The first experiment consisted of continuously indenting an *ex vivo* perfused porcine liver for a set period of time, allowing it to recover for the same amount of time, and repeating across different time scales. Eight trials were conducted at the same location. The first was for 60 minutes, the second for 20 minutes, the third and fourth for ten minutes, and the fifth through eighth for five minutes. A total of 7,200 indentations were recorded across four hours. Force, displacement, and acceleration data were collected at 100 Hz.

The second test focused on 25 seconds of continuous indentation testing (25 cycles was determined to be the point at which steady-state was reached, as will be discussed below). Recovery time was varied between repeat testing. The *ex vivo* perfused livers were allowed to recover for 3, 5, or 60 minutes, and this series was repeated three times for a total of 300 indentations over four hours. In addition to collecting the force, displacement, and acceleration data at 1,000 Hz, biopsy samples were collected on an untested lobe for histology over the course of 6.3 hours. Samples were collected using the same procedure outlined in Chapter 2, and were taken at sacrifice both pre- and post-flush, and then every 60 minutes during perfusion.

All data sets were filtered forward and backward with a 4-pole Butterworth low-pass filter featuring a 20 Hz cutoff frequency.

3.3.4.2. Results

Figure 3.6 shows a typical response to a 1 Hz continuous sinusoidal displacement-controlled indentation using the 10-minute trial of the first experiment. Since this liver was 25.8 mm thick, 7.7 mm peak-to-peak amplitude was commanded to achieve the desired 30% nominal strain. The figure clearly shows the effects of preconditioning: initial indentations resulted in higher forces than the later ones, but a steady-state condition was achieved well before the end of the 600 indentations. Figure 3.7 shows one trial from each experiment where the peak forces for several indentations are highlighted. The first experiment shows a 40% drop in peak force from the first to the 10th indentation across all trials. Comparing this drop in peak force to a 13% change between the tenth and the 25th, a 7.6% change between the 25th and 100th, and a mere 1.2% change between the 100 to 300th indentation suggests that a minimum of 10 to 25 indentations across 10 to 25 seconds should be considered when determining the viscoelastic response of the liver.

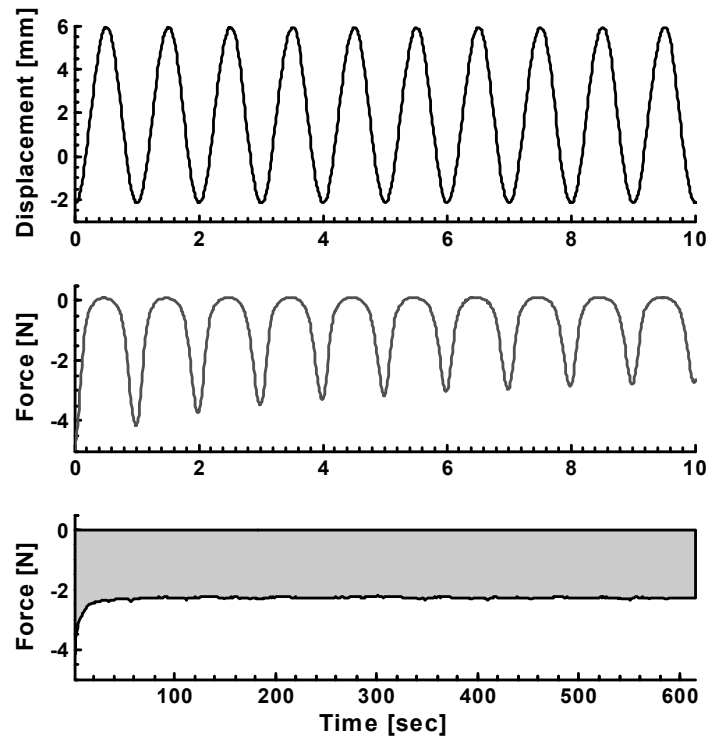


Figure 3.6 A typical response for a 1 Hz sinusoidal displacement waveform. The top and middle show the commanded displacement and the resulting force response for 10 cycles. The bottom graph shows a trace of the minimum and maximum peak force response for each over the full 10 minute trial.

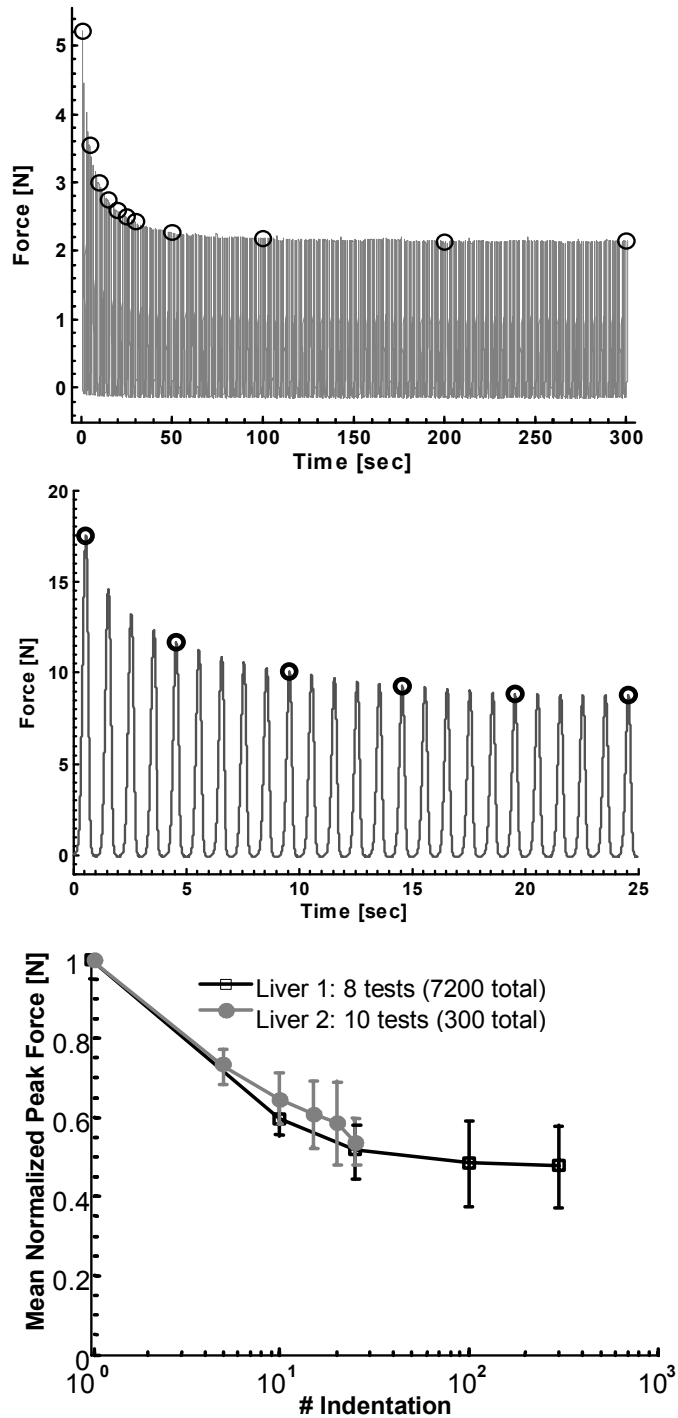


Figure 3.7 A typical force versus time response for 1 Hz sinusoidal displacement waveforms for a 5-minute trial of the first test, highlighting the peak forces for the 1st, 5th, 10th, 15th, 20th, 25th, 30th, 50th, 100th, 200th, and 300th indentation (Top) and a 25-second trial from the second test, highlighting the peak forces of the 1st, 5th, 10th, 20th, and 25th indentations. Note that the forces are plotted as positive for ease of viewing. (Bottom) Plot showing the normalized peak force to the first indentation versus number of indentation for both experiments and all trials.

These results were used to set the number of indentations of the second test to 25. The second experiment yielded a result similar to the first in terms of drop in peak force with indentation. This suggests that it is the recovery time and not necessarily the number of indentations that is important for repeatable multiple indentation testing results.

In addition to recording the peak force for each indentation, another important feature was the amount of hysteresis seen between indentations. Hysteresis is the amount of energy lost between the loading and unloading curves or simply, the area between these two curves. Figure 3.8 shows typical force versus nominal strain curves for the first and 25th indentations from the same trial in the second experiment. The drop in both peak force and hysteresis are clearly seen. Summarizing of the amount of hysteresis for every 5th indentation shows a similar decreasing trend as those for peak force: a 53% drop between the 1st and 5th, 18% between the 5th and 10th, 6% between the 10th and 15th, and 4% between the 15th and 20th and 20th and 25th. This supports that a consistent state is achieved between 10 to 25 indentations (Figure 3.8).

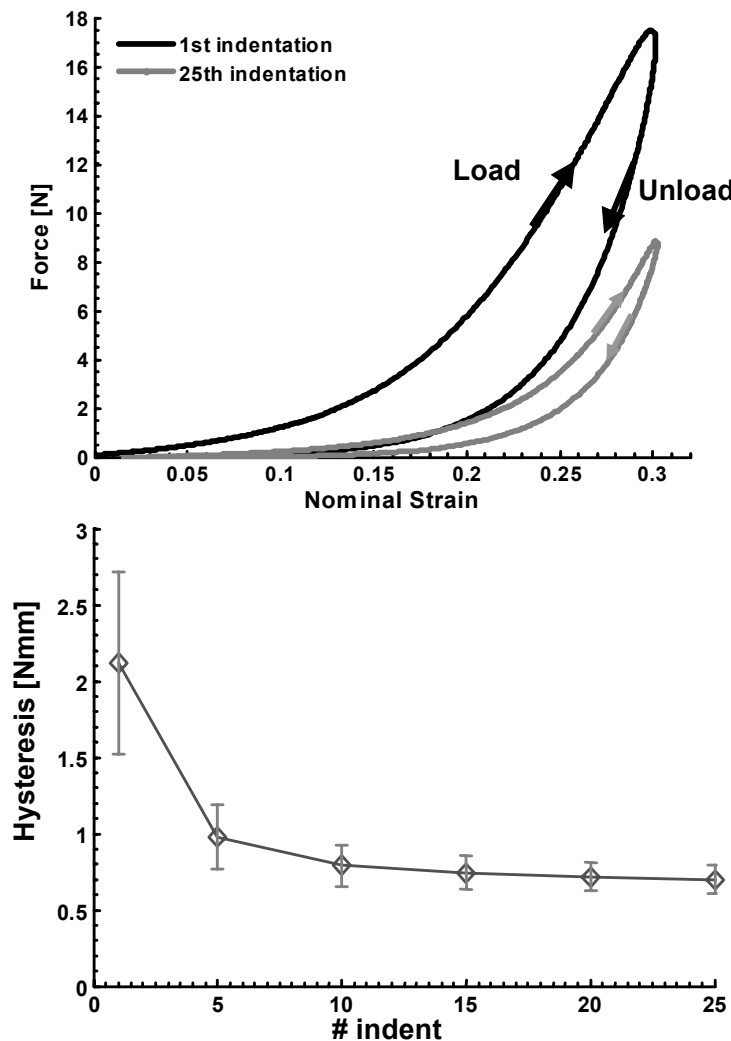


Figure 3.8 (Top) Representative force vs. nominal strain curve for a 1st and 25th indentation of the same trial. (Bottom) The amount of hysteresis observed in the 1st, 5th, 10th, 15th, 20th, and 25th indentations for the second experiment.

The histology report showed that no changes in the cellular structure occurred between all samples over 6.3 hours compared with the control (Figure 3.9). The pathologist report stated, “the cells in general appear to be very viable and well preserved in all samples,” suggesting that the perfusion pressure was appropriate and that the new perfusate is capable of maintaining the cellular integrity for up to 6.3 hours post sacrifice (270 minutes of perfusion).

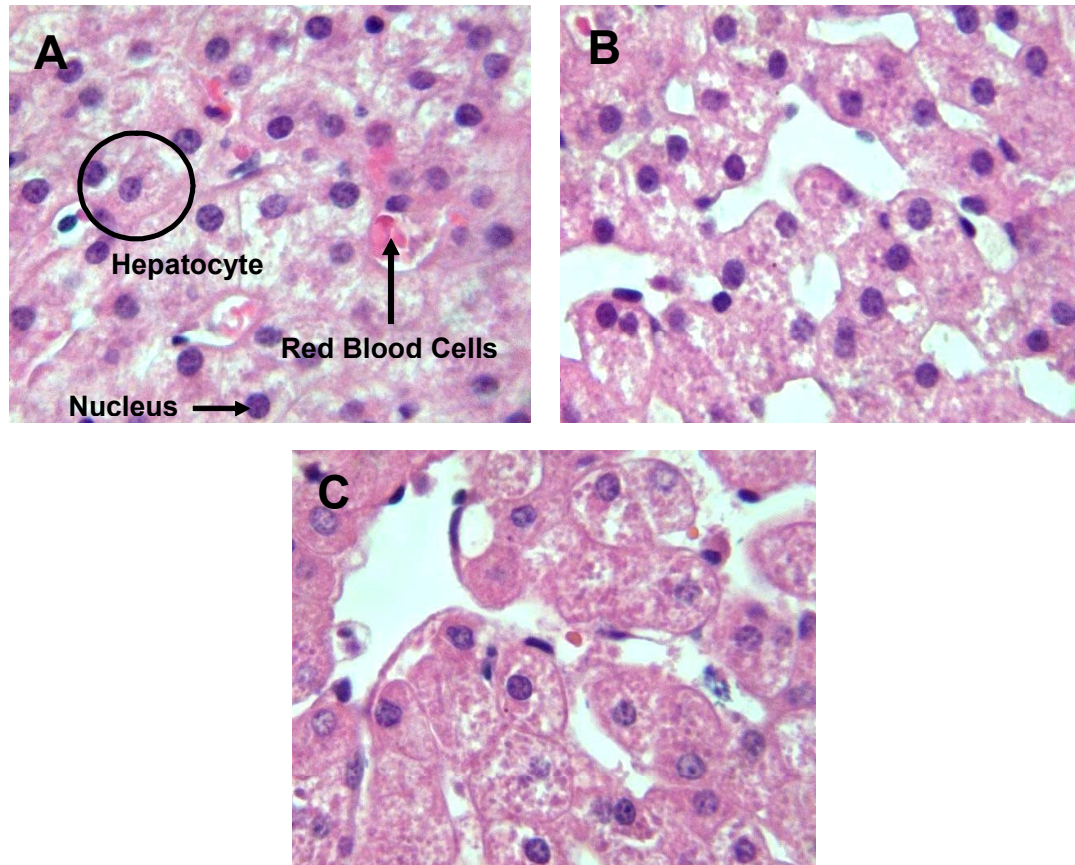


Figure 3.9 Hematoxylin and eosin (H&E) stained sections of the liver over a period of 6.3 hours magnified 400x. (A) A biopsy post sacrifice used as control. (B) A biopsy taken just after flushing the harvested liver with Lactated Ringers Solution (note the voids free of red blood cells). (C) A biopsy taken 6.3 hours after the control, and after 200 minutes of sinusoidal indentation testing in the *ex vivo* perfusion set-up.

3.3.5. Constant Strain-Rate Ramp Testing across Frequencies

3.3.5.1. Methods

This work aims to characterize the large deformation mechanics of a nonlinear tissue. The common viscoelastic analysis used for sinusoidal displacement inputs across frequencies is only valid for small strain deformations on a linear material. The liver is still a viscoelastic material, however, and thus understanding its strain-rate dependency is important. A triangle waveform is a more appropriate modality to ascertain the desired

response, as it allows constant strain-rate loading and unloading ramps to be applied. Also, higher frequency components beyond that of the input signal are expressed, since Fourier series decomposition of a triangular wave stimulus contains frequency components beyond that of the fundamental frequency of the signal.

Three different locations on perfused *ex vivo* livers from two pigs (30 and 80 kg) were used in this study. Displacement loading and unloading ramps inducing nominal strains from 30 to 38% were applied at rates from 0.14 to 316 mm/s (0.01 to 22 Hz). For the first liver, two locations were tested. At the first location (20.6 mm thickness) three load/unload indentation ramps with 6.4 mm amplitudes were carried out at ten different speeds (0.14 to 264.7 mm/s) in order of increasing rate. At the second location (25.2 mm thickness), two to four 10.2 mm indentations were collected in random order at each speed (5.2 to 316 mm/s). There was a 1 to 3 minute rest period between loadings for both of these tests depending on the time of indentation. The second liver was tested at the end of a different experiment and thus viable tissue time only allowed for one indentation at each rate. This 35 mm thick location was displaced 9.2 mm from 1.31 to 197.4 mm/s in order of increasing rate with a 3 to 5 minute rest between indentations.

3.3.5.2. Results

The data from these tests were used to understand the strain-rate sensitivity of the liver under finite deformations. All data were sampled between 2 to 4 kHz and were filtered forward and backward with a 4-pole Butterworth low-pass filter with a cutoff frequency of 60 Hz. Mean force and displacement data were computed for each rate for the two locations of the first liver tested. Excellent repeatability was observed between loadings of the same rate, as evidenced by the 0.5 Hz data set seen in Figure 3.10. Figure 3.11 illustrates the mean force versus displacement curves for the ten rates collected at the initial location of the first liver.

The responses were decomposed into their elastic and viscous components (described below) and plotted against frequency (taken as the inverse of the time to complete one load/unload cycle). To accomplish this, the force versus displacement curves were separated into their loading and unloading components. The elastic recovery force was taken to be the same as the unloading curve, whereas the viscous force was taken to be the difference in the loading and unloading curves (Figure 3.12). The stored elastic energy was then determined by taking the area under the elastic recovery force curve for each rate tested. Similarly, the dissipative energy was taken as the area under the viscous force curve for each rate. Since some rates were near the bandwidth of the indentation system, some of the higher rates either overshoot or did not reach their targeted displacements. Thus, the areas were taken up to the lowest displacement to prevent a bias in the data. Figure 3.13 presents a summary of the elastic storage and dissipative energies as a function of frequency as well as the ratio of the dissipation to the elastic storage energies. Assuming a triangle input has a similar period to a sine input, and observing that the strain input was one half cycle, this ratio is equal to π times the tangent of the phase shift between the strain input and stress response. Results suggest that the liver is strain-rate sensitive and that the elastic component saturates at frequencies above ~ 10 Hz and below ~ 0.05 Hz. The dissipation shows a steady increase across the frequency range tested, nearing zero at the lower end. Lastly, the ratio of the two shows a saddle-type

response, suggesting that there are potentially two time constants in the liver: one greater than 10 seconds, and another less than 0.1 second.

Due to the small sample size and noise in the data, the results presented here serve merely as a guide for the general response of liver across indentation number and frequency and should not be taken as absolute. In the next chapter, these results are used to analytically support the form of the constitutive model and to estimate initial values of the model's parameters.

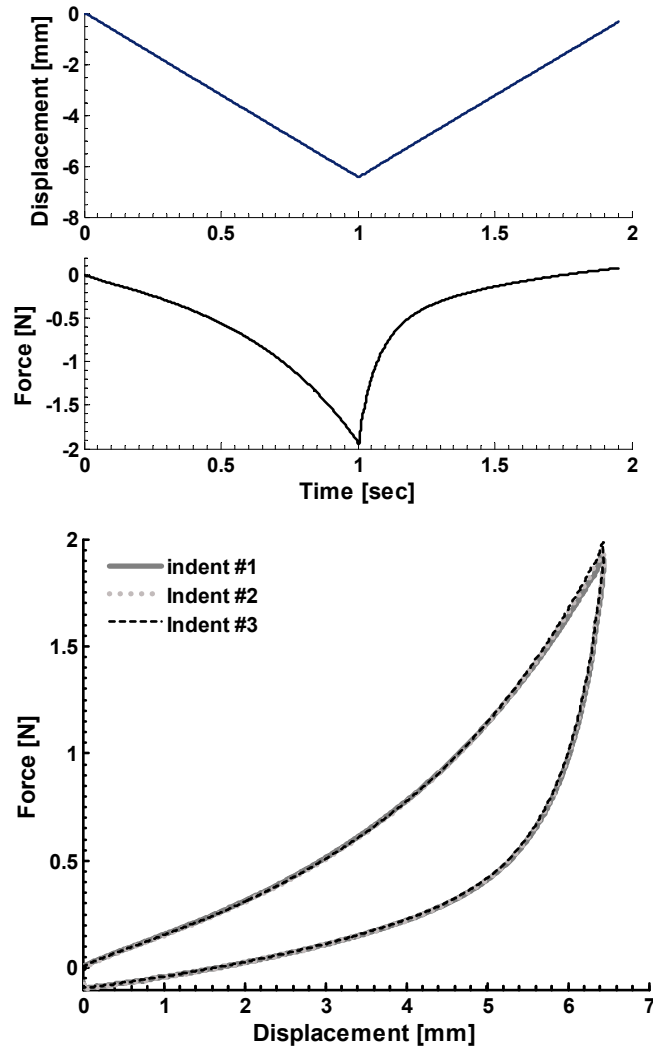


Figure 3.10 (Top) Example of the ramp load/unload displacement waveform used for the 0.5 Hz test on a 20.6 mm thick liver and the corresponding force response. (Bottom) The resulting force versus displacement data for the three load/unload ramp indentations at 0.5 Hz.

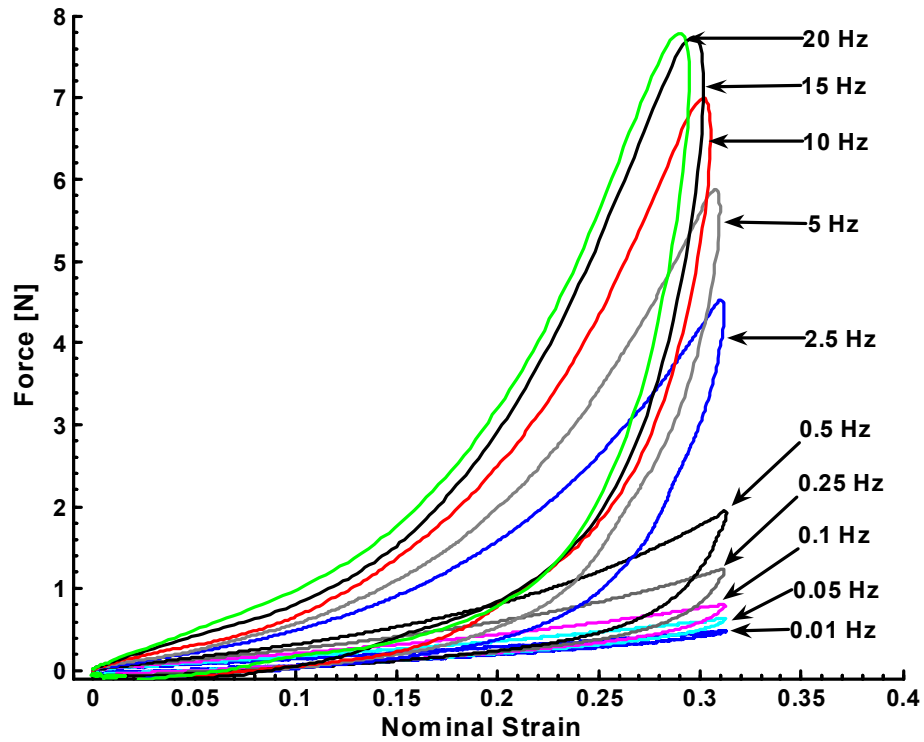


Figure 3.11 The mean force versus nominal strain (displacement/thickness) responses from 30 load/unload ramp indentations taken at one location from one liver, across 10 rates.

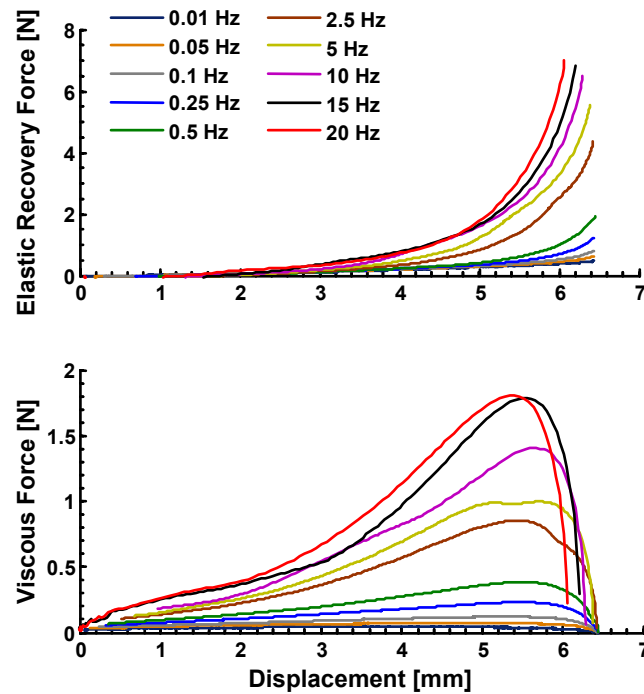


Figure 3.12 Example of elastic (Top) and dissipative components (Bottom) of the force versus displacement data in Figure 3.11.

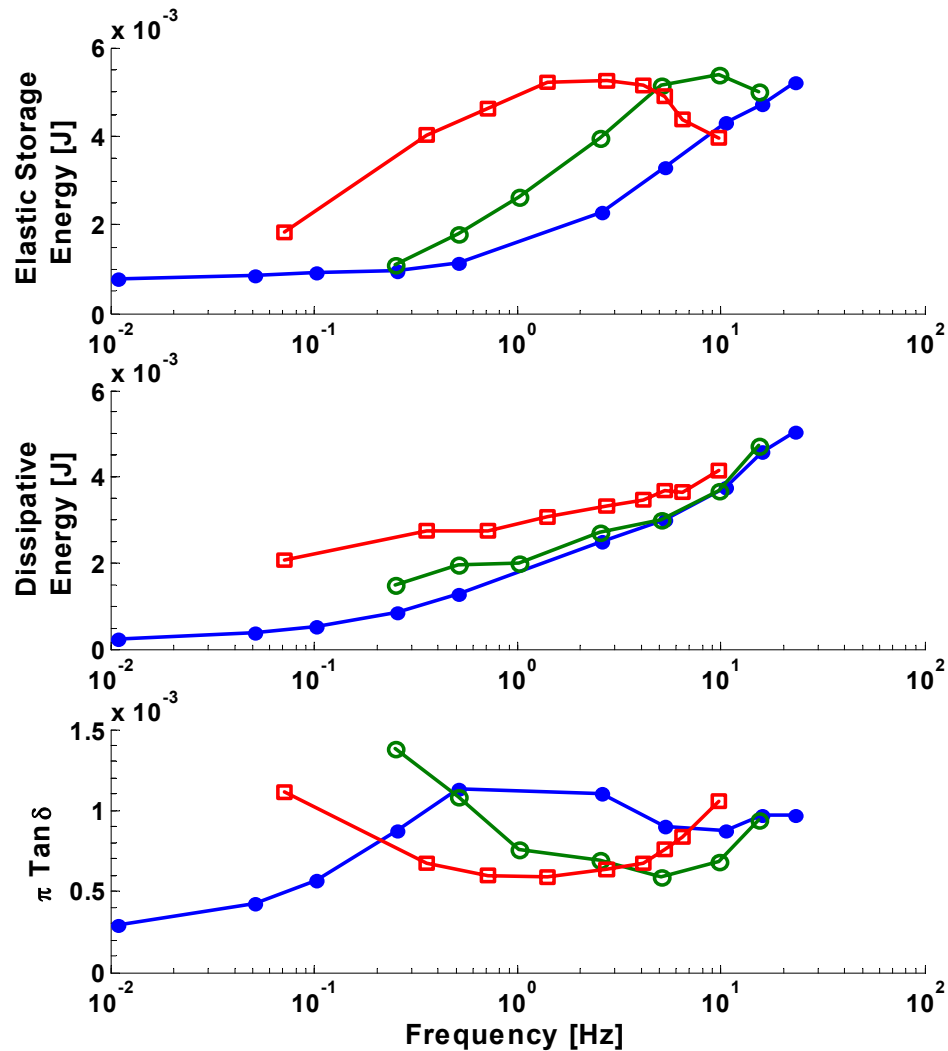


Figure 3.13 A summary of the elastic storage (Top) and dissipative (Middle) energies versus frequency for three locations on two livers. The ratio of the energy dissipated to the energy stored ($\pi \tan \delta$, since only a half of cycle is collected) is also shown (Bottom).

3.3.6. Multiple Ramp Indentation Testing

3.3.6.1. Methods

Initial studies revealed that strain-rate and rest-time affect the indentation response of liver, and that at least 10 indentations are needed to obtain decent repeatability in the response. The goal of the work described in this section is to use that information while trying to capture the response of liver to surgically relevant rates and deformations. Livers from three pigs were harvested and perfused for this study (81, 40, and 80 kg). Three blocks of 9 or 12 loading and unloading ramp indentations at rates from 0.2 to 40 mm/s, up to 40% nominal strain were performed on one location of each liver. As will be described in the next two sections, creep indentation testing was simultaneously conducted at a different location using a modified version of the device

used in Chapter 2, while stress relaxation tests were conducted at the same location using the motorized indenter after the multiple ramp indentation tests were complete.

For the multiple ramp indentation tests, contact was established and initial thickness was determined as mentioned above. A block waveform was then created in the control software that ramped the indenter to a level equal to $\sim 30\%$ nominal strain (between 9 and 12.5 mm) and back nine times at three different rates (0.2, 2, and 20 mm/s) for the first liver, and 12 times at four different rates (0.2, 2, 20, and 40 mm/s) for the second and third livers. The order of the rates varied, but the first indentation of the first block and the last indentation of the last block were always done at 2 mm/s. The order of rates for the indentations for the three livers is shown in Table 3.1 and a representative loading profile is shown in Figure 3.14. Data was collected between 2 to 4 kHz. After a block of indentations was complete, the level of the indenter was brought back to the contact position and held for 120 seconds while the force and displacement data continued to be collected at 1kHz. The liver was then allowed to recover for 30 minutes before the next block of indentations was carried out.

3.3.6.2. Results

Figure 3.15 shows a series of force versus displacement results for the 12 indentations of the waveform shown in Figure 3.14. Three consecutive indentations were taken at 40, 20, 2, and 0.2 mm/s, respectively. The results illustrate the same effects observed previously, with the first indentation having a higher force and more hysteresis than the rest, faster rates having higher forces, and a repeatable response achieved by the 10th indentation. These force-versus-displacement curves present a rather shallow-sloped initial region before turning up in the typical nonlinear fashion. There is an initial rapid drop in force during unloading, followed by a gradual return to zero. This suggests that although hysteresis is clearly present, there is no permanent deformation.

Table 3.1 The rate of each indentation for the nine blocks of multiple ramp indentation tests conducted on three livers.

Indentation Number and Ramp Rate (mm/s)												
Liver: Trial #	1 st	2 nd	3 rd	4 th	5 th	6 th	7 th	8 th	9 th	10 th	11 th	12 th
Liver 1: 1	2	2	2	20	20	20	0.2	0.2	0.2	na	na	na
Liver 1: 2	0.2	2	20	0.2	2	20	0.2	2	20	na	na	na
Liver 1: 3	20	20	20	0.2	0.2	0.2	2	2	2	na	na	na
Liver 2: 1	2	2	2	20	20	20	40	40	40	0.2	0.2	0.2
Liver 2: 2	2	2	2	20	20	20	0.2	0.2	0.2	40	40	40
Liver 2: 3	40	40	40	0.2	0.2	0.2	20	20	20	2	2	2
Liver 3: 1	2	2	2	20	20	20	0.2	0.2	0.2	40	40	40
Liver 3: 2	40	40	40	20	20	20	2	2	2	0.2	0.2	0.2
Liver 3: 3	40	40	40	0.2	0.2	0.2	20	20	20	2	2	2

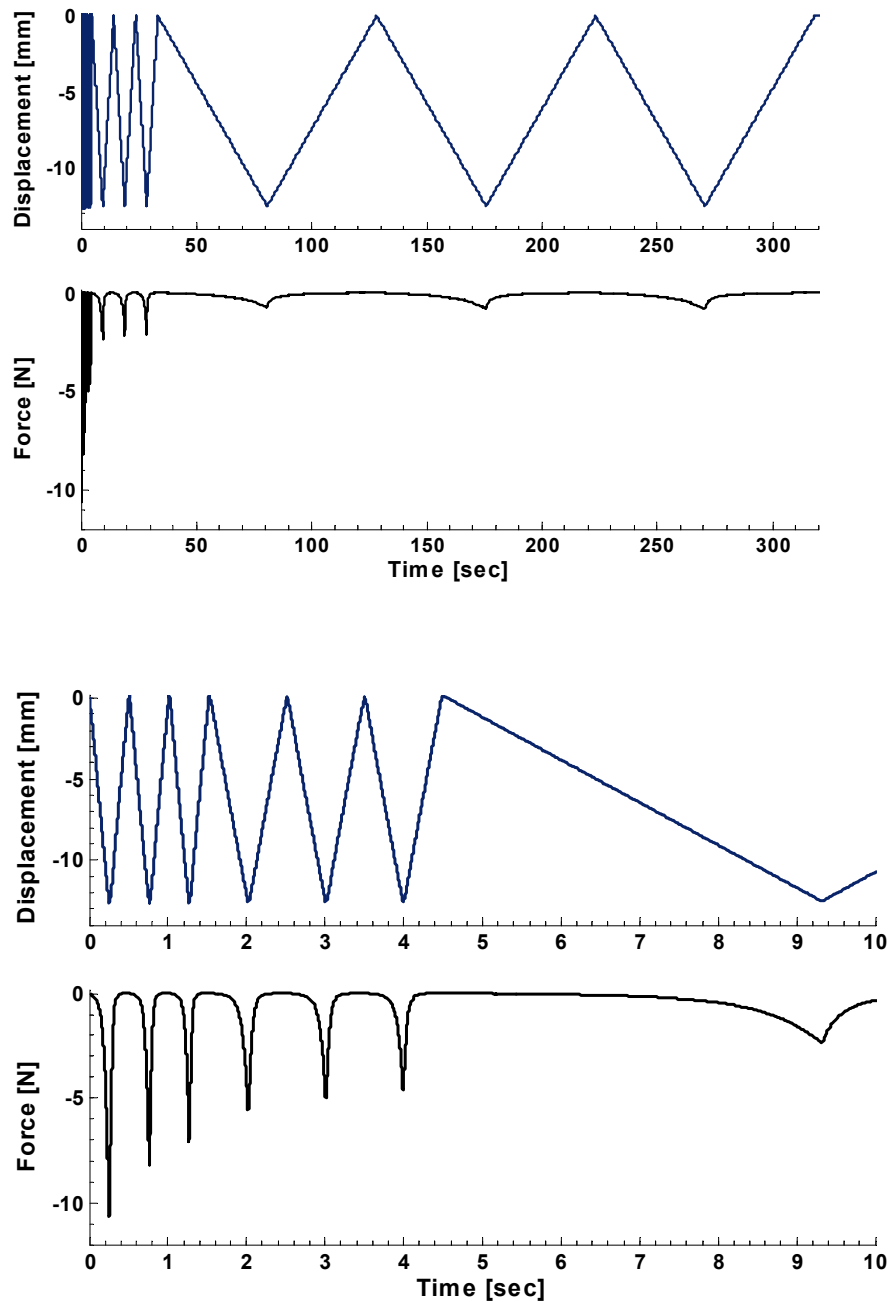


Figure 3.14 (Top) Example of the commanded ramp loading/unloading waveform and the force response for 12 indentations at 40, 20, 2, 0.2 mm/s. (Bottom) An expanded view of the first 10 seconds and the resulting force response versus time.

The third liver was chosen as representative because it was similar in size to the first and had the same loading profile as the second (four speeds as opposed to just three).

Observing all of the indentations for each of the three blocks tested in this liver, separated by speed of indentation, reveals more about the behavior of the tissue (Figure 3.16). Although the first indentation of each block has more hysteresis and higher peak

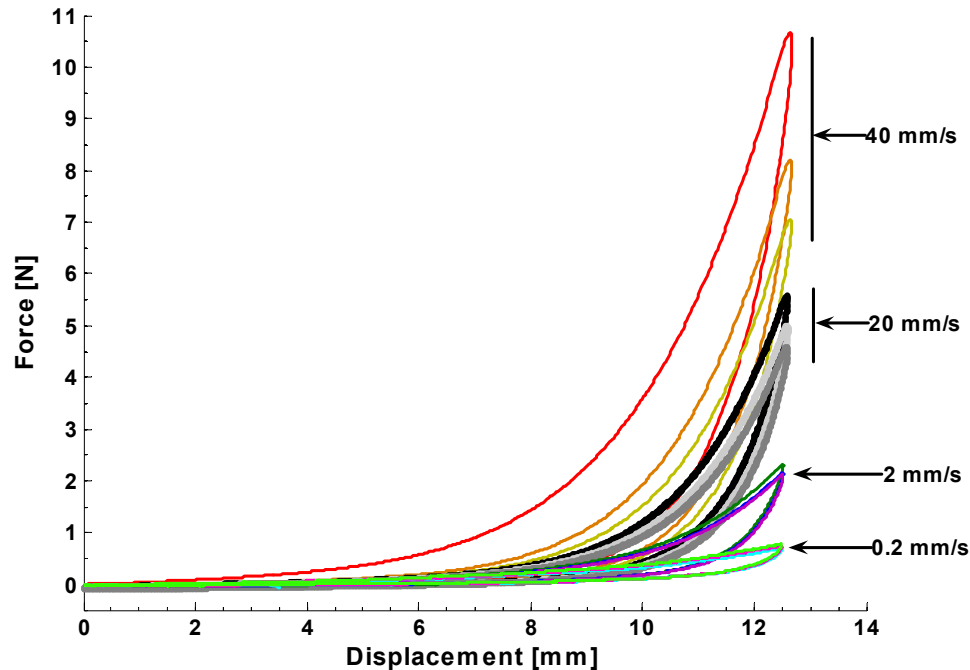


Figure 3.15 The force versus displacement response for the 12 indentations of the representative ramp waveform in Figure 3.14. The indentation block consisted of 3 consecutive indentations each at 40, 20, 2, and 0.2 mm/s.

force than the rest, the indentation that occurs directly after the 0.2 mm/s indentation behaves in a similar manner. The indentations taken at 0.2 mm/s demonstrate notable repeatability across time and indentation and also exhibit a lower response than the other speeds. All trials show an increase in peak force with speed, and better repeatability with increasing number of indentation. Although the tests were conducted within one hour of each other, it was noted that the third block had a nearly zero contact force ($F_0 = 0.008\text{N}$) as compared to the -0.013 N force of the first block. This could be attributed to a decrease in thickness and could thus account for the decreased overall forces observed in the third block.

The responses from the other two livers are consistent with those described for the representative liver, as is illustrated in Figure 3.17. The 2 and 20 mm/s indentations for all blocks and all three livers are shown. These two speeds were chosen for comparison since all three livers were tested at these rates and because 0.1 to 1 Hz represents the most surgically relevant rates that were tested. The results show that the tissue response to 32 to 36% nominal strains with mean peak forces of 3.7, 6, 6.4, and 8.5 N for the 0.2, 2, 20, and 40 mm/s cases, respectively. The 2 and 20 mm/s indentations for all blocks and all three livers are shown. These two speeds were chosen for comparison since all three livers were tested at these rates and because 0.1 to 1 Hz represents the most surgically relevant rates that were tested. The results show that the tissue response to 32 to 36% nominal strains with mean peak forces of 3.7, 6, 6.4, and 8.5 N for the 0.2, 2, 20, and 40 mm/s cases, respectively. The large swing in response largely depends on the rate order that the indentations were conducted at since the first indentation showed peak forces and hysteresis that were much larger ($\sim 40\%$ and $\sim 50\%$, respectively) than

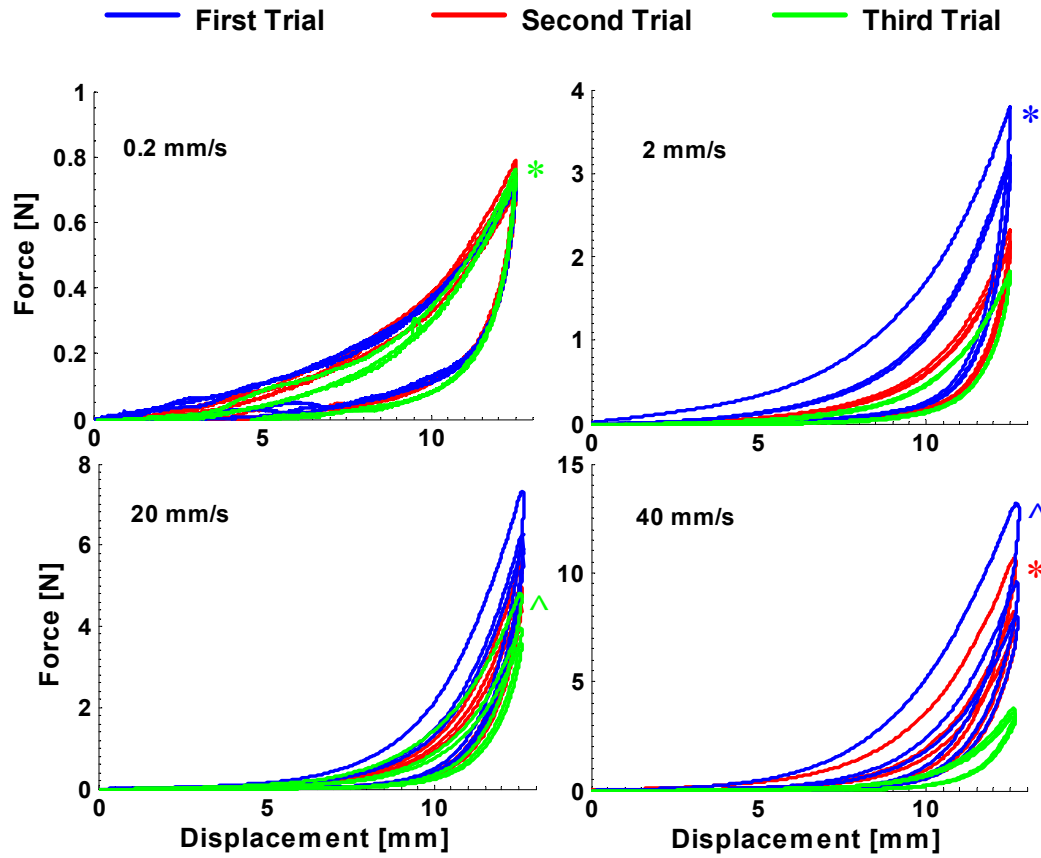


Figure 3.16 The force versus displacement curves for all three multiple indentation trials on the third liver. All trials had three consecutive indentations at each of four speeds. The blue curves are from the first series of indentations (2, 20, 0.2, 40 mm/s), the red curves from the second series (40, 20, 2, 0.2), and the green curves from the third series (0.2, 20, 40, 2 mm/s). The tests were taken within 1 hour of each other, with a 30-minute recovery time between tests. The colored asterisk (*) indicates which indentation was the first of its trial, and the caret (^) indicated the first indentation after the 0.2 mm/s indentations. Note that the vertical axes are different in each plot.

sequential indentations. Also, the response of the indentation immediately following the third 0.2 mm/s indentation behaved as if it were a “first” indentation. This suggests that the time scale for recovery (reperfusion) was on the same order of magnitude as the time it takes to conduct the 0.2 mm/s indentation (70-100 seconds) depending on the liver. Lastly, a 50, 60, and 30 mN change in force over the 120-second dwell time following each series of indentations was seen in each of the three livers, respectively. This force is indicative of a “refilling” or back-pressure since the suction indenter was simply brought back to the commanded zero-displacement point and the force from the indenter was recorded over time.

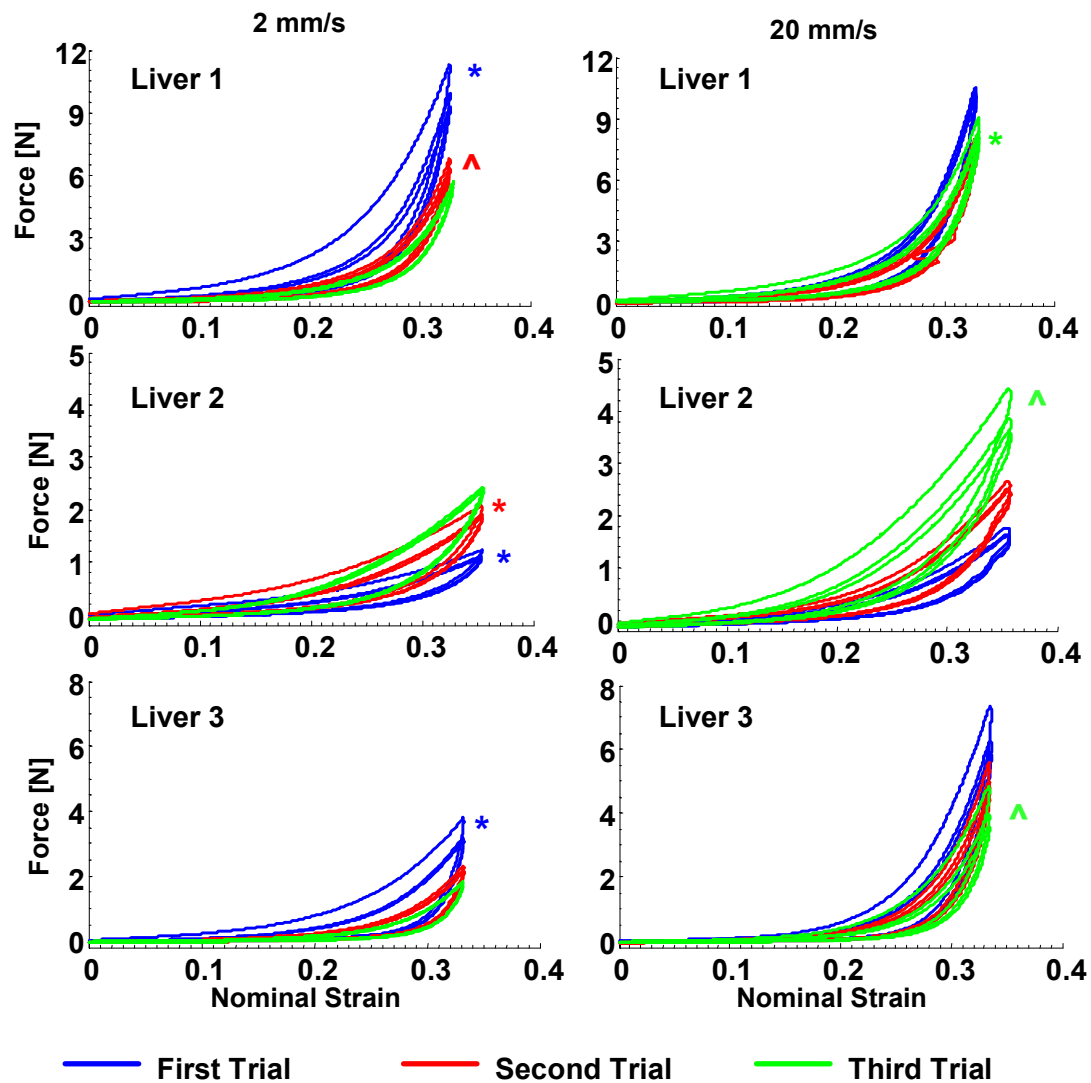


Figure 3.17 The force versus nominal strain responses for the 2 and 20 mm/s ramp indentations for all three livers. The blue curves are from the first trial for each liver, the red from the second, and the green from the third. The colored asterisks (*) and carot (^) highlight the curves that were either the first indentation of their block, or the one following the 0.2 mm/s indentation, respectively.

3.3.7. Stress Relaxation

3.3.7.1. Methods

After the multiple indentation ramp tests were complete (1.5 to 2 hours), the liver was allowed to recover for 30 minutes and then stress relaxation indentation tests were carried out at the same location. Again, the thickness was measured and the desired displacement to achieve a 30% nominal strain indentation depth was determined. A single 1 Hz cycle was commanded to that depth, resulting in ramp velocities between 431 and 543 mm/s for the three livers tested and then held for either 20 or 30 minutes. Two trials were run on the first liver with a 20-minute hold and recovery, two on the second

with a 30-minute hold and recovery, and one on the third with a 30-minute hold. Unfortunately, 2 cycles of the square wave were mistakenly applied prior to the hold phase for the first liver. The effects of this “pre-indentation” are discussed below. Data was collected at 4 kHz for the ramp and 100 Hz for the dwell.

3.3.7.2. Results

The force versus time results for the ramp and hold stress relaxation indentation tests are shown in Figure 3.18 for all three livers. The top figure shows the results versus log time and the bottom plot focuses on the first five seconds. In all cases there is a nearly linear load followed by a nonlinear relaxation. The relaxation initially drops off very quickly before flattening out into a steadily decreasing response. This suggests that a nonlinear dissipation, two dissipative components, or both are responsible for the relaxation. The peak forces are proportional to the amount of deformation given the thickness of the organ. Although these ramp and hold tests were conducted at rates ten times faster than the indentation tests described in the previous section, the peak forces are only slightly (1.75 times) larger than the peak forces seen in the indentation tests. An exception to this trend is the first liver, whose peak forces match those of the indentation tests, likely due to the pre-indentation that occurred. Similarly, this pre-indentation likely accounts for the smaller relaxation response of the first liver. All cases resulted in a near steady-state value by the end of testing (1200 to 1800 seconds).

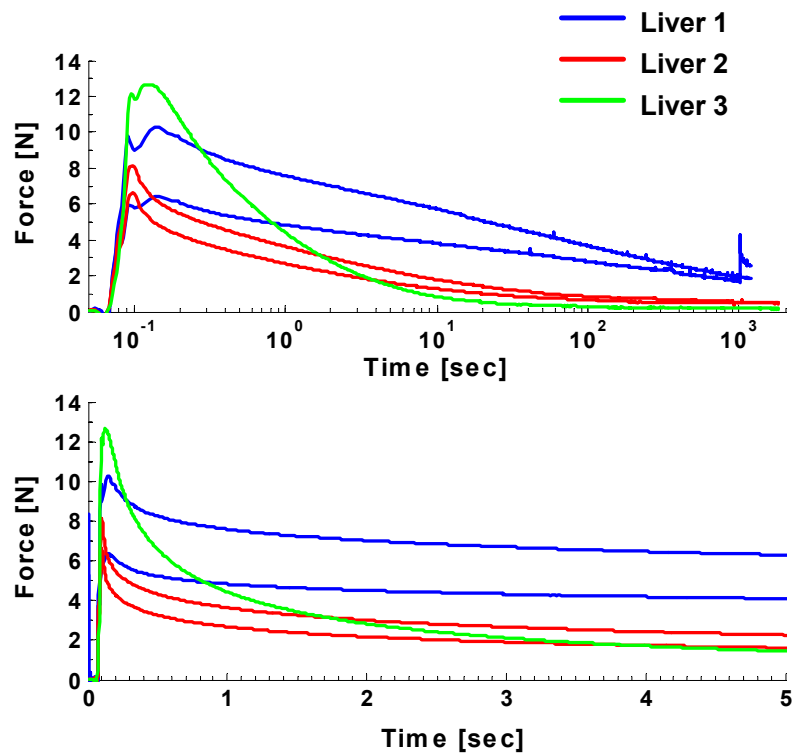


Figure 3.18 1 Hz ramp and hold stress relaxation force versus time results for all 3 livers. (Top) log scale. (Bottom) Linear plot of first 5 seconds of data.

3.3.8. Creep

3.3.8.1. Methods

The final test conducted on these livers was a long time creep indentation test. To allow concurrent creep testing with the indentation tests, the manually loaded creep indentation arm featured in Chapter 2 was used. A longer arm (29.7 cm from pivot to indenter tip) allowed better small-angle approximation, more linear vertical motion, and better reach for placement onto the organ. The sensors were the same as in Chapter 2. A new mounting clamp permitted the creep device to be directly mounted to the motorized indenter's support rig. As before, a 32.5 g brass weight was manually applied to a peg aligned collinearly to the 6 mm diameter indenter tip.

Creep testing was performed on a location different from the multiple-indentation and stress relaxation tests, and began shortly after perfusion was established. The thickness was determined by adjusting the mount to ensure that the creep arm was level when the indenter was in contact with the surface. After the tests were complete, the distance of the level indenter to the surface where the liver rested was measured and taken to be the thickness of the organ at that location. Displacement data were collected at 1 kHz for the first 30 seconds and then at 1 Hz for the remaining hour of testing. The load was removed and the liver allowed to recover for 1 hour before the second trial was conducted. Two trials were carried out on each of the three livers. For the first liver, the first trial was only held for 30 minutes.

3.3.8.2. Results

The nominal strain-versus-time results for the creep indentation test are shown in Figure 3.19. The data was filtered with a 9th order median filter. The top plot shows the full creep response over the course of the hour, while the bottom shows the response after the initial loading (and hence transient) on a log scale. Loading was determined by taking the mean of the initial two seconds of data (prior to load application) and finding the first point where the data deviated from that mean. The initial response was then taken from the new zero point to the peak of the first transient in the response. The mean time for loading was 0.106 s (± 0.039). The mean steady-state nominal strain value for all six trials was 51% ($\pm 3\%$).

The nearly linear response on the semi-log plot contrasts with the nonlinear response seen in the stress relaxation tests. This is likely due to the limitations of manual loading as an approximation to a true step input. The noise seen in one of the third liver trials came from a repositioning of the lobe and that was being tested using the motorized indenter, thus affecting perfusion.

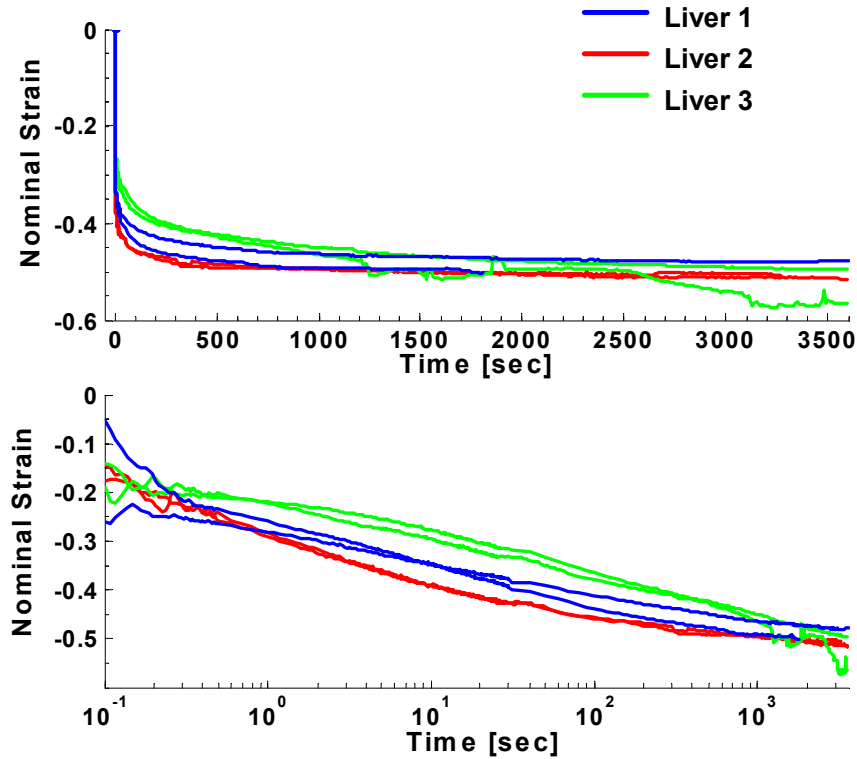


Figure 3.19 Nominal strain versus time creep responses for all three livers. (Top) The full creep response to 3,600 seconds. (Bottom) The creep response after the 0.1 second initial loading response, plotted on a log scale.

3.4. Discussion

This chapter focused on obtaining a complete set of experimental results from which a full viscoelastic characterization of liver could be obtained under finite deformations and rates typical of surgical manipulation. The new perfusate showed to maintain the mechanical viability of the liver for up to 6.3 hours post sacrifice. Uniaxial tension tests to failure were done on *ex vivo* segments of the liver capsule, while indentation tests to up to 40% nominal strain were done on *ex vivo* whole perfused livers. The capsule results revealed a nonlinear response typical of stiff collagenous biomaterials. The various indentation tests also demonstrate a nonlinear force-displacement response with a shallow toe region followed by nonlinear stiffening. The liver was found to be strain-rate sensitive and exhibited large amounts of hysteresis, stress relaxation, and creep. Results also indicated that the response of the first indentation was different from the rest, resulting in higher peak forces (~40%) and more hysteresis (~50%). This was mistakenly highlighted in the “pre-indented” stress relaxation case whose peak forces equaled those of ramp tests conducted at 1/10th the speed, and where relaxation was stiffer than the other tests. The responses are repeatable at a particular rate within 25 indentations, given ample recovery time between indentations. Both the rate and stress relaxation tests demonstrated that at least two dissipative components are involved in the mechanics of the liver: one less than 0.1

seconds, and one between 10 and 100 seconds. The rate tests also indicated that deformations below 0.05 Hz saturated both the elastic force and viscous force components. This was further evidenced during the multiple indentation ramp tests where the 0.2 mm/s (~ 0.01 Hz) tests were repeatable, and that the indentation occurring immediately after these indentations behaved similar to a first indentation.

This work represents a unique compilation of data on the dynamic finite deformation of liver. Although several other groups have performed mechanical viscoelastic testing of the liver, their data sets are limited, thus making direct comparisons difficult. Brown et al. have done extensive viscoelastic testing on the liver across various conditions using both indenters and a motorized endoscopic grasper (Brown 2003; Brown, et al. 2003; Brown, et al. 2002). Although they also recognized the importance of the first “response” of the tissue, they only captured the first indentation at each tested location. They did note tissue stiffening with 10 successive squeezes using the grasper, yet they saw no rate dependencies up to 3 Hz. Their inability to accurately determine the thickness of the tissue tested and the nonuniform loading of their graspers makes their data difficult to interpret. One unique and important observation from these studies is the importance of rest time between measurements given a perfused organ. Kauer et al. similarly report the effects of preconditioning while aspirating an *in vivo* liver (2001). However, their device was only capable of small deformations and the unknown stress concentrations at the outer ring of the aspiration tube were not accounted for. In addition, their results primarily pull on the surface of the liver, and thus they could be experiencing effects mainly resulting from the capsule.

The importance of the capsule on the mechanical response of the liver must not be overlooked. Stingl et al. attempted to measure the response of the capsule by placing cadaveric livers and spleens in a tearing machine (2002). Although the protocol was ill defined, a rough interpretation of their results suggests that the liver’s capsule has a Young’s Modulus of 1.1 kPa at 17.5% axial strain. Assuming a true uniaxial testing scenario, a 15 to 21 MPa modulus is shown for the linear region of the capsule response collected here. They also report that the liver capsule contains 24.33% collagen, which supports the observation that the force-displacement response behaves similarly to that of collagen.

In summary, although many more data sets are necessary to show the significance of these results, this work demonstrates that the testing methods outlined here are adequate to fully characterize the nonlinear viscoelastic response of liver under large deformations. The next chapter will use the information obtained from these results to develop a physically based and physiologically relevant constitutive model for the liver.

Chapter 4

Nonlinear Physically-Based Constitutive Model and Parameter Identification

The mechanics of a material are governed by the behavior of its constituents. A constitutive relation determines the state of stress at any point in a body in response to any arbitrary history of motion (Holzapfel 2000). Knowing the structure and the constitutive relationships that describe the material behavior of a composite body (i.e. an intact organ), the response of the body to any prescribed loading condition (i.e. surgical manipulations) can be obtained. The challenge is to define constitutive relations that are both simple enough to be easily implemented and realistic enough to accurately describe the material's behavior across different loading conditions. Currently, the lack of elegant and robust constitutive relations for soft biological tissues hinders the development of predictive biomechanics necessary for medical simulation (Fung 1993; Humphrey 2002).

Humphrey proposes a five-step procedure for developing a constitutive relation (Humphrey 2002):

1. Determine the general characteristics of interest
2. Establish a theoretical framework
3. Identify the specific functional forms of the constitutive relations
4. Calculate the values of the material parameters
5. Evaluate the predictive capability of the final relation

The results and analysis of the data presented in Chapters 2 and 3 summarize the general mechanical behavior of the liver. The nonlinear, viscoelastic, strain-rate dependent response to large deformations was found to be sensitive to its geometric and physiologic boundary conditions. These results are used to identify the functional form of the constitutive relations under the theoretical framework of continuum mechanics. The finite element method is used to solve the inverse boundary value problem. An iterative approach minimizes a prescribed objective function to identify the material parameters of the model from the multiple ramp indentation and stress relaxation data. Finally, the predictive capability of the model and its parameters are validated using stress relaxation, multiple ramp indentation, and the creep indentation data.

4.1 Physiologically Derived Constitutive Model

In Chapter 3 the liver was described as being mainly comprised of a tough collagenous capsule, vast cellular parenchyma, and pressurized fluid-filled vessels. In this chapter, the contribution of each of these constituents is accounted for while developing a model that allows for the cooperative nature of the tissue response.

The multi-physics based continuum model developed here relies on the previous modeling work of other soft tissue researchers. Socrate and Boyce developed a similar model for the large strain behavior of articular cartilage (2001). Febvey further developed their model to describe the mechanics of cervical stroma (2003). Both of these solid soft tissue structures were modeled as hyperelastic collagen and viscoelastic proteoglycan networks in parallel with a pressurized interstitial fluid network. Using a similar approach, the liver is modeled as a homogenous, initially isotropic, fluid-filled structure, containing a hyperelastic collagen network in series with a viscoelastic cellular network. A third porous network represents the volumetric response due to the fluid flow. Finally, the tough outer capsule structure is modeled as a hyperelastic collagenous membrane similar to Prevost's treatment of the chorioamnion (fetal membrane sac) (2006).

4.1.1 Motivation

The extracellular matrix (ECM) of soft tissues regulates the cell's shape, orientation, movement, and overall function (Park and Lakes 1992). ECM is comprised of elastin and collagen proteins in a hydrated ground substance. Elastin is considered the most linearly elastic bio-solid with a Young's modulus of 0.6 MPa at 100% stretch (Park and Lakes 1992). Elastin is a long, flexible, cross-linked molecule whose molecular configuration changes with stretch. Collagen is the basic structural element in all tissues, with wavy fibers acting as mechanical units that dominate the force-stretch response. The initially compliant fibers stretch and reorient under a tensile load producing a nonlinear stiffening response with increased levels of stretch (Fung 1993; Liu and Bilston 2000).

Holzappel suggests that soft biological tissues and solid polymers are unique in that they are the only materials that experience a nonlinear mechanical response to finite strains relative to an equilibrium state (2000). Since the polymer chain networks mimic the assembly of the wavy cross-linked collagen, the model used to describe the behavior of collagen is derived from models used in rubber elasticity. In particular, the 3D network model first described by Arruda and Boyce (1993) was used to describe the collagen in the parenchyma, and a 2D version of this model, proposed by Prevost, was used to represent the capsule (2006).

The ground substance of the ECM, and the cellular content of soft tissues, resist compressive forces, and maintain tissue structure. Under a compressive force, these molecules rearrange to produce a time-dependent viscoelastic response. Therefore, a model with a spring (to provide a back-stress) in parallel with a viscous component (to account for the time-dependant viscous shear relaxation) was used.

Lastly, the extracellular fluid in the liver (blood, bile, lymph, etc.) was accounted for by treating the liver like a fluid-filled elastic sponge. Using biphasic mixture theory, the fluid component responds to local changes in volume by creating a dynamic pressure term allowing for fluid flow within a porous elastic network. This flow in turn provides resistance to changes in volume with load over time. The solid component was

represented by an elastic spring whose bulk modulus contributes to changes in volume by resisting the flow from the fluid. This component works with the other elastic components described above to establish the equilibrium state of the tissue.

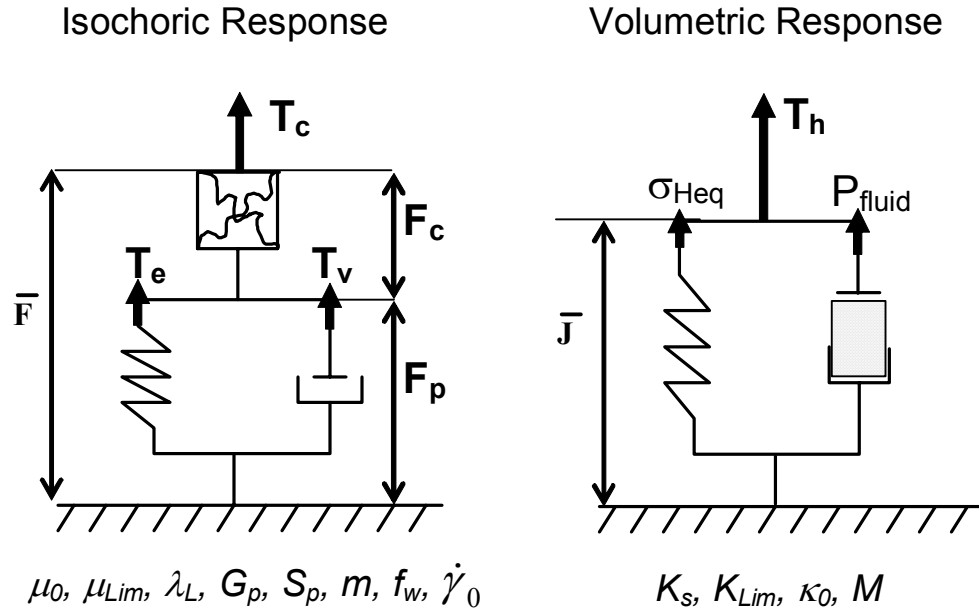


Figure 4.1 Rheological representation of constitutive model separated into the isochoric (deviatoric) response and volumetric (hydrostatic) response. Material parameters for the model elements are listed below the respective figure.

4.2 Constitutive Framework

The constitutive relation chosen to describe the liver is separated into its isochoric and volumetric components and can be represented by the rheological model in Figure 4.1. The total stress response of the tissue (\mathbf{T}_{tissue}) under an imposed deformation (\mathbf{F}) can be obtained by summing the deviatoric (\mathbf{T}_{iso}) and hydrostatic (\mathbf{T}_h) stresses that arise from the isochoric and volumetric component responses respectively

$$\mathbf{T}_{tissue} = \mathbf{T}_{iso} + \mathbf{T}_h. \quad (4.1)$$

As can be seen in Figure 4.1, the total deformation gradient tensor \mathbf{F} is decomposed into its isochoric component $\bar{\mathbf{F}}$ and its volumetric component $J^{1/3} \underline{\mathbf{I}}$ (where $\underline{\mathbf{I}}$ is the identity tensor) and can be defined as:

$$\mathbf{F} = J^{1/3} \underline{\mathbf{I}} \bar{\mathbf{F}} \quad (4.2)$$

where J is the scalar volumetric Jacobian defined as the current volume (V) divided by the initial volume (V_0), and satisfies the condition: $\det(\bar{\mathbf{F}}) = 1$.

4.2.1 Isochoric Network

Consider a multiplicative decomposition for the isochoric deformation where

$$\bar{\mathbf{F}} = \mathbf{F}_c \mathbf{F}_p. \quad (4.3)$$

The collagen responds to the \mathbf{F}_c component of the deformation gradient, while the \mathbf{F}_p component is accommodated by the parenchyma through a dissipative constitutive response. A representation of the finite strain kinematics of this network is shown in Figure 4.2. \mathbf{F}_p can be further decomposed into a left stretch tensor (\mathbf{V}_p) and a rotation tensor (\mathbf{R}_p) so that

$$\mathbf{F}_p = \mathbf{V}_p \mathbf{R}_p \quad (4.4)$$

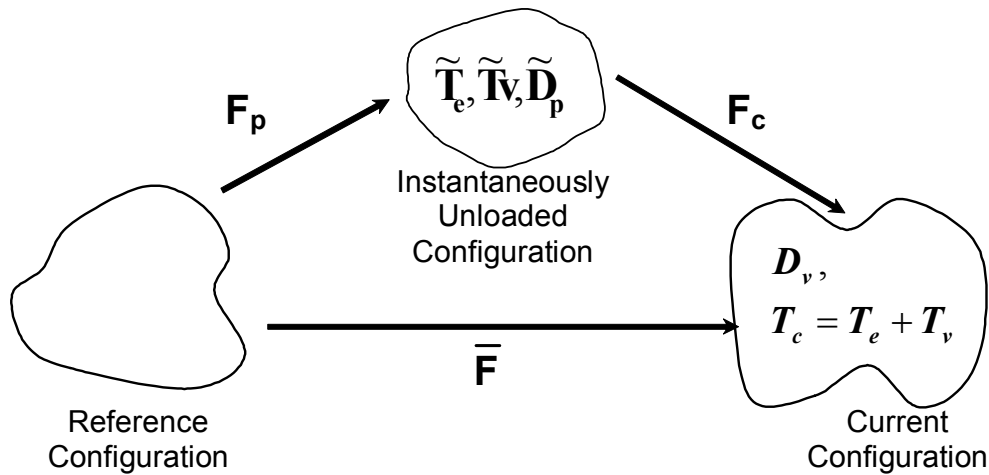


Figure 4.2 Finite strain kinematics for collagen network.

4.2.1.1 3D Hyperelastic Collagenous Component

The formulation of the hyperelastic collagen component of the constitutive relation relies on the 8-chain network model proposed by Boyce and Arruda (2000). This formulation uses a statistical model to represent the entropic state of the individual polymer chains in a network. A complete derivation of the model, as well as comparisons to other such models, can be found in (Arruda and Boyce 1993; Boyce and Arruda 2000). Although the Arruda-Boyce model is derived from an entropic understanding, it has also been successfully used to represent the nonlinear response of biological networks where the elastic response is controlled by the internal energy (Bischoff, et al. 1999). The force-stretch relationship can be defined for the individual fibrils of the collagen network by:

$$f_{fibril} = \frac{K_i}{b} L^{-1} \left(\frac{\lambda_f}{\lambda_L} \right) \quad (4.5)$$

where K_i is a reference stiffness, b is the persistence length for the fibril, λ_f and λ_L are the current stretch and locking stretch of the collagen fibril, respectively. L^{-1} is the inverse Langevin function defined by (Kuhn and Gruhn 1942):

$$\beta = L^{-1} \left(\frac{\lambda_f}{\lambda_L} \right), \text{ where} \quad (4.6)$$

$$L(\beta) = \coth \beta - \frac{1}{\beta}. \quad (4.7)$$

A simple representative cubic unit structure defines the geometry of the 8-chain network such that the response of a single chain (fibril) can be linked to the global deformation of the network due to symmetry (Figure 4.3).

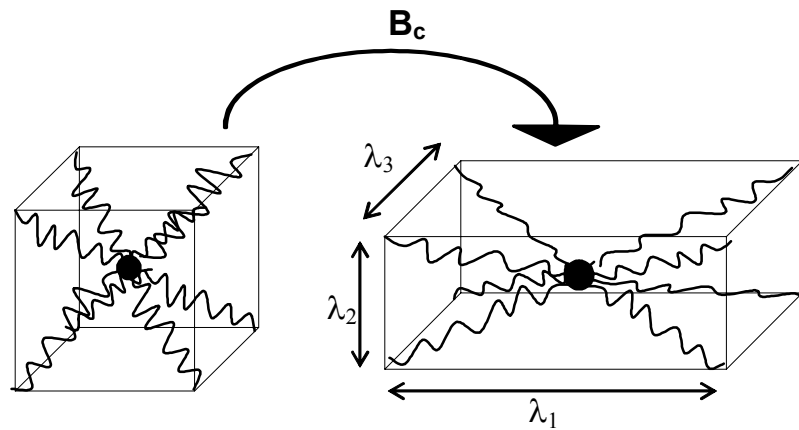


Figure 4.3 The 8-fibril collagen network unit cell and principal stretches under deformation.

The unit cell deforms with the principal stretches, while the junction point remains centered, allowing the stretch in each fibril to be shared equally amongst all of the others via

$$\lambda_f = \sqrt{\frac{\lambda_1^2 + \lambda_2^2 + \lambda_3^2}{3}}. \quad (4.8)$$

In addition to experiencing the same stretch, each fibril also rotates towards the direction of highest stretch.

The Cauchy stress exerted by the collagen network is obtained in terms stretching a collagen fibril by the left Cauchy-Green stretch tensor (\mathbf{B}_c)

$$\mathbf{B}_c = \mathbf{F}_c \mathbf{F}_c^T \quad (4.9)$$

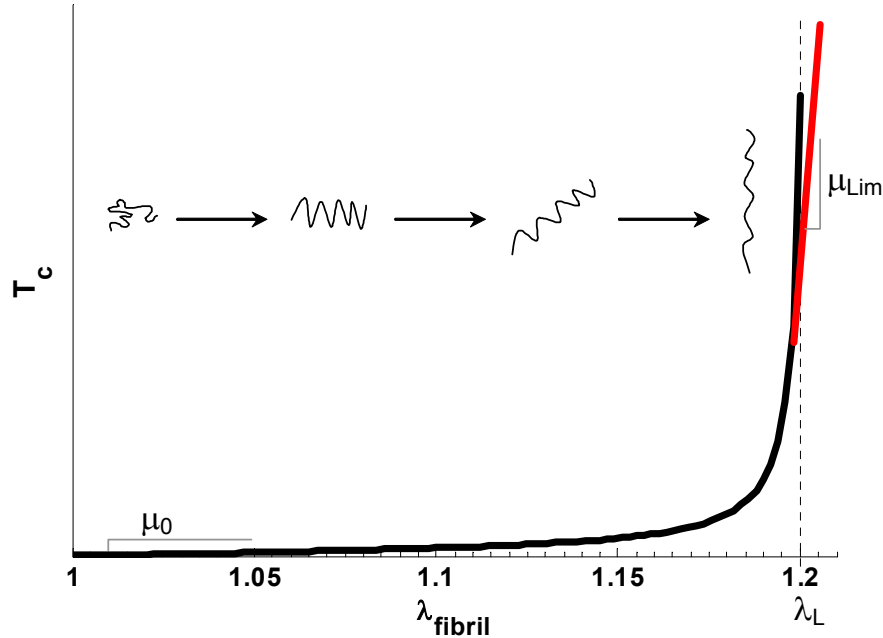


Figure 4.4 A representative stress-stretch response of the collagen network highlighting a response of a single fibril, the initial and limiting shear moduli, and the locking stretch.

through the following constitutive law

$$\mathbf{T}_c = \frac{I}{J} \left(\mu_0 \left(\frac{\lambda_L}{\lambda_f} \right) \beta (\mathbf{B}_c - \lambda_f^2 \mathbf{I}) \right) \quad (4.10)$$

where the initial shear modulus (μ_0) and the fibril locking stretch (λ_L) are the material parameters. The stress-stretch response for this relation, and a depiction of the fiber orientation is shown in Figure 4.4. Since tissues cannot experience infinite stress, and are capable of stretches beyond the locking stretch, the slope of the stress-stretch response near the locking stretch ($0.995 \lambda_L$) is used to define a limiting shear modulus (μ_{Lim}).

The collagen stress is considered to be purely deviatoric ($\text{tr } \mathbf{T}_c = 0$): the collagen is not allowed to account for any of the volume changes seen in the overall tissue response. This “split” approach was taken due to the observation that the majority of the volume change in liver is due to the movement of the extracellular fluid, rather than taken up by the stretch of the collagen (Figure 4.5). An initial trial allowing the collagen to account for changes in volume proved problematic as the volumetric too dominant. The split approach also has the advantage of easier parameter identification through simplified initial calculations.

4.2.1.2 Viscoelastic Parenchyma Component

A portion of the deviatoric Cauchy stress (\mathbf{T}_c) derived above is balanced by the elastic back stress (\mathbf{T}_e) carried by the non-dissipative component of the parenchyma

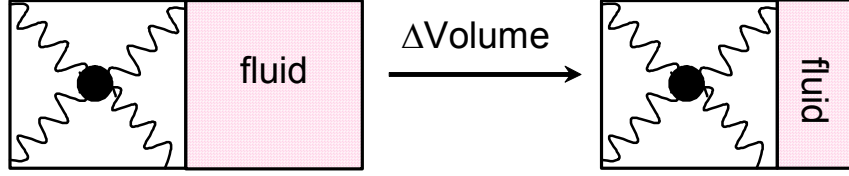


Figure 4.5 Representation of the assumption that the fluid component of the model takes up the majority of the change in volume.

network. The remainder of the stress (\mathbf{T}_v) drives the evolution of the viscous component of the deformations gradient,

$$\mathbf{T}_c = \mathbf{T}_e + \mathbf{T}_v. \quad (4.11)$$

The back stress element is modeled through a linear elastic constant shear modulus (G_p) so that the associated Cauchy stress is

$$\tilde{\mathbf{T}}_e = \frac{I}{J} \left(2G_p \left[\mathbf{E}_p - \frac{\text{tr} \mathbf{E}_p}{3} \mathbf{I} \right] \right). \quad (4.12)$$

Here \mathbf{E}_p is the Hencky strain associated with the viscous stretch (V_p): $\mathbf{E}_p = \ln V_p$. Since the definition of a isochoric response requires that the $\det(\bar{\mathbf{F}}) = \det(\mathbf{F}_c) = \det(\mathbf{F}_p) = 1$, and that the $\det(\mathbf{R}_p) = \det(V_p) = 1$, the $\text{tr}(\mathbf{E}_p) = 0$ and the elastic back stress is reduced to

$$\tilde{\mathbf{T}}_e = \frac{I}{J} 2G_p \mathbf{E}_p. \quad (4.13)$$

This response is again purely deviatoric, thus $\text{tr}(\tilde{\mathbf{T}}_e) = 0$. $\tilde{\mathbf{T}}_e$ is defined in the instantaneously-unloaded configuration. To properly prescribe the evolution of the viscous deformation, the back stress needs to be pushed forward to the current configuration by,

$$\mathbf{T}_e = \frac{1}{J} \mathbf{F}_c \tilde{\mathbf{T}}_e \mathbf{F}_c^T. \quad (4.14)$$

The deviatoric driving stress for the viscous deformation ($\tilde{\mathbf{T}}_v$) is obtained from

$$\mathbf{T}_v = \mathbf{T}_c - \mathbf{T}_e \quad (4.15)$$

The magnitude (τ) and direction (\mathbf{N}) of the deviator of the viscous stress are defined as:

$$\mathbf{N} = \frac{\mathbf{T}'_v}{\|\mathbf{T}'_v\|} = \frac{\mathbf{T}'_v}{\sqrt{2\tau}}, \quad \text{where} \quad (4.16)$$

$$\mathbf{T}'_v = \mathbf{T}_v - \frac{1}{3} \text{tr} \mathbf{T}_v \mathbf{1} \quad (4.17)$$

The viscous stretching tensor (\mathbf{D}_p) is constitutively prescribed to be parallel to the deviator of the viscous stress (\mathbf{T}'_v) through

$$\mathbf{D}_p = \dot{\gamma}^v \mathbf{N} \quad (4.18)$$

where the viscous shear strain-rate $\dot{\gamma}^v$ depends on a power law relationship through the magnitude of the driving stress (τ) and on material parameters S_p (shear strength modulus) and m ,

$$\dot{\gamma}^v = \dot{\gamma}_0^v \left(\frac{\tau}{S_p} \right)^m. \quad (4.19)$$

For $m = 1$, this relationship reduces to a linear viscous response. For $m > 1$ this relationship can be used to account for the effect of thermally activated processes.

The rate of change of the viscous component of the deformation ($\dot{\mathbf{F}}_p$) can be expressed as

$$\dot{\mathbf{F}}_p = \tilde{\mathbf{L}}_p \mathbf{F}_p \quad (4.20)$$

where $\tilde{\mathbf{L}}_p$ is the viscous velocity gradient in the instantaneously-unloaded configuration and can be expressed as the sum of the stretching tensor ($\tilde{\mathbf{D}}_p$) and spin tensor ($\tilde{\mathbf{W}}_p$),

$$\tilde{\mathbf{L}}_p = \tilde{\mathbf{D}}_p + \tilde{\mathbf{W}}_p. \quad (4.21)$$

The stretching tensor in the instantaneously-unloaded configuration is obtained by pulling back the viscous stretching tensor via

$$\tilde{\mathbf{D}}_p = \mathbf{F}_c^{-1} \mathbf{D}_p \mathbf{F}_c. \quad (4.22)$$

The arbitrary rotation associated with the definition of the instantaneously-unloaded configuration is eliminated by setting $\tilde{\mathbf{W}}_p = 0$.

The stress from the isochoric network (\mathbf{T}_{iso}) is therefore defined as the stress in the collagen network (\mathbf{T}_c), which is equal to the sum of the stresses from the elastic (\mathbf{T}_e) and viscous (\mathbf{T}_v) components of the parenchyma network (\mathbf{T}_p)

$$\mathbf{T}_{iso} = \mathbf{T}_c = \mathbf{T}_p = \mathbf{T}_e + \mathbf{T}_v. \quad (4.23)$$

4.2.2 Volumetric Network

There are two components to the liver response due to local changes in volume. One component considers an equilibrium response arising from the combined effect of osmotic pressure, volumetric elastic response of the solid matrix, perfusion pressure, and resistance to extracellular flow. The other component arises from the establishment of the non-equilibrium pressure gradient that drives the fluid flow through the tissue.

4.2.2.1 Equilibrium Response

A simplistic model of the liver is considered in which an initial volume fraction (f_w) can be associated with the amount of free fluid in the system. The remaining volume ($1-f_w$), represents the solid phase and its associated (bound) hydrated fluid tissue component. As long as the volumetric strain ($J-1$) is greater than f_w , an effective volumetric Jacobian (J^*) can be defined as

$$J^* = \frac{f_w - (J-1)}{f_w}. \quad (4.24)$$

The volumetric equilibrium stress response (Figure 4.6) is then simply expressed as

$$\sigma_{Heq} = K_s \ln(J^*) \quad (4.25)$$

where K_s is a constitutive parameter that relates to the small strain bulk modulus (K_0) through

$$K_s = K_0 f_w \quad (4.26)$$

As the volumetric strain approaches the limit of f_w , this formulation asymptotes to an infinite stress state. Under this condition it is important to recognize that the solid component (f_s) is not incompressible, and can be associated with a limiting bulk modulus K_{Lim} . The relationship between the hydrostatic equilibrium stress and the volumetric strain has therefore been formulated to have an asymptotic linear slope equal to K_{Lim} .

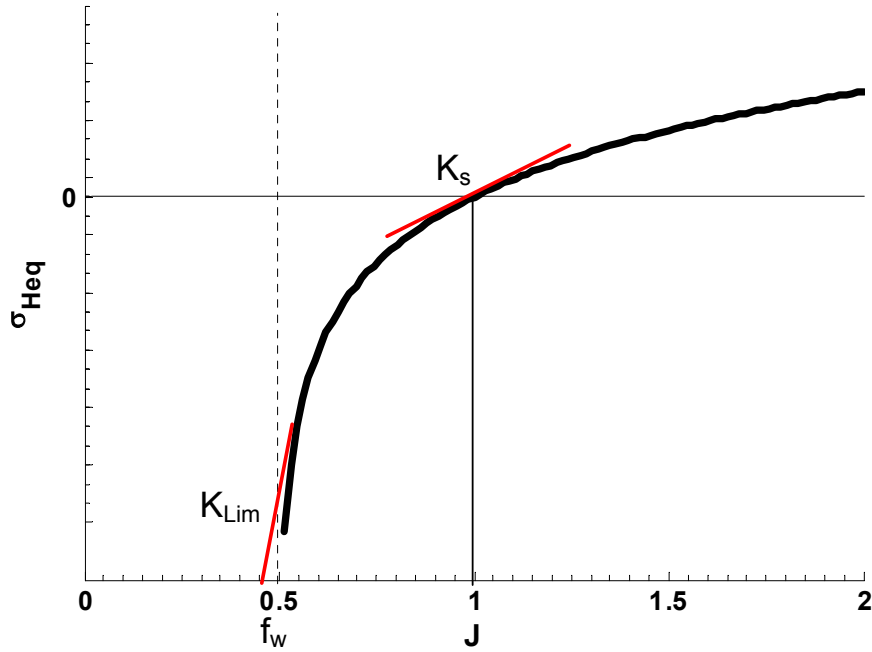


Figure 4.6 Representation of hydrostatic equilibrium stress versus the volume highlighting the equilibrium (K_s) and limiting (K_{Lim}) bulk moduli and the amount of free water (f_w).

4.2.2.2 Transient Response

Finally, the volumetric transient response is based on fluid flow through a porous medium as governed by a simple linear Darcy's Law,

$$q = -\kappa \nabla P_{fluid} \quad (4.27)$$

where q is the macroscopic volume flow rate, κ is Darcy's hydraulic permeability representing the resistance to flow under zero strain, and P_{fluid} is the dynamic fluid pressure. To account for variations in permeability with deformation, the permeability is considered to be a function of volumetric strain ($\varepsilon_V = J - 1$) through the relationship given by (Ateshian, et al. 1997)

$$\kappa = \kappa_0 \left[\frac{\phi_0 \phi_f}{(1 - \phi_0) \phi_s} \right]^2 e^{\frac{M \varepsilon_V}{2}}. \quad (4.28)$$

Here ϕ_s and ϕ_f are the respective solid and fluid contents of the tissue (where $\phi_s + \phi_f = 1$), κ_0 and ϕ_0 are the permeability and solid content of the tissue in the absence of volumetric strain, respectively, and M is the nonlinear permeability coefficient. κ_0 and M are material parameters for finite deformations.

The time dependent fluid-pressure in the tissue can be obtained by solving the following equation at each material point over the liver domain

$$\left[\frac{I}{K_{Lim}} \right] \dot{P}_{fluid} = \kappa \nabla^2 P_{fluid} - \frac{\dot{J}}{J}. \quad (4.29)$$

The volumetric stress response (\mathbf{T}_h) is therefore represented as the sum of the contributions from the hydrostatic equilibrium response (σ_{Heq}) and the transient fluid pressure response (P_{fluid}),

$$\mathbf{T}_h = \sigma_{Heq} \mathbf{I} - P_{fluid} \mathbf{I}. \quad (4.30)$$

4.2.3 Hyperelastic 2D Collagenous Capsule

The liver capsule was modeled as a 2D representation of the 3D hyperelastic collagen network. This work relies on the previous modeling work of Prevost, who modeled the human chorioamnion as an “idealized” continuum membrane whose in-plane response is dominated by the collagen fiber network (Prevost 2006). A four-fibril network is used as the unit cell, and in this case the collagen network is allowed to respond to changes in area. Hence in addition to the locking stretch λ_{LCap} , initial (μ_{0Cap}) and limiting shear moduli (μ_{LimCap}), and area expansion modulus (K_{Cap}) is also required as a material parameter. The Cauchy membrane stress is given by,

$$\mathbf{T}_{Cap} = \frac{\mu_{0Cap} \lambda_{LCap}}{J} \left[\frac{\beta}{\lambda_{LCap}} \mathbf{B}_{cap} - \beta_0 \mathbf{I}_{2D} \right] + K_{Cap} (J - I) \mathbf{I}_{2D} \quad (4.31)$$

where \mathbf{B}_{cap} is the 2D left Cauchy-Green stretch tensor, and β_0 is the inverse Langevin function of ($1/\lambda_{LCap}$). For the capsule, the limiting shear modulus was defined by its critical stretch (λ_{linear}). This stretch is the point beyond which the network starts responding with a linear force-stretch relationship

4.3 Physical Interpretation of Framework in Relation to Observed Experimental Response

The constitutive framework for the response of liver tissue outlined in sections 4.6.1 and 4.6.2 resulted in a model for the liver where the total stress response from an imposed deformation is a sum of the contributions from the isochoric and volumetric responses

$$\mathbf{T}_{tissue} = \mathbf{T}_c + \sigma_{Heq} \mathbf{I} - P_{fluid} \mathbf{I}. \quad (4.32)$$

To understand the physical meaning that correlates the biologically relevant material parameters to the proposed constitutive framework, the model’s response to a step deformation is considered. The instantaneous ($t = 0^+$), long term ($t \rightarrow \infty$), and transient ($0 < t < \infty$) responses for different modes of deformation (change in volume, pure shear, and indentation) are discussed.

An instantaneous change in volume gives rise to very large hydrostatic stresses because K_{Lim} dominates the instantaneous bulk modulus. Since most biological tissues

have a high water content ($\sim 70\%$), the modulus is expected to be similar to those of incompressible materials, having the same order of magnitude as that of water (2.2 GPa).

Instantaneous changes in shape (shear or isochoric deformations) are accounted for by an immediate shear response controlled by the hyperelastic collagen network. The collagen network provides the nonlinear “stiffening” character of the tissue response (Figure 4.4). At low levels of stretch, the curve has an initially flat response described by a low initial shear modulus (μ_0). The response then sharply increases with stretch as the limiting stretched is approached before becoming linear again with a modulus much larger than the initial shear modulus (μ_{Lim}). For a nonhomogenous mode of deformation, like indentation, the material should behave in a nearly incompressible manner since K_{Lim} is much greater than the hyperelastic shear moduli (μ_0, μ_{Lim}).

The dissipative mechanisms are recruited when a constant level of deformation is held over time. These elements are responsible for a portion of the imposed deformation. At long times ($t \rightarrow \infty$), the material reaches an equilibrium steady-state in which the response to changes in volume is controlled solely by the equilibrium bulk modulus (K_s). The response to change in shape is accommodated by both the hyperelastic collagen network and the reconfiguration of the viscoelastic parenchymal structure. This is portrayed through a series combination of the collagen moduli and a lower shear parenchyma modulus (G_p).

The transient response of the material is accounted for by the material properties of the dissipative components of the model. The characteristic time for changes in volume is controlled by the permeability (κ) and the length-scale associated with the diffusion paths. For a linear poroelastic model of a tissue specimen of height l in confined compression, this time can be defined by,

$$\tau_{vol} = \frac{l^2}{H\kappa}, \quad (4.33)$$

where H is the confined compression modulus. In the case where the elastic response of the material is nonlinear, κ is an exponential function of volume, and the diffusion paths are 3D (recall the complicated structure of the liver vasculature and its hexagonal lobule comprised of longitudinal portal veins, hepatic arteries, bile ducts, and central veins and densely packed transversely oriented fenestrated sinusoids). Therefore, the relationship of the volumetric time constant (τ_{vol}) presented in Equation 4.33 is an over simplification. However, it does provide the correct dimensional framework to begin to interpret the experimental data. Note that the size dependency of this model feature cannot be replaced by a simple viscoelastic formulation since no length-dependant behavior of the tissue response is possible with viscoelastic models.

Lastly, the material’s transient isochoric response is described by the nonlinear viscous element shown in Equation 4.19. This relationship is graphically depicted in Figure 4.7. A linear response is obtained for $m=1$. As the value of m is increased, the strain-rate dependence diminishes, and the material is allowed to flow easily at high rates when the driving stress (τ) exceeds the material strength (S_p). These strain-rate independent behaviors are more indicative of biological materials, where it has been shown that hysteresis is constant over a wide variety of strain-rates (Fung 1993), and where the tissue is filled with blood, a non-Newtonian fluid.

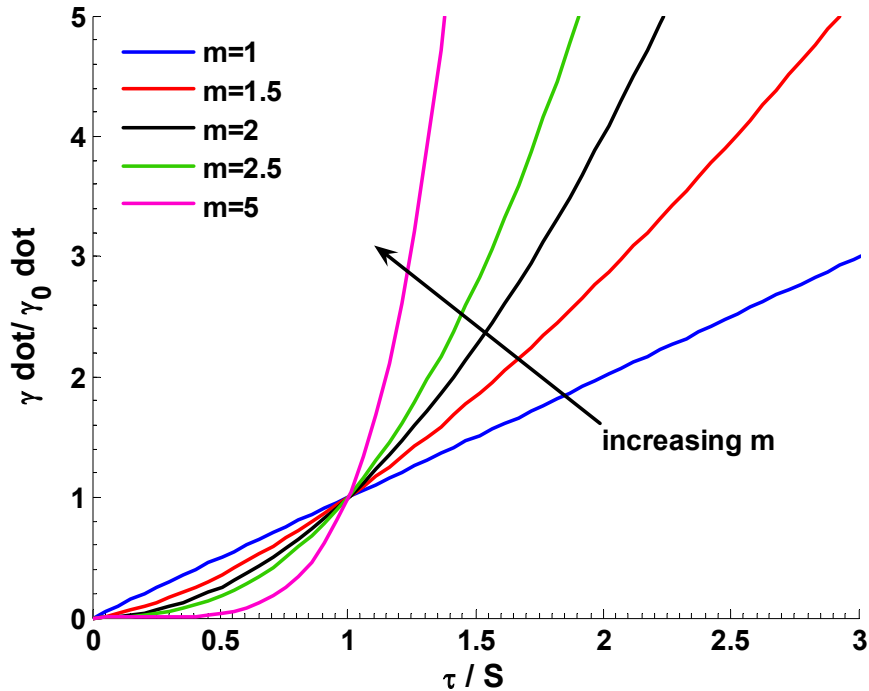


Figure 4.7 The effects of changing m on the stress response of the parenchyma viscous network.

4.3.1 Material Parameter Estimation

The preceding sections sought to define an appropriate constitutive model and its physiologically based parameters to appropriately depict the mechanical response of liver to finite deformations. Before implementing an iterative numerical approximation scheme to realize the values of these parameters, an ad hoc approach to determine reasonable start values for the parameters is presented based on the literature, and features from the experimental data.

- K_{Lim} is set to 0.22 GPa based on the high strain-rate dynamic testing reported by Saraf et al. (Saraf, et al. 2005)
- μ_0 is bounded based on the initial slopes of the ramp indentation tests (1-100 Pa)
- μ_{Lim} is set based on the initial slope of the unloading curves during ramp indentation testing. The rapid change in direction of the displacement is mainly accounted for by the unloading of the hyperelastic network. This value was set to 1.5 MPa based on experimental indentation data.
- λ_L is bounded based on the curvature of the ramp indentation data. Observing where the response turned nonlinear approximated the locking stretch asymptote (1.01-1.2). The force-displacement response of the model is extremely sensitive to this parameter as it drives the nonlinear loading response, effects the peak force, and dominates the initial unloading response (where μ_{Lim} is set).

- f_w is determined given the typical mass of the liver (1.1-1.7 kg) and the amount and densities of free fluid (namely blood, bile, and lymph) stored within the organ at any time. Given values from the literature, the fraction of free fluid in the liver was determined to be 50-70% of it's mass, and f_w was set to 0.5 (Gray 1977).
- G_p was found to be rather insensitive to ramp indentation tests. Instead the stress relaxation data was used. Knowing that $K_{Lim} \gg \mu_{Lim} \gg G_p$, this elastic shear modulus was determined such that an appropriate steady-state stress relaxation response was achieved (10-25,000 Pa).
- K_s was determined based on the peak force of indentation ramp tests, the stress relaxation steady-state response and curvature, and an independent test conducted where the mass of the liver was measured over time after a step increase in perfusion pressure. Prior to indentation testing, a harvested liver from an 81 kg pig was allowed to perfuse for 45 minutes in the *ex vivo* perfusion system following the protocol in Chapter 3. The liver was placed on a digital scale and the IVC was cannulated so that the liver could drain elsewhere. The hepatic arterial perfusion was clamped (to ease the control of the outflow) and the portal venous pressure was quickly raised 76 mm inducing a step change in pressure (dP) of 0.75 kPa. The mass of the liver was recorded over time and converted to volume (dV) (Figure 4.8). This procedure was repeated twice. The results were fit to a decaying exponential whose constants (V_{eq} and τ_{perf}) were determined by minimizing the mean square error and the derivative of the response to the model,

$$dV = V_{eq} \left(1 - e^{-\frac{t}{\tau_{perf}}} \right). \quad (4.34)$$

V_{eq} was found to be 3.614×10^{-5} and $5.123 \times 10^{-5} \text{ m}^3$ for the two tests with τ_{perf} 's of 32.1 and 44.54 seconds respectively. K_s was then estimated using

$$K_s = \frac{dP}{dV} V_0, \quad (4.35)$$

where V_0 was the initial volume of the liver prior to the step change in pressure. The results suggest an equilibrium bulk modulus of 37-59 kPa. Since the other elastic moduli in the model are also likely resisting the change in volume, and recalling that K_s is related to the amount of free water in the organ, K_s was bounded to be between 1 and 50 kPa.

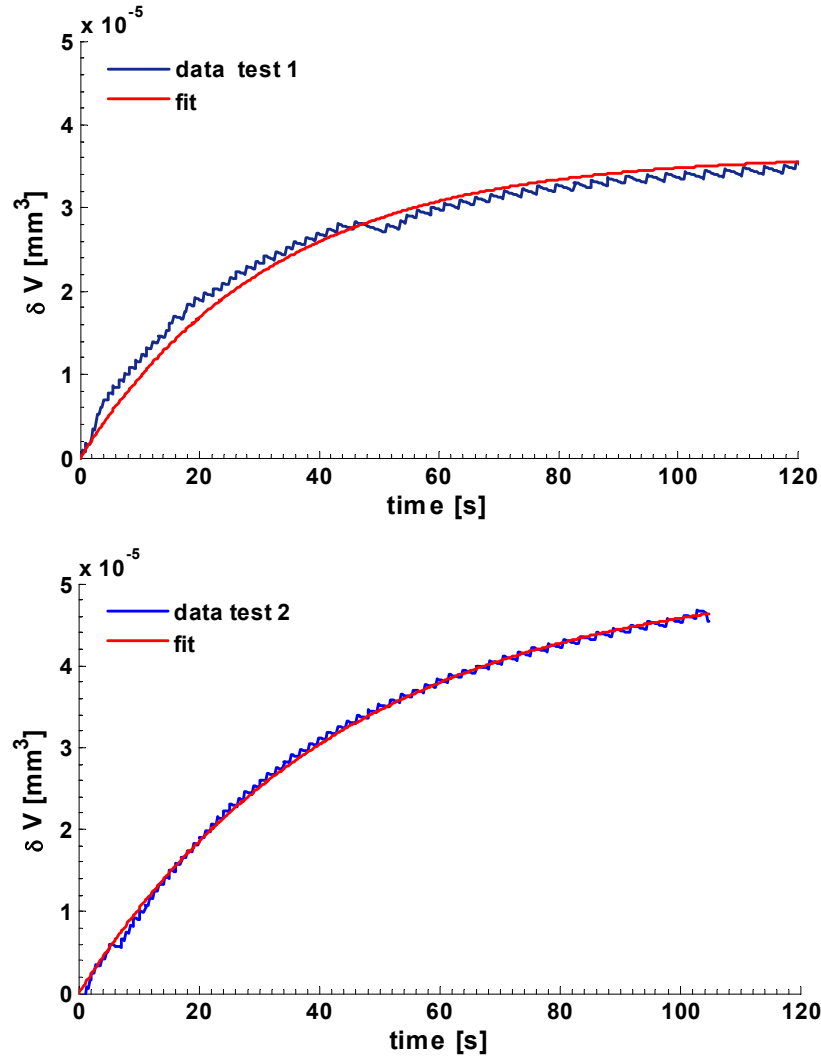


Figure 4.8 Change in volume over time data from filling test to determine start values for κ_0 .

- κ_0 was also estimated from the results of the swell test. Solving Equation 4.31 for κ_0 ,

$$\kappa_0 = \frac{l^2}{K_s \tau_{perf}}, \quad (4.36)$$

- using K_s as the moduli, assuming a length-scale equal to $\frac{1}{2}$ the length of one of the liver lobules (~ 0.1 m), and using the results of the fit for τ_{perf} , initial estimates for κ were found to be between 5.8×10^{-9} and 6×10^{-9} m⁴/Ns. Looking at the response of the model to changes in κ (namely peak force and amount of hysteresis in the ramp indentation tests) suggests that κ can range between 1×10^{-6} and 10×10^{-9} m⁴/Ns.
- M was determined from the results of the uniaxial confined compression tests done on cartilage by Ateshian et al (1997). They showed that M ranges from 0.4 to 4.3, and that κ changes by 10% when M changes by $> 100\%$. Given the nonhomogenous

indentation tests, and this insensitivity of M on the response, M was set to 4 assuming that liver would fall on the higher end of values for cartilage.

- $\dot{\gamma}_0^v$ was set to 0.01. Since the parameter for the viscoelastic parenchyma network can be represented by $\frac{\dot{\gamma}_0^v}{S_p^m}$, the initial shear rate was set so that flow would occur at 1% strain/second when the driving stress was equal to the shear strength (S_p).
- S_p and m affect the strength of the viscous response from the parenchyma network. This network is assumed to be responsible for the slower time constant of the response. Therefore, the stress relaxation data was used to determine these material parameters. S_p affected both the steady-state stress level as well as the curvature of the response, whereas m drastically affected the curvature of the response. Higher m 's resulted in a steeper initial stress relaxation. The value of m was set for each liver using the stress relaxation tests, and checked in the multiple rate ramp indentation tests to ensure that hysteresis remained consistent with rate. Since the response was more sensitive to m than S_p , the range of m was set from 1.1-10, and S_p was more loosely bounded to be between 0.1-100 kPa.

In summary, the 12-parameter physically-based constitutive model presented in this section can be reduced to five dependent material parameters (K_{Lim} , μ_{Lim} , $\dot{\gamma}_0^v$, f_w , M), and seven independent material parameters (μ_0 , λ_L , K_s , G_p , S_p , m , κ_0). The identification of these seven material parameters is done through iterative inverse finite modeling and is discussed below.

4.4 Parameter Identification via Iterative Inverse FEM

4.4.1 Numerical Approximation of Constitutive Model

Although indentation testing lends itself well for obtaining the mechanical response of whole perfused livers to known forces and/or displacements, the interpretation of the results is complicated, particularly under finite deformation. In addition, the constitutive relationship defined in the preceding section (Equation 4.32 from Equations 4.10, 4.14, 4.19, 4.25, and 4.30) cannot be analytically solved in a straightforward manner. The two components of stress giving rise to the deviatoric response (\mathbf{T}_c , \mathbf{T}_p) are entirely defined by solving the initial boundary value problem by following the evolution of the deformation gradient at each material point. The volumetric component can only be obtained by solving the diffusion equation at each material point over the entire domain. The resulting nonlinear multiphysics-based problem cannot be solved without the use of numerical approximation methods such as finite element modeling.

To solve the inverse problem (identifying the material parameters from the known force-displacement response), the model was implemented using commercial finite element software (ABAQUS version 6.5, Providence, RI). The constitutive equations describing the behavior of the 2D liver capsule and 3D tissue structure were coded as user defined materials (UMAT) in a subroutine. The implicit formulation of the time integration used in the subroutine is beyond the scope of this work, but details can be found in Appendix A of Febvay (2003). The implementation of the isochoric network is

straightforward. The diffusion equation however is realized to be analogous to a heat diffusion equation,

$$\rho c_p \dot{T} = \kappa_T \nabla^2 T + r_{gen}, \quad (4.37)$$

where ρ is the density, c_p is the specific heat, T is temperature, κ_T is the thermal conductivity, and r_{gen} is the heat source term. The local equation for the time evolution of the fluid pressure is therefore treated as a coupled thermal-mechanical problem.

4.4.2 Inverse Finite Element Modeling

Solving the inverse problem requires replication of the experimental boundary conditions in the form of a finite element model (Figure 4.9). Either the force or the displacement data are used as prescribed inputs to the model. The constitutive relation and its material parameters govern the model's response to the prescribed loading condition. Initial estimates are given to the material parameters and an error estimate between the model's response and the experimental data is determined. The parameters are then updated in an iterative fashion until the model's result matches that of the data.

Given the length scale of the liver lobe ($\sim 250 \times 130$ mm) to the size of the indenter (6-12 mm diameter), the indentation tests were represented with an axisymmetric geometry assuming an infinite half-space (Figure 4.10). The width (w) and height (h) of the mesh were changed according to the actual dimensions of the liver. The tissue was modeled as a homogenous, deformable, solid with 8-node, axisymmetric, thermally-coupled, quadrilateral, biquadratic, bilinear, temperature elements (CAX8T). The mesh was biased to have increased density in the area under the indenter, but kept as coarse as possible to increase computation time. Comparing the results from meshes with

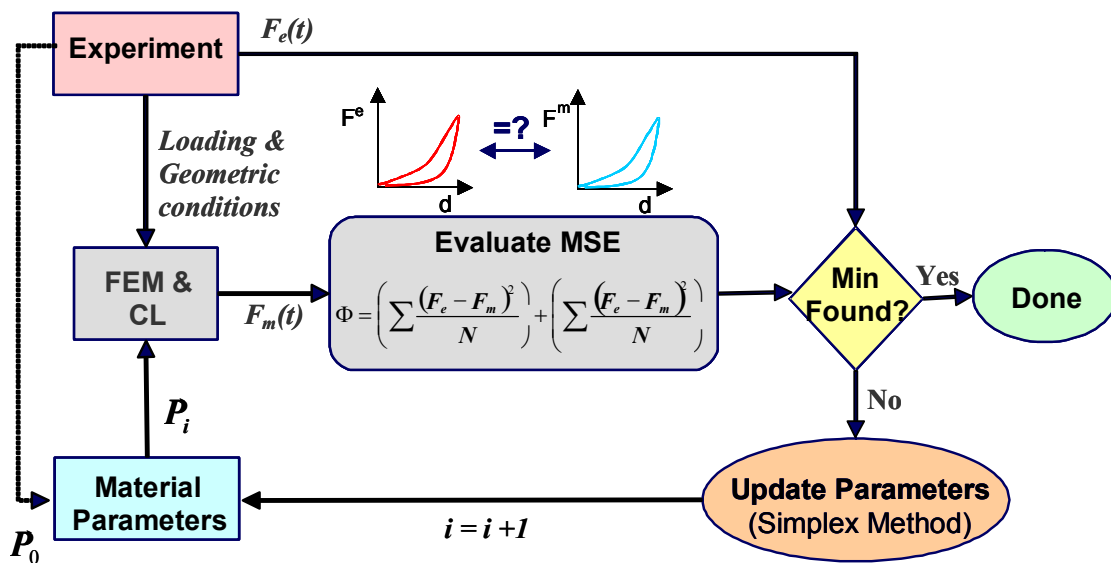


Figure 4.9 A schematic of the iterative algorithm used to solve the inverse problem with a finite element model (FEM).

10x finer resolution showed no noticeable change in reaction force. The total number of elements ranged from 147 to 160 depending on the size of the specimen, but each had a 6 mm x 12 mm area directly under the indenter with 47 elements.

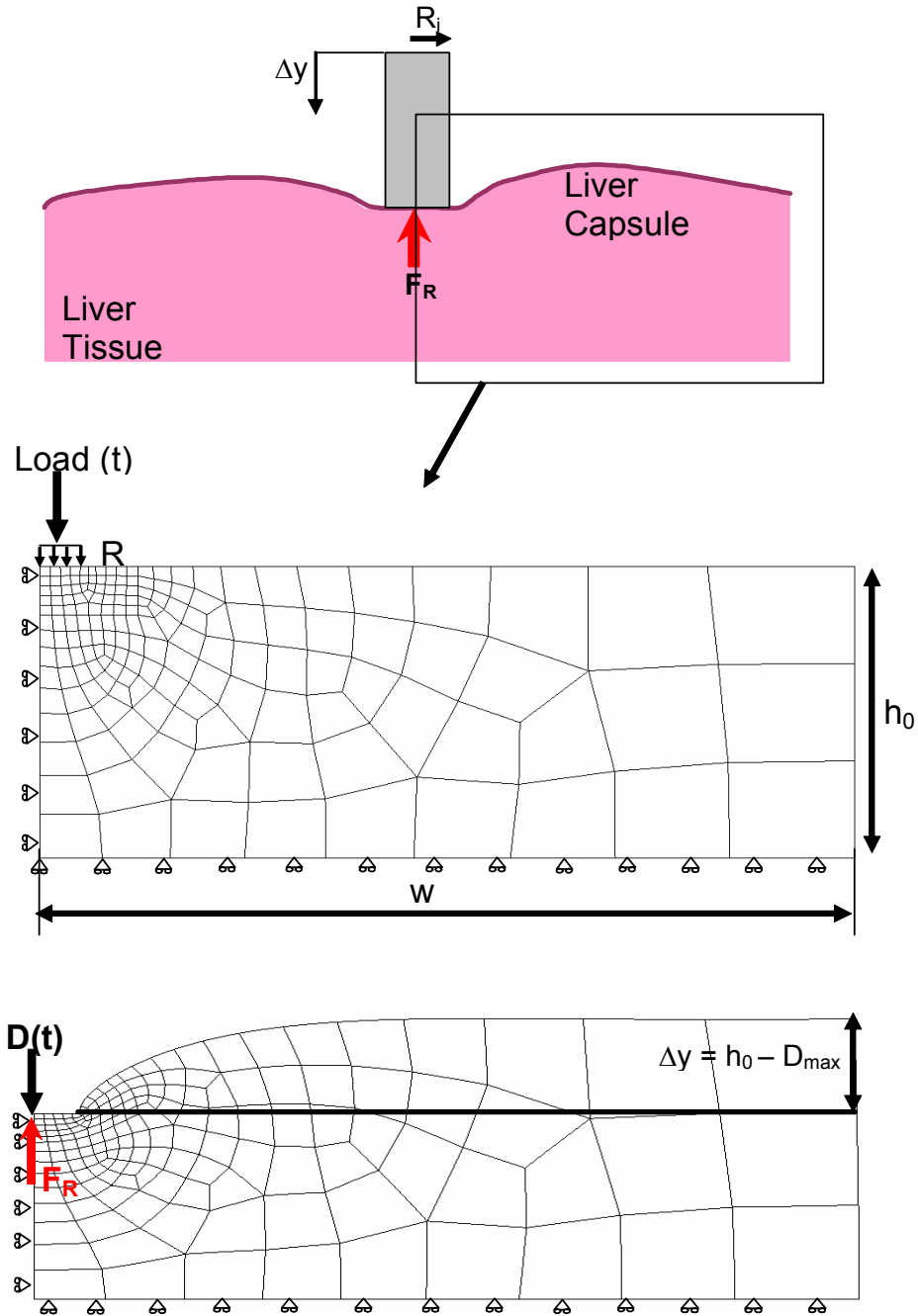


Figure 4.10 (Top) A schematic representation of the indentation experimental conditions. Middle) The axisymmetric meshed geometry and boundary conditions used in ABAQUS to represent the experimental conditions. (Bottom) An example of a deformed mesh showing the reaction force on the indented area.

The capsule was modeled as a 100 μm thick homogenous shell using the skin feature in ABAQUS. The mesh was matched in number to the tissue below, with 3-noded quadratic axisymmetric thin-shelled elements (SAX2). An independent model was created to solve for the capsule parameters using the uniaxial tension experiments. The user defined material for capsule required that an axisymmetric condition be modeled. Therefore a tube in uniaxial loading approximated a thin sheet in confined uniaxial tension, and a correction factor for the force was used to relate their areas

$$F_{cap} = \frac{F_{model}}{0.99\pi} \quad (4.38)$$

Twenty, 2-node, linear, axisymmetric, thin-shelled, elements (SAX1) 100 μm thick were used to model the capsule. The bottom of the capsule model was held fixed, the top was constricted to vertical motions, and the displacement history from the data was used for the loading condition.

Since the motorized indentation tests used a suction indenter, the complete liver model was deformed by directly displacing the nodes equal to the radius of the indenter. The reaction force was taken from a master node constrained to the load nodes. A 12 mm diameter discrete, analytical, rigid, indenter with a fillet radius of 0.4 mm, was also created and the contact problem solved by allowing a no-slip condition (tangential friction set to 0.9) under the area of the indenter, and a frictionless condition on the corners. Normal contact was defined using an augmented Lagrange “Hard” contact pressure-overclosure for the no-slip area, and an exponential pressure-overclosure for the frictionless section with pressure equal to $1\text{e}6$ Pa and a clearance of $4\text{e-}5$ m. There were minimal differences seen in the force responses from the model with direct indentation to the one using the indenter. Therefore, the direct indentation was used since it greatly decreased computation time. The 6 mm diameter indenter for the creep experiment was modeled, however, and a frictionless condition like the one described above was used.

The displacement data from the motorized indentation experiments were directly implemented into the loading conditions for the model using the AMPLITUDE feature in ABAQUS. The displacement history was applied to the master node, while the reaction force was recorded. For the creep tests, an initial displacement was imposed on the indenter to simulate the inertial loading of the dropped mass ($\sim 20\%$ nominal strain in 0.1 sec), and then a -0.3188 N load was maintained for the duration of the test. In all cases the bottom of the tissue was allowed to slip in the transverse direction. Lastly, the temperature was initially set to be 0 everywhere, and then was inactivated to resemble a pressurized tissue covered in a non-permeable membrane.

4.4.3 Optimization Technique

The seven-dimensional parameter space of the constitutive model was systematically explored and the results compared to the data using an optimization scheme. A link between Matlab (version 7 R14, Mathworks Inc, Natick, MA) and ABAQUS environments carried out an iterative adjustment of the material parameters according to the Nedler-Mead simplex method (Jordan, et al. 2005a; Lagarias, et al. 1998). The objective function (Φ) to be minimized was defined using the mean square error between

the data and the model of the force versus displacement (or time in the case of multiple indentations) curve and the time derivative of that curve

$$\Phi = \left(\sum \frac{(F_{data} - F_{model})^2}{n} \right) + \left(\sum \frac{(\dot{F}_{data} - \dot{F}_{model})^2}{n} \right) \quad (4.39)$$

The simplex was allowed to only sample the solution space within the bounds given for each parameter, and convergence was highly sensitive to the initial parameter estimation. Convergence, or termination, conditions were set to either a maximum of 1,000 iterations, or a normalized simplex diameter less than 1×10^4 . If a numerical solution was not possible, and the model “crashed”, a large error (~ 100) was returned and the iterations continued. An iterative solution for a single indentation consisting of 200 iterations required approximately 10 hours of computation time on a 3.0 GHz Pentium 4 machine with 2 GB of RAM.

4.5 Results

4.5.1 Uniaxial Capsule Tests

The optimization scheme was first tried for the 4-parameter membrane constitutive model (Equation 4.31) on the capsule uniaxial tension tests. Initial values for the material parameters (μ_{0Cap} , λ_{LCap} , λ_{linear} , K_{Cap}) were estimated by manually fitting the models response to the data. The optimization was then run for each of the 9 tests until a minimum was found (mean MSE = 0.00184 in 195-595 iterations). The results for the parameters are shown in Table 4.1, and the mean results are plotted against the data for each test in Figure 4.11.

The mean and standard deviation of the results suggest that the model was more sensitive to changes in the stretch parameters than the shear and bulk moduli. The model response is in excellent agreement with the data. The combined values for the parameters were used in the indentation testing models below.

Table 4.1 The optimized material parameters for the liver capsule from uniaxial tension testing

	λ_{linear}	λ_{LCap}	μ_{0Cap} [Pa]	K_{Cap} [MPa]	MSE
Test 1 Mean (SD)	1.023 (0.021)	1.040 (0.02)	7383.364 (2830.034)	1.040 (0.510)	0.0022 (0.002)
Test 2 Mean (SD)	1.045 (0.021)	1.061 (0.021)	7385.913 (2266.511)	0.671 (0.249)	0.00144 (0.001)
Combined Mean (SD)	1.026 (0.021)	1.043 (0.019)	7081.432 (2507.71)	0.948 (0.483)	0.00184 (0.002)

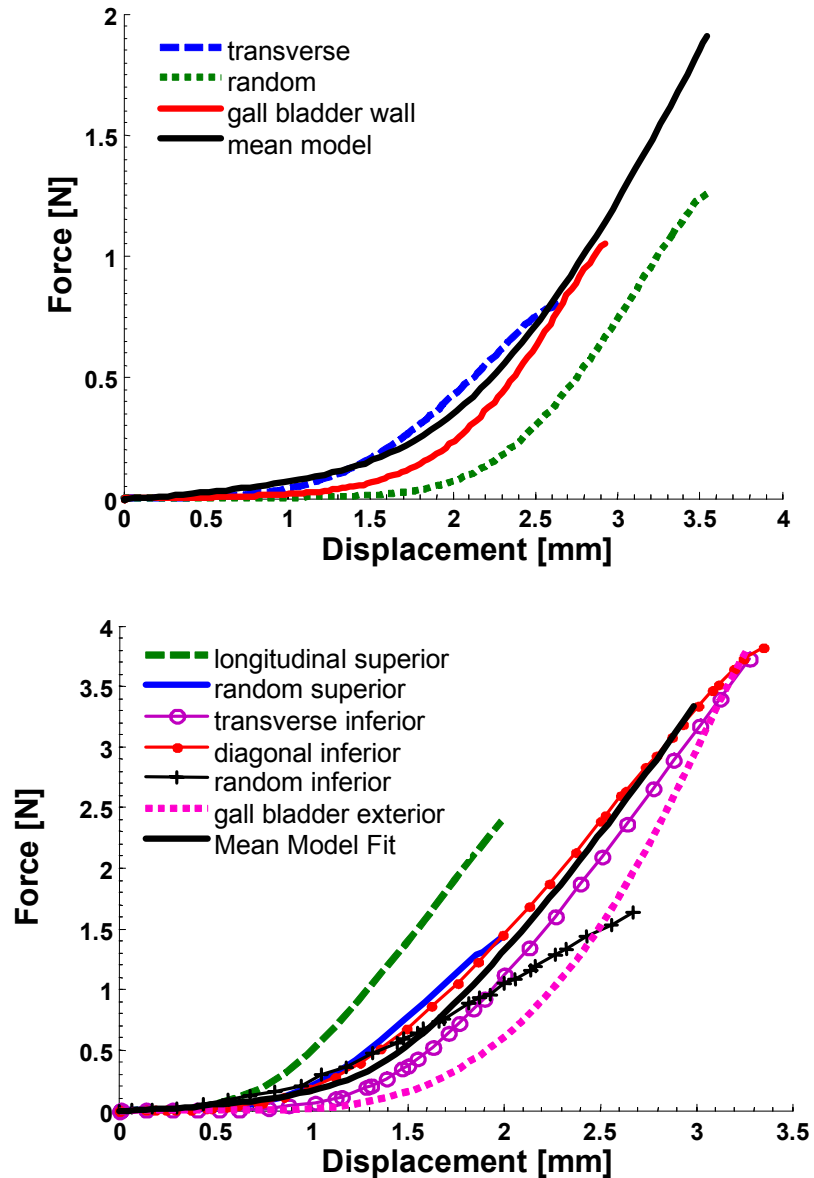


Figure 4.11 Results of uniaxial capsule model with mean parameter values and the test data.

4.5.2 Liver Ramp Indentation Optimization

Since each parameter of the constitutive relation is sensitive to the type of loading condition the tissue experiences, several deformation modalities were looked at concurrently to identify appropriate values for the parameters.

The data from the multiple ramp indentation and stress relaxation tests described in Chapter 3 were used to identify the seven parameters of the constitutive model for liver defined in section 4.3. Initially, the results of the second indentation for each speed from the first block of indentations (rate order: 2, 0.2, 20, 40 mm/s) were used to gain an

understanding of the effect each parameter had on the model's response. The results of the parameters were then used and compared to the stress relaxation data. Fitting parameters to both of these modalities in parallel provided confidence in the start values used for an optimization of a full block of multiple ramp indentation tests. It was assumed that the complete time history of 9-12 ramp indentations with a 120 second dwell time at rates spanning at least 2 orders of magnitude would capture the contribution from each parameter. However, since these models were computationally expensive to run (>20 minutes per trial), the start values obtained from looking at the stress relaxation and individual indentations at each speed was necessary.

The estimated start values and allowable ranges for the parameters outlined in section 4.3 were used to manually obtain good fits to the stress relaxation and individual indentation data at 0.2, 2, and 20 mm/s for the first liver. Start values were selected from these studies, and an optimization trial was run to identify 6 of the parameters (m was set to 2 from manual matching to the stress relaxation data). The force versus displacement response for each indentation was compared to the model's response after 448 iterations (Figure 4.12). The total error was based on the fit of all three curves to the data. The evolution of the parameters and the error are shown in Figure 4.13. The resulting parameters were run on a stress relaxation model and the results compared to the data (Figure 4.12). Due to the poor fit, an optimization trial was then run on the stress relaxation data using the final parameters obtained for the indentation test as start values. This was carried out for 337 iterations, and included m . Results for this test and the evolution of the error are shown in Figure 4.14. With better confidence in the start values and with m set to 2.5, a final optimization was run to identify the remaining 6 parameters using the entire set of 9 indentations and the 120 sec dwell period for the first block of the first liver comparing the force versus time data. These models took ~20 minutes to complete per trial. Final parameters were obtained after 64 iterations (Table 4.2). The resulting force versus time plots for the block of multiple indentations across speed for the model and the data, as well as the error evolution, are shown in Figure 4.15.

Table 4.2 Final optimized parameter values for liver 1. MSE is the mean squared error between the model response and the data force versus time curves for all 9 indentations and the 120-second dwell time. Units for moduli in Pa, κ_0 is in m^4/Ns .

K_s	G_p	m	S_p	μ_0	λ_L	κ_0	MSE
25,048	116.04	2.5	13,038	26.06	1.039	6.4	0.1675

The results show that the model is able to capture many of the salient features of the time-history data, including an increased peak force from the first indentation, increased peak force with loading rate, decreasing peak force with multiple indentations, nearly strain-rate independent hysteresis, and the 120 second dwell time.

Despite being able to capture many of the characteristics of the liver's response, the model fails to completely predict the observed behavior. There is clearly an underestimated hysteretic response, and an over exaggerated nonlinear curvature. The predicted rapid increase in loading force during stress relaxation also disagrees with the

data. However, realizing that absolute parameter values will take some time to achieve (discussed below), these values are used as estimates for the initial guesses of the other liver's material parameters.

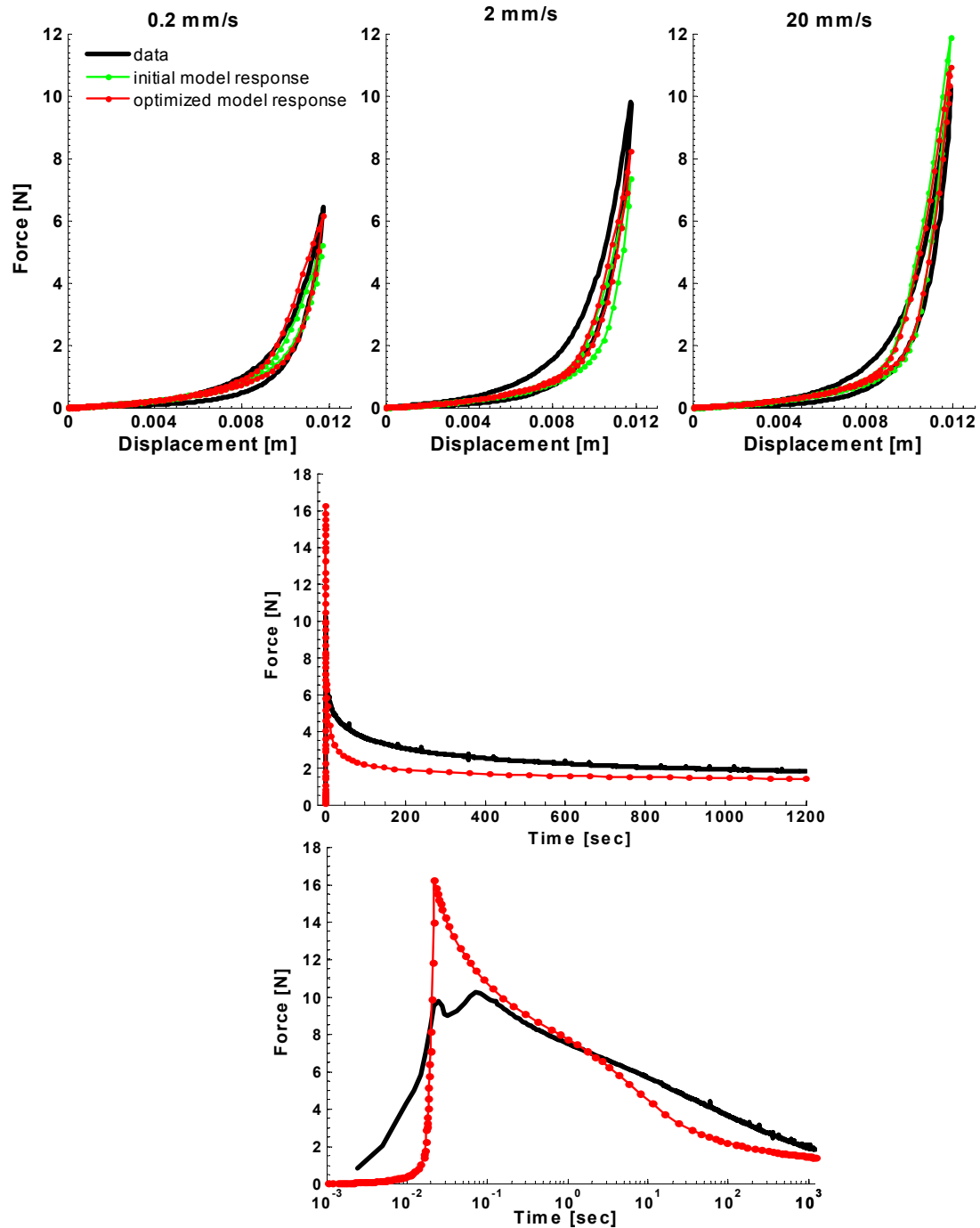


Figure 4.12 (Top) Results showing the model response (initial and final runs of the optimization) to the individual indentation data at three rates for Liver 1. (Bottom) The response using the resulting parameters compared to stress relaxation of the same liver shown in linear and log time.

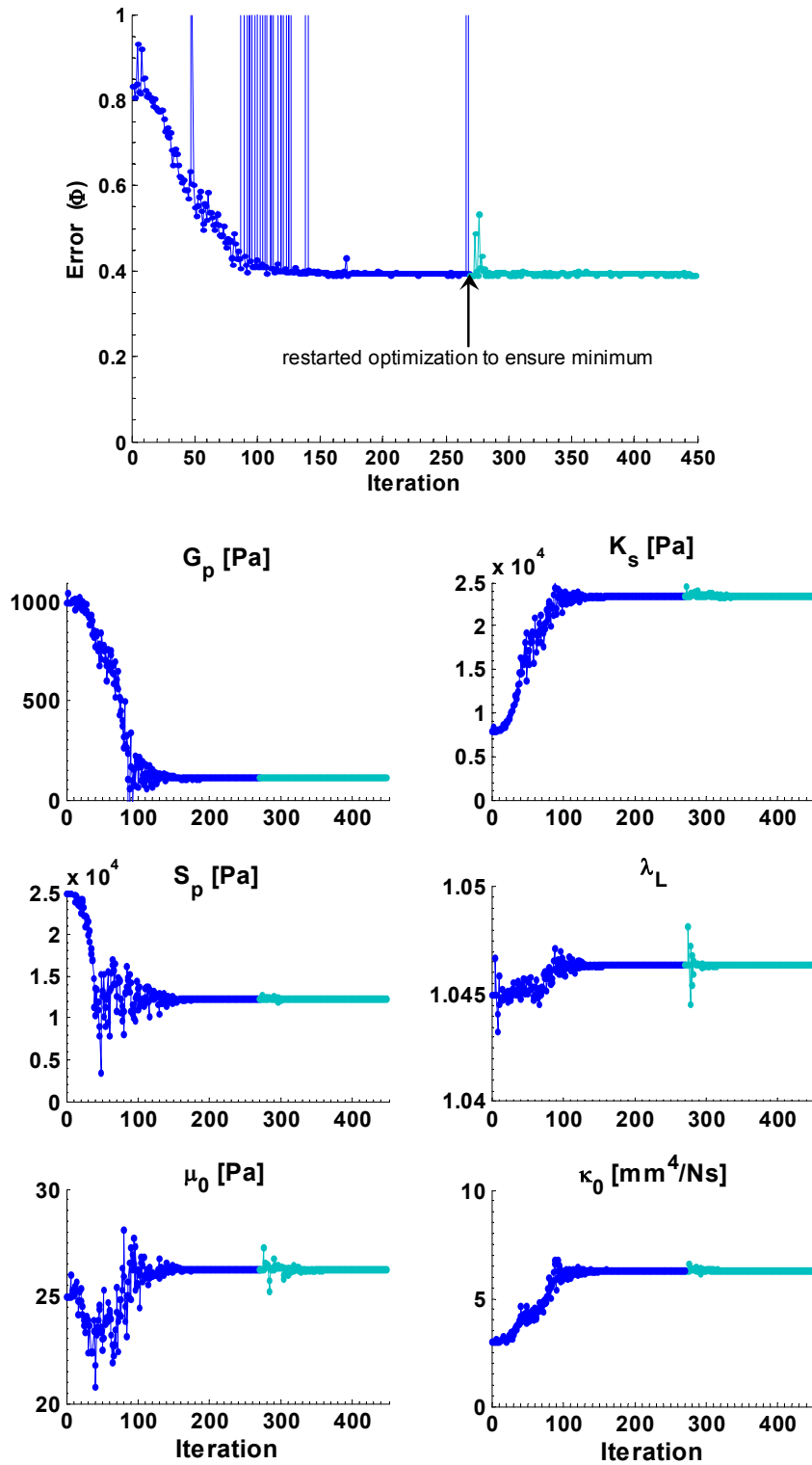


Figure 4.13 The evolution of the error and the parameter search for the 448 iterations comparing the model response to the force-displacement data of individual indentations at 0.2, 2, 20 mm/s for Liver 1 (evolution of Figure 4.12).

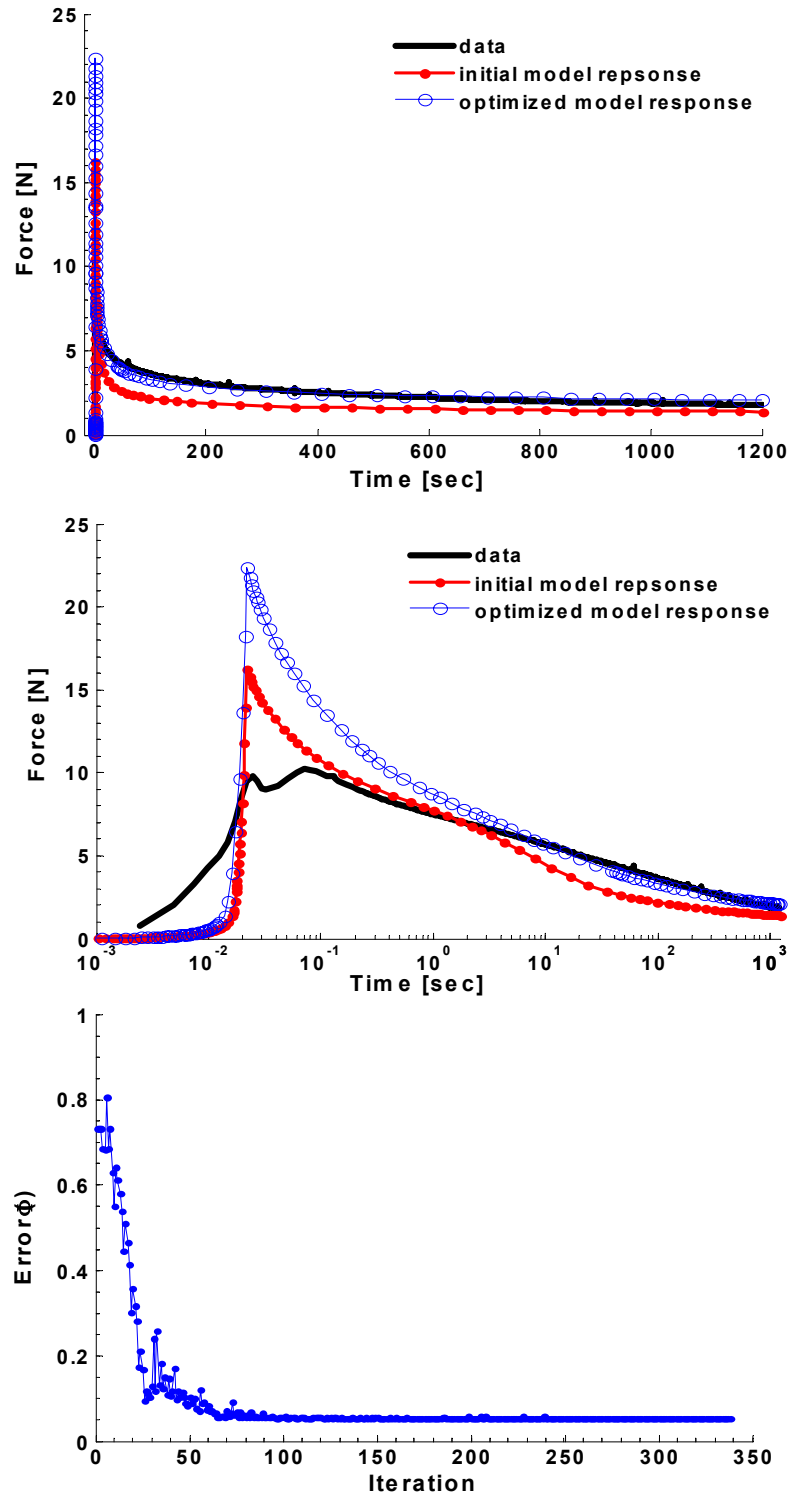


Figure 4.14 (Top) The initial and final optimized model responses compared to the data for the first stress relaxation test in Liver 1 in both. (Bottom) The evolution of the error.

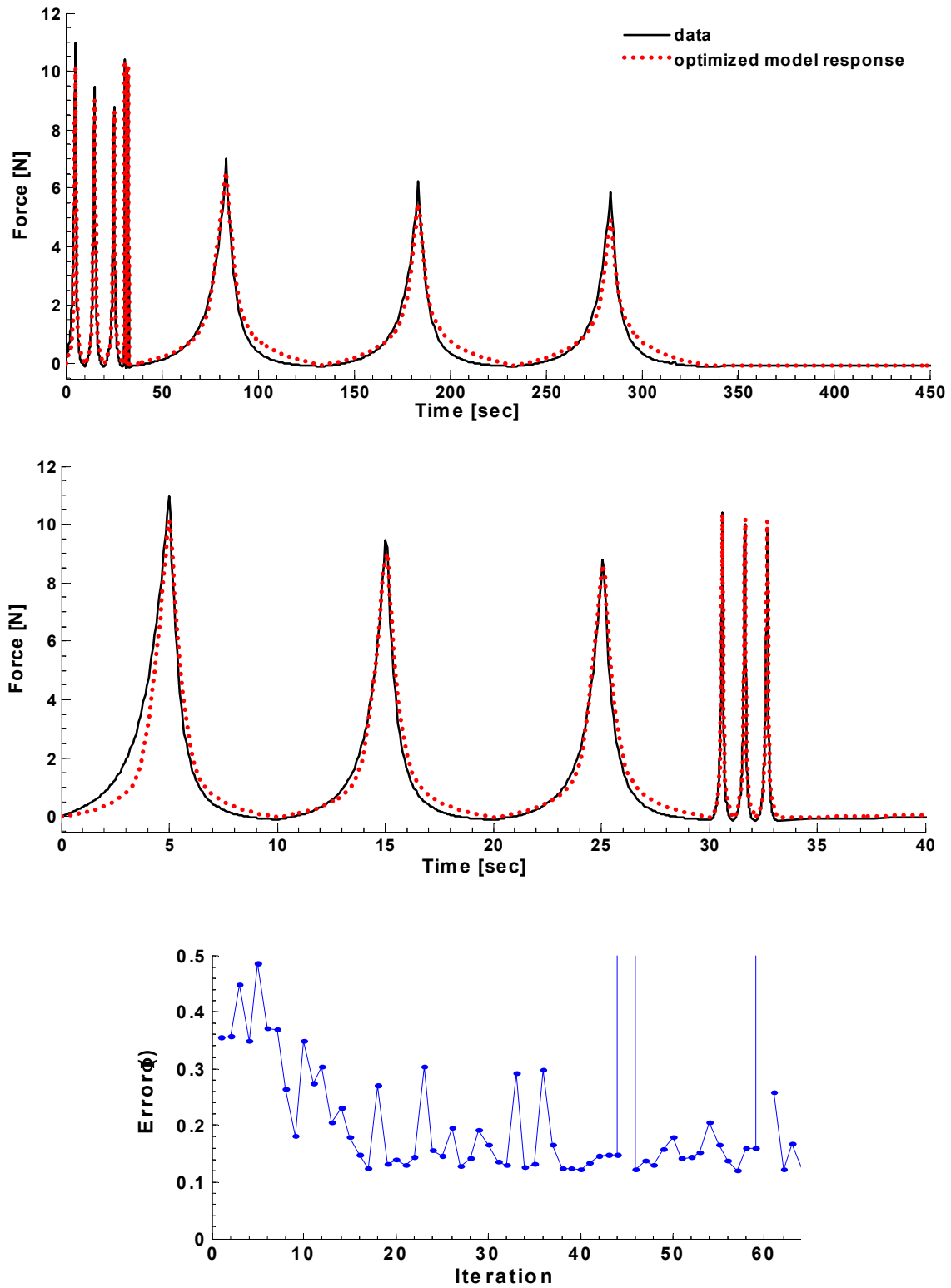


Figure 4.15 (Top) The optimized model response to the entire block of 9 indentations for Liver 1 as force versus time. (Bottom) The evolution of the error.

The third liver was modeled next, as the second had some inconsistencies in the data that the model might not be able to capture. The data from the second indentation of each speed for the first block of 12 indentations was brought through the same process described above. The first block was chosen so the first three speeds were done in the same order as the first liver modeled (2, 20, 0.2, and 40 mm/s). Using the values for the parameters in Table 4.2 as a guide, the model parameter values were manually adjusted on the 20 mm/s indentation and the stress relaxation data, until a decent match was obtained (Figure 4.16). The optimization across 4 speeds and all 7 parameters was run for 134 iterations. Although the MSE was slowly improving, the results were converging poorly. Therefore, the values for the parameters at run 134 were used to fully optimize the stress relaxation response instead. The results of this optimization (483 iterations) are shown in Figure 4.17. The single indentation at 4 speeds was run again with the newly identified parameters as the start values and m set to the stress relaxation optimized value of 1.18. This search was stopped after 158 iterations as the results were again converging poorly. The force versus displacement data for the 4 indentations is shown in Figure 4.18 along with the “optimized” responses for each of the trials run. The resulting values for the parameters from the stress relaxation, and both indentation optimizations are shown in Table 4.3.

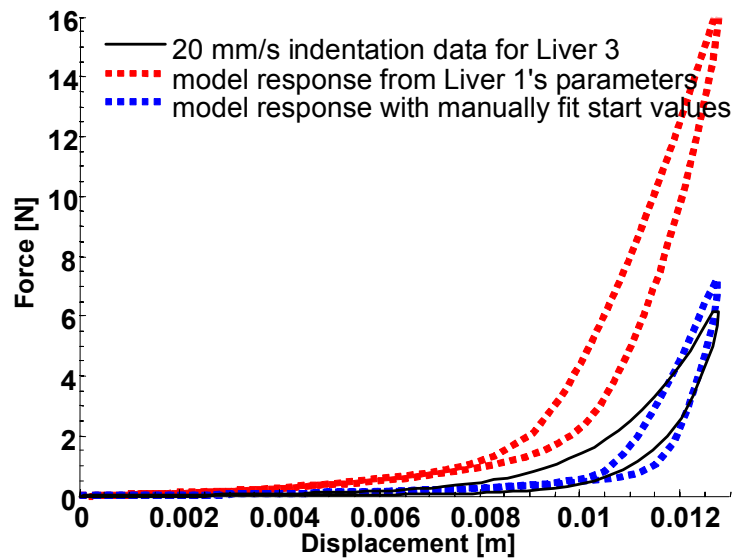


Figure 4.16 The model’s response to the first block of the 3rd liver’s second 20 mm/s indentation. The red dotted line used the parameters identified for Liver 1. The blue dotted line is a manual fit used to obtain start values for the optimization.

Due to the poor agreement in parameter values seen in Table 4.3, an optimization for the entire block was not attempted. However, a model of the full block was run using the mean values of the parameters, and the results are shown in Figure 4.19. Although clearly not an exact fit, the model is capable again of capturing the salient features of the data with the exception of the 40 mm/s peak forces. Similar issues as were described for the first liver are observed. Namely, the model fails to capture the true hysteresis, and is

unable to obtain an appropriate loading response for all speeds. In particular, the 40 mm/s indentations not only had peak forces

Table 4.3 Constitutive law parameter values for Liver 3 from three different optimization trials. Units for moduli in Pa, κ_0 is in m^4/Ns .

TEST	K_s	G_p	m	S_p	μ_0	λ_L	κ_0	MSE
Indentation Trial 1	8,253	40.8	1.495	4,447	8.579	1.051	9.774	0.674
Stress Relaxation	14,914	69.3	1.187	3,142	1.404	1.040	0.860	0.023
Indentation Trial 2	15,569	43.7	1.18 (set)	2,393	1.354	1.054	1.022	1.39
Mean	12,912	51.3	1.287	3,327	3.780	1.048	3.885	-

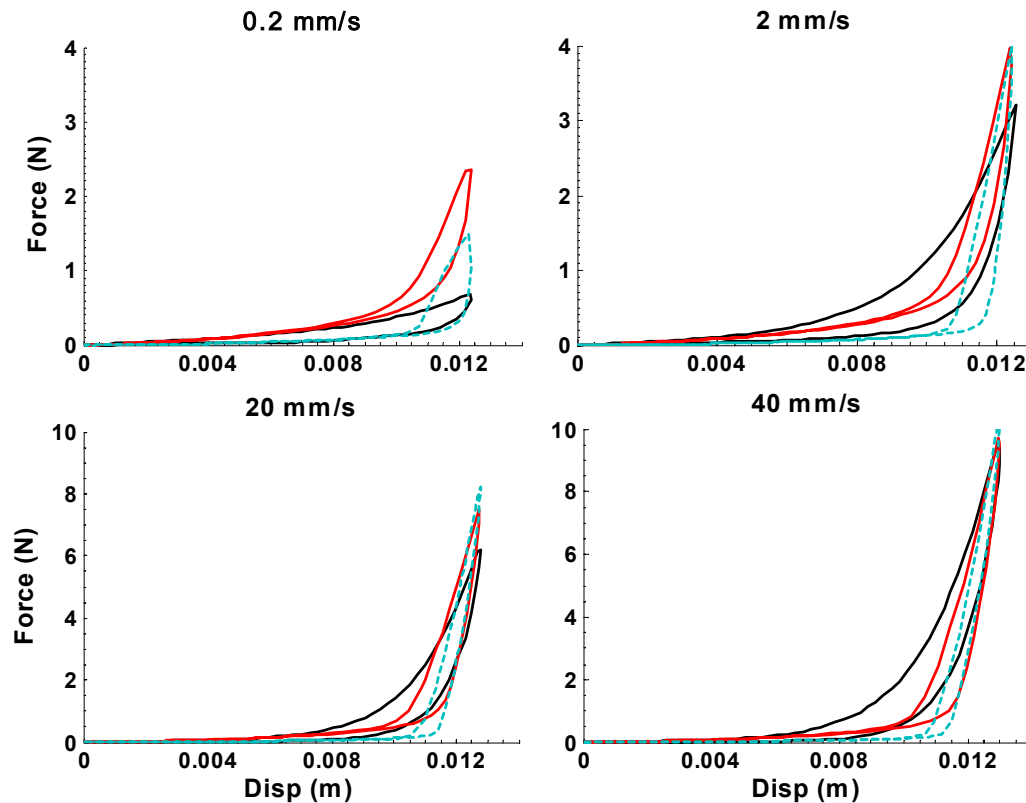


Figure 4.18 Model responses for two different optimization trials compared to the second indentation of each speed for liver 3. Black is the data, red is the 134th trial of the optimization of all 7 parameters from the manually fir start estimate in Figure 4.17 (MSE = 0.6742), and blue dashed is the 158th trial of an optimization with the parameter results from the stress relaxation test as start values (MSE=1.39).

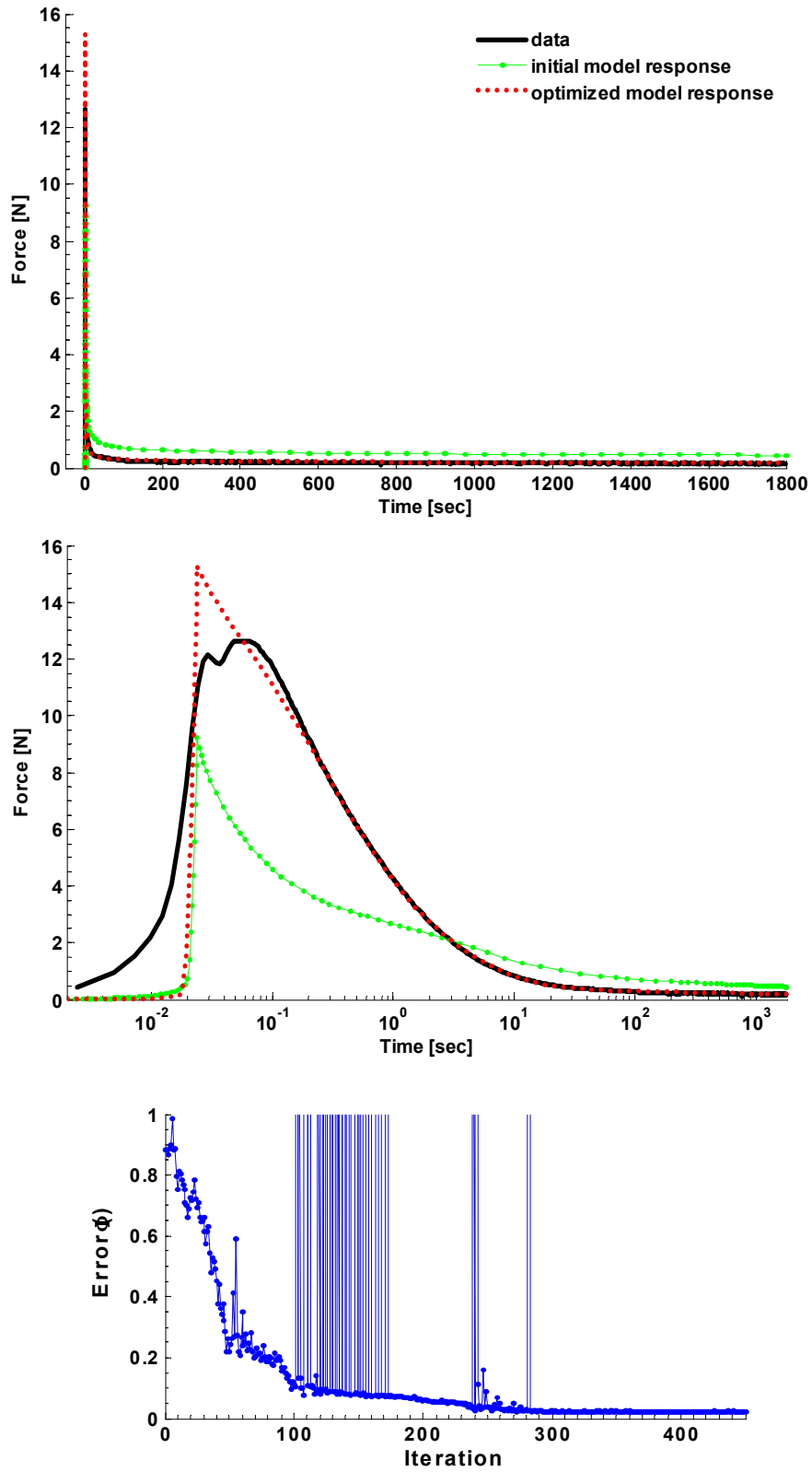


Figure 4.17 (Top) The model response to stress relaxation for liver 3 compared to the data with both initial and optimized parameters shown in both linear and log time. (Bottom) The evolution of the error function.

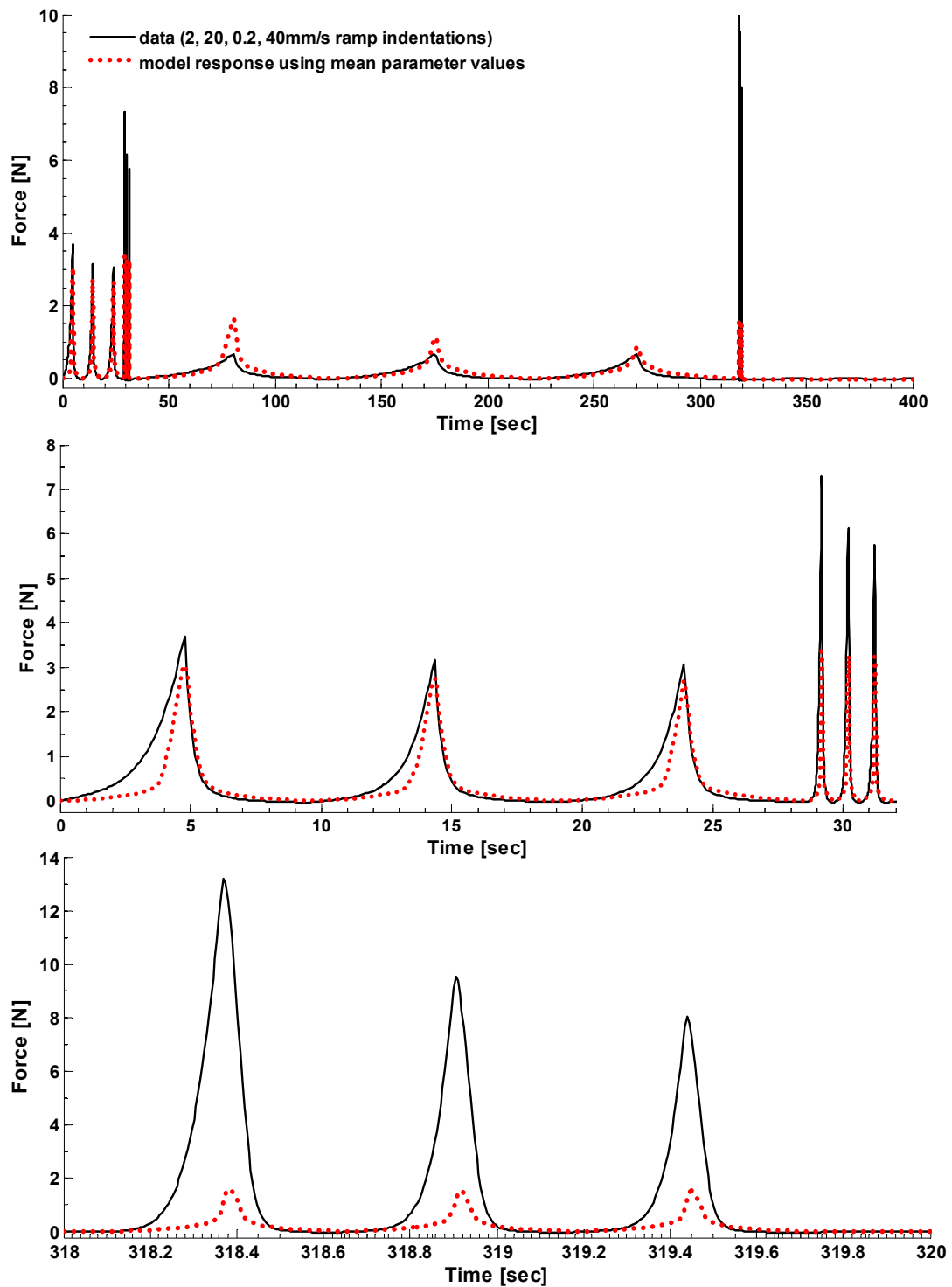


Figure 4.19 Force versus time data from the first block of data for liver 3 and the model response using the mean material parameters in Table 4.3.

Similar issues as were described for the first liver are observed. Namely, the model fails to capture the true hysteresis, and is unable to obtain an appropriate loading

response for all speeds. In particular, the 40 mm/s indentations not only had peak forces that were 20% of what they should be, but also were smaller than the forces for the 2 and 20 mm/s indentations. This suggests that perhaps not enough fluid returned to the indented volume indicating that the permeability was too low.

4.5.3 Validation

Although it was already shown that the results of one liver might not necessarily be true for another liver, testing the predictive capability of the model can still validate the identified parameter ranges. This was done by using the final values of the parameters in Tables 4.2 and 4.3 and modeling the response to the creep response. Figure 4.20 shows the results of this validation using the data from the first liver (recall that all creep data were similar in Chapter 3). The material parameters for the first liver capture the initial dynamic behavior, but do not bode well over time. The mean material parameters identified for the third liver actually produce a better fit to the data, particularly in the steady-state case. This suggests that the elastic moduli are too stiff for the first liver, since they are half the magnitude of those in the third liver, and that the viscous parameters for the third liver are better matched to the liver's actual response: having a softer shear stretch and lower exponent for the parenchyma network.

Although not uniquely identified, the results of the various optimization trials suggest a working range for each parameter. These are presented in Table 4.4.

Table 4.4 Range of material parameter values during the optimization of the first and third livers.

	K_s [Pa]	G_p [Pa]	m	S_p [Pa]	μ_0 [Pa]	λ_L	κ_0 [m ⁴ /Ns]
Parameter Range During Optimization (Max – Min)	6,615 -	40.3 -	1.18 -	2,393 -	1.35 -	1.035 -	0.86 -
	25,048	116.0	2.50	14,214	28.96	1.051	11.2

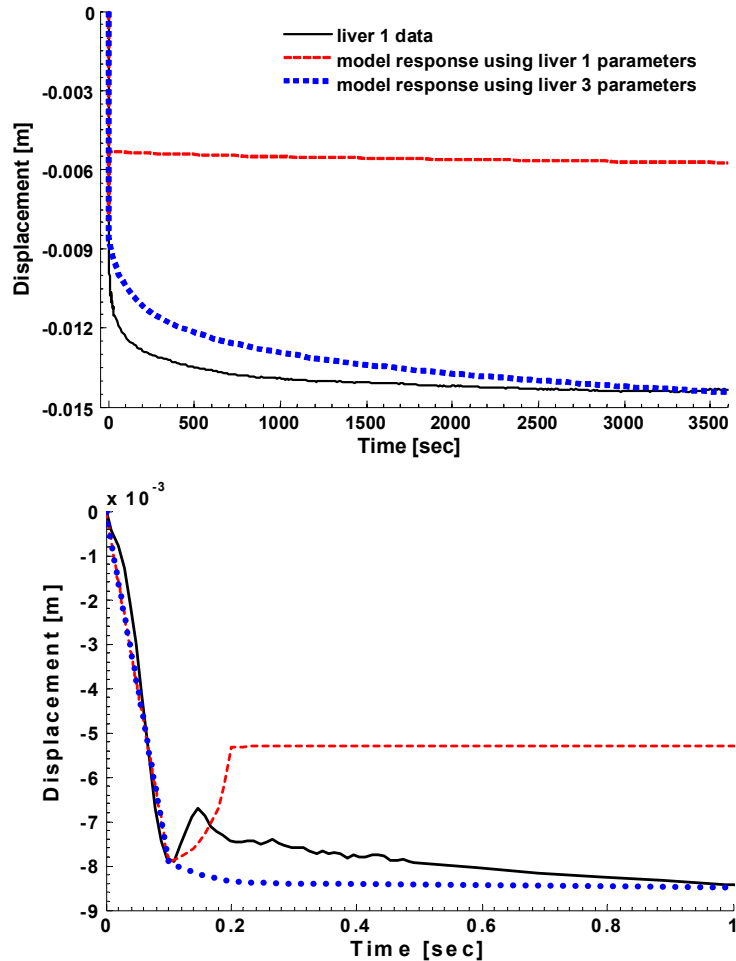


Figure 4.20 Model prediction of the creep response of liver 1 using the parameter identified for liver 1 in Table 4.2, and the parameters found for liver 3 in Table 4.3.

4.6 Discussion

This chapter presents the development of a physically-based nonlinear constitutive model for liver, under finite deformations typical of surgical manipulation. Although others have tried to model the mechanical response of liver (Brown, et al. 2003; Carter, et al. 2001; Chen, et al. 1996; Hu and Desai 2003; Kim, et al. 2003; Liu, et al. 2004; Liu and Bilston 2000; Miller 2000b; Ottensmeyer 2001; Picinbono, et al. 2001), no one has captured the finite deformation, viscoelastic response of liver with a physically-based model like the one described here. Most models assume some form of linearity, incompressibility, and are incapable of handling large strain indentation over time. The closest model is one presented by Snedeker et al for the kidney (2005a). They model the impact failure of the entire kidney using a multi-constitutive model approach. The model represents the capsule, parenchyma, calyces, renal pelvis, and fluid within the kidney. The capsule is modeled with a nonlinear Cowper-Symonds model (Snedeker, et al. 2005b). The response of the parenchyma is modeled using a second order Mooney-Rivlin strain energy function with second order prony viscosity. The calyces and renal pelvis are considered to be

linear elastic fluid filled tubes and the blood vessels are treated as pressurized tubes filled with a linear elastic fluid (represented with a low shear modulus). Despite obtaining good agreement to their impact data, it is unlikely that a model for the kidney under such conditions could represent the liver under surgically relevant deformation.

This chapter described a model and a technique towards realizing the material parameters of the liver's components. The constitutive framework developed shows promise in representing solid perfused organs like the liver, under finite deformations. Shortcomings of the model's ability to predict the true viscoelastic response of the results obtained in Chapter 3, suggest that some improvements to the model ought to be considered.

One of the strengths of this model is the recognition that soft biological tissues are compressible. Although the total stress can be separated into components from its isochoric (deviatoric) and volumetric (hydrostatic) responses, assuming that the changes in volume come solely from the fluid response is an over simplification. In reality, the overall change in volume should come from an initial change in volume from the fluid moving out (the permeability network) and from the collagen network losing water over time. Allowing the collagen to contribute to the volumetric response would result in an additional material parameter: a prestretch λ_0 . Having a pre-stretch is relevant since the fibrous component of biological materials are in a state of pretension to balance the osmotic pressure depending on the level of hydration of the tissue. This prestretch gives rise to a residual stress observed in other tissues, which is considered necessary for successful modeling of finite deformation behavior (Bischoff, et al. 2000). The curvature of the force displacement response will likely improve (soften) by adding a prestretch to the model, and by allowing the collagen to change volume, albeit slightly. Jordan et al presented the effects of this prestretch in a breast pathology model (Jordan, et al. 2005a).

Other potential changes to the model include adding a relaxation term to the capsule. The creep response from the model proved to be much stiffer than that of the data. Relaxing the parameters of the capsule helped achieve a more desirable response. The results of the uniaxial tension tests to failure were likely not enough information to establish an appropriate model for the capsule. Stress relaxation and/or creep tests on the capsule should be carried out to understand the time dependencies of the tissue (Prevost 2006). The creep indentation test also assumed a frictionless contact condition. Dedicated tests in the future should use the motorized suction indenter to ensure known boundary conditions.

The axisymmetric assumption inadvertently forces the fluid to stay contained within the confines of the given mesh geometry. The fluid has nowhere to dissipate to during long time-constant tests, such as the hour long creep tests. The model therefore predicts higher steady-state forces than what is observed. Future models should reconsider the geometric assumptions, and better model the flow path of the vasculature.

Lastly, while the optimization results produced believable fits between the model and experimental data, the issues of global convergence and uniqueness of solution need to be addressed. The results presented here suggest that solving the inverse problem of a 7-dimensional solution space is not straightforward, and that the initial estimates for the parameter values is critical in ensuring that convergence is met. There are at least two ways in which to address this critical dependence on the initial parameter values. A densely sampled, exhaustive search of the 7-dimensional parameter space, could be used

to understand the contour of the solution space. Although extremely helpful in providing an overall understanding of the parameter space, and in addressing the issue of uniqueness, the large computational expense for performing such a search is daunting. Another approach would be to solve the model analytically by simplifying the results of the indentation tests with a uniaxial compression approximation. A linear attempt is presented in Appendix B.

The technique presented in this chapter also suggests that optimizing different modes of time-dependant deformation simultaneously may be better than doing them sequentially. To keep the computational cost of this initial search to a minimum, it is suggested that a single indentation from each speed of the multiple ramp tests and one from the stress relaxation tests be optimized together for all independent material parameters. The error function may also need to be revised. Other measures for error were tried in an attempt to match peak force, hysteresis, initial slope, and curvature. These measures failed to improve the outcome. However, other measures of error should be considered that perhaps weigh the short and long term response of the stress relaxation more equally, etc.

In conclusion, this chapter describes a physically based, physiologically relevant, nonlinear 3D constitutive relation for the liver. The goal of this thesis work was to create a “ground-truth” physically relevant model for liver. Simplifications to the model will be required for implementation into surgical simulations that require large deformations to run in real-time. The next chapter addresses how to evaluate such simplifications by assessing the speed versus accuracy tradeoff that exists in real-time soft tissue modeling.

Chapter 5

Assessing the Accuracy of Real-Time Surgical Simulation

Models

Accurate models of soft tissue behavior are key elements in medical simulation systems. Previous chapters have presented such a “ground truth” model for the liver. The need for fast computation in surgical simulations, however, requires simplifications to this robust model that will hinder the deformation accuracy. These real-time models need to be quantitatively validated and understood. Once properly validated, the level of accuracy necessary to bring surgical simulation into practical reality can be determined. This chapter focuses on the development of a technique to validate simulation algorithms against a physical standard.

5.1 Motivation

The healthcare industry is the only industry that does not have a computer representation of its product. Technology and proficiency-based methods such as the use of medical simulation are creating a training paradigm in procedure-based medicine (Gallagher and Cates 2004). Simulators provide an environment in which to observe specific skills in the absence of uncontrollable influences, immediate performance feedback, the opportunity to examine a surgeon’s performance under conditions too dangerous in actual operating room settings, and the opportunity to examine interactions with rare or infrequent conditions (Dawson 2002; Gordan 2002; Liu, et al. 2003; Tendick, et al. 2000).

A simulation system consists of instruments, an optics device, mechanical engine, graphics engine, and a communications link that all must work in parallel (Szekely, et al. 2000b). A user will manipulate the instruments to perform a maneuver to interact with the simulated tissue model while visualizing the region of interest on a graphical monitor. The model must detect the collision, calculate the reaction forces, deform, and provide the user with realistic visual (30 Hz) and haptic (1,000 Hz) feedback in a continuous and transparent manner. Implementing such a modeling system has proved difficult mainly due to the tradeoff between fast computation time and calculated deformation accuracy (Figure 5.1). Depending on the simulation’s particular application, emphasis may be shifted towards the real-time aspect (e.g. surgical procedure training) or towards the accurate deformation aspect (e.g. material characterization) (Delingette 1998). The nature of

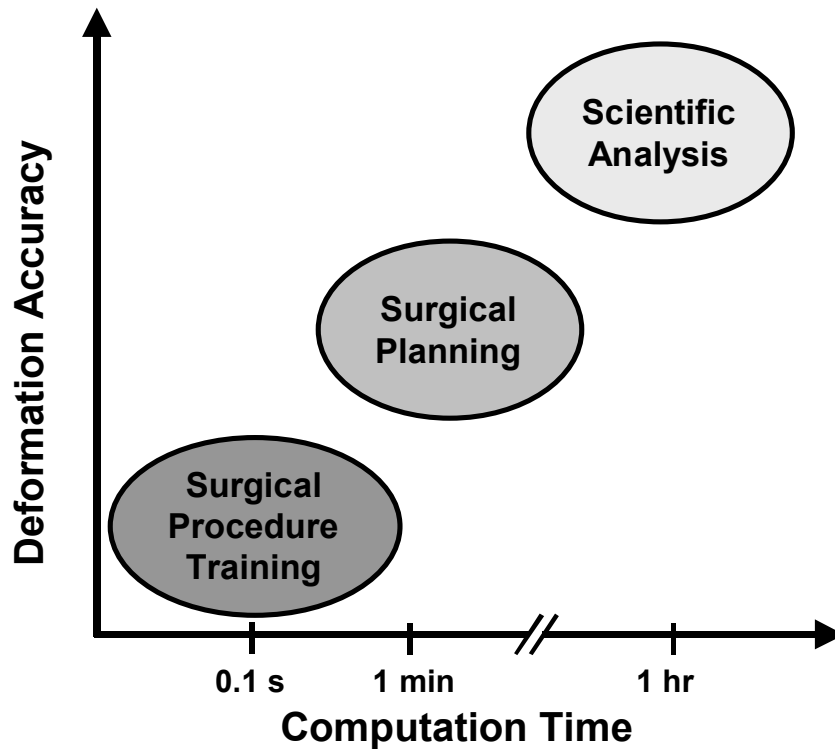


Figure 5.1 A depiction of the trade-off between biomechanical deformation accuracy and computation time for a given application. Adapted from (Delingette 1998).

this tradeoff is not well understood, and it is difficult to evaluate the relative performance of new systems when speed, accuracy, tissue properties, and geometry all vary. For instance, modeling tissue surfaces proves to be faster but less accurate than modeling tissue volumes (Cotin, et al. 1996). Similarly, spring-mass systems have limited accuracy but work well in real-time (Waters, 1992; Kuhnappel et al., 1997; Downes et al., 1998), while finite element modeling (FEM) has proven successful for accurately modeling small deformations of linearly elastic materials where calculation speed is not a paramount concern (Bro-Nielsen and Cotin 1996; Cotin, et al. 1996).

Although it is generally agreed that the utility of simulators relies on the level of realism achieved, the accuracy required for portraying this realism is not understood. The necessary resolution is limited by the perceptual capabilities of the user. For instance, people are capable of differentiating material compliance only after a 17% change has occurred (Ottensmeyer and Salisbury 2001a). This is more sensitive at higher testing frequencies. Before addressing what level of accuracy is needed for surgeons to believe that the simulated organ looks and feels authentic, a validation tool is needed that can quantitatively compare the simplified real-time models with both the robust models they are derived from and the complicated tissues they imitate.

Currently, real-time modeling is at best validated from subjective surgeon feedback or against finite element models that have their own intrinsic limitations. Current surgeon feedback on hepatic simulators suggest a need for “improved

biomechanical realism” (Picinbono, et al. 2004). The robust liver model described in the previous chapters was created and validated using iterative inverse FEM to compare the model’s response to one-dimensional force-displacement data. The response of a simplified liver model needs to be compared to both this robust model and to the actual 3D behavior of the organ it attempts to simulate. FEM serves as a possible soft tissue validation tool for simple geometries as well as completely defined materials and loading conditions. However, given that FEM is an approximation method in itself, the accuracy of its results heavily relies upon the quality of its input. Also, boundary conditions involving large deformations have difficulty converging when using FEM methods. Given these limitations, employing FEM to assess the accuracy of the various simplified algorithms used in real-time simulations of tissues with nonlinear material properties undergoing large deformations is of limited value.

This work provides a method and preliminary data for quantifying the accuracy of real-time soft tissue models. Towards this end I have developed a physical standard to assess the ability of a real-time algorithm to precisely describe the simulation of soft tissue under surgical manipulation. Ideally such a standard would take the form of stress, strain, and displacement fields over the tissue surface and throughout the tissue volume for fully specified material properties, under a range of specified surgically relevant boundary conditions. The output of new modeling systems could then be compared to these standard physical results to validate and benchmark their performance (Figure 5.2).

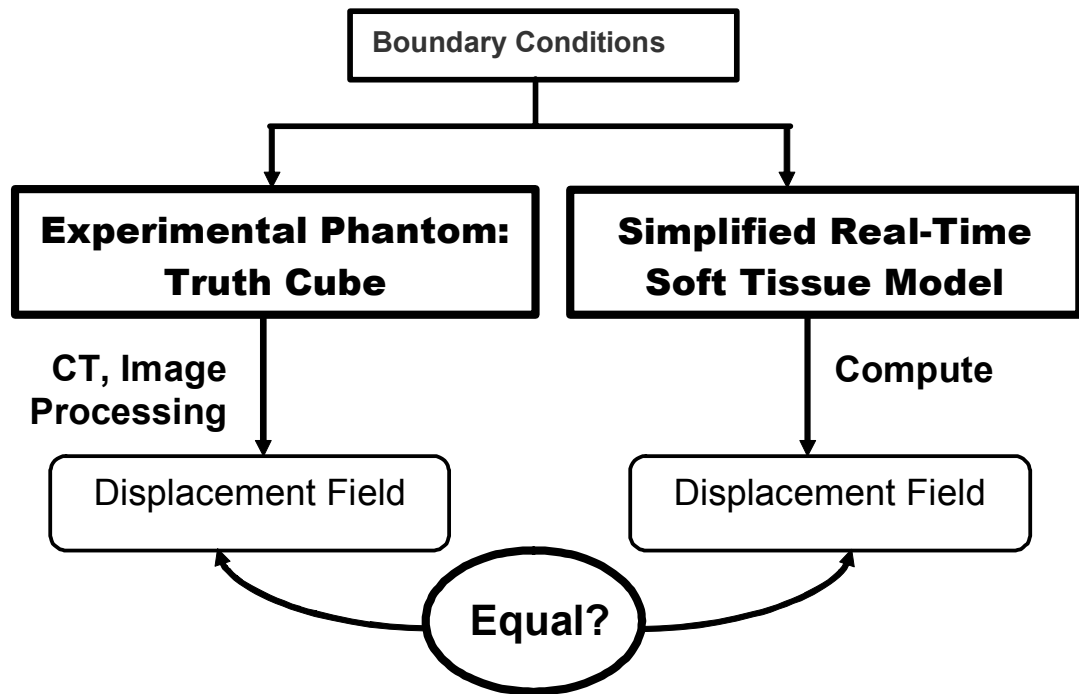


Figure 5.2 Approach for validating soft tissue computational models. Boundary conditions (material property, geometric, loading conditions, etc.) are imposed on the experimental phantom and the model. The displacement fields in the phantom are measured using CT imaging and comparison with the models predicted results.

This chapter presents a technique to assess the deformation accuracy versus real-time trade-off that exists in surgical simulation. A 3D imaging technique is used to experimentally measure a well-characterized test phantom in the form of a cube of soft polymer. This “truth cube” is made of a silicone rubber with fiducial spheres embedded in a 1 cm grid pattern throughout its $8 \times 8 \times 8 \text{ cm}^3$ volume. Computer tomography (CT) scans of the cube in undeformed and loaded states in both uniaxial compression and spherical indentation were acquired, and the relative displacement of each sphere was computed using image-processing techniques. The known material properties, geometry, and controlled boundary conditions resulted in a complete set of volumetric displacement data. These volumetric displacement results, along with details of the cube construction and boundary conditions in the two loading tests, are reported. Two FEM models were developed to compare to the experimental results. Since a rubber cube is a poor substitute for soft tissue, preliminary results for extending the method to biological tissues is presented. This work serves as a proof of concept for a robust physical standard and method for use in validating soft tissue models. A web site has been created to provide access to the database: <http://biorobotics.harvard.edu/truthcube/>

5.2 Methods

A cube was selected as a simple, regular shape to assess the feasibility of the validation approach and to develop the required techniques. The considerations included materials for the tissue phantom and fiducials, 3-D imaging, image processing, and data reporting.

5.2.1 Truth Cube

A 2-part silicone rubber (RTV6166, General Electric Co.) was chosen for the cube because its behavior is similar to soft tissues in the linear range (Ottensmeyer and Salisbury 2001a; Wellman 1999): the material is soft but exhibits linear behavior to at least 30% strain. To enable tracking of the internal deformation of the cube small spheres were embedded as fiducials that would readily appear in CT scans but not significantly alter the material properties of the silicone. The choice of sphere material and size was motivated by the need for high contrast without creating imaging artifacts (Strumas, et al. 1998): this assumes a specific gravity well above silicone (0.98) but much less than steel (~ 8). To enable accurate segmentation and position estimation, the minimum diameter of the spheres had to be slightly larger than the distance between two successive scanning planes (1.0-1.25 mm) yet small enough to avoid compromising the material properties of the silicone. Imaging tests using several commercially available spheres of different materials and sizes embedded in a sample of the silicone gel revealed that Teflon® spheres (specific gravity 2.3) with a diameter of 1.58 mm fulfilled all of these criteria.

The mold for the cube had removable sides, with the bottom serving as a rigid permanent mounting plate that was roughened and dimpled to ensure complete adhesion of the silicone. The two-part silicone rubber was mixed in a 30:70 proportion to obtain material characteristics similar to that of mammalian liver (Kim, et al. 2003; Ottensmeyer and Salisbury 2001a; Rosen, et al. 1999; Tay, et al. 2002). A layer 1 cm deep was poured, the mold was placed in a vacuum chamber to remove air bubbles, and then allowed to set on a level surface before positioning spheres in a 7×7 matrix spaced 1 cm apart. The spheres

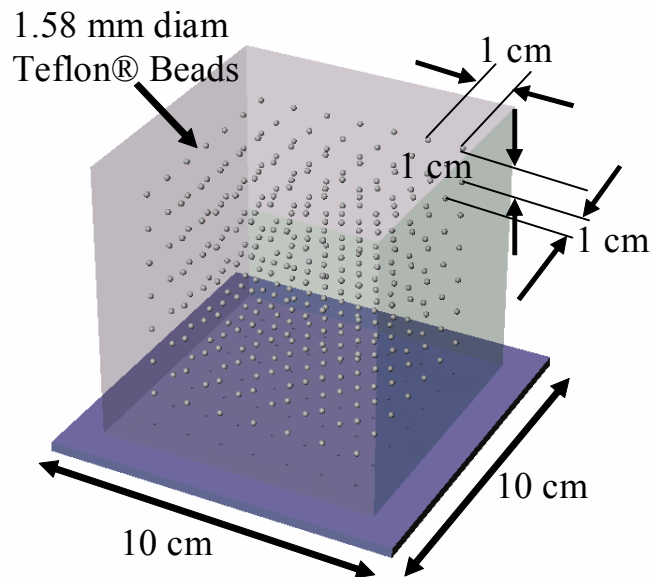
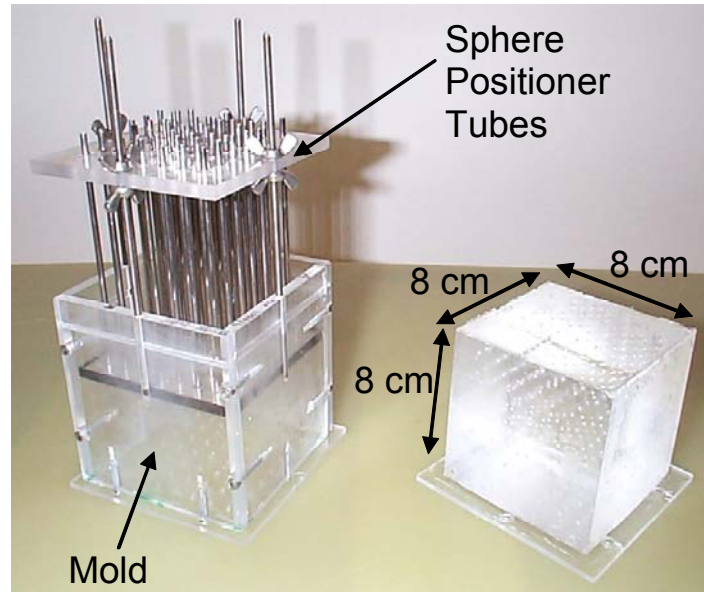


Figure 5.3 (Top) Mold and internal sphere positioner (Left) and resulting Truth Cube (Right). (Bottom) SolidWorks drawing of resulting Truth Cube showing the arrangement of the internal Teflon® fiducials.

were laid on the silicone rubber using a matrix of positioning tubes and allowed to set into the rubber before the next layer was poured. The end result produced a silicone rubber cube 8 cm on each side with 7 rows and 7 columns of Teflon spheres in 7 layers, spaced 1 cm apart in each direction (Figure 5.3).

To ensure that the material properties of the silicone rubber were not affected by the addition of the 343 spheres, I performed indentation tests on three samples of the

silicone rubber: alone, with sparse sphere density, and with 1 cm sphere spacing. Results indicated that the stiffness of the sample with the highest sphere density changed 2.0%, which is less than the 4.4% standard deviation of measurements of the plain sample. I thus conclude that the addition of the spheres had a negligible effect on the material properties of the silicone.

Both a small strain (< 8%) uniaxial compression test and an indentation test were performed on a sample of the silicone rubber used to obtain material property characteristics. Results indicate a Young's modulus of 15.0 ± 0.4 kPa. Poisson's ratio is near 0.5 for this polymer, consistent with many polymers.

5.2.2 *Experimental Setup*

The silicone rubber phantom with embedded fiducial markers (Teflon® spheres) was initially imaged under uniaxial compression to allow for technique development and result comparison with a fully defined FE model. A subsequent test used a spherical indentation loading condition more typical of surgical manipulations.

The experimental setup loaded the cube under controlled boundary conditions during the CT imaging process (Figure 5.4). The fixture base for the uniaxial compression test was constructed of 2.54 cm thick rigid plastic with cutouts that exactly fit the base of the truth cube to ensure consistent alignment within the setup. Registration markers (1.27 cm diameter Delrin® spheres) were attached to the fixture base, to allow for uniform positioning of the experimental setup on the CT Table between tests performed at different times but under the same loading conditions (i.e. when the whole apparatus had to be moved). However, since each loading condition was scanned once without needing to change the experimental setup between successive scans, these markers were mainly used as a visual assessment feature and as an estimate of overall scanner accuracy.

The initial loading test, uniaxial compression, was accomplished with a 2.54 cm thick acrylic plate. This compression plate was attached to a vertical support by a low-friction pivot. The plate was loaded by weights applied to the end opposite the pivot (in addition to the weight of the plate itself). The design confined all metal parts (the vertical support rods and weights) to the ends of the apparatus so that they did not interfere with CT scanning of the cube in the middle. A linear dial indicator measured the distance the plate was translated (Figure 5.5). A similar setup was used for the large deformation spherical indentation test except that a 2.54 cm diameter Delrin® spherical indenter mounted on a 1.9 cm diameter by 4.5 cm long Delrin® cylinder was added to the compression plate (Figure 5.5).

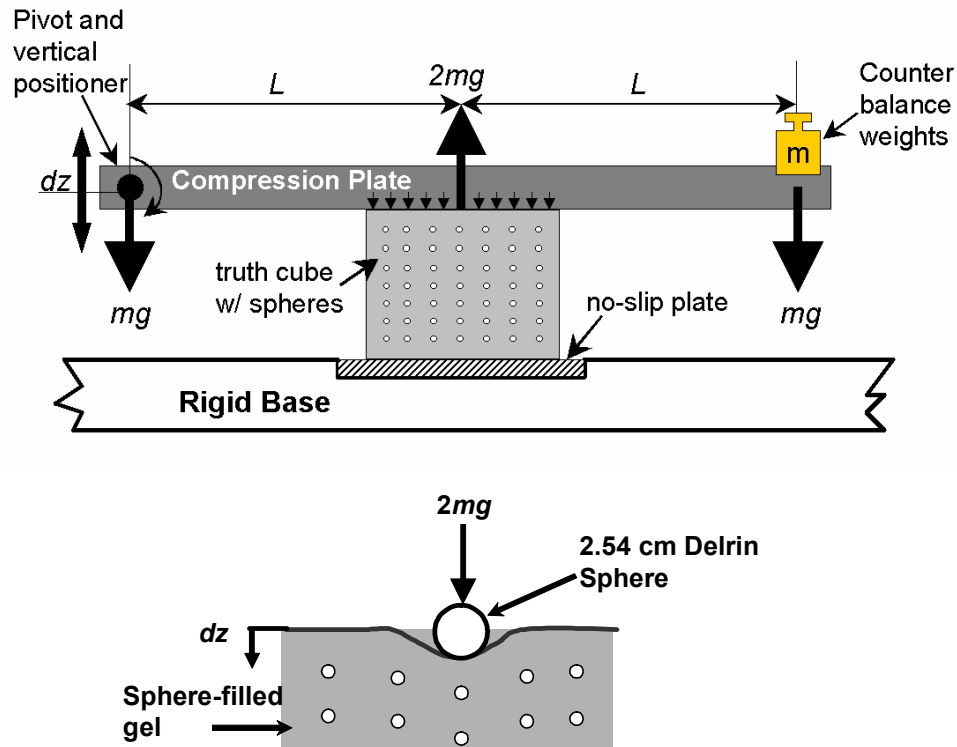


Figure 5.4 Side view of the uniaxial compression experimental setup (Top) and close-up schematic of spherical indentation situation (Bottom). L is the length from the loading points to the center of the cube, dz is the vertical motion, and m is the mass of the counter weights.

5.2.3 Experimental Protocol

A first scan of the uniaxial compression experimental setup was performed while the cube was unloaded to obtain a reference state of the internal sphere locations. The flat compression plate was then held level as it was lowered to a set displacement onto the oiled top surface of the cube (oil was used to approximate a frictionless boundary condition). With the pivot end of the compression plate held in place, masses were added to a pocket in the other end, until equilibrium was established as determined by level indicators. Three loading conditions were scanned: 4, 10, and 14.6 mm displacements, producing 5.0%, 12.5%, and 18.25% nominal strain, respectively.

Once loaded, the cube was scanned in a General Electric LightSpeed® CT scanner. Volumetric images of the truth cube were obtained using the following scanner settings: 120 kV, 180 mA, standard reconstruction type, and high quality scan mode. The field of view was 190 mm, producing a voxel size of $0.37 \times 0.37 \times 1.25 \text{ mm}^3$. Each CT scan was composed of 99 slices 1.25 mm thick (512×512 pixels, 16 bits) exported in DICOM format.

For the spherical indentation tests, the first scan was also conducted with the cube in an unloaded state for reference locations of the internal spheres. The compression plate with the indenter insert was then lowered in a manner similar to that of the uniaxial test. Two loading conditions were scanned: 18 mm and 24 mm displacements producing 22% and 30% local nominal strain, respectively. A third loading condition was attempted at 29 mm (36% nominal strain) but caused the cube to fracture.

The indented cube was scanned in a similar manner and with the same settings as those used in the uniaxial compression test except that the field of view was 150 mm and a thinner slice thickness (1.0 mm) was made possible by a more advanced machine becoming available, producing a voxel size of $0.29 \times 0.29 \times 1.00 \text{ mm}^3$. Each CT scan was composed of 133 slices 1.0 mm thick (512×512 pixels, 16 bits) exported in DICOM format.

5.2.4 Image Processing

A co-investigator, Dr. Stephane Cotin of CIMIT simulation group, is credited with the majority of the image processing described in this section. Commercial software (3D-Doctor®, Able Software Corp., Lexington, MA) was used for manipulating the volumetric images. The minor artifacts present in the lower part of the cube (due to the support plate in the uniaxial compression test) were filtered. Then the internal spheres in each of the scans were segmented from the silicone rubber with thresholding; this was relatively straightforward due to the good contrast between the spheres and the silicone rubber. After segmentation of the 343 internal spheres, a surface model of each sphere was calculated and exported as a 3D polygonal model.

The 1.58 mm diameter spheres embedded in the silicone cube have the size of several voxels (the voxel size is 0.37 mm or 0.29 mm for uniaxial compression and spherical indentation, respectively), so the 3D segmentation process only provided an approximation of the shape and location of the spheres. To accurately determine the location of the center of each internal sphere, Dr. Cotin implemented a least squares algorithm that fit an analytic sphere to the set of points defined by the vertices of the polygonal model of each sphere. This algorithm is integrated in visualization software developed to display polygonal models and vector fields of the relative displacement of the embedded spheres' centroids from their unloaded states to the various loaded states. The relative displacement vectors of the spheres' centroids were manually matched between the various loading conditions. Finally, the surface of the cube at each compression stage was extracted from the images. The large external registration spheres were also segmented in order to evaluate any potential motion of the overall experimental setup between successive scans.

5.2.5 Finite Element Model

A finite element model of the truth cube using commercial FEM software (ABAQUS v. 5.8, Hibbitt, Karlsson & Sorensen, Inc., Pawtucket, RI) was developed to compare with the experimental results. A simple coarse mesh was created for the uniaxial compression test to emulate models used in real-time soft tissue simulations. A more refined model was created to compare to the large deformation, spherical indentation test results.

For the uniaxial test, a mesh of $1 \times 1 \times 1 \text{ cm}^3$, 8-node, solid hexahedral linear elements was created so that the nodes of this model corresponded to the Teflon® spheres. For the spherical indentation test, the truth cube was meshed with 1134 solid axisymmetric triangular elements to represent the cube as a cylinder having an 8 cm diameter (Figure 5.8). Representing the cube as a cylinder was a good approximation as a comparison of the sphere displacement versus radial position for an orthogonal cut and a diagonal cut through the cube image data showed negligible difference in the sphere displacement vs. radial position. The models' material properties were isotropic and linear with a Young's modulus of 15 kPa and an assumed Poisson's ratio of 0.499. For the uniaxial case, large deformation (i.e. nonlinear) analysis was employed using the boundary conditions (frictionless upper surface, fixed lower surface, and free side surfaces) and geometry extracted from the CT scans for the unloaded and 18.25% nominal strain cases. For the spherical indentation case, large deformation (i.e. nonlinear), axisymmetric analysis was employed using the boundary conditions (fixed contact between indenter and upper surface, free side surfaces, and fixed lower surface) and geometry extracted from the CT scans for the unloaded and 22% nominal strain cases.

5.2.6 Biological Tissue Phantom

Preliminary data was collected on an *ex vivo* bovine liver to determine the applicability of using the technique developed for the truth cube on biological tissue. The goal of this experiment was simply to determine whether the same fiducials could be inserted into the tissue, then imaged, segmented, and tracked when the tissue was loaded. As an initial qualitative trial, 7 rows and 6 columns of the Teflon® spherical fiducials were inserted in two layers about 2 cm deep via saline-filled blunt needles throughout a portion of the parenchyma of a freshly excised bovine liver. This liver was then imaged using the standard abdominal/pelvic settings for a human liver in an unloaded and a fully retracted state (strains > 30%) (Figure 5.10). This state is similar to how a surgeon would bend the liver out of the way to access the abdominal structures below. The fiducials were segmented and tracked using the same techniques as the truth cube.

5.3 Results

Figures 5.6 and 5.7 illustrate the processing of the uniaxial compression test and spherical indentation test data, respectively. Figure 5.6 begins with segmented CT data for a vertical slice through the center of the cube, in both unloaded (Figure 5.6A) and 18.25% strain (Figure 5.6B) cases. Figure 5.6C represents the relative displacement field for the central vertical slice across all strains. Reconstructions of the surface of the cube for each strain state are shown in Figure 5.6D.

Figure 5.7 begins with a scan of the center slice of the unloaded state (Figure 5.7A) followed by the 30% nominal strain case (Figure 5.7B) and the vector field of the center slice displacements (Figure 5.7C). Reconstructions of the surface for the 30% strain state are shown in Figure 5.7D.

As an estimate of scanner accuracy, physical measurements of the spherical registration features were compared with measurements made on the raw CT scans. These measurements suggest that the accuracy of the scanner is less than 0.1 mm.

Minimal errors were introduced by the segmentation procedure on the internal spheres (thresholding, polygonal modeling, sphere fitting, centroid calculating, and tracking). Comparing the internal sphere location from raw to segmented data suggests that the error of the sphere locations is less than the size of one voxel in plane and less than half the size of the slice thickness out of plane. Therefore the estimated overall error in plane for the uniaxial compression and spherical indentation data are less than 0.37 mm and 0.29 mm respectively, and less than 1.25 mm and 1.0 mm out of plane.

The predicted results from the center slice of the FE model of the simple uniaxial compression test are shown in Figure 5.8A. There is a 3.5 mm maximum difference from the experimental results for a top surface displacement of 14.6 mm (18.25% nominal strain). The results predicted from a center slice of the more refined spherical indentation FE model at 22% nominal strain (18 mm displacement) are shown in Figure 5.8B. Figure 5.9 compares the internal sphere displacement results of the FE model to the measured data at 22% nominal strain for the spherical indentation case. The maximum difference

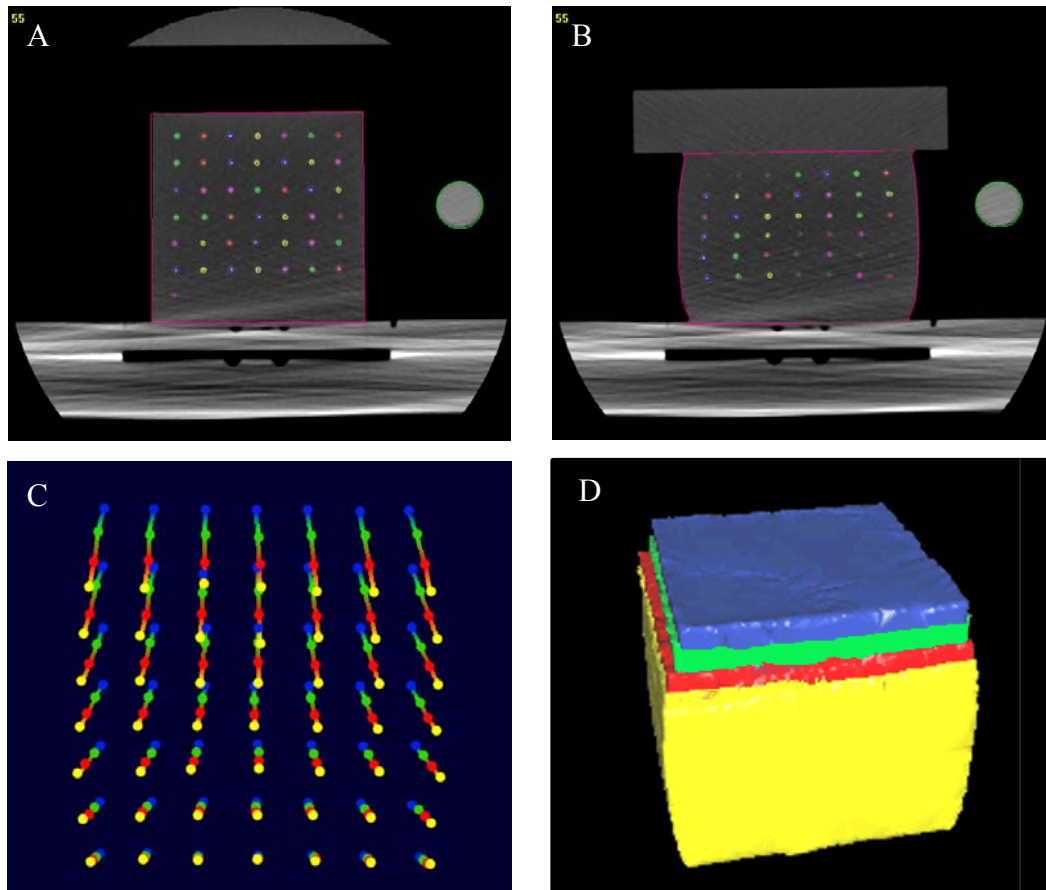


Figure 5.6 The CT image of the central vertical plane of the Truth Cube after segmentation in both the unloaded (A) and maximally uniaxial compressed (B) states. Note the registration marker off to the side. Internal sphere trajectory and location in the central plane (C) (blue = unloaded, green = 5%, red = 12.5%, yellow = 18.25% strain). (D) Outer surface of the cube in its four strain states.

between the model and the test results is 1.7 mm. This FE model was unable to converge at 30% nominal strain.

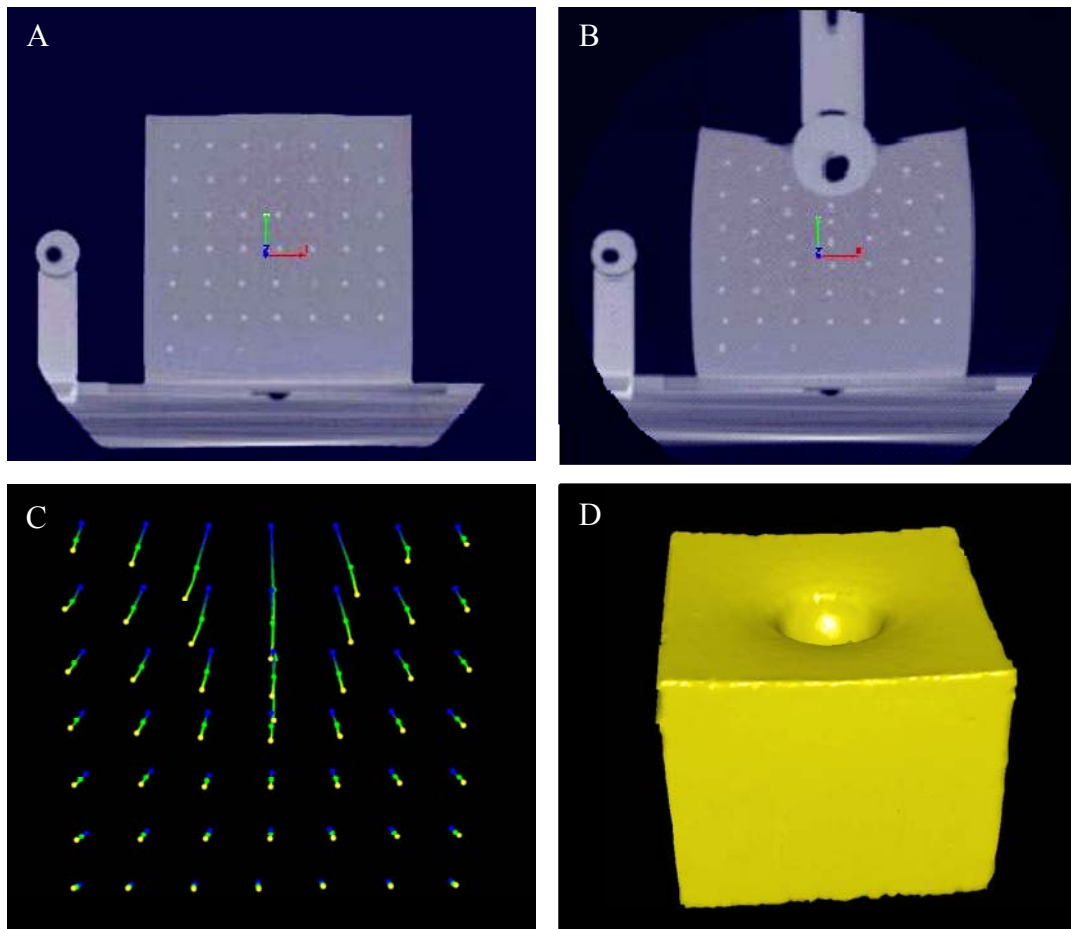


Figure 5.7 CT of center vertical slice for spherical indentation in unloaded state (A) and under 30% nominal strain (B). Note the registration marker off to the side. The trajectory and locations of the internal spheres for the same slice is shown in (C) where blue represents no indentation, the 22% nominal strain case is shown in green, and the 30% nominal strain case is yellow. The surface for the 30% strain case is represented in (D).

The preliminary results for the biological tissue phantom showing the CT slices of the unloaded and retracted liver are shown in Figure 5.10. The image processing technique easily captured and tracked the surface and the fiducial markers within the tissue in both the deformed and retracted states, suggesting that only minor modifications to our current technique will be needed to obtain volumetric data of actual soft tissue.

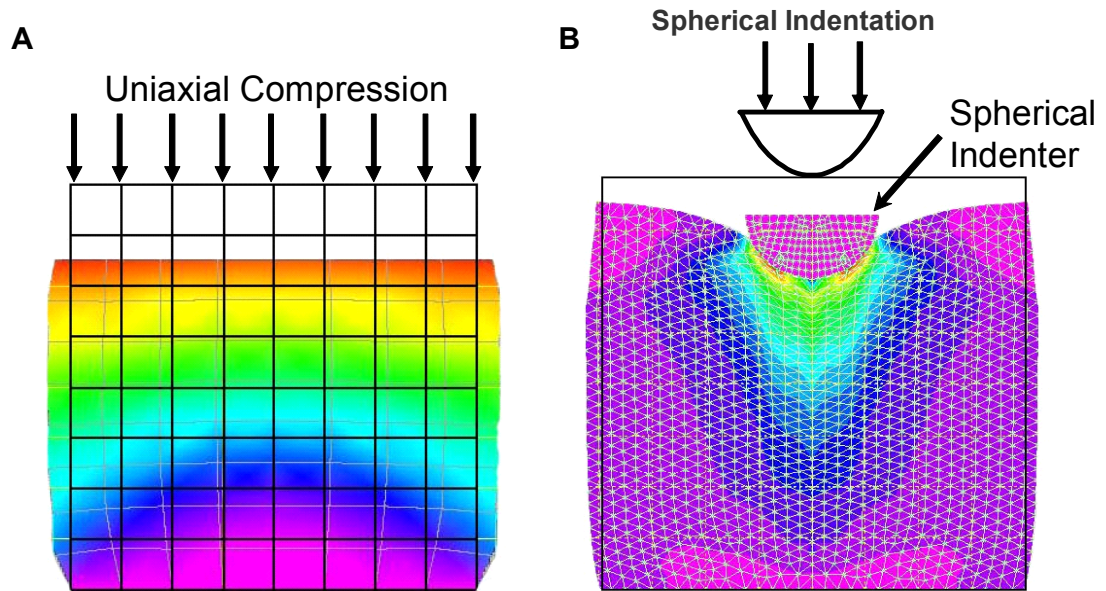


Figure 5.8 (A) Center slice of the uniaxial compression coarse mesh under 18.25% strain. (B) Center slice of the refined spherical indentation FEM mesh displaying the predicted results of the 22% strain experiment. The magnitude of the strain is color coded with red indicating the highest strain and violet indicating the lowest. Note that the undeformed model is outlined in black.

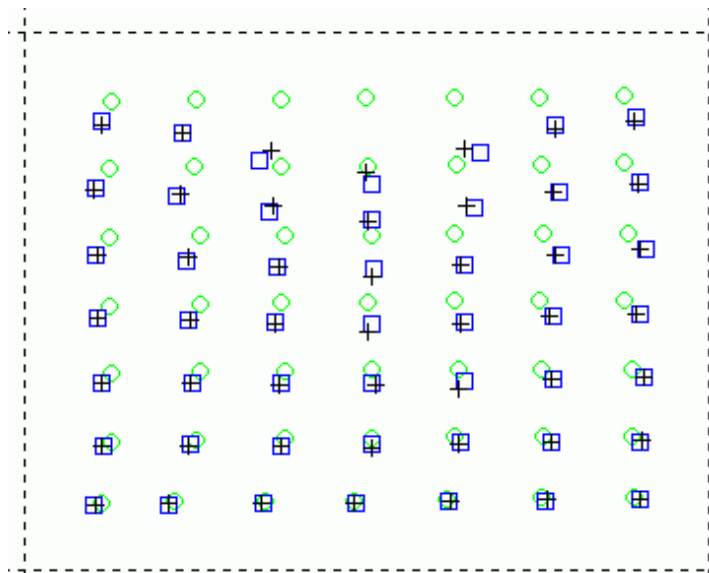


Figure 5.9 Comparison of the measured internal sphere displacement (boxes) versus the FE model's predicted sphere displacement (crosses) for the 22% nominal strain spherical indentation case. The circles are the original internal sphere locations and the dashed line is the undeformed outer surface.

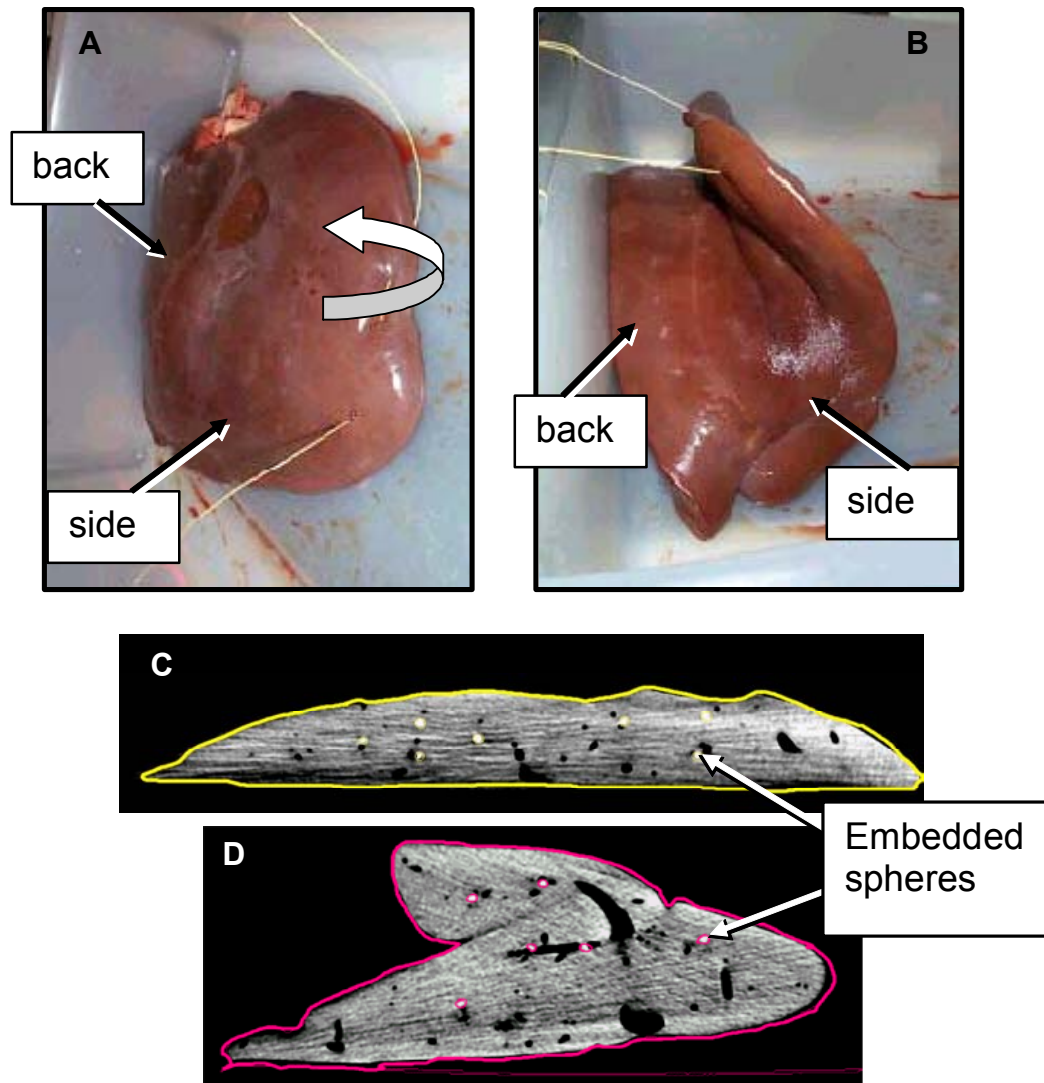


Figure 5.10 Bovine liver retraction experimental setup and results. The liver was cut to size, embedded with Teflon® spheres, and imaged in the unloaded (A) and retracted (B) states. CT slices of the undeformed (C) and of the retracted liver (D). Spheres and surfaces are highlighted.

5.4 Discussion

This study demonstrates a technique for creating physical standards for validating the accuracy of real-time soft tissue simulation models. The goal was to show that experimentally measured, local internal displacement data from soft materials can serve as a means of validating these models.

The ideal physical standard would provide measurements of the deformation and stress fields over the surface and throughout the volume of soft tissues under large deformations ($> 30\%$ strain) typical of surgical manipulation. This physical standard

would also need to have well-characterized material properties similar to the simulated tissue, surgically relevant specified boundary conditions, and known geometry. A solution to fulfill this need is the truth cube, which has a modulus in the range of liver, $E \sim 15$ kPa as reported by Ottensmeyer (2001). Imaging at strains of over 30% was easily accomplished. The external surface and the embedded fiducial spheres were readily segmented, permitting calculation of the relative displacement fields throughout the volume. The result is a local displacement data set with well-characterized material properties and boundary conditions that can be used to assess the precision of soft tissue models under similar situations. Full displacement results and raw CT scans of both experiments are available on the project web site:

<http://biorobotics.harvard.edu/truthcube/>.

Because FEM is the current standard used to check the accuracy of soft tissue simulation models, the results were also compared with the output of these computational models. The simple FEM calculation presented for the uniaxial compression test used a minimal number of elements to reflect some of the speed-vs-accuracy tradeoffs of real-time tissue simulations. While the FEM and experimental data showed qualitative agreement, even with these simple loading conditions on a linearly elastic material the maximum single-point differences between the model and the experimental results were 3.5 mm for the 14.6 mm uniaxial displacement. Such an error may result in significant consequences for applications such as surgical planning. Some portion of the difference may be due to inexact specification of the boundary conditions on the top of the cube during compression as well as experimental error. Refinement of the model (e.g. smaller mesh size) should bring closer agreement to the experiment, albeit at the expense of increased computation time.

For the spherical indentation situation, a finer resolution mesh was used to better replicate the experimental results. The maximum single-point differences between the model and the experimental results were relatively small (1.7 mm) for the 18 mm indentation case. The model failed to converge for the 26.4 mm indentation situation (30% nominal strain) that was experimentally measured, and thus no comparison could be drawn for this larger deformation. This demonstrates one of the limitations of using FE modeling as a validation tool: even the most robust FE models do not readily converge for large deformations of the complex materials typically seen in surgical manipulations (Szekely, et al. 2000a).

Strains larger than 30% may be expected in surgical procedures on biological tissues: i.e. organ retraction. FEM techniques for dealing with gross deformation, such as regriding or explicit schemes, are difficult to implement and of uncertain accuracy. This emphasizes the need for physical models as validation standards. Therefore, although FEM is a powerful tool, it may not be the most appropriate means of validating real-time soft tissue simulation models. The truth cube technique, however, results in an experimentally measured, internal strain field with good resolution for all material properties, and thus should be the validation method of choice.

Several refinements to the measurement techniques are indicated by these results. First, the accuracy of the local internal sphere positions in this initial dataset is estimated. More precise accuracy specifications can be obtained through an analysis of the imaging and image processing procedures, and through reproducibility measurements. Another

area for improved characterization is the top surface boundary condition, where oiling the cube served to limit and regularize friction, but where a truly “frictionless” condition did not apply. Fortunately, the contact area is readily measured during the experiment and in the processed CT images, so additional boundary information is available.

This initial study demonstrates the feasibility of experimental measurement of volumetric displacement fields for soft material phantoms under large strains, and provides useful internal strain field data that can readily be used to validate soft tissue models. Although the truth cube has regular geometry, well-characterized material properties, and loading conditions that were helpful with the development process, fast tissue simulations must accommodate vastly different conditions, involving very large deformations, irregular shapes, and complex materials.

To address these challenges, a biological tissue phantom was preliminary tested. A bovine liver was injected with Teflon® fiducials and then imaged by CT in both the unloaded and retracted state. Results suggest that only minor modifications to the current technique are needed to obtain volumetric data of actual soft tissue.

Given the material properties of liver presented in Chapter 4, geometry of the organ, and controlled boundary conditions, volumetric displacement data (internal strain) can be obtained using either the CT methods mentioned here or perhaps 3D ultrasound (see Chapter 6). A real-time soft tissue model can then be validated by comparing the deformations of the ground truth to the real-time model under the same loading conditions. Once a system is validated, the simulator’s accuracy can be determined. A comparison of real and simulated surgery can then be conducted to quantitatively assess whether the achieved level of accuracy is enough to ensure that any errors made are due to the surgeon rather than the virtual environment. Finally, such simulation systems can then be used to conduct virtual reality (VR) to operating room (OR) studies in order to validate the capability of simulators to provide safe and effective clinical learning (Dawson 2002).

Chapter 6

Conclusions and Future Work

Much of the technology is in place to employ minimally invasive surgical simulation for training and planning purposes. However, the implementation of this technology is mired by a lack of the fundamental understanding of the mechanical response of biological tissues to surgical manipulation. It was the goal of this work to address this need by characterizing the nonlinear mechanical response of liver to finite deformations typical of these manipulations.

The work was motivated in Chapter 1 with an introduction to MIS and the inherent problems associated with simulating such procedures. A complete description of the liver was given, followed by a review of the work done to measure the mechanical response of soft biological tissues, and to identify the material parameters of the constitutive models that govern these responses. The specific aims of this work were:

1. To obtain a qualitative understanding of the liver's unique anatomy by studying the effects perfusion has on the viscoelastic response.
2. To measure the complete viscoelastic response of liver under time-dependent finite deformations.
3. To develop a physically based constitutive model with biologically relevant material parameters.
4. To realize the parameters of the model using the viscoelastic data, through an iterative, inverse FEM technique.
5. To assess the accuracy-versus-speed trade-off that exists when implementing complex constitutive models to work in real-time surgical simulations.

This chapter serves to recapitulate the key findings of this work, and to propose directions for future efforts.

6.1 Nonlinear Viscoelastic Mechanical Response of Perfused, Whole Livers, Under Finite Indentation

Chapter 2 described a standard testing method to test the mechanical response of liver under controlled *ex vivo* conditions, while still capturing physiologically relevant behaviors. The system allowed for concurrent control of both geometric and physiologic

boundary conditions including, perfusate, perfusion pressure, temperature, and surface hydration. Other researches have proposed that such a system would be necessary to capture the true mechanical response of perfused organs, such as the liver (Brown, et al. 2003; Fung 1993; Liu, et al. 2003; Melvin, et al. 1973). Similarly, it is widely accepted that the viscoelastic characteristics of soft tissues are drastically altered devoid their natural boundary conditions (Liu, et al. 2003; Seki and Iwamoto 1998b; Yeh, et al. 2002), yet there is limited data comparing the response of the same deformation across tissue condition, to support these findings (Brouwer, et al. 2001; Brown 2003; Davies 2002; Gefen and Margulies 2004a; Kalanovic, et al. 2003; Kauer, et al. 2001; Miller, et al. 2000b; Snedeker, et al. 2005a).

The results of large strain creep indentations across four different conditions were used to both qualitatively and quantitatively show that the perfused state of the liver significantly alters its viscoelastic response. The results suggest that unperfused conditions have unrepeatability and appear stiffer, and more viscous than the perfused livers. This appears to contrast with what others have found: namely that the *in vivo* condition is stiffer than the *ex vivo* condition (Brouwer, et al. 2001; Gefen and Margulies 2004a; Kalanovic, et al. 2003; Kauer, et al. 2001; Melvin, et al. 1973; Miller, et al. 2000b). It is important to note that the tests done in Chapter 2 were creep tests, and thus comparing the results to ramp, shear, and sinusoidal indentation or grasping tests is not initially intuitive. For creep tests, stiffness was determined by looking at the steady-state response. Once the fluid is removed from the local region being interrogated, it makes sense that the steady-state result would result in higher forces than those tests where the fluid was free to move since the elastic tissue is stiffer than the fluid. However, the back-pressure provided by the perfusion was found to maintain the turgor of the liver, which could be related to the *in vivo* response being stiffer than the *ex vivo*. Furthermore, the perfusion system was shown to adequately preserve the *in vivo* mechanical state of the liver in an *ex vivo* setting. Lastly, lumped element modeling suggests that a two time constant model should be considered for constitutive modeling.

Until the 1970's, biological material testing mainly concentrated on obtaining the failure characteristics of the tissue. The need to acquire the viscoelastic response of soft tissues for diagnostic and surgical simulation purposes, has demanded the development of new methods for testing soft tissues that preserve the integrity of the tissue. Viscoelastic testing protocols could be developed and implemented using the *ex vivo* perfusion system of Chapter 2, with the confidence that the results would mimic the *in vivo* response for up to 6.3 hours. Chapter 3 described a full complement of mechanical indentation tests done in an effort to identify the viscoelastic characteristics of liver, and paid particular attention to those deformations and loading rates that were surgically relevant.

Indentation tests to 30% nominal strain, at rates from 0.01 to 20 Hz, revealed the strain-rate sensitivity nature of the liver, while continuous sinusoidal testing at a constant rate (1 Hz) provided information of the liver's response to multiple indentations. The results of these tests suggested that the liver's elastic energy was saturated below 0.05 Hz and above 10 Hz, and had a nearly linear increase in between. A nearly constant increase in dissipative energy at rates greater than 0.05 Hz was also observed. The continuous sinusoidal tests exemplified the importance of capturing the first indentation, and allowing for ample recovery time between tests, regardless of the number of indentations. A 40% decrease in peak force, and a 50% decrease in hysteresis were observed between the first indentation and steady-state (~25 indentations later).

These preliminary test results led to a protocol where viscoelastic testing of surgically relevant deformation and rates (across two orders of magnitude) were conducted. Blocks of multiple indentation ramp tests from 0.2 to 40 mm/s revealed similar characteristics as the preliminary tests. They had the added benefit of capturing the time dependency of multiple indentations across rate. The tissue responded to nominal strains between 32 and 36%, with mean peak forces of 3.7, 6, 6.4, 8.5 N for the 0.2, 2, 20, and 40 mm/s cases, respectively. It was also noted that the first indentation of an entire series resulted in larger peak forces and hysteresis than the others. The first indentation after the 0.2 mm/s series within a block showed a similar response. These results suggest that the time scale for recovery (reperfusion) was on the same order of magnitude as the time scale to conduct the 0.2 mm/s indentation (70-100 seconds depending on the thickness of the location tested). Stress relaxation indentation tests with a 20 to 30 minute dwell period, and creep indentation tests with a 60-minute hold phase, were also performed. A nonlinear dissipative element, and/or a fast time constant (<1 sec), are assumed to be responsible for the rapid drop in force observed in the stress relaxation tests. The 6 to 13 N peak forces are only 1.75 times greater than those of the ramp indentation tests conducted at 1/10th the rate. The creep tests achieved a 50% nominal strain at steady-state under the application of a 32.5 g load within the time course of the test, for all livers. These results were similar to those in Chapter 2.

Lastly, uniaxial tension tests of samples of the liver capsule were performed. Results indicated a nonlinear force-displacement response with failure at between 20 to 30% axial strain, and a mean stiffness of 1.8 kN in the linear region.

Although the results of the *ex vivo* indentation testing are repeatable within each liver, there are differences between the livers necessitating additional experiments to be conducted before a typical response can be reported. Also, one remaining challenge is to account for the initial stress state. Placing the liver on a hard surface induces stresses in the organ that are not present in the *in vivo* state, and should be taken into account. Attempts at “floating” the liver in a basin of perfusate proved to be problematic, and alternative methods should be considered.

6.2 Physically-Based Nonlinear Constitutive Model and Parameter Identification

The extensive viscoelastic data collected on the liver is of little value without a constitutive relationship that correlates the material to its mechanical response. Chapter 4 was dedicated to developing a physically based constitutive model to describe the observed nonlinear, viscoelastic, response of the liver to finite deformations. The material parameters of the model were identified using an iterative inverse finite element modeling technique. The error between the data and the model’s response was minimized through a simplex search optimization scheme. The goal was to determine a form of a model that was able to predict realistic deformations that were not experimentally measurable (i.e. surgical probing, grasping, suturing, dissecting, etc.).

The model represents the three main constituents identified for liver: the tough fibrous outer capsule, the densely populated cellular parenchyma, and the fluid filled vessels. The three networks combine to produce the cooperative nature of the tissue response. The full stress response of the tissue was presented by separating it into its

isochoric response (from the collagenous parenchyma network) and volumetric response (extracellular fluid network). The capsule was treated independently.

An 8-chain modified Arruda-Boyce network model was used to represent the collagen network, while a 2D version was used for the capsule. A viscoelastic network with a linear elastic spring in parallel with a nonlinear viscous element models the parenchyma network. The extracellular fluid network is considered to be a fluid-filled nonlinear elastic porous material. A nonlinear elastic spring captured the equilibrium response, while the transient response was represented by establishing a pressure gradient to drive flow as governed by a nonlinear diffusion equation. The resulting model has 16 material parameters: μ_{0Cap} , λ_{linear} , λ_{LCap} , and K_{Cap} (capsule); μ_0 , μ_{Lim} , λ_L , G_p , S_p , m , and $\dot{\gamma}_0$ (collagenous parenchyma); K_s , K_{Lim} , κ_0 , M , and f_w (extra cellular fluid).

The capsule is required for modeling large strain indentation tests. It served the purpose of smoothing out the large stresses induced by the indenter, and allowed for realistic deformations to be obtained. The four capsule parameters were identified using a finite element model of the uniaxial tension tests in Chapter 3. The values for the initial shear modulus (μ_0), linear extension stretch (λ_{linear}), locking stretch (λ_{LCap}), and area expansion modulus (K_{Cap}) are found to be 7,081 Pa, 1.026, 1.043, and 0.948 MPa, respectively.

Values obtained from the literature were used for the instantaneous bulk modulus ($K_{Lim} = 0.22$ GPa), permeability exponent ($M = 4$), and volume fraction of free fluid in the liver ($f_w = 0.5$). The parameter describing the viscous component of the parenchyma is represented by $\left(\frac{\dot{\gamma}}{S^m}\right)$. Therefore, the initial shear rate $\dot{\gamma}_0$ was set to 0.01 and the shear strength S_p and exponent m were identified. Lastly, given the slope of the unloading force versus displacement ramp indentation data, the limiting shear modulus (μ_{Lim}) was set to 1.5 MPa. The identification of the remaining seven parameters proved to be a difficult task. Although a range is identified for each parameter using an independent swelling test and results from the indentation data, convergence of the optimization technique was highly sensitive to the initial values of the parameters. This difficulty highlights the issue of finding a global minimum in the 7-dimensional parameter space, and the uniqueness of the parameters. Despite these difficulties, the form of the model appears to capture the unique features associated with the data seen in Chapter 3. Although exact values for the remaining material parameters are not possible at this time, approximate ranges (min-max) are as follows: μ_0 (1.35-28.96) Pa, λ_L (1.035-1.051), G_p (40.3-116.0) Pa, S_p (2.4-14.2) kPa, m (1.18-2.5), K_s (6.6-25.0) kPa, and κ_0 (0.86-11.2)mm⁴/Ns.

Inconsistencies between the model and the data, namely the underestimated hysteretic response and overestimated hyperelastic response, suggest that improvements should be made. These considerations were outlined in Chapter 4. One change would be to remove the split dependency of the model, and allow the collagen in the parenchyma network to change volume. Although still considered highly incompressible, small changes in volume, including the allowance of a prestretch, may have large effects on the model response due to the sensitivity of the Langevin function used to define the Arruda-Boyce network. A prestretch has been considered to be a necessary component in representing other hydrated tissues described by the 8-chain network (Bischoff, et al. 2000; Jordan, et al. 2005a). Another change would be to allow the capsule to relax. Collagenous

membranes have been shown to exhibit time-dependant behavior, particularly in the lung (Suki, et al. 2005) and chorioamnion (Prevost 2006), where It is presumed that relaxation is influenced by the fractal properties of individual collagen and elastic fibers.

6.3 Assessing the Accuracy of Real-Time Surgical Simulation Models

The form of the constitutive model can be considered as a “ground truth” model for the liver. Although necessary for characterizing the complete mechanical response for the liver, such a model is excessively complex for real-time implementation into surgical simulation algorithms. Assessing the accuracy-versus-speed tradeoff is a constant concern in surgical simulation. How similar does the simulation need to be to the real tissue response so that no difference in performance is seen? Tendick et al. suggested that the necessary resolution of the model is limited by the perceptual capabilities of the users, and others have reported a 17% just noticeable difference in detecting differences in compliant materials (Ottensmeyer and Salisbury 2001a; Tendick, et al. 2000). Chapter 5 presented a technique for creating physical standards to be used to validate the simplified surgical simulations to real materials.

6.4 Future Work

6.4.1 Constitutive Model Parameter Uniqueness

As was indicated above, ensuring that a global minimum is found in the 7-dimensional solution space requires a good initial estimate for the initial parameter values. One approach to estimating these values would be to approximate the experimental data with a uniaxial assumption. Treating the constitutive model under uniaxial conditions would allow an analytical solution to be obtained. A linear attempt to this solution is described in Appendix B.

Even with good start values for the parameters, the question of uniqueness remains. In this work, a 3D model represented a 3D organ but the data used to identify the model parameters were in 2D (reaction force and displacement). Realizing that the tissue is compressible is an important feature of the model. Others have tried to measure the Poisson’s ratio of soft tissue, but these assumed a linear relationship existed (Carter, et al. 2001; Farshad, et al. 1999; Miller, et al. 2000b). More information can be experimentally obtained using a 3D ultrasound scanner to collect the volumetric strain field beneath the indenter. An optical flow tracking technique could then be used to obtain the volumetric response (Jordan, et al. 2005b). The experimental apparatus has been modified to allow for the ultrasound scanner to be positioned beneath the liver, under the area of indentation. The additional information can be used to better determine the compressibility (represented by the volumetric network component K_v) of the tissue. The assumption is that even though different values of the same material parameters could produce similar force-versus-displacement results, the 3D strain field would serve as a unique “fingerprint” of the response to help identify unique material properties of the tissue.

6.4.2 Applying Techniques to Other Organs

This work focused on developing measurement and modeling techniques to characterize the nonlinear viscoelastic behavior of liver. Under the assumption that a

variety of soft tissues are comprised of similar constituents (collagen, cells, extracellular fluid, etc.) the methods developed here could be implemented to modeling the nonlinear viscoelastic response of other perfused, solid, abdominal, organs such as kidney and spleen. Each tissue would have a unique set of material parameters depending on the amount and type of each constituent within the tissue. For instance, since liver has been shown to have a stiffer response than spleen (Carter, et al. 2001) it would have a higher value for the elastic parameters compared with the spleen. The reverse would be true for the kidney, which has been shown to have a stiffer response than the liver (Melvin, et al. 1973). In this way, a comprehensive atlas of tissue properties could be identified.

Similarly, once the constitutive relations were obtained, and the material parameters identified for the normal state of the tissue, the models could then be used to determine the response of various pathologic states. Comparing the difference in material parameters between the normal and the pathologic state could provide insight into the disease progression, and help with diagnosis. For instance, it has been shown that the disease states of some tissues like breast and prostate manifest with changes in stiffness (Krouskop, et al. 1998; Wellman 1999). Similarly, Carter et al. have reported changes in liver stiffness across pathology (2001).

6.4.3 Internal Parenchyma Measurements

With the exception of the results from Carter et al. (2001), most material testing data have been collected on animal tissues. Although these tissues serve as excellent surrogates to human tissues, the ability to non-invasively collect the mechanical response of human tissue would be invaluable. I have developed an instrumented balloon-catheter to measure the pressure-volume response of the tissue surrounding it. Balloon catheters are commonly introduced transfemorally into the hepatic vein to record the hepatic wedge pressure, which is used as an indicator for various liver diseases. Since the hepatic veins have very little cellular content, I assume that by filling the balloon with an incompressible fluid (i.e. water or saline), and applying known changes in volume, direct measurements of the parenchyma could be ascertained. Visual information from 3D ultrasound could be used to gather the necessary boundary condition information. The results could then be easily implemented into a finite element model, and the inverse solution obtained as described in Chapter 4. Appendix C describes the device in detail and provides preliminary data on perfused, *ex vivo*, porcine livers.

6.5 Final Words

The research presented in this thesis served to establish a realistic, physically-based, constitutive model for the liver. The model is capable of capturing the nonlinear viscoelastic response of liver under finite deformations. Numerous viscoelastic tests were conducted using an *ex vivo* perfusion apparatus allowing the near *in vivo* behavior of liver to be measured and parameters of the model to be identified. This work provides the framework, methodology, and results necessary to advance the progress of surgical simulation, and contribute to the paradigm shift occurring in procedural-based medicine today.

Appendix A

Characterization of Motorized Indentation System

This appendix provides more detail on the motorized indentation system presented in Chapter 3. The LM1 motor was mounted onto a testing frame constructed of 6060 T6 Aluminum profiles (MiniTec Framing Systems, LLC Victor, NY). The stiffness of the frame was measured using the 200 N load cell and a 25.4 mm diameter flat, cylindrical indenter. The indenter pushed onto the framing system while force and displacement were recorded. The stiffness of the system was found to be 456 kN/m.

A rigorous calibration protocol for the displacement, force, and accelerometer sensors was conducted before and after each test. All data were sampled at 1-2k Hz and filtered forward and backward with a 4-pole Butterworth low-pass filter with a cutoff frequency of 60 Hz. With the control software turned off, a spacer was placed between the indenter and the support plate and brass shims of known thickness were placed under the indenter in a step-like fashion (0, 0.85, 1.63, 0.85, 0 mm). The mean response over 2 seconds of the flat region (avoiding the initial spikes due to my manual loading) was taken at each point. The slope of the measured response to the actual displacement was used as a calibration constant for the LVDT (Figure A1.1).

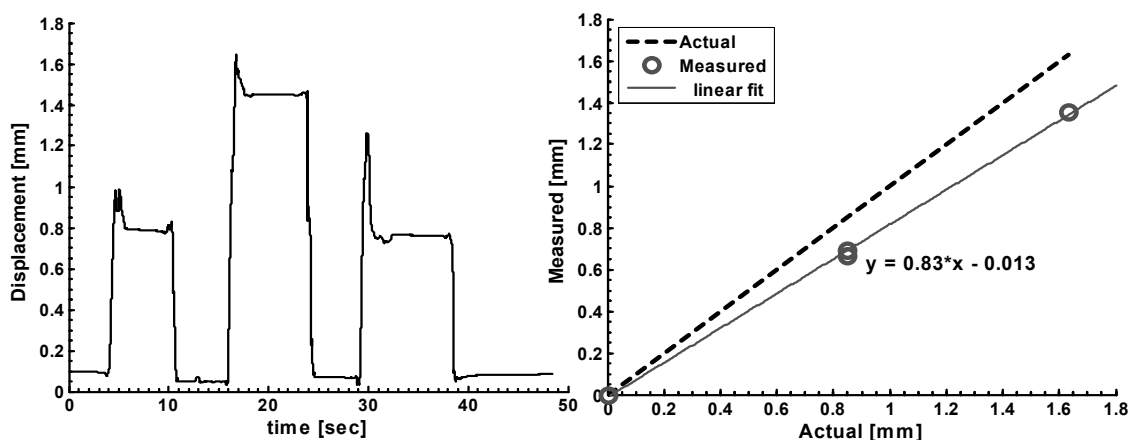


Figure A1.1 Example of the displacement data and calibration curve for the LVDT.

The force sensor was calibrated by hanging masses in a step-like fashion (20, 50, 100, 50, 20 g) from the indenter. Using the same protocol as for the LVDT calibration, the best fit line to the measured versus actual load data was used as a calibration constant for the force sensor (Figure A1.2).

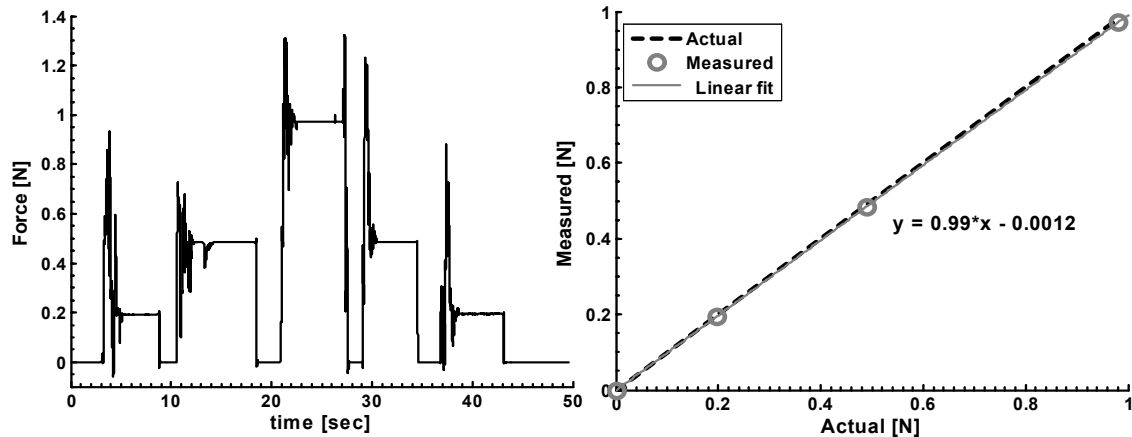
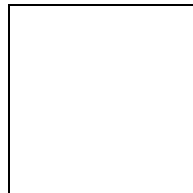


Figure A1.2 Example of a calibration data and curve for the force sensor.

Two tests were done to assess the passive characteristics of the system. Step and impulse inputs to the system revealed a second-order underdamped response. The step input was obtained by using a 9.5 mm diameter spherical indenter (Delrin®) on the end of the 22 N load cell. A 1.6 mm thick shim was used to displace the indenter from the resting zero displacement position. The shim was placed on a polished aluminum plate with a hole cut out to allow for the free motion of the indenter once the shim was removed. The shim was slid out from under the indenter and displacement was recorded over time at 4 kHz (Figure A1.3). Four trials were conducted and the time from zero (taken to be the point of step application) to the peak oscillation (T_{peak}), from zero to the point where the response is within 2% of the steady state value (T_{ss}), the log decrement ($\delta = \ln(x_1/x_2)$ where x_1 and x_2 are values of the first two peak displacements related to the steady state value), and the natural frequency (ω_n) were recorded (Table A1.1). The damping ratio is calculated from the log decrement using



(A1.1)

An impulse input was also applied by tapping a 12 mm diameter cylindrical indenter with a metal rod. Three taps were conducted sequentially and two trials were taken. The same variables were recorded as for the step response. An example of the impulse response and the recorded variables are shown in Figure A1.4 and Table A1.2,

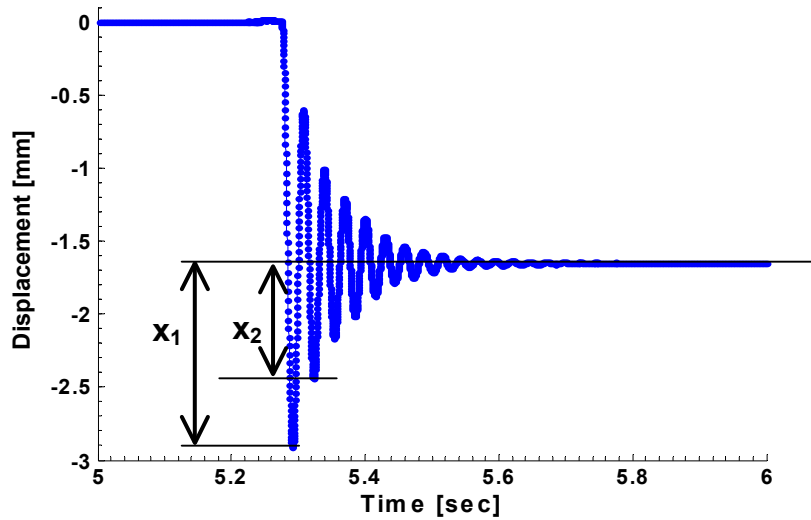


Figure A1.3 Example of passive response from a 1.6 mm step displacement.

respectively. The differences between the two responses are due to the two indenters having different weights.

Variable	Mean	SD
T_{peak} [ms]	19.5	2.1
T_{ss} [ms]	276	12.7
% OS	69.9	3.5
δ	0.473	0.018
ω_n [rad/sec]	206.35	1.68
ξ	0.012	4.5×10^{-4}

Table A1.1 Values for the passive response of system to a step displacement input.

Variable	Mean	SD
T_{peak} [ms]	7.9	0.26
T_{ss} [ms]	465.7	58.9
% OS	13.1	3.97
δ	0.447	0.268
ω_n [rad/sec]	231.42	3.44
ξ	0.0112	0.0067

Table A1.2 Values of the passive response of the system to an impulse.

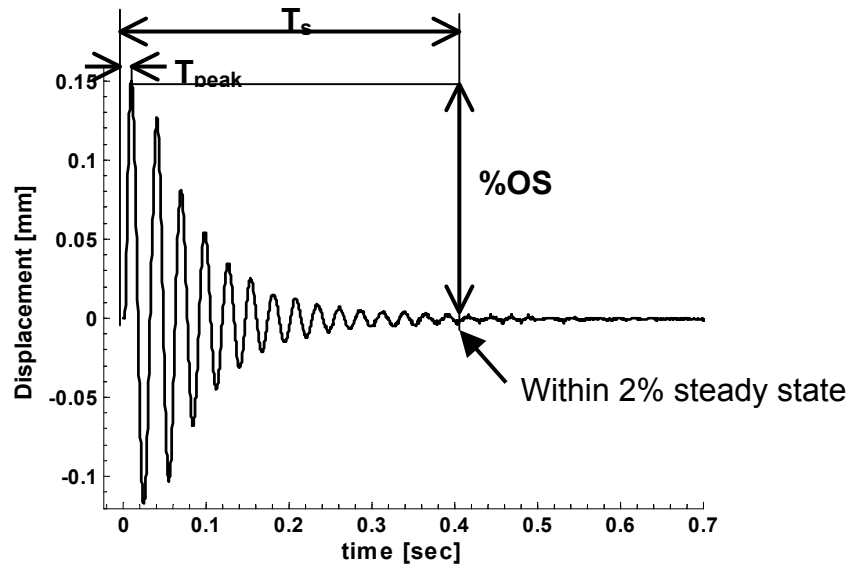


Figure A1.4 Example of system passive response from an impulse input.

Before an active characterization could be carried out, the PID (position, integral, derivative) gains of the WinTest™ Digital Controller were tuned. A similar tuning procedure was done before every indentation test. A 1 Hz square waveform with 6-8 mm peak-to-peak amplitude is commanded to move the indenter with no load. The values for the position, integral, and derivative gains are adjusted until the system response matches the commanded response. A similar protocol is done once the liver is in place and perfusion had begun. A 1 Hz square wave (for the sinusoidal indentation and stress relaxation tests) and a 5 Hz triangle wave (for the constant rate ramp tests) to 30% nominal strain (displacement / thickness) were imposed on a lobe of the liver not used for further testing (Figure A1.5).

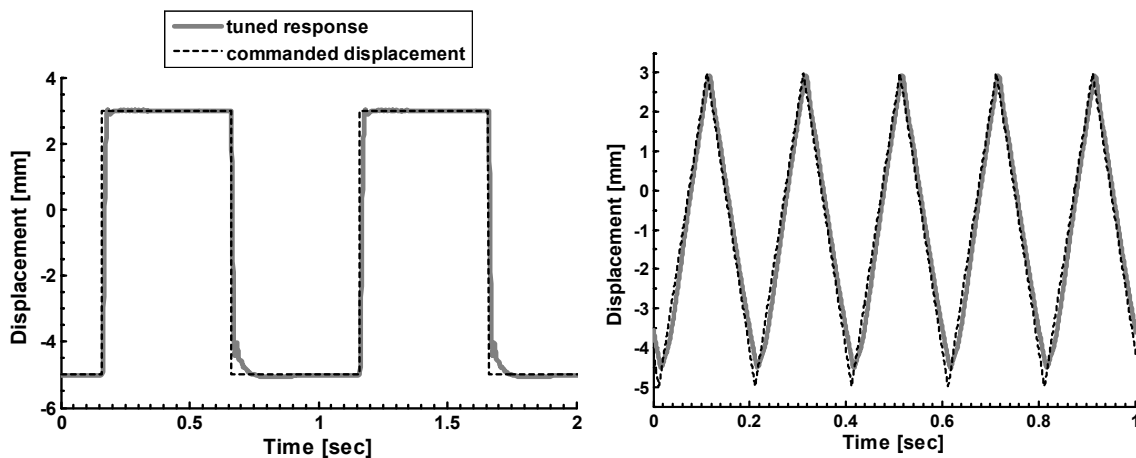


Figure A1.5: Example of the PID tuned responses of the indentation system when subjected to a 1 Hz square wave (Left), and 5 Hz triangle wave (Right) commanded waveforms. Maximum displacement corresponded to 30% nominal strain.

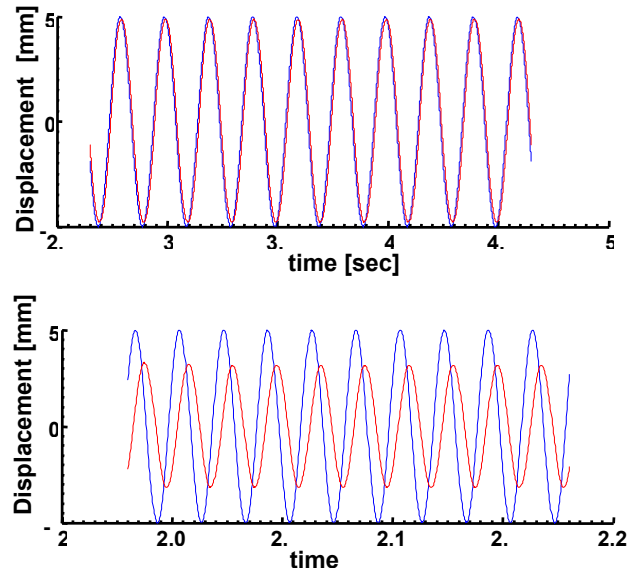
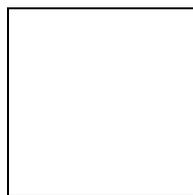


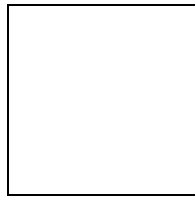
Figure A1.6 Example of a typical response of the system without an indenter for a 10 mm amplitude commanded (blue) and actual (red) displacement for 5 Hz (Top) and 100 Hz (Bottom).

The active system response was determined using sinusoidal displacement waveforms across frequency. The frequency bandwidth and phase shift were established by collecting displacement while commanding either 1, 5, or 10 mm amplitude sine waves from 5 to 120 Hz to the motor. These measurements were performed without an indenter. A typical response of the commanded and actual waveform for the 10 mm trial at 5 and 100 Hz are shown in Figure A1.6.

Figure A.17 is the Bode plot for the mean (across 10 cycles) actual and commanded magnitudes. The results suggest that the system has a 50 Hz frequency bandwidth (where the magnitude drops 3 db) and a maximum frequency of 70 Hz (above which the phase is greater than 90°). A similar test was carried out using the 12 mm diameter indenter to compress into silicone rubber (40:60 mixture of RTV6166, General Electric Co.). The results suggest that the working bandwidth for large displacements ensuring consistency is less than 30 Hz.

To account for inertial effects, an accelerometer was incorporated into the system. Prior to each indentation test, the mass of the indenter and the acceleration calibration constant were found in order to determine the force from acceleration. A 25 Hz sine wave with 8 mm peak-to-peak amplitude was commanded into the air using the square wave PID gains. The amplitude of the accelerometer output was compared to the second derivative of the commanded sine wave to determine the calibration constant (A_{cal})





A1.3

$$\frac{d^2 x}{dt^2} = -M\omega^2 \sin(\omega t) \tag{A1.4}$$

$$A_{cal} = \frac{A_{signal}}{A_{Gain}} \left(\frac{M\omega^2}{A_{amp}} \right) \tag{A1.5}$$

where x is the commanded sine wave, M is the amplitude, ω is the frequency, t is time, A_{signal} is the raw voltage from the accelerometer, A_{Gain} is the gain for the accelerometer (set to 5), and A_{amp} is $-M\omega^2$ from A1.4. Since force is equal to mass times acceleration,

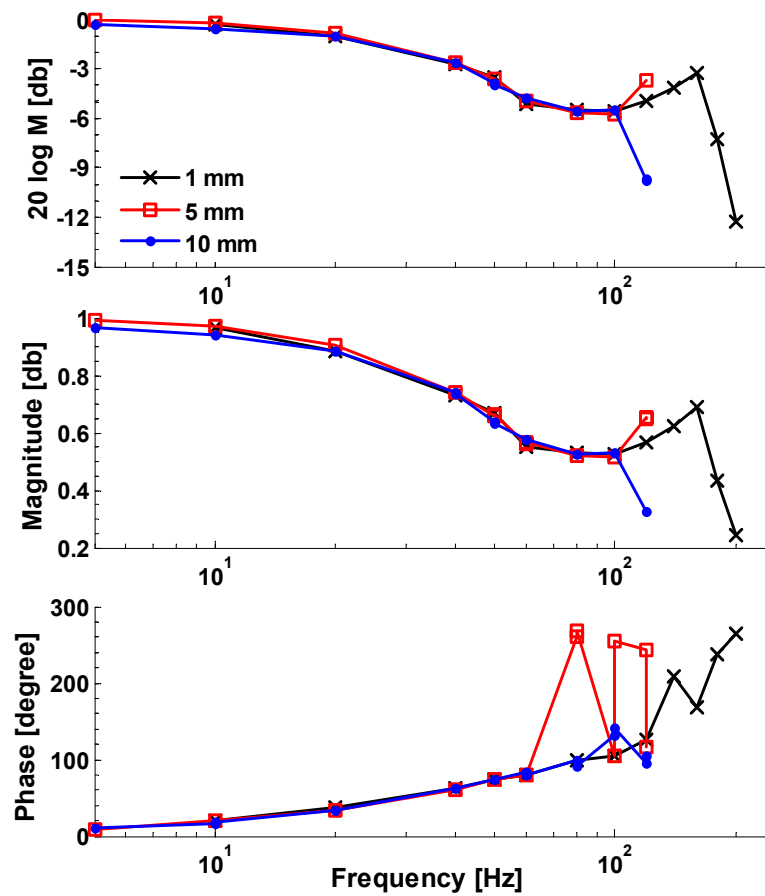


Figure A1.7 Bode plots of the motorized indenter system without an indenter mass.

the mass of the indenter (which includes the mass of the suction tubes, connecting screw, $\frac{1}{2}$ the moving mass in the load cell etc.) is calculated by dividing the force from the load cell by the calibrated acceleration (9.80 ± 1.02 g for the 12 mm diameter indenter used in the indentation tests). For an initial study, a 31 g spherical indenter, the 12 mm diameter test indenter, and no indenter were used to find A_{cal} and the mass of the different scenarios (Figure A1.8). Lastly, the force due to acceleration is calculated by multiplying the mass of the indenter times the acceleration and this is subtracted off of the load cell signal resulting in the true force from the environment (Figure A1.9). This procedure was carried out again by compressing a metal spring 10 mm for a single cycle of a sinusoidal waveform from 1 to 25 Hz. The results show a linear force versus displacement response across speed with slight hysteresis (due to friction of the spring against the well it sat in) and that forces due to acceleration were significant after 10 Hz.

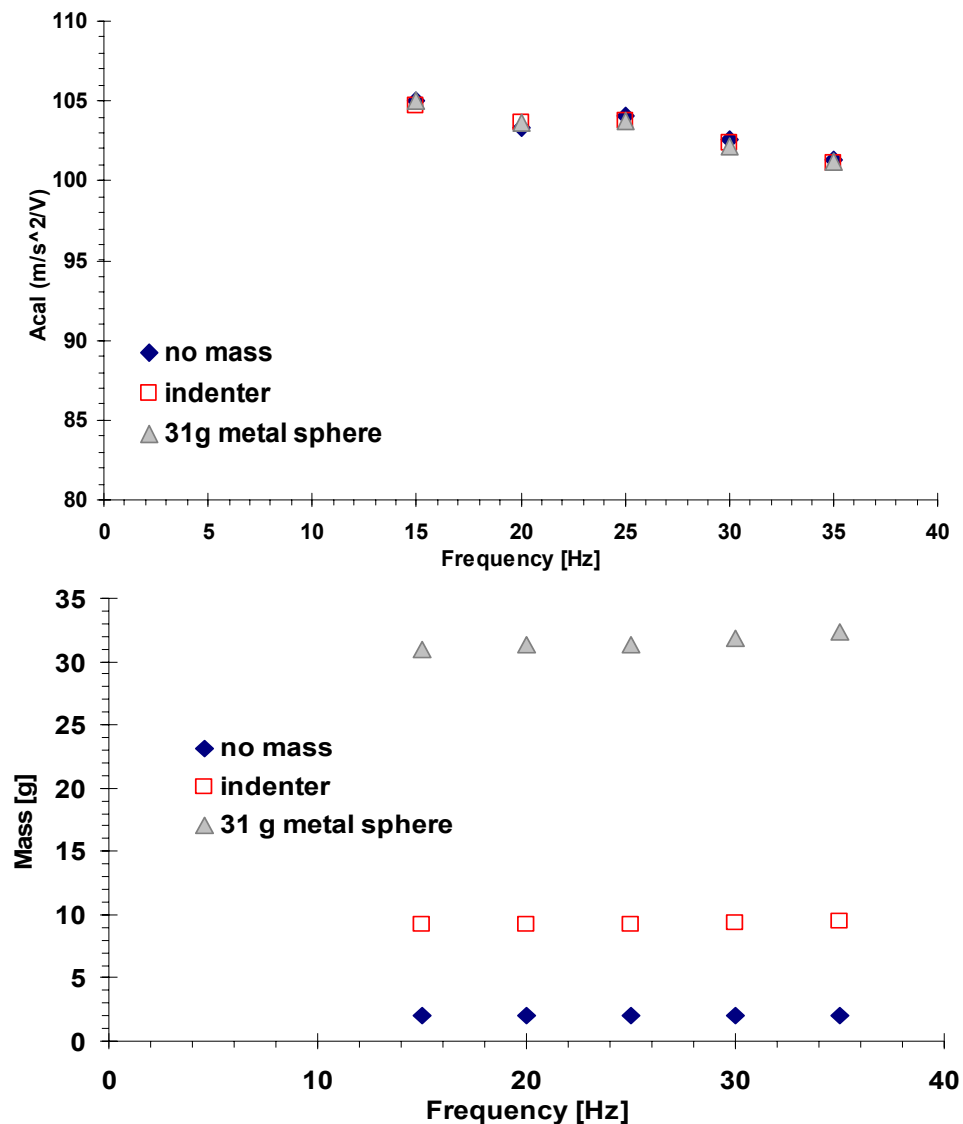


Figure A1.8 Example of determining the accelerometer calibration constant and the mass of three different indenters using 25 Hz sinusoidal waveforms.

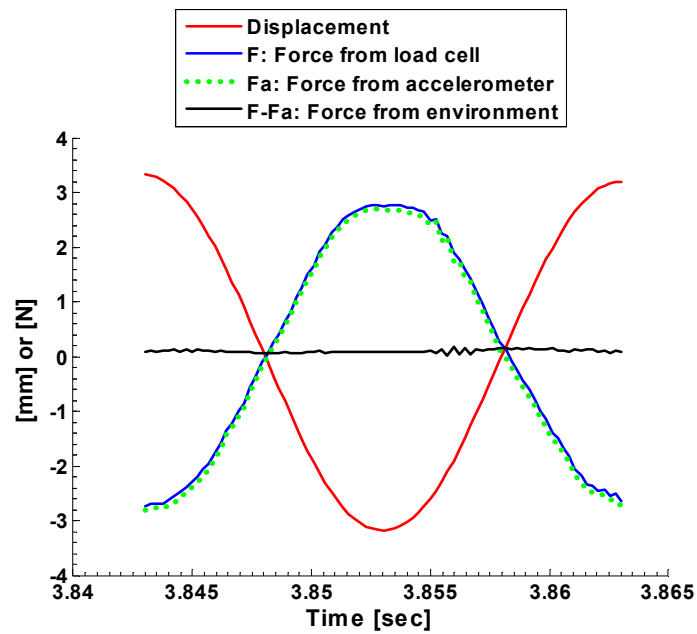


Figure A1.9 Example of the accelerometer calibration resulting in forces due to acceleration cancelling the force read from the force sensor. Shown is 1 cycle of displacement, force from the load cell, calculated force from the accelerometer, and the force from the environment (air) for a 25 Hz commanded sine wave.

Appendix B

Linear Analytical Approximation of the Constitutive Model

In this appendix, the constitutive model presented in Chapter 4 is simplified to an analytical linear approximation. This representation can be used to ensure that the form of the constitutive model is correct, and to determine approximate start values for the material parameters. A nonlinear analytical representation could obtain values for the model's actual material parameters.

The indentation data is represented with a uniaxial compression approximation. The volume of tissue under the indenter is assumed to be the same as a uniaxial section with dimensions equal to 1.5 times the radius of the indenter (R), and with the same thickness (h) (Figure A2.1). With this approximation, stresses and strains can be used instead of forces and displacements, and both sides of the model can be assumed to experience the same strain.

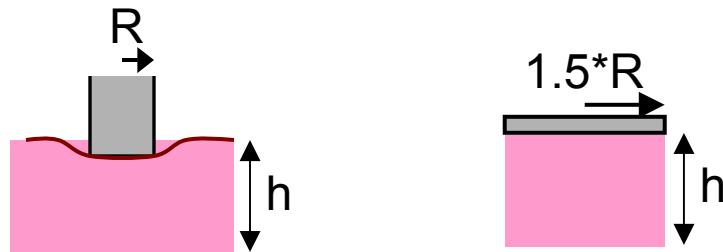


Figure A2.1 Representing the indentation scenario (Left) with a uniaxial approximation (Right).

The lumped parameter model is therefore simplified into the isochoric and volumetric parts with linear springs and dashpots replacing the nonlinear and biphasic components (Figure A2.2). The isochoric side can be treated as a standard linear solid viscoelastic model with a shear modulus G , and the volumetric side is a simple Voigt viscoelastic model with bulk modulus B .

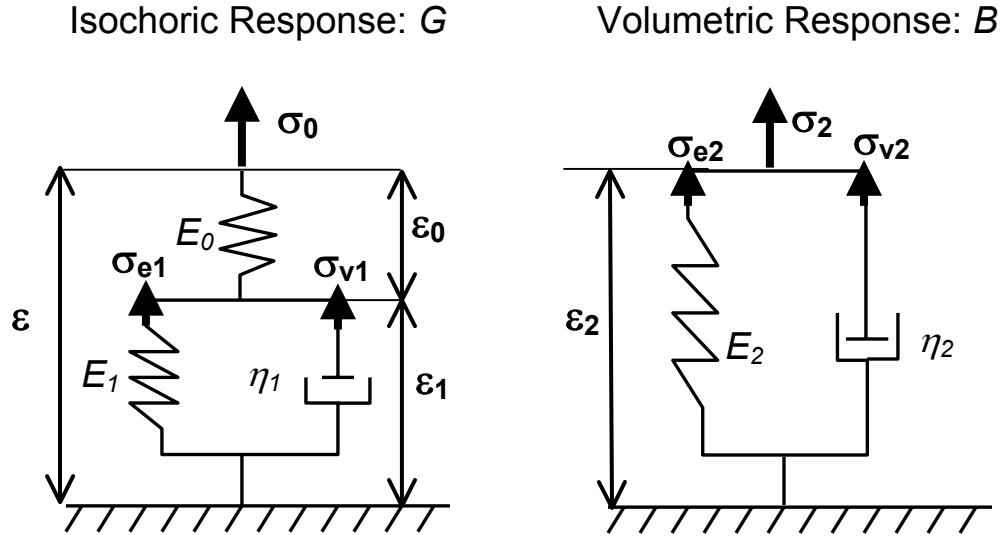


Figure A2.2 Schematic representation of the simplified tissue model.

$$\sigma_0 = \mathbf{E}_0 \varepsilon_0 = \sigma_1 = \sigma_{e1} + \sigma_{v1} \quad \text{A2.1}$$

$$\sigma_{e1} = \mathbf{E}_1 \varepsilon_1 \quad \text{A2.2}$$

$$\sigma_{v1} = \eta_1 \dot{\varepsilon}_1 \quad \text{A2.3}$$

$$\varepsilon = \varepsilon_0 + \varepsilon_1 \quad \text{A2.4}$$

$$\sigma_2 = \sigma_{e2} + \sigma_{v2} \quad \text{A2.5}$$

$$\sigma_2 = \mathbf{E}_2 \varepsilon_2 + \eta_2 \dot{\varepsilon}_2 \quad \text{A2.6}$$

$$\varepsilon = \varepsilon_2 \quad \text{A2.7}$$

The ramp displacement waveform is approximated by a step displacement plus a sinusoidal waveform for ease of analysis. Therefore, assuming that both sides of the model experience the same strain (Equation A2.7), the strain and strain rate can be represented by

$$\varepsilon(t) = \varepsilon - \varepsilon_i \sin \omega t \quad \text{A2.8}$$

$$\dot{\varepsilon}(t) = -\varepsilon_i \omega \cos \omega t \quad \text{A2.9}$$

where ε_i is the initial strain, ω is the frequency of the sine wave and t is time. The stress response for the sine wave part is assumed to also be a sine wave shifted in time by phase shift δ ,

$$\sigma(t) = -\sigma_i \sin(\omega t + \delta) \quad \text{A2.10}$$

$$\dot{\sigma}(t) = -\sigma_i \omega \cos(\omega t + \delta) \quad \text{A2.11}$$

while the step response is assumed to have an exponentially decaying stress response. Substituting equations A2.8-11 into equations A2.1-6 results in the equation of motion for each side

$$\sigma_0(t) = \varepsilon_i \left(\frac{E_0 E_1}{E_0 + E_1} \right) \left[1 - e^{-t \left(\frac{E_0 + E_1}{\eta_1} \right)} \right] + \quad \text{A2.12}$$

$$\left(\frac{E_0 \varepsilon_i}{(E_0 + E_1)^2 + \omega^2 \eta_1^2} \right) \left[\sin \omega t (E_1 (E_0 + E_1) + \omega^2 \eta_1^2) + \cos \omega t (E_0 \eta_1 \omega) \right]$$

$$\sigma_2(t) = -E_2 \varepsilon_i - \varepsilon_i \left[\sin \omega t (E_2) + \cos \omega t (\eta_2 \omega) \right] \quad \text{A2.13}$$

The right hand term of each equation of motion is the response from the sinusoidal input, and these can be used to determine the shear and bulk storage (in phase) and loss (out of phase) moduli (G_S , G_D , B_S , B_D) and the shear and bulk complex moduli (G^* , B^*)

$$G_S = \frac{E_0 (E_1 (E_0 + E_1) + \omega^2 \eta_1^2)}{(E_0 + E_1)^2 + \omega^2 \eta_1^2} \quad \text{A2.14}$$

$$G_D = \frac{\omega \eta_1 E_0^2}{(E_0 + E_1)^2 + \omega^2 \eta_1^2} \quad \text{A2.15}$$

$$G^* = (G_S + iG_D) \quad \text{A2.16}$$

$$B_S = E_2 \quad \text{A2.17}$$

$$B_D = \omega \eta_1 \quad \text{A2.18}$$

$$B^* = (B_S + iB_D) \quad \text{A2.19}$$

Assuming uniaxial compression, an overall elastic moduli (E^*) for the model can be represented by

$$E^* = \frac{9B^* G^*}{G^* + 3B^*} = E_S + iE_D \quad \text{A2.20}$$

where the storage (E_S) and loss (E_D) moduli for the whole model can be determined by substituting equations A2.14-A2.19 into A2.20.

$$E_S = \frac{9E_0(\text{num})}{\text{den}} \quad \text{A2.21}$$

$$\text{num} = (3(E_1^2 + \omega^2 \eta_1^2)(E_2^2 + \omega^2 \eta_2^2) + E_0(E_2(E_1^2 + 3E_1 E_2 + \omega^2 \eta_1^2) + 3\omega^2 E_1 \eta_2^2)) \quad \text{A2.22}$$

$$\begin{aligned} \text{den} = & 9(E_1^2 + \omega^2 \eta_1^2)(E_2^2 + \omega^2 \eta_2^2) + 6E_0(E_2(E_1^2 + 3E_1E_2 + \omega^2 \eta_1^2) + 3\omega^2 E_1 \eta_2^2) + E_0^2((E_1 + 3E_2)^2 + \omega^2(\eta_1 + 3\eta_2)^2) \end{aligned} \quad \text{A2.23}$$

$$E_D = \frac{9\omega E_0^2(3E_2^2 \eta_1 + \eta_2(E_1^2 + \omega^2 \eta_1(\eta_1 + 3\eta_2)))}{\text{den}} \quad \text{A2.24}$$

At high and low frequencies the loss modulus tends towards zero while the storage modulus reduces to

$$\lim_{\omega \rightarrow \infty} (E_S) \rightarrow 3E_0 \quad \text{A2.25}$$

$$\lim_{\omega \rightarrow 0} (E_S) \rightarrow \frac{9E_0 E_1 E_2}{3E_1 E_2 + E_0(E_1 + 3E_2)} \quad \text{A2.26}$$

The tangent of the phase shift is taken to be the loss modulus divided by the storage modulus

$$\tan \delta = \frac{\omega E_0(3E_2^2 \eta_1 + \eta_2(E_1^2 + \omega^2 \eta_1(\eta_1 + 3\eta_2)))}{3(E_1^2 + \omega^2 \eta_1^2)(E_2^2 + \omega^2 \eta_2^2) + E_0(E_2(E_1^2 + 3E_1E_2 + \omega^2 \eta_1^2) + 3\omega^2 E_1 \eta_2^2)} \quad \text{A2.27}$$

Assigning values for the spring and dashpot constants, the storage modulus, loss modulus, and $\tan \delta$ (Equations A2.21, A2.24, A.27) are plotted versus frequency in Figure A2.3. The values for the constants are: $E_0 = 5,131.4$ Pa (from a spring constant $K_0 = 50$ N/m), $E_1 = 513.15$ Pa (from a spring constant $K_1 = 5$ N/m), $E_2 = 2,565.7$ Pa (from a spring constant $K_2 = 25$ N/m), $\eta_1 = 10,263$ Pa s (from a dashpot constant $b_1 = 100$ Ns/m), and $\eta_2 = 1,026.3$ Pa s (from a dashpot constant $b_1 = 10$ Ns/m).

Given Figure A2.3 and the equations presented above, the constants for the model can be determined. A more robust interpretation of the model would provide a better estimation of the model parameters by comparing the predicted moduli to the moduli from the single ramp rate data collected in Chapter 3. Changes to this analytical model would include using the appropriate nonlinear springs and dashpots and using the combined modulus for indentation in place of Equation A2.20 (although meant for infinitesimal strains)

$$E^* = \frac{12G^*(-3B^* + G^*)^2}{(9B^* - 4G^*)(3B^* + G^*)} \quad \text{A2.28}$$

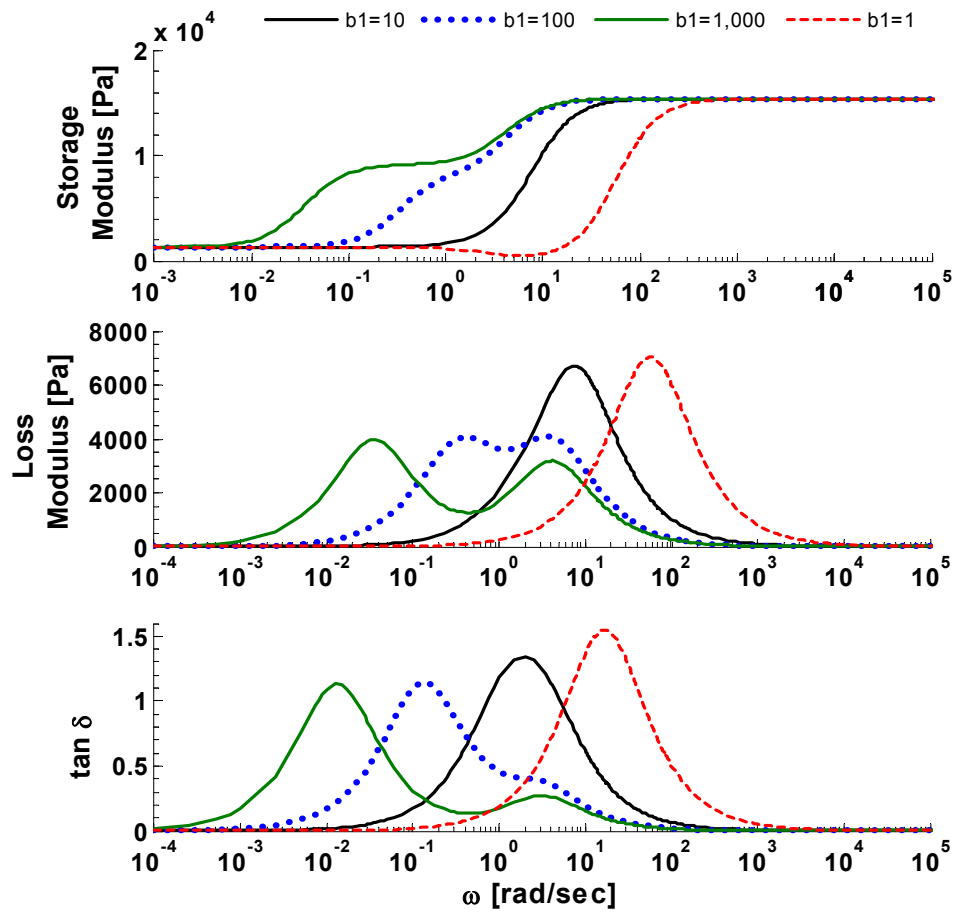


Figure A2.3 The storage modulus (Top), loss modulus (Middle), and $\tan \delta$ (Bottom) of the linear model across frequency. The different curves represent different values for the isochoric dashpot [units for $b = \text{Ns/m}$].

Appendix C

Instrumented Balloon Catheter

This appendix describes a device to measure the pressure response of the parenchyma directly from known changes in volume. Due to the minimal cellular content of the hepatic veins, inflating an occlusion balloon catheter in these veins to known volumes while recording the pressure response allows for direct parenchyma material property information. Since these catheters are already commonly used to measure hepatic wedge pressure, such a device could allow for *in vivo* measurements to be made on humans.

The catheter used for the prototype was 65 cm long, 2.3 mm diameter with a 20 mm diameter balloon (Equalizer Balloon Catheter, Boston Scientific, Cork Ireland). The air was removed from the catheter and replaced with saline solution. The catheter was connected to a 10 cc syringe attached to a syringe pump constructed using a high precision linear actuator (43.4 mm of travel, 2.7 μm RMS [Smart Motor, Ultramotion]). The end of the syringe was securely attached to the actuator, which was commanded to move a set distance at a certain rate and back. Pressure was recorded using a differential pressure sensor (0.03 psi RMS) (PX26-o30GV, Omega). The setup is shown in Figure A3.1, and an example of the balloon inside the liver is shown in Figure A3.2.

Several calibrations were conducted to ensure proper balloon volume control and pressure response. First the pressure sensor was calibrated by attaching a 0-15 psi pressure gauge in line with the catheter and the sensor. The syringe was compressed manually while recording the pressure off of the gauge and the voltage off of the DAQ card at 2 kHz (Figure A3.3 top).

To determine the actual syringe displacement compared to the commanded displacement, one end of a digital caliper was directly clamped to the end of the actuator while the other was secured to a stationary block. The motor was commanded to move a specific displacement while the digital caliper recorded the actual displacement (Figure A3.3 middle). The actuator speed was determined by considering the slope of the voltage versus time data (Figure A3.4).

Finally, a graduated cylinder was connected to one end of the syringe while the other was connected to the calibrated linear actuator. The actuator moved in 1 mm increments while the volume in the cylinder was recorded (Figure A3.3 bottom). All data were collected at 2 kHz and filtered forwards and backwards with a 4-pole Butterworth low-pass filter with cutoff frequency of 10 Hz.

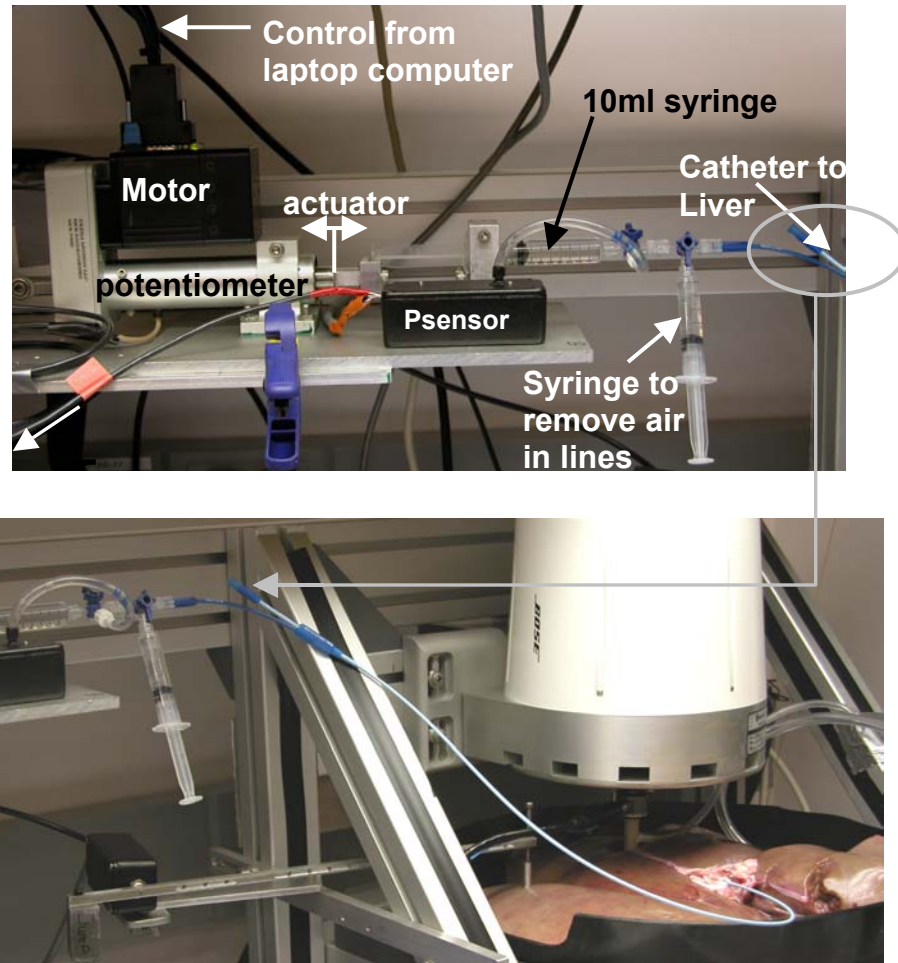


Figure A3.1 Pressure-Volume sensing balloon catheter device with linear actuator positioned in a porcine liver.



Figure A3.2 A dissection of a porcine liver post testing showing an inflated balloon inside the hepatic vein.

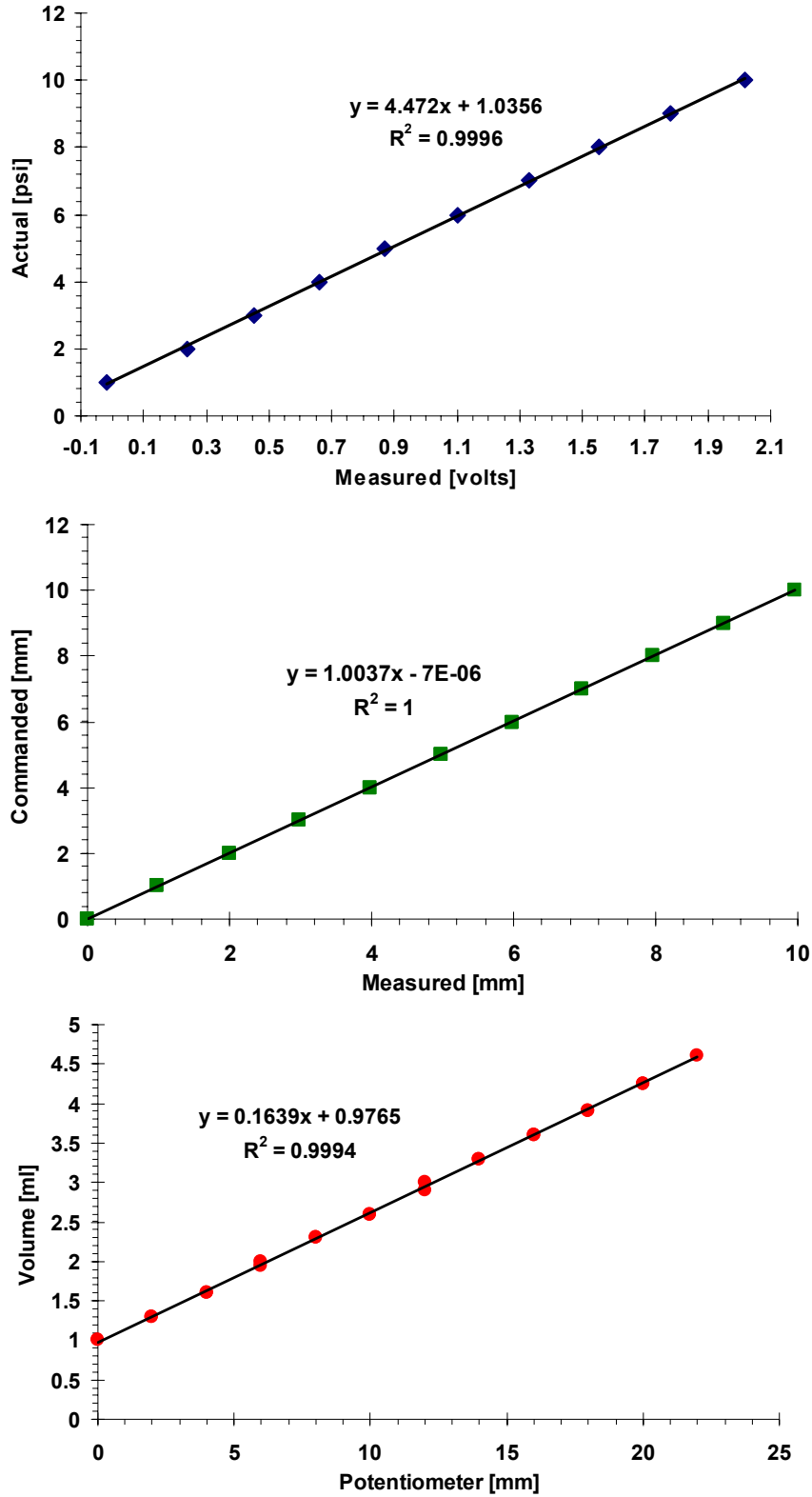


Figure A3.3 (Top) Pressure sensor calibration. (Middle) Linear actuator calibration. (Bottom) Volume calibration.

Three trials were conducted in the same porcine livers used to collect the multiple ramp indentation, stress relaxation, and creep tests in Chapter 3. All trials were done following the completion of the indentation tests. The balloon catheter was inserted through the inferior vena cava into the hepatic vein (~5-10 cm), and 3D Ultrasound was used to observe inflation within the liver.

Prior to testing tissue, the balloon was allowed to inflate in air (no resistance) while pressure and volume were recorded. The balloon was inflated anywhere from 20-45 mm at 1-10 mm/s. Once in the liver, several protocols were tried. Incremental inflations of set volumes at set rates or constant rate inflations at set volumes were used to inflate the balloon with saline. The balloon was either allowed to rest at the inflated volume before deflating to the initial volume, or was commanded to deflate immediately after inflation (Figure A3.4). Either way, several rates and volumes were tried for each liver tested. The data were collected at 2 kHz and filtered forward and back with a 4-pole Butterworth filter with 20 Hz cutoff frequency.

An example of the pressure volume response within a porcine liver compared to one in air for 2 livers is shown in Figure A3.5. The initial rise in pressure for all cases is indicative of the pressure it takes to initially begin balloon inflation (from 0-0.8 ml). The air case then experiences a fall in pressure with increasing volume while the vessel cases experience a rise in pressure. The first inflation in the tissue for all livers tested showed a larger increase in pressure than the others. This could either be attributed to preconditioning, or that the tissue had failed (Figure A3.5 bottom). Faster rates of inflation led to increased hysteresis in the pressure-volume curve. Future tests should be done using the 3D US as a guide to ensure that the balloon volume does not damage the vessel, and to gather more far-field boundary condition as well as internal strain information within the parenchyma.

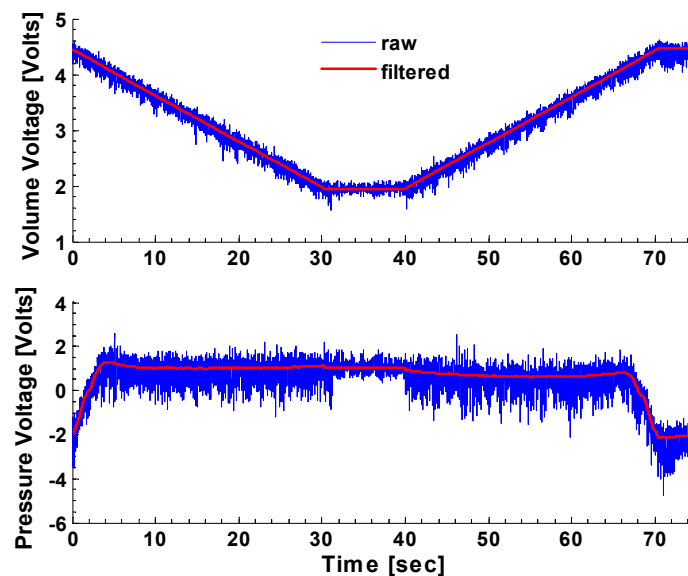


Figure A3.4 Example of the raw and filtered volume and pressure voltage recordings versus time for a ± 30 mm loading at 1 mm/s with a 10 second wait in porcine liver.

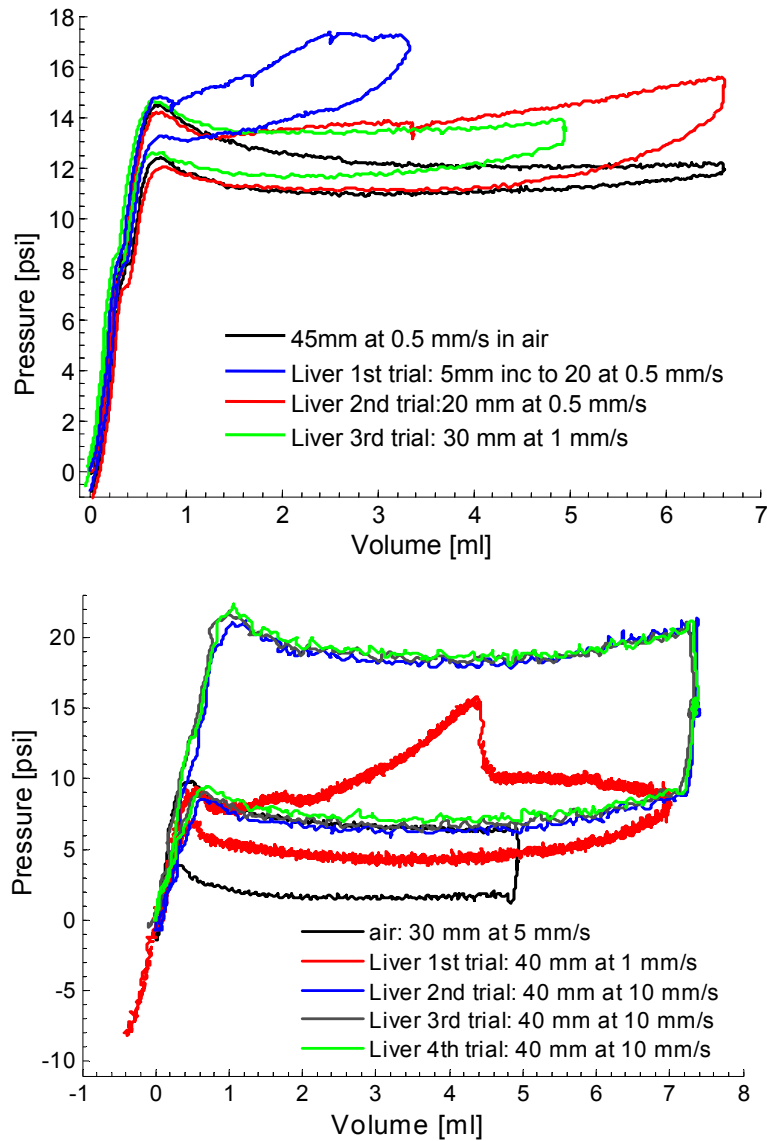


Figure A3.5 Pressure versus volume response for 2 different porcine livers as compared to air at different inflation volumes at different rates. (Top) Liver 1 up to 30 mm at 1 mm/s. (Bottom) Liver 2 to 40 mm between 1-10 mm/s showing more hysteresis, and a potential failure in the tissue for the first loading (red).

References

- ABAQUS. Abaqus Theory Manual, Version 6.3. Pawtucket, RI: Hibbitt, Karlsson, & Sorensen, Inc., 1997.
- Alexander DE, Ratzlaff KL, Roggero RJ, Hsieh JS-Y. Inexpensive, Semi-Automated System for Measuring Mechanical Properties of Soft Tissue. *J. Experimental Zoology* 1999; 284:374-378.
- Anand L. A Constitutive Model for Compressible Elastomeric Solids. *Computational Mechanics* 1996; 18:339-355.
- Arbogast KB, Thibault KL, Pinheiro BS, Winey KI, Marguiles SS. A High-Frequency Shear Device for Testing Soft Biological Tissues. *J. Biomechanics* 1997; 30:757-759.
- Arruda EM, Boyce MC. A Three-Dimensional Constitutive Model for the Large Stretch Behavior of Rubber Elastic Materials. *J. Mech. Phys. Solids* 1993; 41:389-412.
- Ateshian GA, Warden WH, Kim JJ, Grelsamer RP, Mow VC. Finite Deformation Biphasic Material Properties of Bovine Articular Cartilage from Confined Compression Experiments. *J. Biomechanics* 1997; 30:1157-1164.
- Bischoff JE, Arruda E, Grosh K. Finite Element Modeling of Human Skin Using an Isotropic, Nonlinear Elastic Constitutive Model. *Journal of Biomechanics* 2000; 33:645-652.
- Bischoff JE, Arruda EM, Grosh K. Constitutive Modeling of Human Skin Allowing for Anisotropy and Growth, Proceedings of the First Joint BMES/EMBS Conference, Atlanta, GA, 1999. Vol. 1.
- Boyce MC, Arruda EM. Constitutive Models of Rubber Elasticity: A Review. *Rubber Chemistry and Technology* 2000; 73:504-523.
- Braet F, Wisse E. Structural and Functional Aspects of Liver Sinusoidal Endothelial Cell Fenestrae: A Review. *Comparative Hepatology* 2002; 1.
- Bro-Nielsen M, Cotin S. Real-Time Volumetric Deformable Models for Surgery Simulation Using Finite Elements and Condensation, Eurographics, 1996. Vol. 15. Blackwell Publishers.
- Brouwer I, Ustin J, Bentley L, Sherman A, Dhruv N, Tendick F. Measuring in Vivo Animal Soft Tissue Properties for Haptic Modeling in Surgical Simulation, *Medicine Meets Virtual Reality*, Newport Beach, CA, 2001. Vol. 81. IOS Press.
- Brown JD. In-Vivo and Postmortem Biomechanics of Abdominal Organs under Compressive Loads: Experimental Approach in a Laparoscopic Surgery Setup. *Bioengineering*. Seattle: University of Washington, 2003:239.
- Brown JD, Rosen J, Chang L, Sinanan MN, Hannaford B. Quantifying Surgeon Grasping Mechanics in Laparoscopy Using the Blue Dragon System. In: *Studies in Health Technology and Informatics, Medicine Meets Virtual Reality*, Newport Beach, CA, 2004.
- Brown JD, Rosen J, Kim YS, Chang L, Sinanan MN, Hannaford B. In-Vivo and in-Situ Compressive Properties of Porcine Abdominal Soft Tissues, *Medicine Meets Virtual Reality*, Newport Beach, CA, 2003. Vol. 94. IOS Press.
- Brown JD, Rosen J, Moreyra M, Sinanan M, Hannaford B. Computer-Controlled Motorized Endoscopic Grasper for in Vivo Measurements of Soft Tissue Biomechanical Characteristics, *Medicine Meets Virtual Reality*, Newport Beach, CA, 2002. Vol. 85. IOS Press.

- Brown RA. Digestive System: Liver: Colorado State University, 1997.
- Bruyns C, Ottensmeyer MP. Measurements of Soft-Tissue Mechanical Properties to Support Development of a Physically Based Virtual Animal Model, Medical Image Computing and Computer-Assisted Intervention, MICCAI, Tokyo, Japan, 2002.
- Burkitt HG, Young B, Heath JW. Wheater's Functional Histology. New York: Churchill Livingstone, 1997:407.
- Butler AJ, Rees MA, Wight DGD, et al. Successful Extracorporeal Porcine Liver Perfusion. Transplantation 2002; 73:1212-1218.
- Carter FJ, Frank TG, Davies PJ, McLean D, Cuschieri A. Measurements and Modeling of the Compliance of Human and Porcine Organs. Medical Image Analysis 2001; 5:231-236.
- Casson FBd, Laugier C. Modeling the Dynamics of a Human Liver for a Minimally Invasive Simulator, Medical Image Computing and Computer Assisted Intervention (MICCAI), Cambridge, UK, 1999.
- Chen EJ, Novakofski J, Jenkins WK, Jr. WDOB. Young's Modulus Measurements of Soft Tissues with Application to Elasticity Imaging. IEEE Transactions on Ultrasonics, Ferroelectrics, and Frequency Control 1996; 43:191-194.
- Cotin S, Delingette H, Ayache N. Real-Time Elastic Deformations of Soft Tissues for Surgery Simulation. IEEE Transactions on Visualization and Computer Graphics 1999; 5:62-73.
- Cotin S, Delingette H, Ayache N. A Hybrid Elastic Model Allowing Real-Time Cutting, Deformation, and Force Feedback for Surgery Training and Simulation. The Visual Computer 2000; 16:437-452.
- Cotin S, Delingette H, Clement JM, Bro-Nielsen M, Ayache N, Marescaux J. Geometrical and Physical Representations for a Simulator of Hepatic Surgery, Medicine Meets Virtual Reality (MMVR'96), 1996.
- Davide Brunelli MD. Human Liver Illustration. Med Art Studio, 2001.
- Davies P. Mathematical Modeling for Keyhole Surgery Simulations: A Biomechanical Model for Spleen Tissue. IMA Journal of Applied Mathematics 2002; 67:41-67.
- Dawson SL. A Critical Approach to Medical Simulation. Bulletin of the American College of Surgeons 2002; 87:12-18.
- Debunne G, Desbrun M, Cani MP, Barr AH. Dynamic Real-Time Deformations Using Space & Time Adaptive Sampling, Siggraph, Computer Graphics Annual Conference Series, Los Angeles, August, 2001.
- Delingette H. Towards Realistic Soft Tissue Modeling in Medical Simulation, IEEE: Special Issue in on Virtual and Augmented Reality in Medicine, 1998. Vol. 86.
- Dokos S, LeGrice IJ, Smaill BH, Kar J, Young AA. A Triaxial-Measurement Shear-Test Device for Soft Biological Tissues. Journal of Biomechanical Engineering 2000a; 122:471-477.
- Dokos S, LeGrice IJ, Smaill BH, Kar J, Young AA. A Triaxial-Measurement Shear-Test Device for Soft Biological Tissues. J. Biomechanical Engineering 2000b; 122:471-477.

- Dubois P, Meseure P, Peugnet F, Rouland JF. Training Simulator for Retinal Laser Photocoagulation: A New Approach for Surgeons, SPIE Conference 3262 on Surgical-Assist Systems, 1998.
- Dubois P, Thommen Q, Jambon AC. *In Vivo* Measurement of Surgical Gestures. IEEE Transactions on Biomedical Engineering 2002; 49:49-54.
- Duck FA. Physical Properties of Tissue, a Comprehensive Reference Book. Boston: Academic Press, Harcourt Brace Jovanovich, 1990.
- Farshad M, Barbezat M, Flueler P, Schmidlin F, Graber P, Niederer P. Material Characterization of the Pig Kidney in Relation with the Biomechanical Analysis of Renal Trauma. Journal of Biomechanics 1999; 32:417-425.
- Febvay S. A Three-Dimensional Constitutive Model for the Mechanical Behavior of Cervical Tissue. Mechanical Engineering. Cambridge, MA: Massachusetts Institute of Technology, 2003:144.
- Febvay S, Socrate S, House MD. Biomechanical Modeling of Cervical Tissue. A Quantitative Investigation of Cervical Funneling, ASME International Mechanical Engineering Congress and Exposition (IMECE), Washington, DC, November 16-21, 2003, 2003.
- Fung YC. Biomechanics: Mechanical Properties of Living Tissues. New York: Springer-Verlag, 1993:568.
- Fung YC. A First Course in Continuum Mechanics. Englewood Cliffs, NJ: Prentice Hall, 1994.
- Gaba D, Fish K, Howard S. Anesthesia Crisis Resource Management. New York: Churchill Livingstone, 1994.
- Gallagher AG, Cates CU. Approval of Virtual Reality Training for Carotid Stenting: What This Means for Procedural-Based Medicine. JAMA 2004; 292:3024-3026.
- Gallagher RH, Simon BR, Johnson PC, Gross JF. Finite Elements in Biomechanics. New York: John Wiley & Sons, 1982:404.
- Gandsas I. History of Laparoscopy: www.laparoscopyhospital.com, 2005.
- Gao L, Parker KJ, Lerner RM, Levinson SF. Imaging of the Elastic Properties of Tissue - a Review. Ultrasound in Medicine & Biology 1996; 22:959-977.
- Gefen A, Margulies S. Are in Vivo and in Situ Brain Tissues Mechanically Similar? Journal of Biomechanics 2004a; 37:1339-1352.
- Gefen A, Margulies S. Are in Vivo and in Situ Brain Tissues Mechanically Similar? Journal of Biomechanics 2004b; 37:1339-1352.
- Gordan JA. Bringing Good Teaching Cases "to Life" in Undergraduate Medical Education: A Case-Study of a Simulator-Based Medical Education Service, 10th International Ottawa Conference on Medical Education, Ottawa, Canada, 2002.
- Gordan JA, Pawlowski J. Education on-Demand: The Development of a Simulator-Based Medical Education Service. Academic Medicine 2002; 77:751-752.
- Gordan JA, Wilkerson WM, Shaffer DW, Armstrong EG. "Practicing" Medicine without Risk: Student's and Educators' Response to High-Fidelity Patient Simulation. Academic Medicine 2001; 76:469-472.

- Grantcharov TP, Kristiansen VB, Bendix J, Bardram L, Rosenberg J, Funch-Jensen P. Randomized Clinical Trial of Virtual Reality Simulation for Laparoscopic Skills Training. *British Journal of Surgery* 2004; 91:146-150.
- Gray H. *Gray's Anatomy*. In: Pick TP, Howden R, eds. *The Classic Collectors Edition*. New York: Gramercy Books, 1977:1257.
- Guyton AC, Hall JE. *Textbook of Medical Physiology*. Philadelphia: W. B. Saunders Company, 1996:1148.
- Hayashi K. *Mechanical Properties and Histological Structure of Soft Tissues, Advanced Course in Soft Tissue Biomechanics*, Udine, Italy, in press, 2001. Springer-Verlag.
- Holmes S. *Liver in Situ*. University of Texas Liver Center, 2003.
- Holzapfel GA. *Nonlinear Solid Mechanics: A Continuum Approach for Engineering*. West Sussex, England: John Wiley & Sons Ltd., 2000.
- Howe RD, Matsuoka Y. Robotics for Surgery. *Annual Review of Biomedical Engineering* 1999; 1:211-240.
- Hu, Desai. A Biomechanical Model of the Liver for Reality-Based Haptic Feedback, MICCAI, 2003.
- Hu T, Desai JP. Characterization of Soft-Tissue Material Properties: Large Deformation Analysis, International Symposium on Medical Simulation, Cambridge, MA, 2004. Springer.
- Humphrey JD. Continuum Biomechanics of Soft Biological Tissues. *Proc. R. Soc. Lond. A* 2002:1-43.
- Hutter R, Schmitt K-U, Niederer P. Mechanical Modeling of Soft Biological Tissues for Application in Virtual Reality Based Laparoscopy Simulators. *Technology and Health Care* 2000; 8:15-24.
- Jordan P, Kerdok AE, Socrate S, Howe RD. Breast Tissue Parameter Identification for a Nonlinear Constitutive Model, Biomedical Engineering Society Annual Meeting, Baltimore, MD, 2005a.
- Jordan P, Zickler T, Socrate S, Howe R. Non-Rigid Soft Tissue Tracking with Three Dimensional Ultrasound, 4th International Conference on the Ultrasonic Measurement and Imaging of Tissue Elasticity, Austin, TX, 2005b.
- Kalanovic, Ottensmeyer MP, Gross, Buess, Dawson. Independent Testing of Soft Tissue Viscoelasticity Using Indentation and Rotary Shear Deformations, MMVR, 2003.
- Kauer M, V. Vuskovic, J. Dual, G. Szekely, M. Bajka. Inverse Finite Element Characterization of Soft Tissues, Medical Image Computing and Computer-Assisted Intervention - MICCAI, Utrecht, The Netherlands, 2001. Springer.
- Kerdok AE, Howe RD. A Technique for Measuring Mechanical Properties of Perfused Solid Organs, ASME Summer Bioengineering Conference, Key Biscayne, FL, 2003.
- Kerdok AE, Ottensmeyer MP, Howe RD. The Effects of Perfusion on the Viscoelastic Characteristics of Liver. *Journal of Biomechanics* 2005; In Press.
- Kim J, Tay B, Stylopoulos N, Rattner DW, Srinivasan MA. Characterization of Intra-Abdominal Tissues from in Vivo Animal Experiment for Surgical Simulation, MICCAI, 2003.

- Krouskop TA, Wheeler TM, Kallel F, Garra BS, Hall T. Elastic Moduli of Breast and Prostate Tissues under Compression. *Ultrasonic Imaging* 1998; 20:260-274.
- Kuhn W, Gruhn F. Beziehungen Zwischen Elastischen Konstanten Und Dehnungsdoppelbrechung Hochelastischer Stoffe. *Kolloid-Z* 1942; 101:248-271.
- Kuhnappel UG, Kuhn C, Hubner M, Krumm HG, MaaE H, Neisius B. The Karlsruhe Endoscopic Surgery Trainer as an Example for Virtual Reality in Medical Education. *Minimally Invasive Therapy and Allied Technologies* 1997; 6:122-125.
- Lagarias JC, J. A. Reeds JA, Wright MH, Wright PE. Convergence Properties of the Nelder-Mead Simplex Method in Low Dimensions. *SIAM Journal of Optimization* 1998; 9:112-147.
- Liu A, Tendick F, Cleary K, Kaufmann C. A Survey of Surgical Simulation: Applications, Technology, and Education. *Presence* 2003; 12:599-614.
- Liu Y, Kerdok AE, Howe RD. A Nonlinear Finite Element Model of Soft Tissue Indentation, Second International Symposium on Medical Simulation, Boston, MA, 2004. Springer Verlag.
- Liu Z, Bilston L. On the Viscoelastic Character of Liver Tissue: Experiments and Modeling of the Linear Behavior". *Biorheology* 2000; 37:191-201.
- Liu Z, Bilston LE. Large Deformation Shear Properties of Liver Tissue. *Biorheology* 2002; 39:735-742.
- Maaß H, Kuhnappel U. Noninvasive Measurement of Elastic Properties of Living Tissue, 13th International Congress of Computer Assisted Radiology and Surgery (CARS '99), Paris, France, June 23-26, 1999. Elsevier.
- Marko JF, Siggia ED. Stretching DNA. *Macromolecules* 1995; 28:8759-8770.
- Meadows M. Computer-Assisted Surgery: An Update. *FDA Consumer Magazine*. Vol. July-August, 2005.
- Medicine Io. To Err Is Human: Building a Safer Health System. In: Kohn LT, Corrigan JM, Donaldson MS, eds. Washington, D.C.: National Academy Press, 2000.
- Medina M. *Laparoscopic Surgery: The Society of Laparoendoscopic Surgeons*, 2003.
- Melvin JW, Stalnaker RL, Roberts VL. Impact Injury Mechanisms in Abdominal Organs. *SAE Transactions* 1973; 730968:115-126.
- Meseure P, Davanne J, Hilde L, Lenoir J. A Physically-Based Virtual Environment Dedicated to Surgical Simulation, International Symposium on Surgery Simulation and Soft Tissue Modeling (IST4TM), Juan-Les-Pins, France, 2003. Springer-Verlag.
- Miller K. Biomechanics of Soft Tissues. *Med. Sci. Monit* 2000a; 6:158-167.
- Miller K. Constitutive Modeling of Abdominal Organs. *Journal of Biomechanics* 2000b; 33:367-373.
- Miller K. How to Test Very Soft Biological Tissues in Extension? *J. Biomechanics* 2001; 34:651-657.
- Miller K, Chinzei K, Orssengo G, Bednarz P. Mechanical Properties of Brain Tissue in-Vivo: Experiment and Computer Simulation. *J. Biomechanics* 2000a; 33:1369-1376.
- Miller K, Chinzei K, Orssengo G, Bednarz P. Mechanical Properties of Brain Tissue in-Vivo: Experiment and Computer Simulation. *Journal of Biomechanics* 2000b; 33:1369-1376.

- Mitzner W. Hepatic Outflow Resistance, Sinusoid Pressure, and the Vascular Waterfall. *American Journal of Physiology* 1974; 227:513-519.
- Mow VC, Kuei SC, Lai WM, Armstrong CG. Biphasic Creep and Stress Relaxation of Articular Cartilage: Theory and Experiments. *J. Biomechanical Engineering* 1980; 102:73-84.
- Nakata K, Leong GF, Brauer RW. Direct Measurement of Blood Pressures in Minute Vessels of the Liver. *American Journal of Physiology* 1960; 199:1181-1188.
- Nava A, Mazza E, Haefner O, Bajka M. Experimental Observation and Modeling of Preconditioning in Soft Biological Tissues, Second International Symposium on Medical Simulation, Boston, MA, 2004. Springer Verlag.
- Nava A, Mazza E, Kleinermann F, Avis NJ, McClure J. Determination of the Mechanical Properties of Soft Human Tissues through Aspiration Experiments, Medical Image Computing and Computer Assisted Intervention, Toronto, Canada, 2003. submitted paper for review.
- Ottensmeyer M, Salisbury K. In Vivo Data Acquisition Instrument for Solid Organ Mechanical Property Measurement, MICCAI: Medical Image Computing and Computer-Assisted Intervention 4th International Conference, Utrecht, The Netherlands, 2001a. Springer-Verlag.
- Ottensmeyer MP. Minimally Invasive Instrument for in Vivo Measurement of Solid Organ Mechanical Impedance. Department of Mechanical Engineering. Cambridge: Massachusetts Institute of Technology, 2001:165.
- Ottensmeyer MP. In Vivo Measurement of Solid Organ Visco-Elastic Properties, Medicine Meets Virtual Reality 02/10 (MMVR02/10), Newport Beach, CA, 2002. IOS Press.
- Ottensmeyer MP, Salisbury J. In Vivo Data Acquisition Instrument for Solid Organ Mechanical Property Measurement., MICCAI: Medical Image Computing and Computer-Assisted Intervention 4th International Conference, Utrecht, The Netherlands, 2001b. Springer-Verlag.
- Park JB, Lakes RS. *Biomaterials*. New York: Plenum Press, 1992:394.
- Peter SDS, Imber CJ, Friend PJ. Liver and Kidney Preservation by Perfusion. *The Lancet* 2002; 359:604-613.
- Picinbono G, Delingette H, Ayache N. Non-Linear and Anisotropic Elastic Soft Tissue Models for Medical Simulation, ICRA2001: IEEE International Conference Robotics and Automation, Seoul Korea, May 2001, 2001.
- Picinbono G, Dilingette H, Ayache N. Non-Linear Anisotropic Elasticity for Real-Time Surgery Simulation. Sophia Antipolis, France: INRIA, 2004:1-21.
- Picinbono G, Lombardo J-C, Delingette H, Ayache N. Improving Realism of a Surgery Simulator: Linear Anisotropic Elasticity, Complex Interactions and Force Extrapolation. *Journal of Visualization and Computer Animation* 2002; 13:147-167.
- Platz KP, Mueller AR, Schafer C, Jahns S, Guckelberger O, Nehaus P. Influence of Warm Ischemia Time on Graft Function in Human Liver Transplantation. *Transplantation Proceedings* 1997; 29:3458-3459.
- Prevost TP. *Biomechanics of the Human Chorioamnion*. Materials Science and Engineering. Cambridge, MA: Massachusetts Institute of Technology, 2006.

- Rasmussen A, Skak C, Kristensen M, Ott P, Kirkegaard P, Secher NH. Preserved Arterial Flow Secures Hepatic Oxygenation During Haemorrhage in the Pig. *Journal of Physiology* 1999; 516.2:539-548.
- Rolfe J, Staples K. *Flight Simulation*. Cambridge, U.K.: Cambridge University Press, 1986.
- Rosen J, Brown JD, Chang L, Barreca M, Sinanan M, Hannaford I. The Bluedragon - a System for Measuring the Kinematics and Dynamics of Minimally Invasive Surgical Tolls in-Vivo, IEEE International Conference on Robotics and Animation, Washington, DC, 2002.
- Rosen J, Hannaford B, MacFarlane MP, Sinanan MN. Force Controlled and Teleoperated Endoscopic Grasper for Minimally Invasive Surgery - Experimental Performance Evaluation. *IEEE Transactions on Biomedical Engineering* 1999; 46:1212-1221.
- Rossi L. *New Organ Preservation Solution Easier to Use*. Vol. 2003: University of Pittsburg Medical Center, 2003.
- Rubin MB, Bodner SR. A Three-Dimensional Nonlinear Model for Dissipative Response of Soft Tissue. *International Journal of Solids and Structures* 2002; 39:5081-5099.
- Saraf H, Ramesh KT, Lennon AM, Merkle AC, Roberts JC. Mechanical Properties of Soft Human Tissues under Dynamic Loading. *Journal of Biomechanics* 2005; In Press.
- Satava R. *Robotics Science and Systems Workshop on Surgical Simulation*, 2005.
- Schon M, Kollmar O, Wolf S, et al. Liver Transplantation after Organ Preservation with Normothermic Extracorporeal Perfusion. *Annals of Surgery* 2001; 233:114-123.
- Seki S, Iwamoto H. Disruptive Forces for Swine Heart, Liver, and Spleen: Their Breaking Stresses. *Journal of Trauma* 1998a; 45:1079-1083.
- Seki S, Iwamoto H. Disruptive Forces for Swine Heart, Liver, and Spleen: Their Breaking Stresses. *J. Trauma* 1998b; 45:1079-1083.
- Seymour NE, Gallagher AG. Virtual Reality Training Improves Operating Room Performance. *Annals of Surgery* 2002; 236:458-464.
- Snedeker JG, Barbezat M, Niederer P, Schmidlin FR, Farshad M. Strain Energy Density as a Rupture Criterion for the Kidney: Impact Tests on Porcine Organs, Finite Element Simulation, and a Baseline Comparison between Human and Porcine Tissues. *Journal of Biomechanics* 2005a; 38:993-1001.
- Snedeker JG, Niederer P, Schmidlin FR, et al. Strain-Rate Dependent Material Properties of the Porcine and Human Kidney Capsule. *Journal of Biomechanics* 2005b; 38:1101-1021.
- Socrate S, Boyce MC. A Constitutive Model for the Large Strain Behavior of Cartilage, ASME Summer Bioengineering Conference, 2001. Vol. 50. ASME.
- Strumas N, Antonyshyn O, Yaffe MJ, Mawdsley G, Cooper P. Computed Tomography Artifacts: An Experimental Investigation of Causative Factors. *Canadian Journal of Plastic Surgery* 1998; 6:23-29.
- Suh J-K, Spilker RL. Indentation Analysis of Biphasic Articular Cartilage: Nonlinear Phenomena under Finite Deformation. *J. Biomechanical Engineering* 1994; 116:1-9.

- Suki B, Majumdar A, Brewer KK, Parameswaran H, Lutchan K. Lung Tissue Viscoelasticity: From Fibers to Constitutive Equations, Biomedical Engineering Society Annual Meeting, Baltimore, MD, 2005.
- Szekely G, Brechbuhler C, Dual J, Et. a. Virtual Reality-Based Simulation of Endoscopic Surgery. *Presence* 2000a; 9:310-333.
- Szekely G, Brechbuhler C, Hutter R, Rhomberg A, Ironmonger N, Schmid P. Modeling of Soft Tissue Deformation for Laparoscopic Surgery Simulation. *Medical Image Analysis* 2000b; 4:57-66.
- Tay BK, Stylopoulos N, De S, Rattner DW, Srinivasan MA. Measurement of *in-Vivo* Force Response of Intra-Abdominal Soft Tissues for Surgical Simulation, *Medicine Meets Virtual Reality*, 2002. IOS Press.
- Tendick F, Downes M, Goktekin T, et al. A Virtual Environment Testbed for Training Laparoscopic Surgical Skills. *Presence* 2000; 9:236-255.
- Tholey G, Pillarisetti A, Green W, Desai JP. Design, Development, and Testing of an Automated Laparoscopic Grasper with 3-D Force Measurement Capability, *Second International Symposium on Medical Simulation*, Boston, MA, 2004. Vol. 8. Springer Verlag.
- Thomas CL. *Taber's Cyclopedic Medical Dictionary*. Philadelphia: F. A. Davis Company, 1997:2446.
- Tonuk E, Silver-Thorn MB. Nonlinear Elastic Material Property Estimation of Lower Extremity Residual Limb Tissues. *IEEE Transactions on Neural Systems and Rehabilitation Engineering* 2003; 11:42-53.
- Tullius SG, Filatenkow A, Horch D, et al. Accumulation of Crystal Deposits in Abdominal Organs Following Perfusion with Defrosted University of Wisconsin Solutions. *American Journal of Transplantation* 2002; 2:627.
- Umehara M, Totsuka E, Ishizawa Y, Nara M, Hakamada K, Sasaki M. In Vitro Evaluation of Cross-Circulation System Using Semipermeable Membrane Combined with Whole Liver Perfusion. *Transplantation Proceedings* 2004; 36:2349-2351.
- Valtorta D, Mazza E. Dynamic Measurements of Soft Tissue Viscoelastic Properties with a Torsional Resonator Device, *MICCAI*, 2004. Springer-Verlag.
- Vuskovic V, Kauer M, Dual J, Bajka M. Method and Device for in-Vivo Measurement of Elasto-Mechanical Properties of Soft Biological Tissues. *Machine Graphics and Vision* 1999; 8:637-654.
- Wahlberg J, Southard J, Belzer F. Development of a Cold Storage Solution for Pancreas Preservation. *Cryobiology* 1986; Dec 23:477-82.
- Wellman PS. *Tactile Imaging*. Division of Engineering and Applied Sciences. Cambridge: Harvard University, 1999:137.
- Wu X, Downes MS, Goktekin T, Tendick F. Adaptive Nonlinear Finite Elements for Deformable Body Simulation Using Dynamic Progressive Meshes, *Eurographics 2001, Computer Graphics Forum*, 2001. Vol. 20.
- Yamada H. *Strength of Biological Materials*. Baltimore: The William & Wilkins Company, 1970.
- Yeh W-C, Li P-C, Jeng Y-M, et al. Elastic Modulus Measurements of Human Liver and Correlation with Pathology. *Ultrasound in Medicine & Biology* 2002; 28:467-474.

- Zhang M, Zheng YP, Mak AF. Estimating the Effective Young's Modulus of Soft Tissues from Indentation Tests - Nonlinear Finite Element Analysis of Effects of Friction and Large Deformation. *Med. Eng. Phys.* 1997; 19:512-517.
- Zheng YP, Mak AFT. Extraction of Quasi-Linear Viscoelastic Parameters for Lower Limb Soft Tissues from Manual Indentation Experiment. *J. Biomechanical Engineering* 1999; 121:330-339.
- Zhu CJ, Wang CC-B. *Biphasic Theory for Hydrated Soft Tissues*: New York Orthopaedic Hospital Research Laboratory, 1998.